Investigating the influence of nucleobase interactions on block copolymer self-assembly in aqueous solution

by

Marjolaine Thomas



A thesis submitted to the University of Birmingham for the degree of
DOCTOR OF PHILOSOPHY

School of Chemistry
College of Engineering and Physical Sciences
University of Birmingham
March 2022

UNIVERSITY OF
BIRMINGHAM

University of Birmingham Research Archive

e-theses repository

This unpublished thesis/dissertation is copyright of the author and/or third parties. The intellectual property rights of the author or third parties in respect of this work are as defined by The Copyright Designs and Patents Act 1988 or as modified by any successor legislation.

Any use made of information contained in this thesis/dissertation must be in accordance with that legislation and must be properly acknowledged. Further distribution or reproduction in any format is prohibited without the permission of the copyright holder.

Abstract

Nucleobase-containing synthetic polymers have been extensively studied for their ability to mimic DNA and for their specific and complementary hydrogen-bonding interactions. The primary aim of this thesis was to explore the pathway dependence of morphologies from polymer self-assemblies through interactions between complementary nucleobase-containing polymers synthesize *via* reversible addition-fragmentation chain-transfer (RAFT) polymerization. In Chapter 1, nucleobase-containing acrylamide monomers were synthesized, and their corresponding synthetic diblock copolymers were prepared *via* RAFT polymerization. Well defined thymine-containing spherical micelles were formed in aqueous solution *via* self-assembly of the amphiphilic copolymers, with the nucleobase-containing segments in the core of the nanoparticles. Following the self-assembly, copolymers with the complementary nucleobase were introduced into the micellar solutions. The influence of the core and/or the corona block length on this morphological transformation mechanism was studied, and these results highlighted that by making straightforward adjustments to the polymers involved in the process, nanoparticle dimensions could be tuned in a control manner.

A novel methodology for the fabrication of nucleobase-containing nano-objects of controllable size and shapes was then developed in Chapter 3, polymerization-induced self-assembly (PISA) in aqueous solutions. It was employed for *in situ* preparation of nucleobase-containing block copolymers nano-objects *via* aqueous reversible addition-fragmentation chain-transfer (RAFT) polymerization allowing to access long adenine-containing polymer chains at relatively high concentrations and highlighted the potential of this method for understanding fundamental self-assembly process during PISA route. Various nano-objects of different morphologies were obtained by this method (*i.e.*,

spheres, worms, and vesicles), and access to higher DPs compared to conventional RAFT polymerization was achieved. This work highlights the potential of aqueous RAFT-mediated PISA as a method to access longer polymer chains for adenine-functionalized monomer and these nano-objects as platforms for understanding fundamental self-assembly process during the PISA process.

In particular in Chapter 4,vesicles adenine nano-objects (**PAn**) showed a controlled shape transformation induced by the addition of a complementary base-paired polymer. The addition of a complementary short thymine polymer (**$PT_{20}n$**) into a **PAn** solution induced deformations into the vesicular membrane of **PAn** and increasing the amount of **$PT_{20}n$** led to node growth and eventual detachment. .Quantitative analysis of nano-object shapes revealed that the extent of deformation of **PAn** correlated to the amount of added **$PT_{20}n$**. Confocal experiments confirmed that the shape transformation was due to the complementary interaction of the nucleobase moieties contained in the block copolymers. This result suggests that vesicle shape transformations can be controlled by externally added a complementary nucleobase-containing to the membrane, which can serve as a potential method for further understanding of membrane curvature process. Furthermore, polymer insertion induced shape changing could open up new routes for the design of new functional complex shapes nanocarriers and nanomachines for diverse applications.

A mon père

Acknowledgements

If I had to describe my PhD it will be a multiple of small stories into a big one, my time here was filled with different adventures. I like to use this word, because for me life is an adventure and we are here to explore, enjoy and learn from every single one of them.

I am grateful to have shared so many memories for these past three and a half years with amazing people, in as well as outside the lab.

First, I would like to thank my supervisor, Professor Rachel O'Reilly, for providing me the opportunity to work in her group. I am grateful for your guidance and mentorship over the past 3 years. I'm very happy and proud to have been able to smuggle some French cheese for you.

I would like to thank Dr. Tom Wilks, who has been for me my second supervisor. Thank you for your help, guidance and patience and great discussions we had.

Next, I would like to thank my friends from the O'Reilly and Dove groups who have made my everyday life in the lab a fun and memorable experience and supported me for more than 3 years. My Mount Fuji gang, Dr Viviane Chiaradia (Oiii, cha-cha-cha and chichi coco) and Dr Yujie Xie (Queen of Figures and Fashion). The Frunch team, Ms Anissa Khalfa (C'est pour toi Daniel), Dr Matthieu Miclotte (More French than Belgium but don't tell him and I know you miss Haworth) and Dr Setuhn Jimaja (or Jumanji pour les intimes, le plus Suisse des Suisses), for the incredible French moments and raclettes parties we shared together. Also, the famous Chinese mafia and the Friday fish and chips crew, Dr Bo Li (King of Shanghai, and like Matthieu said it's true he has a fake Instagram account), Dr Spyridon Varlas (king of PISA and TEM guru), Dr Jeff Foster (I'm still regretting for not bringing a beer on that train), Dr Stefan Lawrenson (Bouge ton cul et pas trop mal to say with a thick English accent) Dr Turgay Yildirim (Waaaaaar, and by

the way Beşiktaş sucks), Dr Wei Yu (Basketball MVP, Hey Wei), Dr Rob Keogh (aka Dr. K.). But also, other group members, Dr Joe Jones (Uncle Joe, the Light scattering boss), Ms Irem Akar (Iremita my grandma biggest fan, I'm sure the cucumber study will go in Nature), Mr Ben Allott (Bennie Ben), Mr David Londono aka Davicito (who spends more time on the 2nd or 6th floor than the office), Mr Maher Alraddadi (Maher my hair, Salam), Ms Ana Alvarez (Dramaaaaaaa, ca va bebe) and Ms Siriporn "Snook" Chaimueangchuen (Bubble Tea lover).

I would like to thank Ms. Cinzia Clamor (I know deep down you're happy about all this GOOD influence), Mr Jan Goelen (The best pharmacist in CDSA) and Mr Simon Dale (hope your knee will make it until the end of your PhD and I'm sure I will find my phone, Club 54), I've met you on our first day and sticked united since, it was a pleasure to do this PhD with you.

A special thanks for my French team from Warwick. I'm glad I've met you during the YRM and enjoyed all these French evenings, Dr. Fannie Burgevin (I know I'm leaving you in this country mais ce n'est qu'un aurevoir), Dr Chris Atkins (don't tell him but it's not his real name). I should probably thank Dr Satu Häkkinen, who without her I would have not met you. Thanks also to all the other people I've met from Warwick it was great to see you every time I was there for Cryo.

On that one, I would like to thank Dr Saskia Bakker for her incredible help and patience during my Cryo-TEM sessions over the past 2 years. But also, the cryo crew over the years, Dr Spyridon Varlas, and Dr Rob Keogh (cryo-cat and cryo-songs) and Ms Alisha Miller (Oh wow) and Dr Stephen Fielden (**Behave!**).

Thank you for your proofreading, Dr Thomas Wilks, Dr Sam Parkinson (team bus 41), and Dr Stephen Fielden. I would also like to thank the research administrator and

technician Ms Tessa Kintail and Ms Julia Valverde for providing their invaluable assistance to me and the rest of the O'Reilly group members and making our lives much easier by sorting out the numerous admin and lab issues over the years.

To my friends in France, thank you for being here for me for my ups and downs and welcoming back every time I was back.

An amazing, unexpected thing that happened to me in the last months. Though unexpected, I'm so grateful that I've met you and shared these precious moments with you. Thank you for believing in me and pushing me to finish this thesis. We don't know what life is made of, and maybe it's for the best as it forces us to live every single moment. I can't wait to see what life has in store for us. Hopefully more (French) wine.

And finally, I would like to thank my family for their constant support during my PhD even though they had not and pretty sure still don't have a clue of what I've been doing (The perk of being the only scientist in the family I guess). My parents Catherine Tissier and Eric Thomas, but also Claire Delaunay and Dominique Doat, thank you.

Pour finir, je dédie cette thèse à mes grands-parents Michel et Annie Tissier, ces quelques mots en français sont pour vous j'espère que vous êtes fiers de moi autant que je suis fière d'être votre petite fille. Également pour vous mamie Carmen et papy Guy vous qui n'êtes plus là, je suis sûre que vous seriez fières. A vous ma famille, je vous aime.

Table of contents

Table of contents I

List of Figures V

List of Schemes XVII

List of Tables XIX

List of Symbols and Abbreviations XXI

List of publications XXIX

Declaration of authorship XXX

1 : Introduction 1

1.1 Mimicking biological functionality with synthetic polymers 2

1.1.1 Mimicking the biological world 2

1.1.2 Introduction to synthetic polymers 2

1.2 Polymerization techniques 4

1.2.1 Controlled radical polymerization 6

1.3 Block copolymer self-assembly in solution 14

1.4 Polymerization-Induced Self-Assembly (PISA) 18

1.5 H-bonding in BCP self-assembly in water 21

1.6 Syntheses of nucleobase-containing synthetic polymers and their self-assembly properties 25

1.6.1 Syntheses of nucleobase-containing synthetic polymers 25

1.6.2 Novel self-assembly properties of nucleobase-containing synthetic polymers 26

1.7 Well-controlled anisotropic polymeric nanoparticles 30
1.7.1 Bottlebrush polymers (BBPs) 30
1.7.2 Polymerization-induced self-assembly 30
1.7.3 Crystallization-driven self-assembly (CDSA) 31
1.7.4 Morphological transformation (MORPH) 32
1.8 Characterization techniques for polymer self-assemblies 35
1.8.1 Electron microscopy 35
1.8.2 Light scattering techniques 38
1.9 Summary 41
1.10 References 42
2 : Nucleobase-containing nanoparticles with pathway dependent morphologies through interactions between complementary nucleobase-containing synthetic polymers in aqueous solutions 60
2.1 Introduction 61
2.2 Results and discussion 64
2.2.1 Synthesis of nucleobase-containing acrylamide monomers TAm and AAm 64
2.2.2 Synthesis and characterization of nucleobase-containing synthetic diblock copolymers 68
2.2.3 Self-assembly of nucleobase-containing diblock copolymers 73
2.2.4 Tuning spherical thymine-containing micelles through complementary nucleobase interactions 79
2.3 Conclusion 86

2.4 General experimental section 87
2.4.1 Materials 87
2.4.2 Instrumentations and analysis 87
2.4.3 Synthetic methods 90
2.5 References 99
3 : Synthesis and characterization of adenine-containing block copolymers prepared *via* aqueous RAFT-mediated PISA 104
3.1 Introduction 105
3.2 Results and discussion 109
3.2.1 RAFT-mediated PISA 109
3.2.2 Study of the vesicle phase 129
3.3 Conclusions 142
3.4 Experimental section 143
3.4.1 Materials 143
3.4.2 Instrumentations and analysis 143
3.4.3 Synthetic methods 143
3.5 References 147
4 : Nucleation, growth, and detachment of worm-like nanoparticles from an isotropic polymersome seed/template 154
4.1 Introduction 155
4.2 Results and discussion 158
4.2.1 Synthesis and characterization of adenine and thymine-containing block copolymers *via* RAFT-mediated PISA 158

4.2.2 Co-assembly of nano-objects 166

4.2.3 Insertion mechanism 179

4.3 Conclusions 191

4.4 Experimental section 192

4.4.1 Materials 192

4.4.2 Instrumentations and analysis 192

4.4.3 Synthetic methods 192

4.5 References 205

4.6 Annex 210

5 : Conclusions and future work 216

Annex 220

List of Figures

Figure 1.1. Different compositions, topologies, and functionalities of polymers. 4

Figure 1.2. Evolution of the molecular weight of polymers *versus* monomer conversion for (A) step-growth polymerization, (B) conventional chain-growth polymerization, and (C) living polymerization. 5

Figure 1.3. Typical structures of chain transfer (or RAFT) agents. 11

Figure 1.4. Guidelines for Selection of the R- and Z-group of RAFT Agents for various polymerizations. The dashed lines represent limited or poor polymerization control. Abbreviations: MMA = methyl methacrylate, HPMAM = *N*-(2-hydroxypropyl)methacrylamide, St = styrene, MA = methyl acrylate, AM = acrylamide, AN = acrylonitrile, VAc = vinyl acetate, NVP =*N*-vinylpyrrolidone, and NVC = *N*-vinylcarbazole. Reproduced from ref. [40] 13

Figure 1.5. Electron microscopy images of various morphologies formed from amphiphilic block copolymer self-assembly in solution. Images reproduced from the following references: spherical micelles,[50] worm-like micelles,[51] lacunal spheres,[52] tubular vesicles,[53] "j jellyfish"-like particles,[54] spherical vesicles,[55] porous vesicles,[56] and large compounds vesicles.[57] 15

Figure 1.6. The different morphologies for amphiphilic block copolymer nano-objects obtained by targeting different packing parameters, p. Figure reproduced from ref. [62] . 16

Figure 1.7. Schematic illustration of the morphological evolution of diblock copolymer nano-objects developed during RAFT-mediated PISA under dispersion polymerization conditions. Reproduced from ref.[82] 19

Figure 1.8. A representative RAFT-PISA system $PGMA_{78}$-*b*-$PHPMA_n$, with its corresponding phase diagram and TEM images of different morphologies Reproduced from ref. [83] 20

Figure 1.9. (a) Monofunctional ureidotriazines **1** and **3** and their mode of association *via* quadruple hydrogen bonds. Structures of bifunctional derivatives **2** and **4** are also shown. (b) A schematic representation of the organization of mixtures of mono- and bifunctional compounds upon increasing the fraction of monofunctional compound. In **I**, columns are formed by the stacking of dimers. In **II** (with p and m corresponding to the right- and left-handed helical conformation, respectively), consecutive disks of dimeric ureidotriazines are connected by hexamethylene spacers. Figure reproduced and adapted from ref.[106]. 22

Figure 1.10. Schematic representations of possible supramolecular structures of a) PEG–PLLA and b) PEG–TU (or U)–PLLA assemblies. Reproduced from ref.[74] 23

Figure 1.11. Synthesis of thiourea-containing PEGylated amphiphiles with different hydrophobic groups such as stearyl amine, oleyl amine, and1-amino dodecanol leading to the formation of different morphologies, rod-like, spherical, and disk-like micelles respectively. Adapted from ref.[108] 24

Figure 1.12. Characterization data of the nanostructures obtained from the self-assembly of diblock copolymers PLLA-*b*-PTHPA and PDLA-*b*-PTHPA. Reproduced from ref.[109] 24

Figure 1.13. Schematic demonstration of vesicle formation between diaminopyridine-based polymer **1** and thymine-based polymer **2**. (a) Illustration showing molecular recognition within vesicle wall. (b) The corresponding recognition dyads. Reproduced from ref.[126] 27

Figure 1.14. Schematic representation of the effect of copolymers compositions and solvents on the self-assembled nanostructures. Reproduced from ref.[119] 28

Figure 1.15. Representative TEM images of self-assemblies prepared by RAFT dispersion polymerization for a target copolymer $PMMA_{220}$-*b*-$PTMA_{50}$ in (a), chloroform; (b), 1,4-dioxane. Scale bar: 100 nm. Reproduced from ref.[127] 29

Figure 1.16. Realization of monodisperse cylindrical micelles through bidirectional epitaxial growth from small, uniform, stub-like crystallites as initiators for the crystallization-driven living self-assembly of PFS block copolymers with a crystallizable, core-forming block. Reproduced from ref.[136] 32

Figure 1.17. Methods for the growth of anisotropic polymer nanostructures with controlled dimensions. Previous efforts have been based on 1-dimensional growth from an anisotropic seed particle (top). We report a qualitatively different process based on the global morphological transformation of an isotropic seed particle (bottom). Reproduced from ref.[142].....33

Figure 1.18. Single-step transformation of spherical nanoparticles into different anisotropic morphologies by MORPH. **a** Schematic representation of MORPH using nucleobase-containing polymers. Spherical nanoparticle **NT** with a thymine-containing core was formed by self-assembly of the polymer **PT** using a solvent switch method from DMF to water. Introduction of the adenine-containing polymer **PA** induced MORPH at A:T molar ratios above 0.20. **b** TEM images of the nanoparticles formed before and after addition of **PA** at different A:T molar ratios to separate solutions of **NT**. Particles were imaged stain-free on graphene oxide (GO). Scale bars = 200 nm. Reproduced from ref.[142] 34

Figure 1.19. Positive and negative staining using heavy metal salts. In negative staining (A) the stain fully envelops the macromolecular complex; in the micrograph the complex appears white on a dark background. Positive staining (B) results in a small amount of stain forming a thin shell around the molecule, meaning the sample appears dark against a light background. Reproduced from ref.[145] 36

Figure 1.20. Examples of vitreous and non-vitreous ice. A) Empty, vitreous ice (Scale bar 50 nm). B) Hexagonal ice (scale bar 400 nm). C) Large ice crystal (white arrow) (scale bar 400 nm). D) Probable ethane contamination (scale bar 200 nm). Reproduced from ref.[145] 38

Figure 2.1. ^{1}H NMR spectrum of 3-(adenine-9-yl) propyl acrylamide (**AAm**) in DMSO-d_6 (500 MHz) 66

Figure 2.2. ^{13}C NMR spectrum of 3-(adenine-9-yl) propyl acrylamide (AAm) in DMSO-d_6 (500 MHz) 66

Figure 2.3.^{1}H NMR spectrum of 3-(thymine-1-yl)propyl acrylamide (**TAm**) in DMSO-d_6 (500 MHz) 67

Figure 2.4. ^{13}C NMR spectrum of 3-(thymine-1-yl)propyl acrylamide (**TAm**) in DMSO-d_6 (500 MHz) 68

Figure 2.5. ^{1}H NMR spectra of $PNAM_{40}$ in D_2O, **PA1** ($PNAM_{40}$-*b*-$PAAm_{20}$) and **PT3** ($PNAM_{40}$-*b*-$PTAm_{288}$) in DMSO-d_6 (400 MHz). 70

Figure 2.6. SEC traces of macro-CTAs chain extended with different PNAM macroCTA, (A) $PNAM_{40}$ (**P1**), **PA1**, **PT1**, **PT2** and **PT3**. (B) $PNAM_{100}$ (**P2**), **PA2** and **PT4** (DMF + 5 mM NH_4BF_4 as eluent, PMMA standard. 71

Figure 2.7. (A), (B), (C), and (D) DLS analysis of self-assembled micelles **MT1**, **MT2**, **MT3** and **MT4** respectively at 0.5 mg mL^{-1}. 74

Figure 2.8. TEM images of self-assembled micelles **MT1**, **MT2**, **MT3** and **MT4** respectively. obtained samples were then imaged by TEM using graphene oxide (GO) grids without staining.[38] 75

Figure 2.9. Histograms of the diameters of PNAM-*b*-PTAm spherical micelles (A) **MT1**, (B) **MT2**, (C) **MT3** and (D) **MT4** as determined by TEM analysis. The TEM image was analysed using the ImageJ software, and over 100 particles were counted to obtain number-average diameter D_n. (E) represents the Dave evolution when increasing either the corona or core block length of the **MT** micelles. 76

Figure 2.10. DLS analysis and corresponding correlogram of self-assemblies **MA1** and **MA2** in water of $PNAM_{40}$-*b*-$PAAm_{20}$, and $PNAM_{100}$-*b*-$PAAm_{20}$. 77

Figure 2.11. Histograms of the diameters of PNAM-*b*-PAAm spherical micelles **MA1** and **MA2** as determined by TEM analysis using graphene oxide (GO) grids without staining.[38] 100 particles were measured and analyzed using imageJ software. 78

Figure 2.12. Dry-state TEM images on GO grids of micelles (a-c) **MT1** after addition of the complementary copolymer **MA1** at (a) A:T = 0.33, (b) A:T = 1 and (c) A:T = 1.33. (b-e) **MT2** after addition of the complementary copolymer **MA1** at (a) A:T = 0.33, (b) A:T = 1 and (c) A:T = 1.33. 80

Figure 2.13. Dry-state TEM images on GO grids of micelles **MT4** after addition of the complementary copolymer **MA1** at (a) A:T = 0.33, (b) A:T = 1 and (c) A:T = 1.33. 82

Figure 2.14. Analysis of lengths (A) and widths (C) of the nanoparticles **MT1**and **MT2** after addition of **MA1**. Analysis of lengths (B) and widths (D) of the nanoparticles **MT4** after addition of **MA2**. 84

Figure 2.15. ^{1}H NMR spectrum of 2-(((butylthio)carbonothioloyl)thio)propanoic acid (CTA) in $CDCl_3$ (400 MHz). 94

Figure 2.16. ^{13}C NMR spectrum of 2-(((butylthio)carbonothiolyl)thio)propanoic acid (CTA) in $CDCl_3$ (400 MHz). 95

Figure 2.17. ^{1}H NMR of the $PNAM_{40}$ macro-CTA in D_2O (300 MHz). 96

Figure 2.18. Normalized molecular weight distribution trace of $PNAM_{40}$macro-CTA (DMSO + 0.1% w/w LiBr as eluent, PMMA standards). 97

Figure 2.19. TEM images of micelle **MT3** (Left) and **MT3** after addition of **MA1** at molar ratio A:T = 1 (right). Dry-state on graphene oxide without stain. 98

Figure 2.20. DLS analysis of micelle **MT3** after addition of **MA1** at molar ratio A:T = 1. 98

Figure 3.1. ^{1}H NMR spectrum of crude of $PNAM_{40}$-b-$PAAm_{200}$ obtained by aqueous RAFT-mediated PISA in DMSO-d_6 (400 MHz). 110

Figure 3.2. SEC traces of different polymerizations of $PNAM_{40}$-b-$PAAm_y$ at 2.5% w/w (DMSO + 0.1% w/w LiBr as eluent, PMMA standards). 111

Figure 3.3. SEC traces of different polymerizations of $PNAM_{40}$-b-$PAAm_y$ at 5% w/w (DMSO + 0.1% w/w LiBr as eluent, PMMA standards). 112

Figure 3.4. SEC traces of different polymerizations of $PNAM_{40}$-b-$PAAm_y$ at 10% w/w (DMSO + 0.1% w/w LiBr as eluent, PMMA standards). 113

Figure 3.5. Pseudo phase diagram for $PNAM_{40}$-b-$PAAm_y$ diblock copolymer nanoparticles prepared by aqueous RAFT-mediated PISA using VA-044 initiator at 50 °C. The diblock copolymer morphologies were assigned by dry-state TEM stained with 1% w/w uranyl acetate (UA) solution. (Key: S – spheres, W – worm-like micelles, V – vesicles. N.P.: No polymer obtained. 116

Figure 3.6. TEM images of $PNAM_{40}$-b-$PAAm_{20}$ diblock copolymer nanoparticles prepared by aqueous RAFT-mediated PISA using VA-044 initiator at 50 °C at 2.5, 5 and 10% w/w. The samples were stained with 1% w/w uranyl acetate (UA) solution. 117

Figure 3.7. DLS (A,C and E) and corresponding correlogram (B, D and F) graph results of $PNAM_{40}$-*b*-$PAAm_{20}$ nano-objects obtained *via* aqueous RAFT-mediated PISA at 2.5, 5 and 10% w/w. 118

Figure 3.8. TEM images of $PNAM_{40}$-b-$PAAm_{28}$ diblock copolymer nanoparticles prepared by aqueous RAFT-mediated PISA using VA-044 initiator at 50 °C at 2.5, 5 and 10% w/w. The samples were stained with 1% w/w uranyl acetate (UA) solution. 119

Figure 3.9. DLS (A,C and E) and corresponding correlogram (B, D and F) graph results of PNAM40-b-PAAm28 nano-objects obtained *via* aqueous RAFT-mediated PISA at 2.5, 5 and 10% w/w. 120

Figure 3.10. TEM images of $PNAM_{40}$-b-$PAAm_{50}$ diblock copolymer nanoparticles prepared by aqueous RAFT-mediated PISA using VA-044 initiator at 50 °C at 2.5, 5 and 10% w/w. The samples were stained with 1% w/w uranyl acetate (UA) solution. 121

Figure 3.11. DLS (A,C and E) and corresponding correlogram (B, D and F) graph results of $PNAM_{40}$-*b*-$PAAm_{50}$ nano-objects obtained *via* aqueous RAFT-mediated PISA at 2.5, 5 and 10% w/w. 122

Figure 3.12. TEM images of $PNAM_{40}$-b-$PAAm_n$ diblock copolymer nanoparticles prepared by aqueous RAFT-mediated PISA using VA-044 initiator at 50 °C at 2.5, 5 and 10 % w/w at DP ≥ 100. The samples were stained with 1% w/w uranyl acetate (UA) solution. 123

Figure 3.13. DLS (A,C,E,G,I,K and M) and corresponding correlogram (B, D, F, H, J, L and FN) graph results of $PNAM_{40}$-*b*-$PAAm_n$ nano-objects obtained *via* aqueous RAFT-mediated PISA at 2.5, 5 and 10% w/w for DPs ≥ 100. 126

Figure 3.14. Representative cryo-TEM images of PNAM-b-$PAAm_y$ diblock copolymers vesicle nano-objects at different DP and [solids] along with their corresponding membrane thicknesses measured over at least 100 particles using image J. 130

Figure 3.15. Top image, the degree of polymerization of PAAm at different solids concentration versus the vesicle membrane thickness, (the error bars represent the standard deviation from 100 measurements). With the corresponding table (bottom). 131

Figure 3.16. Representation of the difference in the polymer core block chain length (A),packing (B) and aggregation number (N_{agg}) (C) on the size of the vesicles which could explain the difference in the membrane thickness. 133

Figure 3.17. DLS analysis of the reassembled particles obtained by solvent-switch method at different DP and % w/w and their corresponding correlograms. 137

Figure 3.18. Comparison of PISA and reassembled particles by dry-state TEM. The top images show the TEM images of the PISA particles at different DP and % w/w. The bottom ones show the results for the reassembled particles. Using 1% w/w uranyl acetate (UA) solution for staining. 138

Figure 3.19. Comparison of PISA and reassembled particles by cryo-TEM. The top images show the cryo-TEM images of the PISA particles at different DP and % w/w. The bottom ones show the results for the reassembled particles. 139

Figure 3.20. Comparison between Hu *et al.* paper and this study on the formation of multicompartment vesicles. The circled area correspond to the similar parameters used in both studies, adapted from ref.[49] 140

Figure 3.21. Normalized molecular weight distribution trace of $PNAM_{40}$macro-CTA (DMSO + 0.1% w/w LiBr as eluent, PMMA standards). 144

Figure 4.1. ^1H NMR spectra of (A) $PNAM_{40}$ macroCTA in D_2O, (B) crude $PNAM_{40}$-b-$PTAm_{20}$ (**PT_{20}**) and (C) crude $PNAM_{40}$-b-$PAAm_{200}$ (**PA1**) obtained by aqueous RAFT-mediated PISA recorded in DMSO-d_6 (400 MHz). 159

Figure 4.2. Combined SEC traces of $PNAM_{40}$ macroCTA, **PT_{20}**, **PA1** and **PA2** (recorded in DMSO + 0.1% w/w LiBr as eluent, PMMA standards). 161

Figure 4.3. (a, c) TEM images of **PA1n** and **PA2n** and (b, d) CryoTEM images of **PA1n** and **PA2n**, respectively. (a, c) The samples were stained with 1% w/w uranyl acetate (UA) solution. 163

Figure 4.4. DLS (A, C) and corresponding correlogram (B, D) graph results of **PA1** and **PA2** respectively. 164

Figure 4.5. TEM image of **PT_{20}n** ($PNAM_{40}$-b-$PTAm_{20}$) diblock copolymer nanoparticles. The sample was stained with 1% w/w uranyl acetate (UA) solution. ... 164

Figure 4.6. DLS and corresponding correlogram graph results of short thymine-containing block copolymer **PT_{20}n**. 165

Figure 4.7. Particles with different morphologies were prepared through mixing complementary **PT_{20}n** solution into the initial spherical micelle **PA1n** under stirring at room temperature. Dry-state TEM images **PA1n** after adding **PT_{20}n** with variable molar ratios of T:A: 0.2, 0.33, 0.67, 1.00, 1.33, 1.5, 2 and 2.5. 168

Figure 4.8. CryoTEM images of nanoparticles **PA1n** before and after adding **PT_{20}n** with variable molar ratios of **T:A** 1.00, 1.33, 2 and 2.5. 170

Figure 4.9. Number of nodes per **PA1n** particles at T:A ratios of 0.2, 0.33, 0.67, 1, 1.33, 1.5, 2 and 2.5. 100 particles were analysed for each T:A ratio. 172

Figure 4.10. Quantitative analysis of the particles obtained at different T:A ratios. (A) Size obtained by DLS versus TEM, (B) Membrane thicknesses of **PA1n**, (C) number of nodes per particles and (D) length of the nodes per particles at different molar ratios, respectively. Particle counting and measurement were done over 100 particles for each parameter. The error bars represent the standard deviation. 174

Figure 4.11. Dry-state TEM images **PA2n** after adding **$PT_{20}n$** with variable molar ratios of T:A 0.2, 0.33, 1.00, 1.33, 2 and 2.5. 175

Figure 4.12. CryoTEM images of **PA2n** after adding **$PT_{20}n$** with variable molar ratios of T:A 1.00, 1.33 and 2. 177

Figure 4.13. (A) Size obtained by DLS versus TEM per particle at different molar ratios (B) Length of the nodes per particle at different molar ratios. Particle counting and measurement were done over 100 particles for each parameter. The error bars represent the standard deviation. 178

Figure 4.14. Control experiments. Dry state TEM images of the addition of short block copolymers with either partially blocked (**$PT^{Me}_{20}n$**) or non-complementary H-bonding (**$PA_{20}n$**) onto **PA1n** vesicles. Dry-state samples were stained using 1% w/w uranyl acetate (UA) solution. 180

Figure 4.15. (A) and (C) combined DLS and corresponding correlogram graph (B) and (D) results of mixing experiments of **PA1n** with a short adenine-containing block copolymer **$PA_{20}n$** or a methylated short thymine-containing block **$PT^{Me}_{20}n$** respectively. 181

Figure 4.16. Control experiments. Dry state TEM images representing the sequential addition of **$PT_{20}n$** in **PA1n** solution (top) and 1 **$PT_{20}n$** + 0.33 **$PT^{Me}_{20}n$** in **PA1n** solutions (bottom). Dry-state samples were stained using 1% w/w uranyl acetate (UA) solution.

Histogram representing the length of the nodes (length measured over at 100 particles using image J). 183

Figure 4.17. (A) Combined SEC traces of $PNAM_{40}$ macroCTA^{Gr} and **PA2^{Gr}** and (B) combined SEC traces of $PNAM_{40}$ macroCTARd and **PTRd** (DMSO + 0.1% w/w LiBr as eluent, PMMA standards). 185

Figure 4.18. Representative confocal microscopy images for pure **PA2n** (green; A) and **PT_{20}n** (red; B) diblock copolymer nano-objects and resulting samples for investigation of mixing of **PA2n** and **PT_{20}n** at molar ratio T:A = 1. The scale bars are indicated in the images and the size of the insets is 10μm×10μm. Bottom row represents the cryo-TEM images (**PA2^{Gr}** and **PA2^{Gr}** + **PT$^{Rd}_{20}$**) and dry state (**PT$^{Rd}_{20}$**) of the corresponding experiments. Dry-state samples were stained using 1% w/w uranyl acetate (UA) solution. 187

Figure 4.19. ^{1}H NMR spectrum of 3-(3-methylthymin-1-yl)-propylacrylamide (T^{Me}Am) in DMSO-d_6 (400 MHz). 194

Figure 4.20. ^{13}C NMR spectrum of 3-(3-methylthymin-1-yl)-propylacrylamide (T^{Me}Am) in DMSO-d_6 (500 MHz). 195

Figure 4.21. Normalized molecular weight distribution trace of $PNAM_{40}$ macro-CTA (DMSO + 0.1% w/w LiBr as eluent, PMMA standards). 196

Figure 4.22. Representative ^{1}H-NMR spectra of crude ($PNAM_{40}$-*b*-PT$^{Me}Am_{20}$) **PT$^{Me}_{20}$** and $PNAM_{40}$-b-$PAAm_{20}$ (**PA_{20}**) obtained by aqueous RAFT-mediated PISA recorded in DMSO-d_6 (400 MHz). 198

Figure 4.23. Normalized molecular weight distribution trace of $PNAM_{40}$ macro-CTA, **PT$^{Me}_{20}$** ($PNAM_{40}$-*b*-PT$^{Me}Am_{20}$) and **PA_{20}** ($PNAM_{40}$-*b*-$PAAm_{20}$) (DMSO + 0.1% w/w LiBr as eluent, PMMA standards). 199

Figure 4.24. DLS (A) (C) and corresponding correlogram (B) (D) graph results of the short adeinine-containing block copolymer **PA$_{20}$** and methylated short thymine-containing block copolymer **PT$^{Me}_{20}$** respectively used in control experiments to demonstrate that complementary H-bonding interactions was needed to observe a shape transformation of the seed particles. 200

Figure 4.25. ^{1}H NMR spectra of PNAM$_{40}$ mCTARd, PNAM$_{40}$ mCTA^{Gr}, and unmodified PNAM$_{40}$ recorded in DMSO-d_6 (500 MHz). 202

Figure 4.26. Normalized molecular weight distribution trace of poly(4-acryolylmorpholine)$_{40}$ (PNAM$_{40}$) **mCTA^{Gr}** with BODIPY FL (left) and poly(4-acryolylmorpholine)$_{40}$ (PNAM$_{40}$) **mCTARd** with BODIPY 630/650 (right). (DMSO + 0.1% w/w LiBr as eluent, PMMA standards). 202

Figure 4.27. TEM images for **PA2^{Gr}** and **PT$^{Rd}_{20}$** (A) and (B) respectively. DLS results for, **PA2^{Gr}** and **PT$^{Rd}_{20}$** (C) and (D) respectively and their corresponding correlogram (E) and (F). 204

Figure 4.28. DLS results of the MORPH PISA mixing experiments of **PA1n** at different ratios of A:T. 212

Figure 4.29. DLS results of the MORPH PISA mixing experiments of **PA2n** at different ratios of A:T. 214

List of Schemes

Scheme 1.1. Mechanism of nitroxide mediated polymerization. Reproduced from ref [29]8

Scheme 1.2. Reaction mechanism of atom transfer radical polymerization. Adapted from ref.[35].....9

Scheme 1.3. Mechanism of Reversible Addition–Fragmentation Chain Transfer Polymerization. Reproduced from ref. [40] 11

Scheme 2.1. Syntheses of adenine and thymine acrylamide monomers (AAm and TAm). 65

Scheme 2.2. Synthetic routes for the preparation of $PNAM_{40}$ and $PNAM_{100}$, **P1** and **P2** respectively and the nucleobase-containing block copolymers, **PA1** ($PNAM_{40}$-*b*-$PAAm_{20}$)**, PA2** ($PNAM_{100}$-*b*-$PAAm_{20}$), **PT1** ($PNAM_{40}$-*b*-$PAAm_{100}$), **PT2** ($PNAM_{40}$-*b*-$PAAm_{200}$), **PT3** ($PNAM_{40}$-*b*-$PAAm_{300}$) and **PT4** ($PNAM_{100}$-*b*-$PAAm_{300}$).....69

Scheme 2.3. Synthesis of 2-(((butylthio)carbonothiolyl)thio)propanoic acid (CTA). ...94

Scheme 2.4. Synthesis of poly(4-acryolylmorpholine)$_{40}$ ($PNAM_{40}$) macro-CTA. 96

Scheme 3.1. Synthesis of $PNAM_{40}$-*b*-$PAAm_y$ diblock copolymer nano-objects by aqueous RAFT-mediated polymerization-induced self-assembly (PISA). 110

Scheme 3.2. Synthesis of poly(4-acryolylmorpholine)$_{40}$ ($PNAM_{40}$) macro-CTA. 144

Scheme 4.1. Schematic representation of the synthetic route followed for the development of **$PNAM_{40}$-*b*-$PAAm_n$** diblock copolymer nano-objects *via* aqueous RAFT-mediated PISA, sing a water-soluble $PNAM_{40}$ macroinitiator. 158

Scheme 4.2. Synthesis of $PNAM_{40}$-*b*-$PTAm_{20}$ (**PT_{20}**) diblock copolymer nano-objects by aqueous RAFT-mediated polymerization-induced self-assembly. 159

Scheme 4.3. Synthesis of **PA^{Gr}** diblock copolymer nano-objects by aqueous RAFT-mediated polymerization-induced self-assembly (PISA).....184

Scheme 4.4. Synthesis of **PTRd** diblock copolymer nano-objects by aqueous RAFT-mediated polymerization-induced self-assembly (PISA).....184

Scheme 4.5. Synthesis of poly(4-acryolylmorpholine)$_{40}$ (PNAM$_{40}$) macro-CTA. 195

Scheme 4.6. Synthesis of poly(4-acryolylmorpholine)$_{40}$ (PNAM$_{40}$) **mCTA^{Gr}** with BODIPY FL. 201

Scheme 4.7. Synthesis of poly(4-acryolylmorpholine)$_{40}$ (PNAM$_{40}$) **mCTARd** with BODPI 630/650.....201

List of Tables

Table 2.1. Characterization data of macro-CTA and nucleobase-containing diblock copolymers. 72

Table 2.2. Summary of DLS and TEM characterization data of micelles **MT1-4**..... 76

Table 2.3. Summary of DLS and TEM characterization data of micelles **MA1** and **MA2**. 78

Table 2.4. Summary of DLS and TEM characterization data of morphological transformation of **MT1** with the addition of **MA1** at different A:T molar ratios. 81

Table 2.5. Summary of DLS and TEM characterization data of morphological transformation of **MT2** with the addition of **MA1** at different A:T molar ratios. 81

Table 2.6. Summary of DLS and TEM characterization data of morphological transformation of **MT4** with the addition of **MA2** at different A:T molar ratios. 83

Table 2.7. Morphologies and nanoparticles dimensions comparison between the different polymers **PT1-4** with the addition of the complementary polymer **PA1** or **PA2**. 85

Table 3.1. Characterization data of $PNAM_{40}$-b-$PAAm_y$ adenine-containing diblock copolymers obtained *via* aqueous RAFT-mediated PISA. 115

Table 3.2. Summary of DLS and TEM characterization data of the different $PNAM_{40}$-b-$PAAm_y$ block copolymer nano-objects obtained by aqueous RAFT-mediated PISA .. 128

Table 3.3. Comparison of the DLS results for PISA and reassembled particles. 136

Table 4.1. Characterization data of $PNAM_{40}$-b-$PAAm_y$ adenine-containing diblock copolymers obtained *via* aqueous RAFT-mediated PISA. 161

Table 4.2. Summary of DLS and TEM characterization data of **$PT_{20}n$**, **PA1n** and **PA2n** block copolymer nano-objects obtained by aqueous RAFT-mediated PISA..... 166

Table 4.3. DLS results of the mixing experiments of PA1n with **PT_{20}n** at different ratios of T:A. 171

Table 4.4. Summary of DLS and TEM characterization data of control experiments. 181

Table 4.5. Summary of DLS and TEM characterization data of control experiments. 183

Table 4.6. Characterization data of $PNAM_{40}$ macroCTA, **PA2** and **PT_{20}** modified block copolymers obtained *via* aqueous RAFT-mediated PISA. 186

Table 4.7. Summary of DLS and TEM characterization data of **PT^{Rd}_{20}n** and **$PA2^{Gr}$n** block copolymer nano-objects obtained by aqueous RAFT-mediated PISA..... 186

Table 4.8. Characterization data of $PNAM_{40}$ mCTA, **PT^{Me}_{20}** ($PNAM_{40}$-*b*-$PT^{Me}Am_{20}$) and **PA_{20}** ($PNAM_{40}$-*b*-$PAAm_{20}$) obtained *via* aqueous RAFT-mediated PISA. 199

Table 4.9. Characterization data of $PNAM_{40}$ mCTA, $mCTA^{Rd}$, $mCTA^{Gr}$, $PNAM_{40}$-*b*-$PTAm_{20}$ (**PT^{Rd}**)and $PNAM_{40}$-b-$PAAm_y$ (**$PA2^{Gr}$**)adenine-containing diblock copolymers obtained *via* aqueous RAFT-mediated PISA with modified macroCTA..... 203

Table 4.10. Summarize of data from the quantitative analysis of MORPH PISA using **PA1n** particles..... 215

Table 4.11. Summarize of data from the quantitative analysis of MORPH PISA using **PA2n** particles..... 215

List of Symbols and Abbreviations

% w/w	Solids concentration
[M]	Monomer concentration
$[M]_0$	Initial monomer concentration
°C	Degrees Celsius
A	Adenine
a_0	Area of a surfactant's polar head group
AAm	3-(adenine-9-yl) propyl acrylamide monomer
AIBN	2,2'-Azobis(2-methylpropionitrile)
AM	acrylamide
AN	Acrylonitrile
Aq	Aqueous
ATRP	Atom transfer radical polymerization
BBPs	Bottlebrush polymers
BCP	Block copolymer
BHT	2,6-bis(1,1-dimethylethyl)-4-methylphenol
c	concentration
C	Cytosine
CAC	Critical aggregation polymerization
$CDCl_3$	Deuterated chloroform
CDSA	Crystallization-Driven Self-Assembly
$CHCl_3$	Chloroform
CMC	Critical micelle concentration

Cryo-TEM	Cryogenic transmission electron microscopy
CSIRO	Commonwealth scientific and industrial research organization
CTA	Chain transfer agent
d	Doublet
D	Translational diffusion coefficient
D_2O	Deuterium oxide
D_{ave}	Average diameter recorded by TEM
DCM	Dichloromethane
dd	Doublet of doublets
DD	Direct dissolution
D_h	Hydrodynamic volume
DLS	Dynamic light scattering
$Đ_M$	Molar-mass dispersity by SEC
DMAP	4-(dimethylamino)pyridine
DMF	Dimethylformamide
DMSO	Dimethyl sulfoxide
DMSO-$d6$	Deuterated dimethyl sulfoxide
DNA	deoxyribonucleic acid
DP	Degree of polymerization
DSC	Differential scanning calorimetry
eq.	Equivalents
EtOAc	Ethyl acetate
EtOH	Ethanol

f	Weight-fraction
g	Gram(s)
G	Guanine
GO	Graphene oxide
GTP	Group transfer polymerization
h	Hour(s)
H_2O	Water
HPMAM	*N*-(2-hydroxypropyl)methacrylamide
HR-MS	High resolution mass spectrometry
J	Coupling constant
k_B	Boltzmann constant
k_{FH}	Flory-Huggins interaction parameter at the block junction constant
k_p	Propagation rate constant
LAMs	Less activated monomers
L_{ave}	Average particle length
l_c	Length of a surfactant's hydrophobic tail
m	Multiplet (^{1}H NMR)
m/z	Mass-to-charge ratio
MA	Methyl acrylate
Macro-CTA	Macromolecular chain transfer agent
MADIX	Macromolecular design *via* the interchange of xanthates
MAMs	More activated monomers
M_{ave}	Average membrane thickness

$mCTA^{Gr}$	Modified macroCTA with green dye
$mCTA^{Rd}$	Modified macroCTA with red dye
MeOH	Methanol
mg	Milligram(s)
$MgSO_4$	Magnesium sulfate
MHz	Megahertz
min	Minute(s)
mL	Milliliter(s)
MLVs	Multilamellar vesicles
MMA	Methyl methacrylate
M_n	Average molecular weight
mol	Mole(s)
MORPH	Morphological transformation process
MVVs	Multivesicular vesicles
M_w	Weight average molecular weight
MW	Molecular weight
MWCO	Molecular weight cut-off
$N_2(g)$	Nitrogen gas
N_{agg}	Aggregation number
NAM	4-acryolylmorpholine
nm	Nanometer(s)
NMP	Nitroxide-mediated radical polymerization/N-methyl-2-pyrrolidone
NMR	Nuclear magnetic resonance

NVC	*N*-vinylcarbazole
NVP	*N*-vinylpyrrolidone
p	Packing parameter
PA1	$PNAM_{40}$-*b*-$PAAm_{200}$
$PA1^{Gr}$	$PNAM_{40}$-*b*-$PAAm_{200}$ with green dye
PA2	$PNAM_{40}$-*b*-$PAAm_{216}$
$PA2^{Gr}$	$PNAM_{40}$-*b*-$PAAm_{216}$ with green dye
PD	Polydispersity
PDLA	Poly(*D*-lactide)
PEG	Poly(ethylene glycol)
PEO	Poly(ethyl oxide)
PFS	Poly(ferrocene-dimethylsilane)
PGMA	poly(glyceryl methacrylate)
PHPMA	poly(2-hydroxypropyl methacrylate)
PISA	Polymerization-induced self-assembly
PLLA	Poly(*L*-lactide)
Pm•	Growing radical chain
PMMA	Poly(methyl methacrylate)
Pn•	Growing radical chain
PNAM	Poly(4-acryloylmorpholine)
PNAM-*b*-PAAm	Poly(4-acryloylmorpholine)-*b*-poly(3-(adenine-9-yl)propyl acrylamide)
PNAM-*b*-PTAm	(poly(4-acryloylmorpholine)-b-poly(3-(thymin-1-yl)propyl acrylamide)

PNAM-n-PTAm^{Me}	(poly(4-acryloylmorpholine)-b-poly(3-(3-methylthymin-1-yl)propyl acrylamide)
ppm	Parts per million
PS	Poly(styrene)
PT_{20}	$PNAM_{40}$-*b*-$PTAm_{20}$
PT^{Me}_{20}	(poly(4-acryloylmorpholine)-b-poly(3-(3-methylthymin-1-yl)propyl acrylamide)
PT^{Rd}_{20}	$PNAM_{40}$-*b*-$PTAm_{20}$ with red dye
q	Quartet
q	Scattering vector
r.t.	Room temperature
RAFT	Reversible addition fragmentation chain transfer
R_H	Hydrodynamic radius
RI	Refractive index
RNA	Ribonucleic acid
ROMP	Ring-opening metathesis polymerization
ROP	Ring-opening polymerization
S	Spherical micelles
s	singlet
SS	Solvent switch
SA	Self-assembly
SANS	Small angle neutron scattering
SAXS	Small-angle X-ray scattering
SEC	Size exclusion chromatography

SLS	Static light scattering
St	Styrene
t	triplet
T	Thymine
T	Temperature
TAm	3-(thymin-1-yl)propyl acrylamide
TEA	Triethylamine
TEM	Transmission electron microscope
TFA	Trifluoroacetic acid
TF	Thin film rehydration
T_g	Glass transition temperature
$T^{Me}A_m$	3-(3-methylthymin-1-yl)propyl acrylamide
UA	Uranyl acetate
ULVs	Unilamellar vesicles
UV	Ultraviolet
UV-Vis	Ultraviolet-visible
v	Volume of a surfactant's hydrophobic tail
V	Vesicles
VA-044	2,2'-azobis[2-(imidazolin-2-yl)propane] dihydrochloride
VAc	Vinyl acetate
vs.	*Versus*
W	Worm-like micelles
x	Degree of polymerization
δ	Chemical shift

θ	angle
λ	Wavelength
µL	Microliter(s)

List of publications

4. †**Thomas, M**.; †Varlas, S.; Xie, Y.; Wilks, T.R.; O'Reilly, R. K. *Manuscript in preparation*.

3. Sikder, A.; Xie, Y.; **Thomas, M**.; Derry, M.J.; O'Reilly, R. K. Precise control over supramolecular nanostructures *via* manipulation of H-bonding in π-amphiphiles. *Nanoscale*, 2021,13, 20111-20118.

2. †Varlas, S.; †Hua, Z.; Jones, J. R.; **Thomas, M**.; Foster, J. C.; O'Reilly, R. K. Complementary Nucleobase Interactions Drive the Hierarchical Self-Assembly of Core–Shell Bottlebrush Block Copolymers toward Cylindrical Supramolecules. *Macromolecules* **2020**, *53*, 9747-9757.

1. Hua, Z.; Jones, J. R.; **Thomas, M**.; Arno, M. C; Souslov, A.; Wilks, T.R.; O'Reilly, R. K. Anisotropic polymer nanoparticles with controlled dimensions from the morphological transformation of isotropic seeds. *Nature Communications.* **2019**, *10 (1)*, 1-8.

Declaration of authorship

This thesis is submitted to the University of Birmingham in support of my application for the degree of Doctor of Philosophy. No material contained here has been submitted for any other degree, or at any other institution.

The work presented (including data generated and data analysis) was carried out by myself between October 2018 and February 2022 except in the cases outlined below:

Chapter 2: High resolution mass spectrometry of the nucleobase-containing monomers was performed by Dr. Christopher Williams at the University of Birmingham.

Chapter 3: Dry-state imaging of PISA nano-objects was performed with assistance from Dr. Spyridon Varlas. Cryo-TEM imaging of block copolymer nano-objects was performed with assistance from Dr. Spyridon Varlas, Dr. Robert Keogh, and Dr. Saskia Bakker at the University of Warwick.

Chapter 4: Cryo-TEM imaging of block copolymer nano-objects was performed with assistance from Dr. Stephen Fielden and Dr. Saskia Bakker at the University of Warwick. Confocal microscopy imaging of dye-containing block copolymers samples was carried out with assistance from Dr. Yujie Xie at the University of Birmingham.

1 : Introduction

1.1 Mimicking biological functionality with synthetic polymers

1.1.1 Mimicking the biological world

The gecko, water strider, spider, and sacred lotus: what do they have in common? Their unique properties have inspired scientists to fabricate new materials using synthetic building blocks. From the adhesive footpads of the gecko to the hydrophobic coating of a lotus leaf, [1] nature provides a wide range of systems – from the macroscopic to the molecular level – for scientists to mimic.

In 1953, Franklin, Watson and Crick[2] elucidated the structure of deoxyribonucleic acid (DNA); a sequence specific polymeric double helix bound together by H-bonding between complementary nucleobases (adenine-thymine and guanine-cytosine). Scientists have been inspired to mimic this powerful molecular recognition system to direct the assembly and connection of structured materials [3-5]. DNA is currently still an expensive material to produce, so the incorporation of nucleobases into polymers has received particular attention because of the potential to mimic the functions of DNA in a cheap and scalable manner.

1.1.2 Introduction to synthetic polymers

Polymers are found everywhere, from naturally derived DNA, proteins, and polysaccharides, which are essential for life, to synthetic materials used in medical or even industrial applications. Polymers are high molar mass species (also referred to as macromolecules) composed of many smaller repeated subunits, termed monomers. The monomers can be linked covalently to one another or can be bound by non-covalent intermolecular interactions to form long chains or networks.[6]

Polymers are synthesized *via* a process called polymerization. During this process, the number of repeated monomer units per polymer chain - referred to as the degree of

polymerization (DP) - is a key measure in defining a specific polymer system, as it describes the average length of the chain. For natural polymers the length and composition are often precisely defined, and every polymer chain is chemically identical (*i.e.*, they are *monodisperse*). This is rarely the case for synthetic polymers; usually a sample contains chains of many different lengths (*i.e.*, is *polydisperse*)[7] This variation in chain length is known as dispersity ($Đ_M$) and is defined as the ratio between weight-average molar mass (M_w) and the number-average molar mass (M_n). These two values determine the physiochemical properties of polymers. A high molar mass also imparts properties such as increased viscosity, chemical resistance and mechanical strength and differentiate them from small molecules. These can be tuned by altering a polymer's average chain length and without changing the chemistry, *i.e.*, functional groups, present. A sample of polymer has significantly different properties to a sample of constituent monomers, simply due to the difference in connectivity between chemical units.[8] Polymers also display a unique property not observed for small molecules, a glass transition temperature (T_g) which is defined as the temperature at which undergo a glassy-to-amorphous state transition.[8]

The properties of polymer-based materials can be varied by other means than chain length and dispersity.[9-11] Polymers with more than one monomer display different properties if the relative order of monomers in a chain is varied (Figure 1.1) (*e.g.*, homopolymer, block copolymer, periodic copolymer, random copolymer, *etc.*) or by varying tacticity – relative stereochemistry – (*e.g.*, isotatic, syndiotactic or atactic polymer) of the monomers units along the chain. Additionally, polymers with differing topology (*e.g.*, linear, star, cyclic, hyperbranched, *etc.*) behave differently. Finally, changing the relative position of functional groups with a polymer give different utilities and properties (*e.g.*, telechelic

polymers, where reactive groups are placed at the side or chain ends). Functional groups can allow further modifications of the polymer chain to occur, such as crosslinking or bottlebrush formation.[9-10]

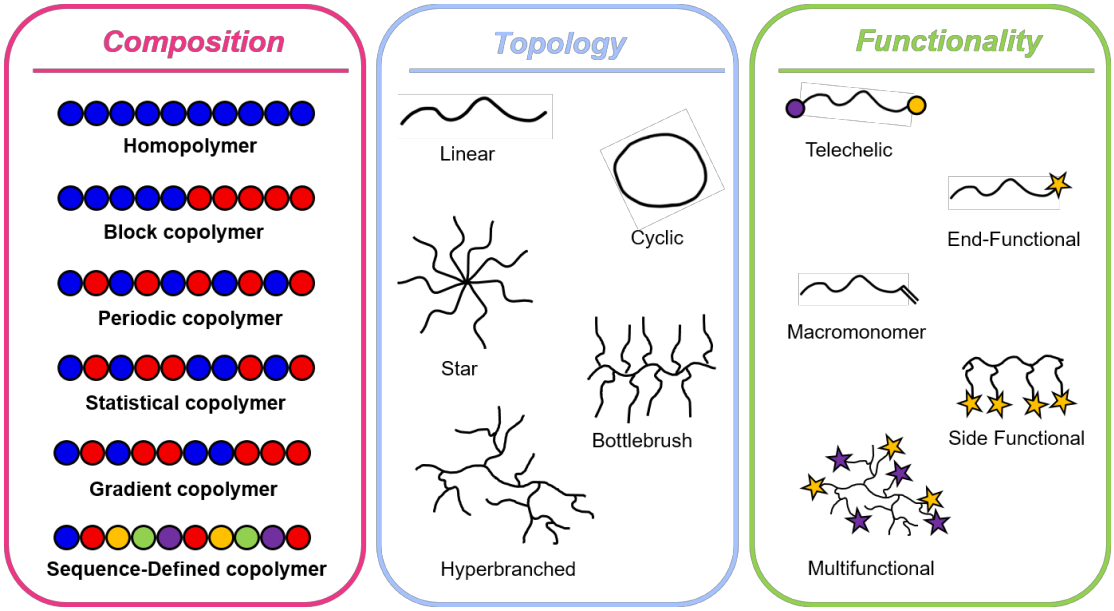


Figure 1.1. Different compositions, topologies, and functionalities of polymers.

1.2 Polymerization techniques

Polymerization – the process of joining monomers together – can occur in two major mechanisms: chain-growth[12] or step-growth.[13-14] Step-growth polymerization, such as polycondensation reactions (*e.g.* Nylon synthesis), remains the most widely utilized and economically viable technique for polymer synthesis at industrial scale. Typically, during step-growth polymerization, monomers with two or more reactive functional groups react to form dimers. These dimers then react with more monomers or combine with other dimers to form tetramers, and short oligomers, until the limiting reagent/monomer is fully consumed. As a result, the average molecular weight of each polymer chain remains relatively low throughout the polymerization until near-full conversion, until a significant increase of the average molecular weight of each polymer chain. The molecular weight

increases greatly at the late stages of the process when only oligomers remain and so react with each other (Figure 1.2A).[14-15]

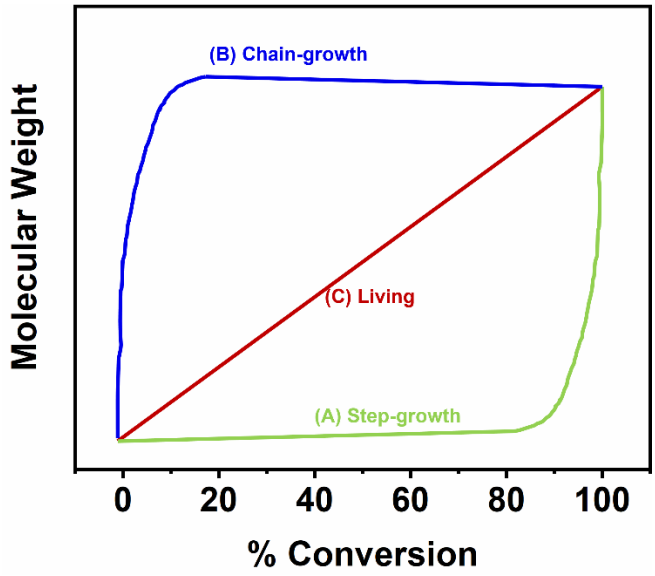


Figure 1.2. Evolution of the molecular weight of polymers *versus* monomer conversion for (A) step-growth polymerization, (B) conventional chain-growth polymerization, and (C) living polymerization.

On the other hand, chain-growth polymerization relies on the addition of monomers onto a growing chain – the monomers do not initiate chain formation themselves. It involves initiation, propagation, and termination events.[16] During the initiation stage, activated species (*e.g.*, radicals or ions) are formed by an external energy supply (*e.g.*, light, heat, *etc.*) and then react with monomers resulting in the formation of a growing chain. This is able to react with additional monomers at the reactive end in a process called propagation. Finally, in the termination step, the chain cannot grow further as a consequence of full monomer conversion or by reacting with another chain or other terminating species. Contrary to step-growth polymerization, monomer concentration decreases constantly, and high molecular weight polymers can be formed throughout the polymerization process (Figure 1.2B).

If there is no termination step for a chain-growth polymerization, then the polymerization is classified as "living". [17] This means the number of growing chains remains constant throughout the polymerization. This means that one monomer can be fully consumed before adding another, enabling the synthesis of block copolymers. In this case, a linear relationship exists between the molecular weight and the monomer conversion (Figure 1.2C). Select examples of living polymerizations from the literature include anionic,[18] cationic,[19] ring opening metathesis polymerization (ROMP)[20] and group transfer polymerization (GTP).[21]

A key aspect of living polymerization is that the rate of initiation is significantly greater than the rate of propagation, ensuring all polymer chains grow at the time and rate.[21] Therefore, polymers obtained *via* living polymerization techniques can have controlled lengths and narrow dispersity.[22]

1.2.1 Controlled radical polymerization

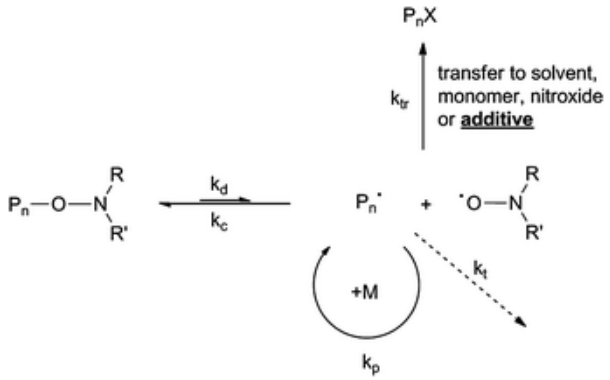
Controlled radical polymerizations have been widely explored for the synthesis of functional polymers. Compared to living controlled radical polymerization relies on a dynamic equilibrium between active propagating radicals and deactivated dormant species. This equilibrium can be achieved by using a so-called capping or chain transfer agent (CTA). This results in a reduction in the overall concentration and simultaneously increases the lifetime of effective radicals and thus limiting the number of undesired chain transfer and termination events.[23] This equilibrium can be achieved *via* approaches exploiting either the persistent radical effect (PRE) or degenerative chain transfer processes.[24]

The three mains example of controlled radical polymerizations, nitroxide-mediated radical polymerization (NMP), atom transfer radical polymerization (ATRP) and reversible addition–fragmentation chain transfer (RAFT) polymerization.

NMP and ATRP, described below, rely on the PRE to mediate the reversible activation/deactivation equilibrium between propagating and dormant radicals. While RAFT relies on degenerative chain transfer processes and will be explained in further detail below.

1.2.1.1 Nitroxide-mediated polymerization (NMP)

Nitroxide-mediated polymerization (NMP) was the first to be developed. It was discovered by scientists based at the Australian research institute CSIRO in 1985.[23] NMP is a catalyst-free polymerization technique, where alkoxyamines (R-N-O-R_2') are used typically as initiators to form nitroxide radicals (R_2'-N-O$^{\cdot}$) and the radical species (R$^{\cdot}$) are formed upon homolysis at elevated temperatures (commonly above 100 °C). The polymerization reversibly initiates by homolyses of the alkyl-oxygen bond at high temperature. The nitroxide radical is stabilized so does not react with monomer (*i.e.*, a persistent radical). Recombination of the nitroxide radical and radical of the growing chain reversibly deactivates polymerization. The equilibrium of this process ensures the majority of chains are dormant at any given time, minimising termination reactions, (*e.g.*, two growing chains join together). In the main equilibrium step as shown as on Scheme 1.1, the activated propagating radicals (Pn) reacts with either monomers units or the stable nitroxide radicals to yield the dormant nitroxide species whereby the polymer end is capped by combination with nitroxide radicals (P_n-N-O-R_2') in a reversible activation/deactivation process. [25-28]



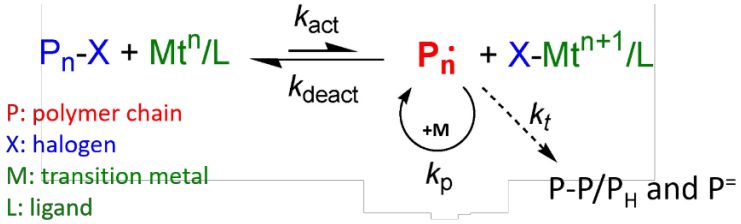
Scheme 1.1. Mechanism of nitroxide mediated polymerization. Reproduced from ref [29]

Although a range of monomer functionalities are compatible with NMP, the requirement for elevated temperature (to allow reversible dissociation of the alkoxyamine products) limits applicability to non-volatile monomers. Recent work has demonstrated the polymerization of a broader range of monomers by lowering temperatures or with the preparation of new nitroxides compatible with various monomers.[28, 30-31] The limitations encountered with NMP, has led to fewer applications than atom transfer radical polymerization (ATRP) or radical addition-fragmentation chain transfer polymerization (RAFT) polymerizations in polymer synthesis.[31]

1.2.1.2 Transition metal-catalyzed polymerization

In 1995, Matyjaszewski and Sawamoto independently developed ATRP.[32-33] Contrary to NMP, ATRP relies on the equilibrium between the propagating polymer chain and its dormant species mediated by a metal catalyst. The redox-active metal catalyst abstracts a leaving group, usually a halogen such as Br from the end of the chain to give an alkyl radical. The produced radicals can then initiate polymerization of vinyl-type monomers and form growing polymer chains (P_n·). The active polymer chain radicals either continue to propagate by reacting with monomer or abstracting the halogen back from the oxidized metal complex, thereby producing dormant polymer chains. Since the dormant form of

the polymer is dominant ($k_{act} << k_{deact}$), the concentration of propagating chains at any given time is low, so side reactions are significantly suppressed and therefore providing good control over the polymerization.[9, 34]



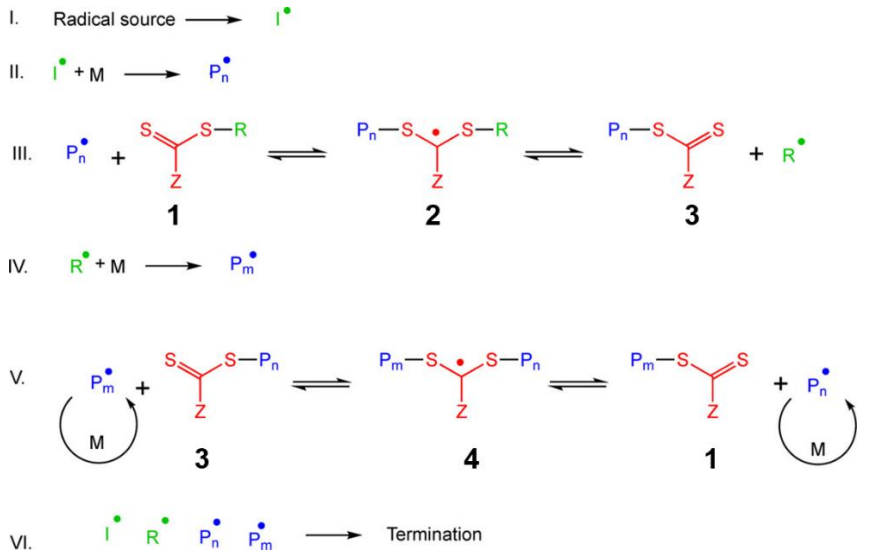
Scheme 1.2. Reaction mechanism of atom transfer radical polymerization. Adapted from ref.[35]

Compared to NMP, ATRP is a versatile polymerization method that offers the ability to utilize a wider range of monomers under mild conditions and in a variety of solvents and therefore making it attractive in many applications.[36]

1.2.1.3 Reversible addition-fragmentation chain transfer (RAFT) polymerization

RAFT polymerization was discovered in 1998 by Moad, Rizzardo and Thang *et al.* from CSIRO.[37] At the same time, a similar process was reported in France, called macromolecular design *via* the interchange of xanthates or MADIX.[38-39] These possess a similar mechanism and the only difference lies in the structure of the polymerization mediators. The mechanism of RAFT, as discussed below, utilises a thiocarbonylthio compound chain transfer agent (CTA) to both reversibility deactivates a propagating polymer chain and ensure a rapid exchange of radical between chains meaning that the number/concentration of radicals remains constant. Moreover, RAFT process also avoids the utilization of metal catalysts, reducing the potential of toxicity in medical applications.[37] Furthermore, RAFT polymerization technique will be utilized in Chapter 2 of this thesis, and so the mechanism is discussed in greater detail below.

The general mechanism of RAFT polymerization (Scheme 1.3) closely mimics the key mechanistic steps of a conventional free radical polymerization with initiation, propagation, and termination events. Step I: The initiator (I-I) decomposes *via* thermolysis (photolysis and other initiation procedures can also be used) to generate free radicals ($I^{\bullet}$) and Step II then reacts with a vinyl monomers units (M) to form a growing polymer chain ($P_n^{\bullet}$). Step III represents the pre-equilibrium step, where the active polymer chains can react with thiocarbonylthio compound, such as Z–(C=S)–S–R, in a reversible manner to form an intermediate stabilized radical species such as Z–($C^{\bullet}$–S– $P_n^{\bullet}$)–S–R, containing two alkyl groups. This can subsequently fragment to generate an alkyl radical and a dormant capped chain growing CTA (CTA, Z–(C–S– $P_n^{\bullet}$)=S) and the CTA-derived radical, $R^{\bullet}$. In Step IV (also known as the preinitiation step), $R^{\bullet}$ can initiate the polymerization of another growing polymer chain ($P_m^{\bullet}$) by reacting with more monomer. Finally, a main equilibrium step is established during step V when the two growing radical polymer chains ($P_m^{\bullet}$ and $P_n^{\bullet}$) can reversibly add onto the RAFT intermediate (Z–($C^{\bullet}$–S– P_n)–S– P_m), or fragment to mediate further propagation through a series of reversible reactions. In this way, the radical is passed between chains, unlike other controlled radical polymerizations. Only one fragmentation at a time can occur, meaning only one chain can propagate from this equilibrium, either $P_m^{\bullet}$ or $P_n^{\bullet}$. However, the equilibrium constants are such that $k_{add}/k_{-add} >> k_p$ meaning addition of the growing chain onto the CTA is faster than fragmentation and propagation reactions resulting in a low concentration of active growing polymer radicals, which avoids termination events (Step VI) (*e.g.*, coupling of $P_m^{\bullet}$ and $P_n^{\bullet}$).



Scheme 1.3. Mechanism of Reversible Addition–Fragmentation Chain Transfer Polymerization. Reproduced from ref. [40]

One of the key features of RAFT polymerization is its ability to use a wide range of functional monomers. Correct selection of the chain transfer (or RAFT) agent is crucial for a well-controlled polymerization. Typical CTAs structures are shown in Figure 1.3, where both R and Z groups affect their efficiencies.[41-42]



Figure 1.3. Typical structures of chain transfer (or RAFT) agents.

The CTA must be carefully selected to match the reactivity of the monomer, which in turn is dictated by the electronics of the monomer alkene. “More activated” monomers (MAMs) better stabilize an intermediate radical than “less activated” monomers (LAMs) (Figure 1.4). MAMs react more readily with radicals than LAMs as the formation of a stable radical is more favored. MAMs have relatively stable vinyl group, which is conjugated to either a double bond, aromatic ring, nitrile, or carbonyl group (*e.g.*,

butadiene, styrene, (meth)acrylamide, acrylonitrile and maleimide). LAMS contain a double bond next to either an oxygen nitrogen, halogen, saturated carbons or sulfur lone pairs (*e.g.*, vinyl acetate, N-vinylpyrrolidone, vinyl chloride, l-alkenes). To ensure good monomer compatibility in RAFT polymerization, the stability of the radical contained in the CTA needs to be tailored to the ligand: for MAMs, a relatively stabilising CTA is required as this ensures rapid deactivation and low concentration of alkyl radicals. Such a CTA would result in low polymerization rates when using LAMs, so the electronic structure of the CTA must be changed to destabilize the radical, so that alkyl radical formation is not prevented. Figure 1.4 shows as well the general guidelines for the selection of both R and Z groups in a CTA.[40]

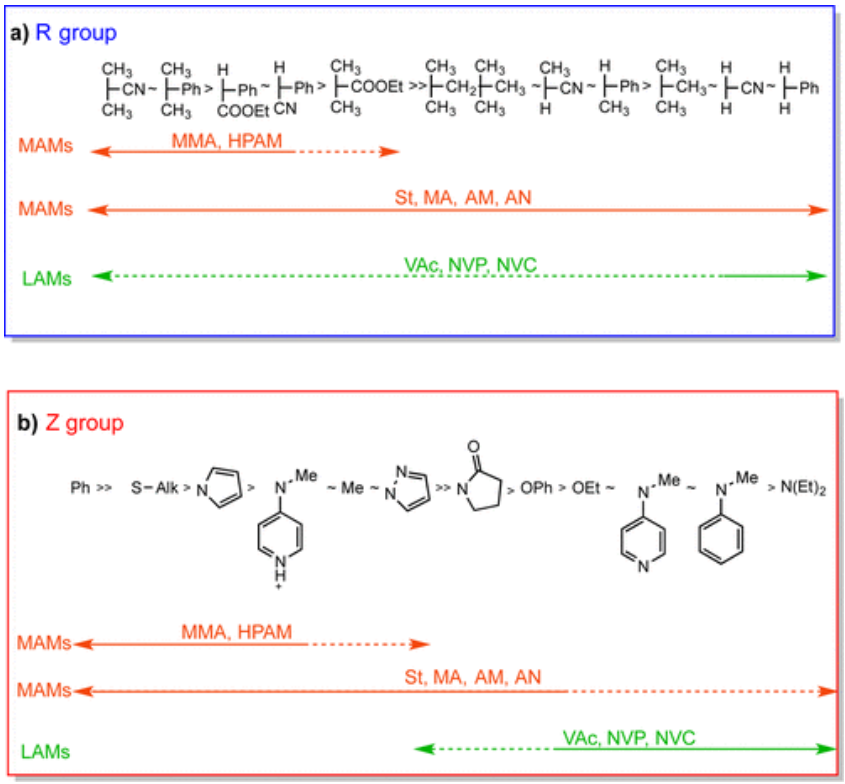


Figure 1.4. Guidelines for Selection of the R- and Z-group of RAFT Agents for various polymerizations. The dashed lines represent limited or poor polymerization control. Abbreviations: MMA = methyl methacrylate, HPMAM = *N*-(2-hydroxypropyl)methacrylamide, St = styrene, MA = methyl acrylate, AM = acrylamide, AN = acrylonitrile, VAc = vinyl acetate, NVP =*N*-vinylpyrrolidone, and NVC = *N*-vinylcarbazole. Reproduced from ref. [40]

The R-group must be a good homolytic leaving group from the intermediate radical as well as efficient, yet stable in order to reinitiate the polymerization. Depending on the nature of the monomer, the ability of the growing Pn to leave decreases in the order, methacrylates, methacrylamides >> styrenics, acrylamides, acrylates > *N*-vinyl amides, vinyl esters.[43]

On the other hand, the Z-group is mostly responsible for the reactivity of the C=S bond toward the radical addition and directly influences the stability of the intermediate radical (Scheme 1.3, compound **4**). Polymerization of MAMs usually produces more stabilized radicals (due to the effective electronic delocalization), and a careful selection of Z-group

to help the stabilization of intermediate radicals is needed, to favour the addition of the radical to the C=S bond. Therefore, CTAs with a Z-group such as dithiobenzoate (Z = Ph) or trithiocarbonate (Z = S-alkyl) are usually chosen to achieve the controlled polymerization of MAMs. In contrast, LAMs are poor homolytic leaving groups due to their high reactivity and require less stable intermediate radicals to achieve controlled polymerization. Using dithiocarbamates (Z = *N*-alkyl) or xanthates (Z = *O*-alkyl) favours the fragmentation of the propagating radical due to the delocalization of the lone pair of electrons on nitrogen (dithiocarbamates) or oxygen (xanthates) in the thiocarbonyl group and therefore deactivates the C=S bond toward radical addition and destabilizes the radical intermediate. Control over LAMs polymerization is achieved with the utilization of these specific Z-groups promoting the propagation and intermediate fragmentation.

Overall, among the degenerative transfer polymerization techniques, RAFT has proven to be the most powerful, robust, and versatile technique. It offers mild reaction reactions and compatibility with various monomers and solvents, commercially available starting materials. It does however have disadvantages, such as the use of toxic and odorous starting materials (*e.g.*, thiol-containing alkyls to synthesis CTAs).[44] This can be resolved by either end-group removal or transformation into other functionalities.[42, 45]

1.3 Block copolymer self-assembly in solution

As discussed in the previous section, the development of controlled/living polymerizations techniques, such as RAFT, has enabled the synthesis of polymers with various compositions and architectures, including well-defined block copolymers (BCPs) (Figure 1.5).[10] Similar to small molecule surfactants (composed of a solvophilic head and a solvophobic tail), such as fatty acids, self-assembly of BCPs occurs in solvents in which at least one block is soluble, and at least one block is insoluble (*i.e.*, the polymer as a

whole is amphiphilic). The solvophobic blocks drive the self-assembly process in order to minimize unfavourable polymer-polymer and polymer-solvent interactions to exclude solvent molecules.[46] This process results in the formation of ordered nanostructures with distinct domains.[47-48]

Numerous morphologies arising from BCP assembly in solution have been observed, including spherical micelles, vesicles (or polymersomes), worm-like micelles, lamellae, large compound micelles (LCMs) and other more complex nanostructures (Figure 1.5).[49]

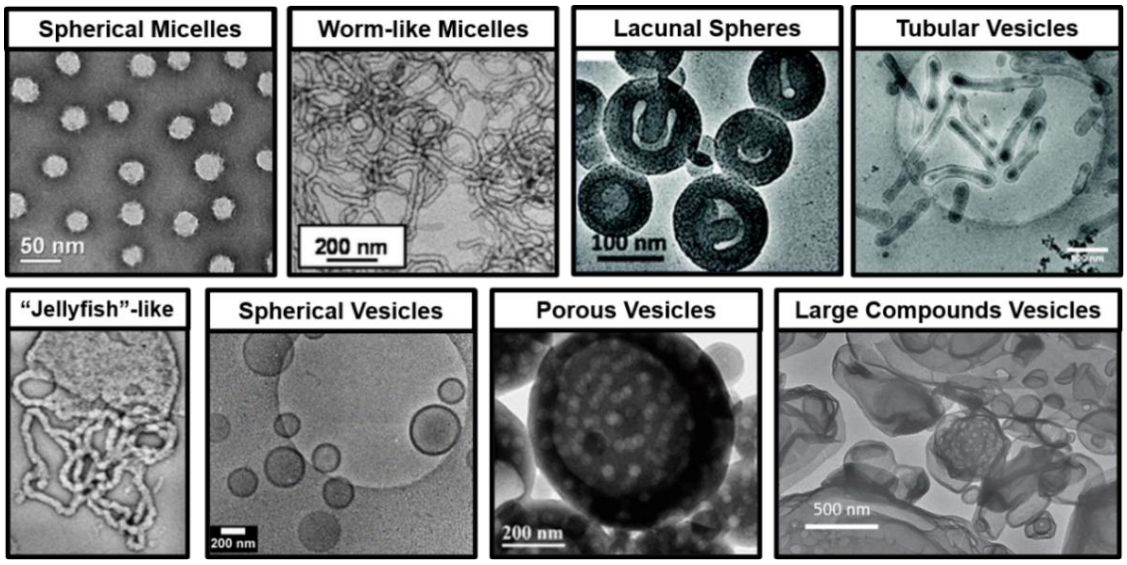


Figure 1.5. Electron microscopy images of various morphologies formed from amphiphilic block copolymer self-assembly in solution. Images reproduced from the following references: spherical micelles,[50] worm-like micelles,[51] lacunal spheres,[52] tubular vesicles,[53] "j jellyfish"-like particles,[54] spherical vesicles,[55] porous vesicles,[56] and large compounds vesicles.[57]

There are a wide range of factors influencing amphiphilic block copolymer self-assembly, such as copolymer structure, composition and molecular weight, extent of the core-stretching and its solvophobicity, rigidity of each constituent block and solvent composition.[49, 58] Most self-assembled aggregates have fast exchange dynamics, so their assembly occurs under thermodynamic control. The obtained morphology is primarily governed by the packing parameter, $p = v/a_0 l_c$, that was first introduced by Israelachvili,

Mitchell and Nimham to describe surfactant micellization.[59] Here, v relates the volume of the solvophobic segment (or tail), l_c to its length and a_0 to the surface area, a_0, (circled in green of Figure 1.6) of the interface of the solvophilic domain to the solvophilic one. Higher ordered morphologies are sequentially formed with an increase in p: formation of spherical micelles is favoured when $p \leq \frac{1}{3}$, whilst cylindrical micelles form for $\frac{1}{3} < p \leq \frac{1}{2}$ and $\frac{1}{3} < p \leq \frac{1}{2}$ gives hollow vesicles and bilayer lamellae (Figure 1.6).[59-60] However, it should be noted that the absolute values of v, a_0 and l_c are very difficult to calculated precisely and so the solvophilic/solvophobic weight fractions (f) for a given block copolymer are often employed instead as a rough approximation to describe a given morphology.[61]

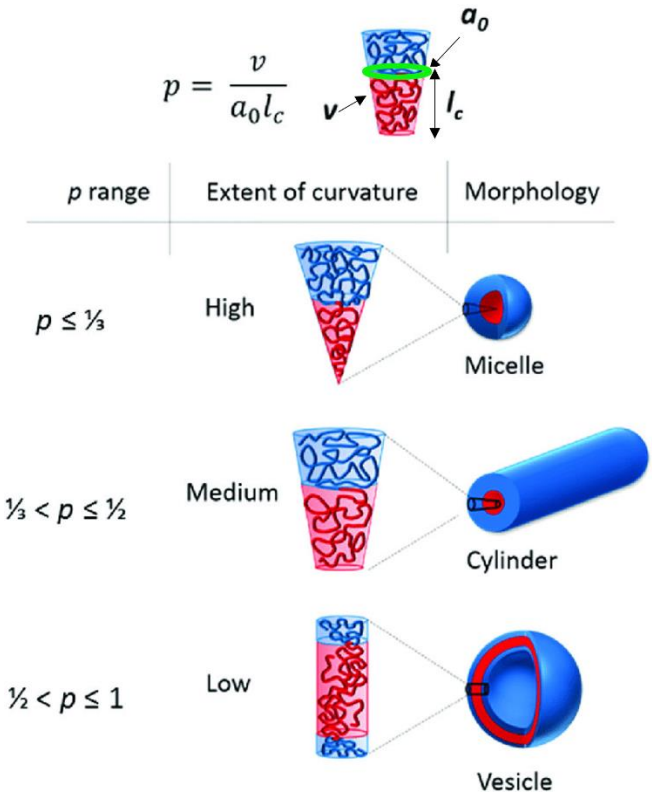


Figure 1.6. The different morphologies for amphiphilic block copolymer nano-objects obtained by targeting different packing parameters, p. Figure reproduced from ref. [62]

Beside the weight/volume ratios of solvophilic and solvophobic blocks, a number of factors can be responsible for the different self-assembled structures under thermodynamic control. Including copolymer composition (*e.g.*, molecular weight[63]) thermal properties of polymers (*e.g.*, crystallinity[64-67], glass transition temperature (T_g)[68-69] and rigidity[70-71] and polydispersity[62, 72-73]). As well the presence of specific interactions between polymers such as hydrogen bonding (H-bonding)[74] or π-π stacking.[75] In certain cases, unimer rearrangement and exchange between single chain BCP and particles can be very slow in comparison to the assembly process, leading to formation of out-of-equilibrium "kinetically trapped" or "frozen" structures.[69, 76-77] In this case, p is no longer an accurate predictor of morphology.

The self-assembly behaviour of amphiphilic BCPs can also be controlled by the method of self-assembly. Direct dissolution (DD) can be considered as the most straightforward and simple method, whereby the purified BCP is directly dissolved into a selective solvent at a suitable concentration to enable the self-assembly. Thin film rehydration (TF) involves the dissolution of the BCP in a good solvent for all blocks, forming dispersed unimers solution. This solvent is then removed at elevated temperature under vacuum, to produce a thin film of BCP. A selective solvent is then added to affect self-assembly. Finally, the solvent switch method (SS) is most often used for BCP self-assembly among the conventional self-assembly approaches. The BCP is first dissolved in a good solvent for all blocks forming a unimers (isolated macromolecules) solution. Then a selective solvent is added slowly to the solution, followed by removal of the good solvent leading to self-assembly at a critical percentage content of the selective solvent.[68] The SS method will be discussed in more detailed as it has been studied in Chapters 2 and 3.

Self-assembly methodologies for amphiphilic block copolymers have been widely used to obtained polymer nanostructures but do present certain disadvantages, such as low concentration, the need for purified or pre-dried polymers and are time consuming.

1.4 Polymerization-Induced Self-Assembly (PISA)

An alternative to the multi-step procedures required for BCP self-assembly is polymerization-induced self-assembly (PISA). Essentially, this combines polymerization and self-assembly in the same pot. A soluble starting polymer can be dissolved into a selective solvent and then further polymerized with a different monomer, either solvent-miscible (dispersion polymerization conditions) or solvent-immiscible (emulsion polymerization conditions) core-forming monomers to give a BCP containing an insoluble block. Once the insoluble block reaches a certain length, self-assembly occurs.[78]

As the polymerization proceeds, the resulting core-forming block becomes gradually insoluble at a critical DP, which induces self-assembly of the amphiphilic block copolymer *in situ* through aggregation to exclude solvent molecules (Figure 1.7). This nano-object micellization onset is typically accompanied with an increase in the polymerization rate as a consequence of a high local monomer concentration located within the formed nanoparticle cores. [79-81]

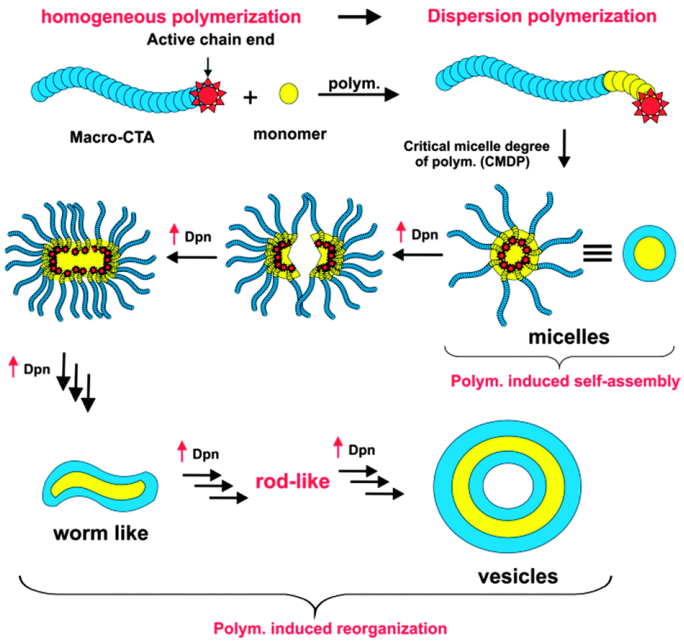


Figure 1.7. Schematic illustration of the morphological evolution of diblock copolymer nano-objects developed during RAFT-mediated PISA under dispersion polymerization conditions. Reproduced from ref.[82]

The final morphology formed in PISA formulations varies with DP and % polymer weight and is often plotted on a phase diagram. Similar to conventional block copolymer self-assembly techniques, in the PISA process, the relative volume fractions of the corona and core-forming blocks (i.e., *p*, the packing parameter discussed in section 1.3) primarily dictate the final morphology obtained under thermodynamic control.[60, 79, 83] This is true for the majority of dispersion PISA formulations, for example, as shown in Figure 1.8, a general trend towards higher order morphologies can be observed with an increase in the core-forming block length and solids content, from soluble polymer to spheres to worms to vesicles and to multilamellae.[54] Overall, assemblies of pure and mixtures of morphologies can be obtained *via* PISA by tuning externally controlled parameters (*e.g.*, total solids content, corona- and core-forming block length, reaction conditions).[83-84]

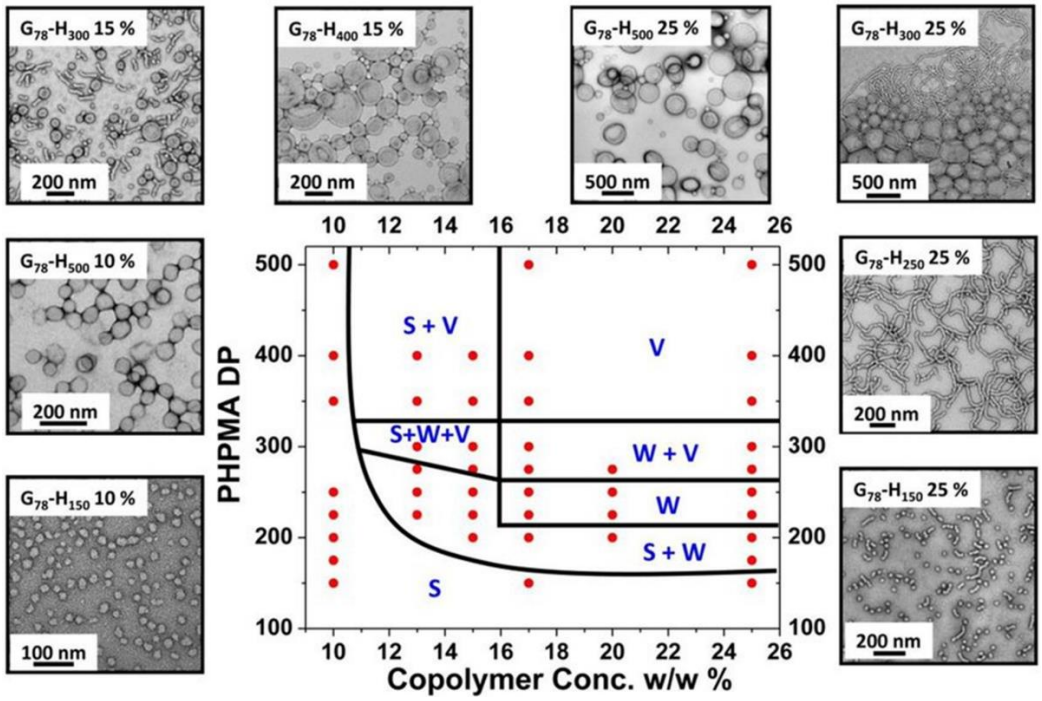


Figure 1.8. A representative RAFT-PISA system $PGMA_{78}$-*b*-$PHPMA_n$, with its corresponding phase diagram and TEM images of different morphologies Reproduced from ref. [83]

Of the rich PISA literature published in recent years, a wide range of methodologies have been developed in both aqueous and organic media utilizing RAFT-mediated polymerization as the most commonly employed technique.[78, 85-86] There have been a small number of reports utilizing other reversible-deactivation radical polymerization techniques such as ATRP, [87-88] and NMP-mediated PISA.[89-90] In addition, non-radical processes have been used to achieve PISA, such as ROMP,[91-93] Ni-catalyzed coordination polymerization[94-95] and ring-opening polymerization (ROP)[96-97].

PISA has been demonstrated to be a powerful technique to obtain nano-objects of different morphologies in one pot and is the subject of discussion in Chapter 3 of this thesis. Chapter 4 will use PISA a convenient synthetic tool for the synthesis of PISA-derived nano-objects for the self-assembly study of complementary nucleobase-nano-objects.

PISA has also proven to be a versatile technique with a wide range of applications (*e.g.*, industrial, and biomedical applications), including drug delivery vehicles[98-101], imaging agents[102], oil modifier[103] and Pickering emulsifiers[104-105] amongst others.

1.5 H-bonding in BCP self-assembly in water

Hydrogen bonding (H-bonding) is an interaction involving a hydrogen atom which is covalently bond to a more electronegative atom. H-bonds exist between atoms in different molecules (intermolecular) or amongst the same molecules (intramolecular). They are stronger than van der Waals interactions but weaker than covalent or ionic bonds. H-bonding are present in molecules such as DNA or proteins are responsible for the folding into functional configuration given rise to the double-helix structure of the two strands of DNA.[2]

Meijer and coworkers have shown that helical self-assembled polymers can be obtained through cooperative stacking of quadruple hydrogen-bonded pairs (Figure 1.9).[106] In their study, they have described a general strategy to design functionalized monomer units. Their association in either alkane solvents or water led to non-covalently linked polymeric structures with controlled chain length and helicity.[107]

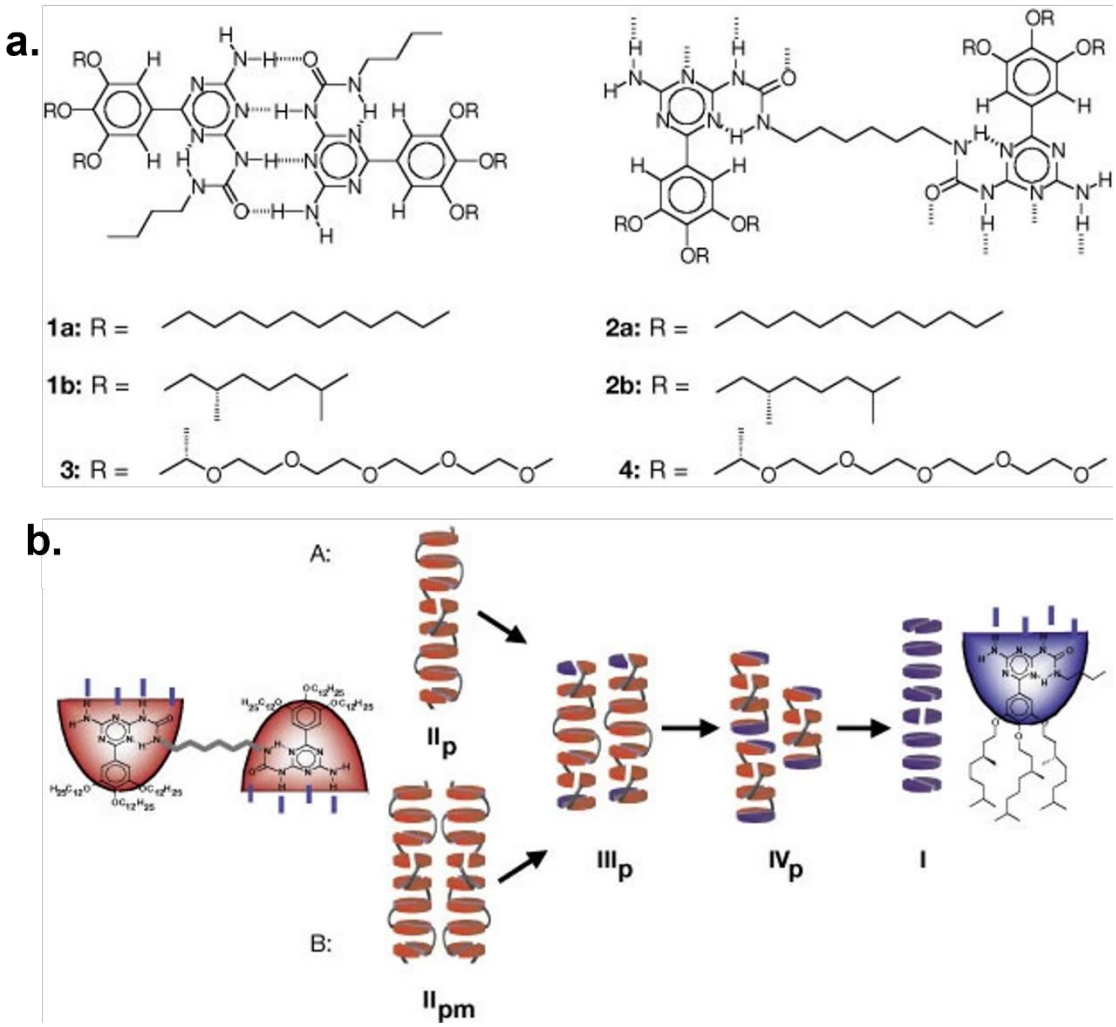


Figure 1.9. (a) Monofunctional ureidotriazines **1** and **3** and their mode of association *via* quadruple hydrogen bonds. Structures of bifunctional derivatives **2** and **4** are also shown. (b) A schematic representation of the organization of mixtures of mono- and bifunctional compounds upon increasing the fraction of monofunctional compound. In **I**, columns are formed by the stacking of dimers. In **II** (with p and m corresponding to the right- and left-handed helical conformation, respectively), consecutive disks of dimeric ureidotriazines are connected by hexamethylene spacers. Figure reproduced and adapted from ref.[106]

Moreover, H-bonding interactions play a crucial role in the influence of amphiphilic block copolymers self-assembly, the morphologies of diblock copolymer PEO_{114}-*b*-poly(*L*-lactide)$_{32}$ (PLLA) in water is influenced by the effect of H-bonding interactions (Figure 1.10).[74]

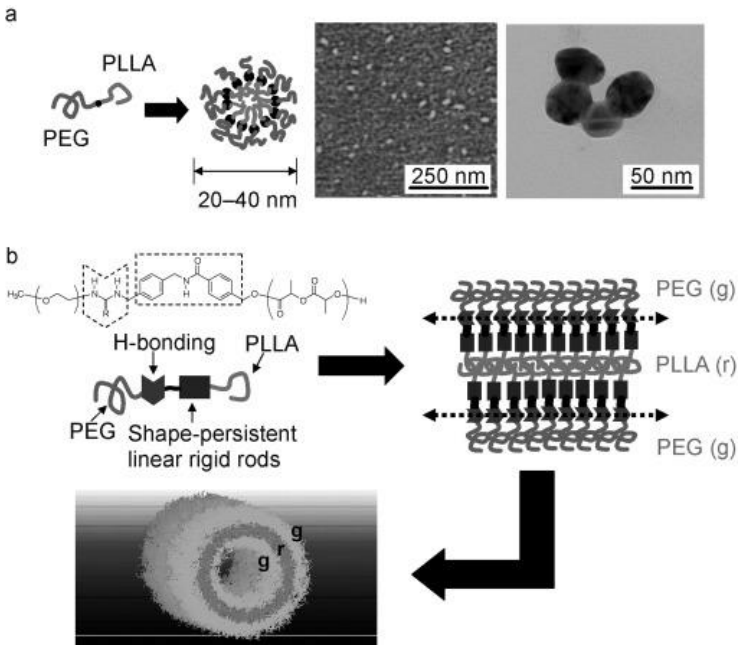


Figure 1.10. Schematic representations of possible supramolecular structures of a) PEG–PLLA and b) PEG–TU (or U)–PLLA assemblies. Reproduced from ref.[74]

By incorporating rigid small-molecule hydrogen-bonding moieties at the interface of the amphiphilic diblock copolymer (with a benzamide group), nanotubes instead of spherical micelles were obtained due to the strong directional nature of the H-bonding interactions. In addition, Yang and coworkers have also shown that by tuning the hydrophobic group at the block junction with H-bonding moieties, nanostructures with different morphologies could be obtained, such as rod-like, spherical and disk-like micelles (Figure 1.11).[108]

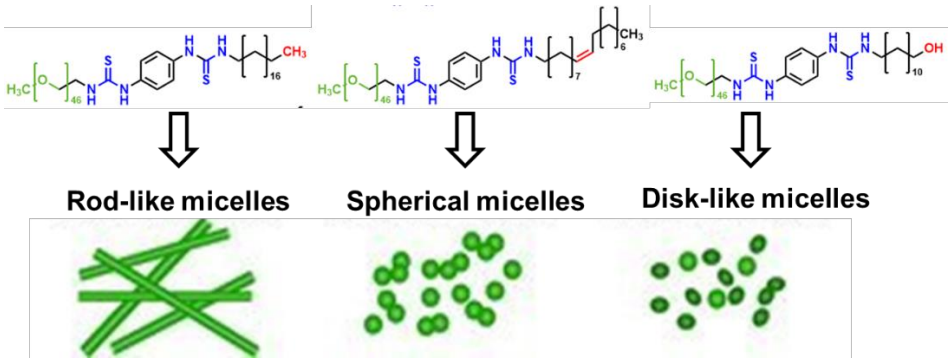


Figure 1.11. Synthesis of thiourea-containing PEGylated amphiphiles with different hydrophobic groups such as stearyl amine, oleyl amine, and1-amino dodecanol leading to the formation of different morphologies, rod-like, spherical, and disk-like micelles respectively. Adapted from ref.[108]

O'Reilly and Dove groups have shown that H-bonding interactions can lead to the formation of stereocomplex spherical micelles (Figure 1.12). In their work, the two opposite homochiral polymer chains, *i.e.*, poly(*D*-lactide) (PDLA) and poly(*L*-lactide) (PLLA), can form a compact conformation with a much denser polymeric packing than the homochiral one. They have demonstrated that the reorganization of homochiral PLA-containing cylindrical micelles can form small stereocomplex spherical micelles by H-bonding stereocomplexation (Figure 1.12).[109]



Figure 1.12. Characterization data of the nanostructures obtained from the self-assembly of diblock copolymers PLLA-*b*-PTHPA and PDLA-*b*-PTHPA. Reproduced from ref.[109]

Incorporation of H-bonding interactions in polymers has allowed fine tuning of nano-object morphology.[110-112] Therefore, it is expected that complementary H-bonding among nucleobases-containing polymers could significantly affect the self-assembly behaviour

of block copolymers, since we know that this plays a vital role in various areas such as DNA origami.

1.6 Syntheses of nucleobase-containing synthetic polymers and their self-assembly properties

1.6.1 Syntheses of nucleobase-containing synthetic polymers

Research into synthetic nucleobase polymers began in 1967 with the attachment of nucleobases to preformed natural polymers, such as cellulose[113]. Roberts and coworkers studied the interactions and possible separation of polynucleotides of different compositions with a guanine derivative of cellulose. This was followed by the preparation of synthetic nucleic acid polymers prepared through conventional radical polymerization of *N*-vinyl derivatives bearing nucleobase functionalities by T'so[114] and Takemoto[115].

The first example of controlled radical polymerization of nucleobase containing monomers was reported in 2006, by Van Hest and coworkers. They reported the synthesis of block copolymers composed of a poly(ethylene glycol) (PEG) chain and a thymine- or adenine-functional polymethacrylate block *via* ATRP.[116] Sleiman and coworkers reported a nucleobase-templated polymerization inspired by biological processes (*e.g.*, biochemical synthesis) which demonstrated good control of polymer molecular weight and dispersity.[117] The template was synthesized by ring-opening metathesis polymerization (ROMP) to give a thymine-containing polymer with narrow molecular weight distribution ($Đ_M$ = 1.07). A daughter adenine-functionalized polymer was obtained by a templated Sonogashira polymerization with a similar narrow distribution and degree of polymerization to the template (DP = 25).[118] This report demonstrated how nucleobase templates could be used to address the poor control of step-growth polymerizations.

RAFT polymerization has also been used for the synthesis of nucleobase-containing polymers with high DPs and moderate dispersities. In 2013, methacryloyl monomers containing adenine and thymine were synthesized by Kang *et al.* using RAFT polymerization with good control over their molecular weight (M_w up to 37 kDa, with a nucleobase-containing block up to DP 10) and relatively narrow dispersity ($Đ_M \leq 1.38$).[119] This was followed by the use of acrylamide-based monomers reported by Hua[120-121] – acrylamide monomers polymerize more rapidly compared to their methacryloyl analogues, allowing better control and the synthesis of longer polymer blocks. High conversion (≥99%) was attained, with higher M_w (up to 49 kDa) and nucleobase-containing block (DP = 100) and $Đ_M \leq 1.40$. RAFT has also proved an efficient method to prepare multi-block polymers with nucleobase functionalities with M_w up to 66.9 kDa and narrower dispersity ($Đ_M \leq 1.27$).[122]

1.6.2 Novel self-assembly properties of nucleobase-containing synthetic polymers

DNA hybridization is partly driven by formation of intermolecular H-bonds between complementary pyrimidine (thymine (T) and cytosine (C)) and purine (adenine (A) and guanine(G))nucleobases. The programmability of DNA base pairing has been repurposed in synthetic settings to give ordered nanomaterials such as DNA origami.[123] Compared to DNA, nucleobase-containing synthetic polymers are cheaper to synthesize. Therefore, there is potentially great benefit to incorporating nucleobases as pendant groups (A, T, C or G) into synthetic polymers, as this will allow the programmability of DNA base pairing to be extended to synthetic polymers – *i.e.*, with reliance of this different backbones.[117, 124-125]

Giant vesicles can be formed by mixing thymine/uracil containing polystyrene or polynorbornene with diacyldiaminopyridine (DAP) functionalized polymers in

chloroform. The complementary H-bonding interactions between the nucleobases and the functional group (DAP) present on the polystyrene backbone formed a three-point hydrogen bonding recognition pair, essential for driving the formation of giant vesicles (Figure 1.13).[126]

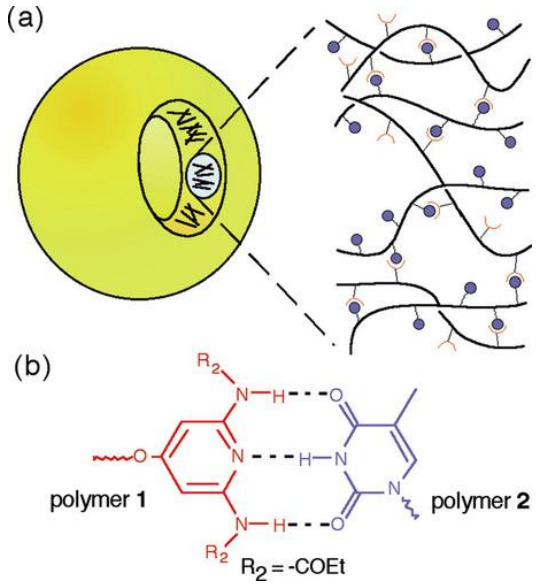


Figure 1.13. Schematic demonstration of vesicle formation between diaminopyridine-based polymer **1** and thymine-based polymer **2**. (a) Illustration showing molecular recognition within vesicle wall. (b) The corresponding recognition dyads. Reproduced from ref.[126]

Other nanostructures have been reported, such as rod-like nanoparticle formation upon the self-assembly of adenine-containing norbornene polymers in THF with a longer solvophilic block compared to the solvophobic one (10:1). In this study, Sleiman and coworkers hypothesized this self-assembly was due to the presence of self-complementary H-bonding interactions and aromatic π-π between adenine moieties.[118]

O'Reilly and coworkers reported that copolymer composition (containing thymine and adenine) and choice of solvent affected the complementary nucleobase interactions and therefore their corresponding self-assembled morphologies (Figure 1.14).[119] When the self-assemblies were prepared in $CHCl_3$ (a solvent that cannot form strong H-bonds),

alternating copolymers were obtained which then formed spherical micelles. In contrast, when using DMF (that can form competitive H-bonds) random copolymers formed, which gave elongated worm-like structures. They hypothesized that the difference in morphology was caused by the solubility of copolymers possessing different copolymer composition.

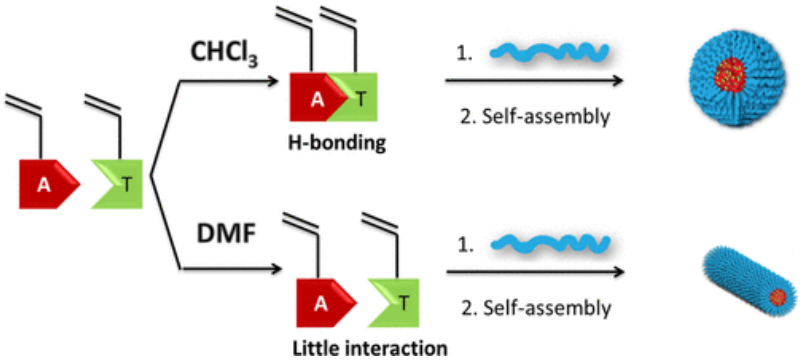


Figure 1.14. Schematic representation of the effect of copolymers compositions and solvents on the self-assembled nanostructures. Reproduced from ref.[119]

The same group also demonstrated that by changing the polymerization solvent ($CHCl_3$ and dioxane) different morphologies of thymine-containing nano-objects could be observed.[127] Spheres were observed in $CHCl_3$, and particles size increased with increasing the core-forming block length. In contrast, a sphere to cylinder to lamellae morphology transition was observed in 1,4-dioxane due to an enhancement of chain mobility (Figure 1.15).[127]

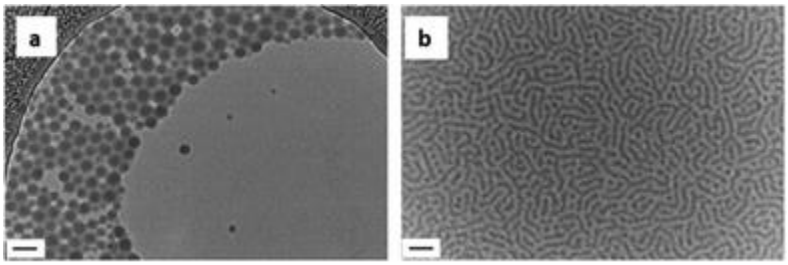


Figure 1.15. Representative TEM images of self-assemblies prepared by RAFT dispersion polymerization for a target copolymer $PMMA_{220}$-*b*-$PTMA_{50}$ in (a), chloroform; (b), 1,4-dioxane. Scale bar: 100 nm. Reproduced from ref.[127]

The hydrophilic phosphate-sugar backbone of DNA and RNA makes these polymers soluble in water. In contrast, nucleobase-containing synthetic amphiphilic polymers have poor solubility in water or other aqueous solutions due to the hydrophobic carbon-carbon backbone. To our knowledge, studies of nucleobase-containing synthetic polymers in aqueous solutions remain limited.

In 2016, Hua *et al.* used amphiphilic nucleobase-containing diblock copolymers synthesized by RAFT polymerization to form self-assemblies in water.[127-128] Well-defined and monodispersed spherical micelles were obtained in aqueous solution and it was demonstrated that the nanoparticle morphology could be tuned through the complementary nucleobase interactions using a long hydrophobic block for the micelle. However, no control over the length or width of the nanoparticles was possible, which was thought to be due to polymer chain exchange and reorganization. Previous studies have demonstrated that polymer chain exchange in aqueous solution depends on hydrophobic block length.[68-69] It was therefore proposed that increasing the length of the hydrophobic block would "freeze" the aggregates, preventing chain exchange and enabling control over the morphological transition process to be retained.

1.7 Well-controlled anisotropic polymeric nanoparticles

The synthesis of stable anisotropic polymer nanoparticles with control over their dimensions remains a key challenge in materials science.[76] Recently, new strategies have been developed for the formation of anisotropic nanoparticles in self-assembled systems, such as the synthesis of bottlebrush polymers, PISA (discussed previously), crystallization-driven self-assembly (CDSA) and more recently, a nucleobase-driven assembly termed MORPH.

1.7.1 Bottlebrush polymers (BBPs)

Bottlebrush polymers (BBPs) can be described as polymers with densely side-chain-grafted to a macromolecular backbone – *i.e.*, a polymer backbone with side chain polymers emanating from it. As a result of this high grafting density, the degree of interaction between side chains causes an extension of the BBP backbone.[129] BBPs are typically synthesized *via* 4 different routes; grafting-to (synthesis by grafting functionalized polymers to a functional backbone), grafting-from (involving the polymerization of the side chain from a polymeric initiator/CTA), transfer-to (similar to grafting-from, but differing in the attachment and behaviour of the CTA moieties) and grafting-through (where the BBPs are prepared *via* polymerization of preformed polymer side chains to give the backbone).[81] BBPs can self-assemble to form structures with large domain sizes, up to several hundred nanometres. Their structures can adopt anisotropic worm-like or other morphologies, such as spherical, cylindrical, or lamellar bilayer micelles.[130-132]

1.7.2 Polymerization-induced self-assembly

As previously described, PISA has been established as an alternative self-assembly methodology to form polymeric nano-objects in a one-pot manner at high solids

concentration, with relatively good control over the targeted morphologies and facile access to anisotropic nanostructures.[133] Despite the advantages of this methodology for the fabrication of high-order nanostructures for instance worm-like micelles, vesicles or "jellyfish"-like, the ability to control the length of anisotropic objects remained elusive.

1.7.3 Crystallization-driven self-assembly (CDSA)

Another approach, using semi-crystalline block copolymers led to the self-assembly in solution driven by the chain folding of semi-crystalline block and access size-controlled cylindrical morphologies. This self-assembly methods was termed crystallization-driven self-assembly or CDSA and can be dated back to mid-1960s, when Lotz *et al*. reported the formation of crystal platelet nano-objects, when chain folded crystalline poly(ethyl oxide) (PEO) were sandwiched between amorphous polystyrene (PS) in solution.[134] In 1998, Manners and Winnik reported their initial work on CDSA, where well-defined "seed" nanoparticles are fabricated from the solution self-assembly of block copolymers containing a crystallizable segment using an organometallic-inorganic diblock copolymer, poly(ferrocenyldimethylsilane)-*block*-poly(dimethylsiloxane) (PFDMS-*b*-PDMS) to form long rod-like micelles in hexane.[66, 135] Upon addition of unimers in solution, these seeds act as initiator to yield long worm-like nanoparticles with controlled length (Figure 1.16). This is favoured since the steric interactions disfavour particle-particle fusion and because the rate of crystallization is more or less constant. This is analogous to a controlled "living" polymerization process. In this process, unimers grow in an epitaxial fashion, by crystallizing onto the exposed crystalline end of cylindrical micelles by one dimensional (1D) growth.

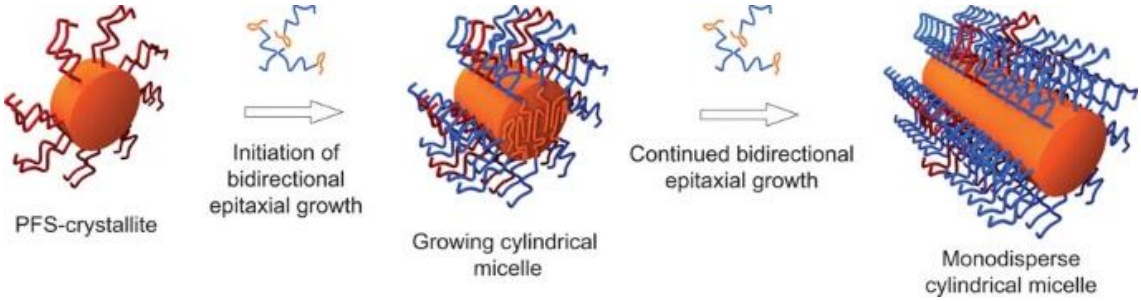


Figure 1.16. Realization of monodisperse cylindrical micelles through bidirectional epitaxial growth from small, uniform, stub-like crystallites as initiators for the crystallization-driven living self-assembly of PFS block copolymers with a crystallizable, core-forming block. Reproduced from ref.[136]

After the success of PFDMS based block copolymers, more recent examples using different core-forming blocks (*e.g.*, PCL,[137] PLA[138]) have been reported for the formation of well-defined 1D and 2D micelles. During the self-assembly process, three factors are considered to determine the resultant morphology: the folding of the crystalline core, the repulsion of the soluble corona, and the exposed area of the crystal surface. Therefore the nanostructures obtained are a result of a balance of these interactions.[139] Depending on the copolymer used, different nanostructures could be obtained from cylindrical micelles, diamond-shaped platelets,[140] to 2D lenticular platelets.[141]

Although CDSA is nowadays a widely studied process, it is limited to the use of (semi)crystalline polymers and different solvents need to be found for the dissolution of the blocks.

1.7.4 Morphological transformation (MORPH)

The O'Reilly group has recently reported a new mechanism to control the dimensions of anisotropic nanoparticles, termed morphological transformation (MORPH).[142] This new mechanism involves the controlled growth of anisotropic nanoparticles from isotopic seeds, based on hydrogen bonding between complementary nucleobases. Unlike CDSA,

a global change in nanoparticle shape and size is observed in MORPH and polymer crystallinity is not required (Figure 1.17).[142]

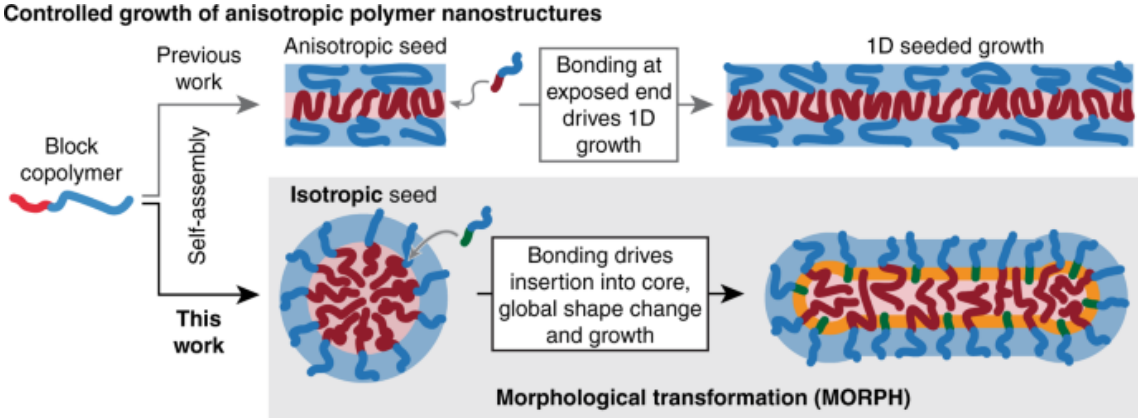


Figure 1.17. Methods for the growth of anisotropic polymer nanostructures with controlled dimensions. Previous efforts have been based on 1-dimensional growth from an anisotropic seed particle (top). We report a qualitatively different process based on the global morphological transformation of an isotropic seed particle (bottom). Reproduced from ref.[142]

A spherical micelle with a given nucleobase is self-assembled in water. Then a short polymer with a complementary nucleobase is added, which interacts with the polymers in the micelle to give a lower effective packing parameter, forcing the particle to elongate in a single dimension (Figure 1.18).[142] The insertion of the complementary short polymer occurs anywhere along the nanoparticle core compared to CDSA, where growth occurs only at the ends of the exposed seed nanoparticles. Each nanoparticle core can be thought of as a reservoir of material capable of driving elongation by forming bonds with the added polymer until the reservoir exhaustion leading to the disassembly of the nanoparticles.

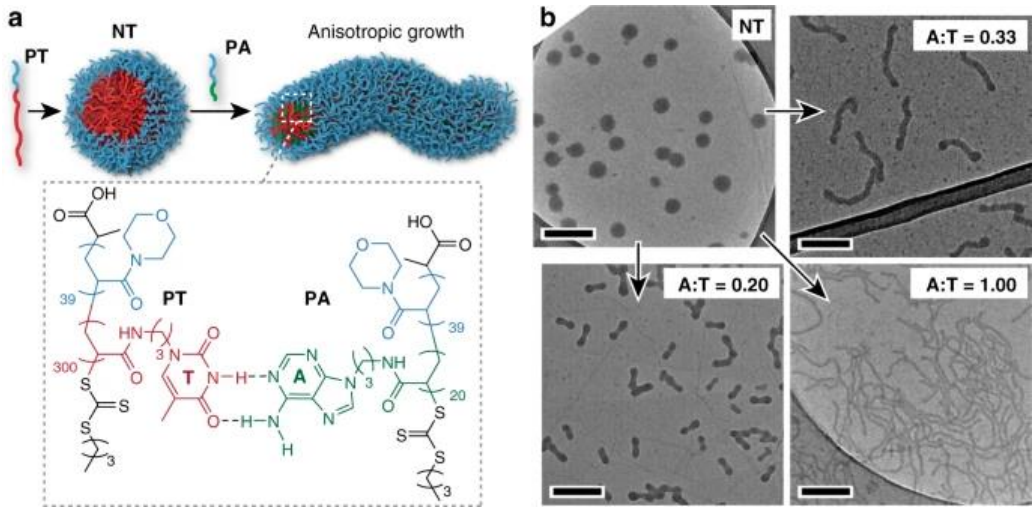


Figure 1.18. Single-step transformation of spherical nanoparticles into different anisotropic morphologies by MORPH. **a** Schematic representation of MORPH using nucleobase-containing polymers. Spherical nanoparticle **NT** with a thymine-containing core was formed by self-assembly of the polymer **PT** using a solvent switch method from DMF to water. Introduction of the adenine-containing polymer **PA** induced MORPH at A:T molar ratios above 0.20. **b** TEM images of the nanoparticles formed before and after addition of **PA** at different A:T molar ratios to separate solutions of **NT**. Particles were imaged stain-free on graphene oxide (GO). Scale bars = 200 nm. Reproduced from ref.[142]

MORPH exhibits other useful features as well, such as the isotropic nature of the seed nanoparticles, making it straightforward to assemble as they are they are the thermodynamic product of a simple self-assembly process. The shape changing can be controlled in a precise manner simply by mixing adjusting the amount of complementary polymer added into the aqueous solutions of nanoparticles.

The discovery of MORPH suggest that it may be possible to explore different supramolecular bonding motifs to perform controlled nanoparticles growth, as well as the influence of the seed nanoparticle morphology on this mechanism. This later will be investigated in this thesis.

1.8 Characterization techniques for polymer self-assemblies

The ability to characterize polymer self-assemblies is essential to have a better understanding of the mechanisms that drive their self-assembly. Microscopy and light scattering techniques are widely used for the analysis of particle size and shape. In this thesis, microscopy was selected as the principal method for the analysis of the self-assembled nanostructures, since it has been the most common way to visualize particles and determining representative morphologies.

1.8.1 Electron microscopy

Electron microscopy is a powerful analytical technique to determine the size and morphology of polymer self-assemblies by direct visualization.[143-144] An electron beam is produced from a source (*e.g.*, a tungsten filament) and accelerated in a vacuum chamber towards the sample using electromagnets. The image from transmission electron microscopy (TEM) measurement is obtained when electrons are scattered by or transmitted through a thin layer of a sample.

Chapters 3 and 4 of this thesis focus on the use of the two electron microscopy techniques, dry state, and cryogenic electron microscopy (TEM and cryo-TEM, respectively). Chapter 2 focuses only on the dry state technique.

Transmission electron microscopy in the dry state

In dry state TEM, samples are prepared by drying nanoparticles from solution onto a thin carbon-coated copper mesh grid to create a thin nanoparticle layer. As polymer nanoparticles are typically made of organic material only (*i.e.*, contain C, H, O, N, S, elements with a low molecular weight), the contrast between the particles and the carbon coating (the background) grid is very low. This is because the electron scattering ability of an element increases with nuclear charge, Z. More scattering of electrons gives better

contrast in TEM. Therefore, in order to obtain a good contrast, the samples are usually stained with high atomic number element, such as molybdenum, tungsten, or uranium salt, which allow the transmission of fewer electrons in comparison to organic material. This type of staining is known as negative stanning as the stain lies only on the carbon coating, making the background darker and the sample appearing lighter. On the other hand, positive staining causes particles to appear darker against a light background (Figure 1.19).

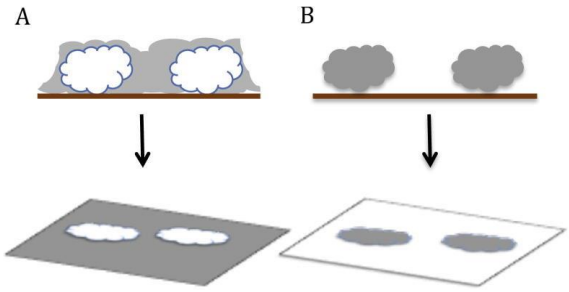


Figure 1.19. Positive and negative staining using heavy metal salts. In negative staining (A) the stain fully envelops the macromolecular complex; in the micrograph the complex appears white on a dark background. Positive staining (B) results in a small amount of stain forming a thin shell around the molecule, meaning the sample appears dark against a light background. Reproduced from ref.[145]

Though staining gives greater contrast, it can also produce artefacts caused by the stain itself, such as uneven background staining and stain crystallization . In some instances, the stain can remove the ability to distinguish the internal features of particles, such as membrane thickness. With that in mind, research has been conducted into creating thinner possible supports, for weakly scattering particles to be imaged without the need for staining. Graphene oxide (GO) grids (used in Chapter 2) were developed in 2009 and allow the analysis of soft materials when low contrast supports are used as it has been demonstrated in the last decade.[142, 146-147]

Drying effects can occur when analysing a sample using dry-state TEM. This includes dehydration of the particle corona, giving a smaller apparent size than in solution (the drying effect). Also, depending on the properties of the polymer, the particles may be unstable upon drying. This can result in particle disassembly or morphological changes; for instance, if core-forming blocks have a low T_g, film formation can occur. Hollow particles (*e.g.*, vesicles can appear to have collapsed or burst when dried under vacuum).

Cryogenic transmission electron microscopy (cryo-TEM)

For more complex structures, cryo-TEM technique is preferred as it allows images to be collected that are more representative of a particle in aqueous solution. In cryo-TEM, a thin sample layer in solution is deposed onto a TEM grid followed by blotting so that only a thin layer of solution remains. The grid is then rapidly cooled down by plunging it into liquid ethane, which results in vitrification of the ice layer. The frozen sample can be then analyzed under vacuum at liquid nitrogen temperatures (− 173 °C). Contrary to dry state TEM, cryo-TEM does not require the use of stain, and some feature such as membrane thickness can be observed such as vesicles prepared in Chapter 3.

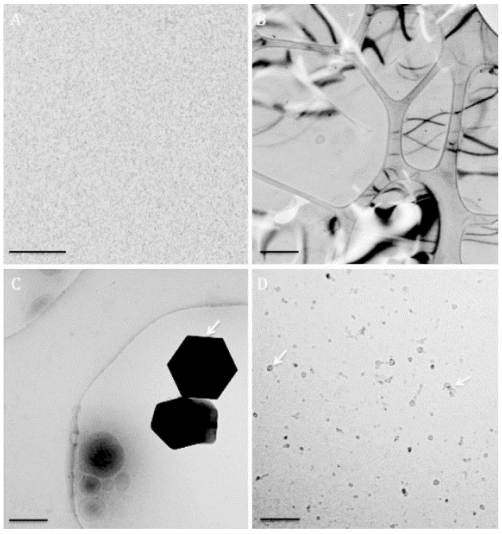


Figure 1.20. Examples of vitreous and non-vitreous ice. A) Empty, vitreous ice (Scale bar 50 nm). B) Hexagonal ice (scale bar 400 nm). C) Large ice crystal (white arrow) (scale bar 400 nm). D) Probable ethane contamination (scale bar 200 nm). Reproduced from ref.[145]

Although cryo-TEM is an extremely versatile and useful technique, it is generally time consuming (imaging one sample can take up to an hour) and some artefacts can be observed, such as ice crystallization, ethane contamination or empty vitreous ice (Figure 1.20).[145] Finally, care must be taken to not damage the sample with the electron beam as the use of high intensity can melt the vitrified ice or even lead to the destruction of the sample and the grid.

1.8.2 Light scattering techniques

Unlike with electron microscopy, light scattering techniques do not offer direct visualization of nanoparticles, but information about nanoparticles such as size, molar mass as well as topology/morphology of a polymer chain, or particle can be obtained in a non-destructive way. The most commonly employed techniques used are dynamic light scattering (DLS), static light scattering (SLS), small-angle X-ray scattering (SAXS) and small angle neutron scattering (SANS). The fundamental principle of these techniques is the illumination of a solution of sample with a radiation source of known wavelength and

the collection/analysis of scattered signals at a range of angles. Particles in solution move under Brownian motion and their speed can be related to their hydrodynamic size by the Stokes-Einstein equation (equation 1).

$$R_H = \frac{k_B T}{6\pi n D} \qquad \text{(Equation 1)}$$

Where k_B is the Boltzmann constant, T is the temperature and n in the refractive index of the solvent. The consequence of this is that the hydrodynamic radius (R_H) reported by DLS is the theoretical radius of a perfect hard sphere which moves with the same translational diffusion coefficient (D) as the particle being measured.

Once the diffusion coefficient has been obtained, it is possible to relate this to the particles' hydrodynamic radius (R_H). This is the radius of a hard sphere that diffuses under Brownian motion with the same *D* as the particle, and therefore is a good approximation for the radii of spherical particles, for example spherical micelles and vesicles, but is of less relevance with anisotropic particles such as worm-like micelles and lamellae. Nevertheless, R_H is often reported from a DLS experiment as a relative size of the particles in solution.

For DLS measurements, the scattered intensity of light is monitored as a function of time at a constant angle. In contrast, for SLS, SAXS and SANS techniques, the signal at different angles is averaged over time, allowing to determine shape, size, and molecular weight of particles. Equation (2) defines the scattering wave vector, q, and is inversely proportional to the length scale measured. λ represents the wavelength of the radiation beam, n is the refractive index of the solution and θ stands for the scattering angle. This means neutrons or X-ray are applied as the incident beam (low wavelength), q value

becomes larger than for visible light, typically used for DLS/SLS and therefore scattering information from a smaller length scale can be obtained.

$$q = \frac{4\pi n}{\lambda} \sin\left(\frac{\theta}{2}\right)$$ (Equation 2)

1.9 Summary

In Chapter 1, the concept of utilizing synthetic polymers to mimic the biological world has been briefly introduced. This was followed by a general introduction to synthetic polymers and common polymerization techniques for the preparation of block copolymers. This included the basics and mechanisms of controlled polymerizations, including RAFT, which has been used for the preparation of nucleobase-containing polymers in this thesis. This was followed by a detailed description of the self-assembly of block copolymers, including some empirical rules related to the packing parameter related to the nanoparticle morphologies. PISA was used in this thesis in Chapter 3 and 4, as a rapid one-pot procedure for the synthesis of nucleobase-containing block copolymer nano-objects. In addition, the influence of H-bonding on self-assembly and the synthesis, properties of nucleobase-containing synthetic polymers have also been highlighted. Techniques to obtain anisotropic polymeric nanoparticles in a control manner was them discussed, with techniques such as PISA, CDSA and BBPs were highlighted. Finally, there was a short introduction to the techniques used for the analysis of polymer self-assemblies.

1.10 References

1. Grewal, H. S.; Cho, I. J.; Yoon, E. S., The role of bio-inspired hierarchical structures in wetting. *Bioinspiration Biomimetics* **2015,** *10*, 026009.

2. Watson, J. D.; Crick, F. H., Molecular structure of nucleic acids; a structure for deoxyribose nucleic acid. *Nat.* **1953,** *171*, 737-738.

3. Williams, D. S.; Pijpers, I. A. B.; Ridolfo, R.; van Hest, J. C. M., Controlling the morphology of copolymeric vectors for next generation nanomedicine. *J. Controlled Release* **2017,** *259*, 29-39.

4. Seeman, N. C.; Sleiman, H. F., DNA nanotechnology. *Nat. Rev. Mat.* **2017,** *3*, 17068.

5. Sivakova, S.; Rowan, S. J., Nucleobases as supramolecular motifs. *Chem. Soc. Rev.* **2005,** *34*, 9-21.

6. Mayadunne, R. T. A.; Jeffery, J.; Moad, G.; Rizzardo, E., Living Free Radical Polymerization with Reversible Addition−Fragmentation Chain Transfer (RAFT Polymerization): Approaches to Star Polymers. *Macromol.* **2003,** *36*, 1505-1513.

7. Stepto, R. F. T., Dispersity in polymer science. *Polym. Inter.* **2010,** *59*, 23-24.

8. Mark, J. E., *Physical Properties of Polymers Handbook*. 2nd ed. 2007. ed.; Springer New York: New York, NY, 2007.

9. Matyjaszewski, K.; Xia, J., Atom transfer radical polymerization. *Chem. Rev.* **2001,** *101*, 2921-2990.

10. Matyjaszewski, K., Chemistry. Architecturally complex polymers with controlled heterogeneity. *Sci.* **2011,** *333*, 1104-1105.

11. Hadjichristidis, N.; Iatrou, H.; Pitsikalis, M.; Mays, J., Macromolecular architectures by living and controlled/living polymerizations. *Prog. Polym. Sci.* **2006,** *31*, 1068-1132.

12. Hiemenz, P. C.; Lodge, T. P., *Polymer Chemistry*. 2007.

13. Flory, P. J., Fundamental Principles of Condensation Polymerization. *Chem. Rev.* **1946,** *39*, 137-197.

14. Stille, J. K., Step-growth polymerization. *J. Chem. Educ.* **1981,** *58*, 862.

15. Billiet, L.; Fournier, D.; Du Prez, F., Step-growth polymerization and 'click' chemistry: The oldest polymers rejuvenated. *Polym.* **2009,** *50*, 3877-3886.

16. Odian, G., *Principles of polymerization*. John Wiley & Sons: **2004**.

17. Szwarc, M., 'Living' Polymers. *Nat.* **1956,** *178*, 1168-1169.

18. Szwarc, M.; Levy, M.; Milkovich, R., Polymerization initiated by electron transfer to monomer. A new method of formation of block polymers1. *J. Am. Chem. Soc.* **1956,** *78*, 2656-2657.

19. Aoshima, S.; Kanaoka, S., A renaissance in living cationic polymerization. *Chem. Rev.* **2009,** *109*, 5245-5287.

20. Bielawski, C. W.; Grubbs, R. H., Living ring-opening metathesis polymerization. *Prog. Polym. Sci.* **2007,** *32*, 1-29.

21. Webster, O. W.; Hertler, W. R.; Sogah, D. Y.; Farnham, W. B.; RajanBabu, T. V., Group-transfer polymerization. 1. A new concept for addition polymerization with organosilicon initiators. *J. Am. Chem. Soc.* **1983,** *105*, 5706-5708.

22. Webster, O. W., Living polymerization methods. *Sci.* **1991,** *251*, 887-893.

23. Moad, G.; Rizzardo, E., Chapter 1 The History of Nitroxide-mediated Polymerization. In *Nitroxide Mediated Polymerization: From Fundamentals to Applications in Materials Science*, The Royal Society of Chemistry: **2016**; pp 1-44.

24. Matyjaszewski, K., Macromolecular engineering: From rational design through precise macromolecular synthesis and processing to targeted macroscopic material properties. *Prog. Polym. Sci.* **2005,** *30*, 858-875.

25. Hawker, C. J.; Bosman, A. W.; Harth, E., New Polymer Synthesis by Nitroxide Mediated Living Radical Polymerizations. *Chem. Rev.* **2001,** *101*, 3661-3688.

26. Hawker, C. J., Molecular Weight Control by a "Living" Free-Radical Polymerization Process. *J. Am. Chem. Soc.* **1994,** *116*, 11185-11186.

27. Benoit, D.; Chaplinski, V.; Braslau, R.; Hawker, C. J., Development of a Universal Alkoxyamine for "Living" Free Radical Polymerizations. *J. Am. Chem. Soc.* **1999,** *121*, 3904-3920.

28. Grubbs, R. B., Nitroxide-Mediated Radical Polymerization: Limitations and Versatility. *Polym. Rev.* **2011,** *51*, 104-137.

29. Petton, L.; Ciolino, A. E.; Dervaux, B.; Du Prez, F. E., From one-pot stabilisation to in situ functionalisation in nitroxide mediated polymerisation: an efficient extension towards atom transfer radical polymerisation. *Polym. Chem.* **2012,** *3*, 1867-1878.

30. Detrembleur, C.; Jérôme, C.; De Winter, J.; Gerbaux, P.; Clément, J.-L.; Guillaneuf, Y.; Gigmes, D., Nitroxide mediated polymerization of methacrylates at moderate temperature. *Polym. Chem.* **2014,** *5*, 335-340.

31. Greene, A. C.; Grubbs, R. B., Nitroxide-mediated polymerization of methyl methacrylate and styrene with new alkoxyamines from 4-nitrophenyl 2-methylpropionat-2-yl radicals. *Macromol.* **2010,** *43*, 10320-10325.

32. Wang, J.-S.; Matyjaszewski, K., Controlled/" living" radical polymerization. atom transfer radical polymerization in the presence of transition-metal complexes. *J. Am. Chem. Soc.* **1995,** *117*, 5614-5615.

33. Kato, M.; Kamigaito, M.; Sawamoto, M.; Higashimura, T., Polymerization of methyl methacrylate with the carbon tetrachloride/dichlorotris-(triphenylphosphine) ruthenium (II)/methylaluminum bis (2, 6-di-tert-butylphenoxide) initiating system: possibility of living radical polymerization. *Macromol.* **1995,** *28*, 1721-1723.

34. Matyjaszewski, K., Atom Transfer Radical Polymerization (ATRP): Current Status and Future Perspectives. *Macromol.* **2012,** *45*, 4015-4039.

35. Matyjaszewski, K.; Spanswick, J., Controlled/living radical polymerization. *Mater. Today* **2005,** *8*, 26-33.

36. Braunecker, W. A.; Matyjaszewski, K., Controlled/living radical polymerization: Features, developments, and perspectives. *Prog. Polym. Sci.* **2007,** *32*, 93-146.

37. Chiefari, J.; Chong, Y. K.; Ercole, F.; Krstina, J.; Jeffery, J.; Le, T. P. T.; Mayadunne, R. T. A.; Meijs, G. F.; Moad, C. L.; Moad, G.; Rizzardo, E.; Thang, S. H., Living Free-Radical Polymerization by Reversible Addition−Fragmentation Chain Transfer: The RAFT Process. *Macromol.* **1998,** *31*, 5559-5562.

38. Destarac, M.; Brochon, C.; Catala, J.-M.; Wilczewska, A.; Zard, S. Z., Macromolecular Design via the Interchange of Xanthates (MADIX): Polymerization of Styrene with O-Ethyl Xanthates as Controlling Agents. *Macromol. Chem. Phys.* **2002,** *203*, 2281-2289.

39. Corpart, P.; Charmot, D.; Biadatti, T.; Zard, S. Z.; Michelet, D. PCT Int. Pat. Appl. WO 9858974. 1998.

40. Perrier, S., 50th Anniversary Perspective: RAFT Polymerization—A User Guide. *Macromol.* **2017,** *50*, 7433-7447.

41. Moad, G.; Rizzardo, E.; Thang, S. H., Living radical polymerization by the RAFT process–a third update. *Aust. J. Chem.* **2012,** *65*, 985-1076.

42. Perrier, S.; Takolpuckdee, P., Macromolecular design via reversible addition–fragmentation chain transfer (RAFT)/xanthates (MADIX) polymerization. *J. Polym. Sci., Part A: Polym. Chem.* **2005,** *43*, 5347-5393.

43. Keddie, D. J.; Moad, G.; Rizzardo, E.; Thang, S. H., RAFT Agent Design and Synthesis. *Macromol.* **2012,** *45*, 5321-5342.

44. Wood, M. R.; Duncalf, D. J.; Findlay, P.; Rannard, S. P.; Perrier, S., Investigation of the Experimental Factors Affecting the Trithiocarbonate-Mediated RAFT Polymerization of Methyl Acrylate. *Aust. J. Chem.* **2007,** *60*, 772-778.

45. Willcock, H.; O'Reilly, R. K., End group removal and modification of RAFT polymers. *Polym. Chem.* **2010,** *1*, 149-157.

46. Borisov, O. V.; Zhulina, E. B.; Leermakers, F. A. M.; Müller, A. H. E., Self-Assembled Structures of Amphiphilic Ionic Block Copolymers: Theory, Self-Consistent Field Modeling and Experiment. In *Self Organized Nanostructures of Amphiphilic Block Copolymers I*, Müller, A. H. E.; Borisov, O., Eds. Springer Berlin Heidelberg: **2011**; pp 57-129.

47. Blanazs, A.; Armes, S. P.; Ryan, A. J., Self-Assembled Block Copolymer Aggregates: From Micelles to Vesicles and their Biological Applications. *Macromol. Rapid. Commun.* **2009,** *30*, 267-277.

48. Brendel, J. C.; Schacher, F. H., Block Copolymer Self-Assembly in Solution—Quo Vadis? *Chem. Asian J.* **2018,** *13*, 230-239.

49. Mai, Y.; Eisenberg, A., Self-assembly of block copolymers. *Chem. Soc. Rev.* **2012,** *41*, 5969-5985.

50. Baranello, M. P.; Bauer, L.; Jordan, C. T.; Benoit, D. S. W., Micelle Delivery of Parthenolide to Acute Myeloid Leukemia Cells. *Cell. Mol. Bioeng.* **2015**, 455-470.

51. Lovett, J. R.; Ratcliffe, L. P. D.; Warren, N. J.; Armes, S. P.; Smallridge, M. J.; Cracknell, R. B.; Saunders, B. R., A Robust Cross-Linking Strategy for Block Copolymer Worms Prepared via Polymerization-Induced Self-Assembly. *Macromol.* **2016,** *49*, 2928-2941.

52. Qu, Y.; Wang, S.; Khan, H.; Gao, C.; Zhou, H.; Zhang, W., One-pot preparation of BAB triblock copolymer nano-objects through bifunctional macromolecular RAFT agent mediated dispersion polymerization. *Polym. Chem.* **2016,** *7*, 1953-1962.

53. Toebes, B. J.; Abdelmohsen, L. K. E. A.; Wilson, D. A., Enzyme-driven biodegradable nanomotor based on tubular-shaped polymeric vesicles. *Polym. Chem.* **2018,** *9*, 3190-3194.

54. Blanazs, A.; Madsen, J.; Battaglia, G.; Ryan, A. J.; Armes, S. P., Mechanistic Insights for Block Copolymer Morphologies: How Do Worms Form Vesicles? *J. Am. Chem. Soc.* **2011,** *133*, 16581-16587.

55. Blackman, L. D.; Varlas, S.; Arno, M. C.; Houston, Z. H.; Fletcher, N. L.; Thurecht, K. J.; Hasan, M.; Gibson, M. I.; O'Reilly, R. K., Confinement of Therapeutic Enzymes in Selectively Permeable Polymer Vesicles by Polymerization-Induced Self-Assembly (PISA) Reduces Antibody Binding and Proteolytic Susceptibility. *ACS Cent. Sci.* **2018,** *4*, 718-723.

56. Tan, J.; Huang, C.; Liu, D.; Li, X.; He, J.; Xu, Q.; Zhang, L., Polymerization-Induced Self-Assembly of Homopolymer and Diblock Copolymer: A Facile Approach

for Preparing Polymer Nano-Objects with Higher-Order Morphologies. *ACS Macro Lett.* **2017,** *6*, 298-303.

57. Lv, F.; An, Z.; Wu, P., Scalable preparation of alternating block copolymer particles with inverse bicontinuous mesophases. *Nat. Commun.* **2019,** *10*, 1397.

58. Nyrkova, I. A.; Semenov, A. N., On the theory of aggregation and micellization: PEO–PVP copolymer in water. *Faraday Discuss.* **2005,** *128*, 113-127.

59. Israelachvili, J. N.; Mitchell, D. J.; Ninham, B. W., Theory of self-assembly of hydrocarbon amphiphiles into micelles and bilayers. *J. Chem. Soc., Faraday Trans. 2* **1976,** *72*, 1525-1568.

60. Blanazs, A.; Armes, S. P.; Ryan, A. J., Self-Assembled Block Copolymer Aggregates: From Micelles to Vesicles and their Biological Applications. *Macromol. Rapid Commun.* **2009,** *30* (4-5), 267-277.

61. Discher, D. E.; Ahmed, F., Polymersomes. *Ann. Rev. Biomed. Eng.* **2006,** *8*, 323-341.

62. Doncom, K. E. B.; Blackman, L. D.; Wright, D. B.; Gibson, M. I.; O'Reilly, R. K., Dispersity effects in polymer self-assemblies: a matter of hierarchical control. *Chem. Soc. Rev.* **2017,** *46*, 4119-4134.

63. Cunningham, V. J.; Alswieleh, A. M.; Thompson, K. L.; Williams, M.; Leggett, G. J.; Armes, S. P.; Musa, O. M., Poly(glycerol monomethacrylate)–Poly(benzyl methacrylate) Diblock Copolymer Nanoparticles via RAFT Emulsion Polymerization: Synthesis, Characterization, and Interfacial Activity. *Macromol.* **2014,** *47*, 5613-5623.

64. Petzetakis, N.; Dove, A. P.; O'Reilly, R. K., Cylindrical micelles from the living crystallization-driven self-assembly of poly(lactide)-containing block copolymers. *Chem. Sci.* **2011,** *2*, 955-960.

65. Massey, J.; Power, K. N.; Manners, I.; Winnik, M. A., Self-Assembly of a Novel Organometallic−Inorganic Block Copolymer in Solution and the Solid State: Nonintrusive Observation of Novel Wormlike Poly(ferrocenyldimethylsilane)-b-Poly(dimethylsiloxane) Micelles. *J. Am. Chem. Soc.* **1998,** *120*, 9533-9540.

66. Wang, X.; Guerin, G.; Wang, H.; Wang, Y.; Manners, I.; Winnik, M. A., Cylindrical Block Copolymer Micelles and Co-Micelles of Controlled Length and Architecture. *Sci.* **2007,** *317*, 644-647.

67. Massey, J. A.; Temple, K.; Cao, L.; Rharbi, Y.; Raez, J.; Winnik, M. A.; Manners, I., Self-Assembly of Organometallic Block Copolymers: The Role of Crystallinity of the Core-Forming Polyferrocene Block in the Micellar Morphologies Formed by Poly(ferrocenylsilane-b-dimethylsiloxane) in n-Alkane Solvents. *J. Am. Chem. Soc.* **2000,** *122*, 11577-11584.

68. Wright, D. B.; Patterson, J. P.; Gianneschi, N. C.; Chassenieux, C.; Colombani, O.; O'Reilly, R. K., Blending block copolymer micelles in solution; obstacles of blending. *Polym. Chem.* **2016,** *7* (8), 1577-1583.

69. Nicolai, T.; Colombani, O.; Chassenieux, C., Dynamic polymeric micelles versus frozen nanoparticles formed by block copolymers. *Soft Matter* **2010,** *6*, 3111-3118.

70. Wang, H.; Wu, C.; Xia, G.; Ma, Z.; Mo, G.; Song, R., Semi-crystalline polymethylene-b-poly(acrylic acid) diblock copolymers: aggregation behavior, confined crystallization and controlled growth of semicrystalline micelles from dilute DMF solution. *Soft Matter* **2015,** *11*, 1778-1787.

71. Barnhill, S. A.; Bell, N. C.; Patterson, J. P.; Olds, D. P.; Gianneschi, N. C., Phase Diagrams of Polynorbornene Amphiphilic Block Copolymers in Solution. *Macromol.* **2015,** *48*, 1152-1161.

72. Schmitt, A. L.; Repollet-Pedrosa, M. H.; Mahanthappa, M. K., Polydispersity-Driven Block Copolymer Amphiphile Self-Assembly into Prolate-Spheroid Micelles. *ACS Macro Lett.* **2012,** *1*, 300-304.

73. Luo, L.; Eisenberg, A., Thermodynamic Stabilization Mechanism of Block Copolymer Vesicles. *J. Am. Chem. Soc.* **2001,** *123*, 1012-1013.

74. Kim, S. H.; Nederberg, F.; Jakobs, R.; Tan, J. P. K.; Fukushima, K.; Nelson, A.; Meijer, E. W.; Yang, Y. Y.; Hedrick, J. L., A Supramolecularly Assisted Transformation of Block-Copolymer Micelles into Nanotubes. *Angew. Chem. Int. Ed.* **2009,** *48*, 4508-4512.

75. He, M.; Zhao, L.; Wang, J.; Han, W.; Yang, Y.; Qiu, F.; Lin, Z., Self-Assembly of All-Conjugated Poly(3-alkylthiophene) Diblock Copolymer Nanostructures from Mixed Selective Solvents. *ACS Nano* **2010,** *4*, 3241-3247.

76. Tritschler, U.; Pearce, S.; Gwyther, J.; Whittell, G. R.; Manners, I., 50th Anniversary Perspective: Functional Nanoparticles from the Solution Self-Assembly of Block Copolymers. *Macromol.* **2017,** *50*, 3439-3463.

77. Hayward, R. C.; Pochan, D. J., Tailored Assemblies of Block Copolymers in Solution: It Is All about the Process. *Macromol.* **2010,** *43*, 3577-3584.

78. Warren, N. J.; Armes, S. P., Polymerization-Induced Self-Assembly of Block Copolymer Nano-objects via RAFT Aqueous Dispersion Polymerization. *J. Am. Chem. Soc.* **2014,** *136*, 10174-10185.

79. Canning, S. L.; Smith, G. N.; Armes, S. P., A Critical Appraisal of RAFT-Mediated Polymerization-Induced Self-Assembly. *Macromol.* **2016,** *49*, 1985-2001.

80. Derry, M. J.; Fielding, L. A.; Armes, S. P., Polymerization-induced self-assembly of block copolymer nanoparticles via RAFT non-aqueous dispersion polymerization. *Prog. Polym. Sci.* **2016,** *52*, 1-18.

81. Foster, J. C.; Varlas, S.; Couturaud, B.; Coe, Z.; O'Reilly, R. K., Getting into Shape: Reflections on a New Generation of Cylindrical Nanostructures' Self-Assembly Using Polymer Building Blocks. *J. Am. Chem. Soc.* **2019,** *141*, 20234-20248.

82. Karagoz, B.; Boyer, C.; Davis, T. P., Simultaneous Polymerization-Induced Self-Assembly (PISA) and Guest Molecule Encapsulation. *Macromol. Rapid. Commun.* **2014,** *35*, 417-421.

83. Blanazs, A.; Ryan, A. J.; Armes, S. P., Predictive Phase Diagrams for RAFT Aqueous Dispersion Polymerization: Effect of Block Copolymer Composition, Molecular Weight, and Copolymer Concentration. *Macromol.* **2012,** *45* (12), 5099-5107.

84. Figg, C. A.; Carmean, R. N.; Bentz, K. C.; Mukherjee, S.; Savin, D. A.; Sumerlin, B. S., Tuning Hydrophobicity To Program Block Copolymer Assemblies from the Inside Out. *Macromol.* **2017,** *50*, 935-943.

85. Guégain, E.; Zhu, C.; Giovanardi, E.; Nicolas, J., Radical Ring-Opening Copolymerization-Induced Self-Assembly (rROPISA). *Macromol.* **2019,** *52*, 3612-3624.

86. D'Agosto, F.; Rieger, J.; Lansalot, M., RAFT-Mediated Polymerization-Induced Self-Assembly. *Angew. Chem. Int. Ed.* **2020,** *59*, 8368-8392.

87. Wang, G.; Schmitt, M.; Wang, Z.; Lee, B.; Pan, X.; Fu, L.; Yan, J.; Li, S.; Xie, G.; Bockstaller, M. R.; Matyjaszewski, K., Polymerization-Induced Self-Assembly (PISA) Using ICAR ATRP at Low Catalyst Concentration. *Macromol.* **2016,** *49*, 8605-8615.

88. Wang, G.; Wang, Z.; Lee, B.; Yuan, R.; Lu, Z.; Yan, J.; Pan, X.; Song, Y.; Bockstaller, M. R.; Matyjaszewski, K., Polymerization-induced self-assembly of acrylonitrile via ICAR ATRP. *Polym. Chem.* **2017,** *129*, 57-67.

89. Qiao, X. G.; Lansalot, M.; Bourgeat-Lami, E.; Charleux, B., Nitroxide-Mediated Polymerization-Induced Self-Assembly of Poly(poly(ethylene oxide) methyl ether methacrylate-co-styrene)-b-poly(n-butyl methacrylate-co-styrene) Amphiphilic Block Copolymers. *Macromol.* **2013,** *46*, 4285-4295.

90. Qiao, X. G.; Dugas, P. Y.; Charleux, B.; Lansalot, M.; Bourgeat-Lami, E., Nitroxide-mediated polymerization-induced self-assembly of amphiphilic block copolymers with a pH/temperature dual sensitive stabilizer block. *Polym. Chem.* **2017,** *8*, 4014-4029.

91. Foster, J. C.; Varlas, S.; Blackman, L. D.; Arkinstall, L. A.; O'Reilly, R. K., Ring-Opening Metathesis Polymerization in Aqueous Media Using a Macroinitiator Approach. *Angew. Chem. Int. Ed.* **2018,** *57*, 10672-10676.

92. Wright, D. B.; Touve, M. A.; Adamiak, L.; Gianneschi, N. C., ROMPISA: Ring-Opening Metathesis Polymerization-Induced Self-Assembly. *ACS Macro Lett.* **2017,** *6*, 925-929.

93. Wright, D. B.; Proetto, M. T.; Touve, M. A.; Gianneschi, N. C., Ring-opening metathesis polymerization-induced self-assembly (ROMPISA) of a cisplatin analogue for high drug-loaded nanoparticles. *Polym. Chem.* **2019,** *10*, 2996-3000.

94. Jimaja, S.; Varlas, S.; Xie, Y.; Foster, J. C.; Taton, D.; Dove, A. P.; O'Reilly, R. K., Nickel-Catalyzed Coordination Polymerization-Induced Self-Assembly of Helical Poly(aryl isocyanide)s. *ACS Macro Lett.* **2020,** *9*, 226-232.

95. Jimaja, S.; Xie, Y.; Foster, J. C.; Taton, D.; Dove, A. P.; O'Reilly, R. K., Functional nanostructures by NiCCo-PISA of helical poly(aryl isocyanide) copolymers. *Polym. Chem.* **2021,** *12*, 105-112.

96. Jiang, J.; Zhang, X.; Fan, Z.; Du, J., Ring-Opening Polymerization of N-Carboxyanhydride-Induced Self-Assembly for Fabricating Biodegradable Polymer Vesicles. *ACS Macro Lett.* **2019,** *8*, 1216-1221.

97. Grazon, C.; Salas-Ambrosio, P.; Ibarboure, E.; Buol, A.; Garanger, E.; Grinstaff, M. W.; Lecommandoux, S.; Bonduelle, C., Aqueous Ring-Opening Polymerization-Induced Self-Assembly (ROPISA) of N-Carboxyanhydrides. *Angew. Chem. Int. Ed.* **2020,** *59*, 622-626.

98. Karagoz, B.; Esser, L.; Duong, H. T.; Basuki, J. S.; Boyer, C.; Davis, T. P., Polymerization-Induced Self-Assembly (PISA) – control over the morphology of nanoparticles for drug delivery applications. *Polym. Chem.* **2014,** *5*, 350-355.

99. Zhang, W.-J.; Hong, C.-Y.; Pan, C.-Y., Fabrication of Reductive-Responsive Prodrug Nanoparticles with Superior Structural Stability by Polymerization-Induced Self-Assembly and Functional Nanoscopic Platform for Drug Delivery. *Biomacromol.* **2016,** *17*, 2992-2999.

100. Zhang, W.-J.; Hong, C.-Y.; Pan, C.-Y., Artificially Smart Vesicles with Superior Structural Stability: Fabrication, Characterizations, and Transmembrane Traffic. *ACS Appl. Mater. Interfaces* **2017,** *9*, 15086-15095.

101. Zhang, W.-J.; Hong, C.-Y.; Pan, C.-Y., Polymerization-Induced Self-Assembly of Functionalized Block Copolymer Nanoparticles and Their Application in Drug Delivery. *Macromol. Rapid. Commun.* **2019,** *40*, 1800279.

102. Zhao, W.; Ta, H. T.; Zhang, C.; Whittaker, A. K., Polymerization-Induced Self-Assembly (PISA) - Control over the Morphology of 19F-Containing Polymeric Nano-objects for Cell Uptake and Tracking. *Biomacromol.* **2017,** *18*, 1145-1156.

103. Derry, M. J.; Smith, T.; O'Hora, P. S.; Armes, S. P., Block Copolymer Nanoparticles Prepared via Polymerization-Induced Self-Assembly Provide Excellent Boundary Lubrication Performance for Next-Generation Ultralow-Viscosity Automotive Engine Oils. *ACS Appl. Mater. Interfaces* **2019,** *11*, 33364-33369.

104. Thompson, K. L.; Mable, C. J.; Cockram, A.; Warren, N. J.; Cunningham, V. J.; Jones, E. R.; Verber, R.; Armes, S. P., Are block copolymer worms more effective Pickering emulsifiers than block copolymer spheres? *Soft Matter* **2014,** *10*, 8615-8626.

105. Mable, C. J.; Warren, N. J.; Thompson, K. L.; Mykhaylyk, O. O.; Armes, S. P., Framboidal ABC triblock copolymer vesicles: a new class of efficient Pickering emulsifier. *Chem. Sci.* **2015,** *6*, 6179-6188.

106. Hirschberg, J. H. K. K.; Brunsveld, L.; Ramzi, A.; Vekemans, J. A. J. M.; Sijbesma, R. P.; Meijer, E. W., Helical self-assembled polymers from cooperative stacking of hydrogen-bonded pairs. *Nat.* **2000,** *407*, 167-170.

107. Tsai, S.-C.; Lin, Y.-C.; Lin, E.-L.; Chiang, Y.-W.; Kuo, S.-W., Hydrogen bonding strength effect on self-assembly supramolecular structures of diblock copolymer/homopolymer blends. *Polym. Chem.* **2016,** *7*, 2395-2409.

108. Venkataraman, S.; Chowdhury, Z. A.; Lee, A. L.; Tong, Y. W.; Akiba, I.; Yang, Y. Y., Access to Different Nanostructures via Self-Assembly of Thiourea-Containing PEGylated Amphiphiles. *Macromol. Rapid. Commun.* **2013,** *34*, 652-658.

109. Sun, L.; Pitto-Barry, A.; Kirby, N.; Schiller, T. L.; Sanchez, A. M.; Dyson, M. A.; Sloan, J.; Wilson, N. R.; O'Reilly, R. K.; Dove, A. P., Structural reorganization of

cylindrical nanoparticles triggered by polylactide stereocomplexation. *Nat. Commun.* **2014,** *5*, 5746.

110. Sijbesma, R. P.; Beijer, F. H.; Brunsveld, L.; Folmer, B. J. B.; Hirschberg, J. H. K. K.; Lange, R. F. M.; Lowe, J. K. L.; Meijer, E. W., Reversible Polymers Formed from Self-Complementary Monomers Using Quadruple Hydrogen Bonding. *Sci.* **1997,** *278*, 1601-1604.

111. Cordier, P.; Tournilhac, F.; Soulié-Ziakovic, C.; Leibler, L., Self-healing and thermoreversible rubber from supramolecular assembly. *Nat.* **2008,** *451*, 977-980.

112. Goor, O. J. G. M.; Hendrikse, S. I. S.; Dankers, P. Y. W.; Meijer, E. W., From supramolecular polymers to multi-component biomaterials. *Chem. Soc. Rev.* **2017,** *46*, 6621-6637.

113. Jones, A. S.; Parsons, D. G.; Roberts, D. G., The interaction of polynucleotides with a guanine derivative of cellulose. *Eur. Polym. J.* **1967,** *3*, 187-198.

114. Pitha, J.; Ts'o, P. O. P., N-Vinyl derivatives of substituted pyrimidines and purines. *J. Org. Chem.* **1968,** *33*, 1341-1344.

115. Ueda, N.; Konda, K.; Kono, M.; Takemoto, K.; Imoto, M., Vinyl polymerization. 217. Vinyl compounds of nucleic acid basis. I. Synthesis of N-vinylthymine, and N-vinyladenine. *Makromol. Chem.* **1968,** *120*, 13-20.

116. Spijker, H. J.; Dirks, A. J.; van Hest, J. C. M., Synthesis and assembly behavior of nucleobase-functionalized block copolymers. *Polym. Chem.* **2006,** *44*, 4242-4250.

117. Lo, P. K.; Sleiman, H. F., Nucleobase-Templated Polymerization: Copying the Chain Length and Polydispersity of Living Polymers into Conjugated Polymers. *J. Am. Chem. Soc.* **2009,** *131*, 4182-4183.

118. Bazzi, H. S.; Sleiman, H. F., Adenine-Containing Block Copolymers via Ring-Opening Metathesis Polymerization: Synthesis and Self-Assembly into Rod Morphologies. *Macromol.* **2002,** *35*, 9617-9620.

119. Kang, Y.; Lu, A.; Ellington, A.; Jewett, M. C.; O'Reilly, R. K., Effect of Complementary Nucleobase Interactions on the Copolymer Composition of RAFT Copolymerizations. *ACS Macro Lett.* **2013,** *2*, 581-586.

120. Kang, Y.; Pitto-Barry, A.; S. Rolph, M.; Hua, Z.; Hands-Portman, I.; Kirby, N.; O'Reilly, R. K., Use of complementary nucleobase-containing synthetic polymers to prepare complex self-assembled morphologies in water. *Polym. Chem.* **2016,** *7*, 2836-2846.

121. Fong, D.; Hua, Z.; Wilks, T. R.; O'Reilly, R. K.; Adronov, A., Dispersion of single-walled carbon nanotubes using nucleobase-containing poly(acrylamide) polymers. *J. Polym. Sci., Part A: Polym. Chem.* **2017,** *55*, 2611-2617.

122. Mather, B. D.; Baker, M. B.; Beyer, F. L.; Berg, M. A. G.; Green, M. D.; Long, T. E., Supramolecular Triblock Copolymers Containing Complementary Nucleobase Molecular Recognition. *Macromol.* **2007,** *40*, 6834-6845.

123. Rothemund, P. W. K., Folding DNA to create nanoscale shapes and patterns. *Nat* .**2006,** *440*, 297-302.

124. South, C. R.; Weck, M., Template-Enhanced Ring-Opening Metathesis Polymerization. *Macromol.* **2007,** *40*, 1386-1394.

125. McHale, R.; Patterson, J. P.; Zetterlund, P. B.; O'Reilly, R. K., Biomimetic radical polymerization via cooperative assembly of segregating templates. *Nat. Chem.* **2012,** *4*, 491.

126. Ilhan, F.; Galow, T. H.; Gray, M.; Clavier, G.; Rotello, V. M., Giant Vesicle Formation through Self-Assembly of Complementary Random Copolymers. *J. Am. Chem. Soc.* **2000,** *122*, 5895-5896.

127. Kang, Y.; Pitto-Barry, A.; Maitland, A.; O'Reilly, R. K., RAFT dispersion polymerization: a method to tune the morphology of thymine-containing self-assemblies. *Polym. Chem.* **2015,** *6*, 4984-4992.

128. Hua, Z.; Pitto-Barry, A.; Kang, Y.; Kirby, N.; Wilks, T. R.; O'Reilly, R. K., Micellar nanoparticles with tuneable morphologies through interactions between nucleobase-containing synthetic polymers in aqueous solution. *Polym. Chem.* **2016,** *7*, 4254-4262.

129. Li, Z.; Tang, M.; Liang, S.; Zhang, M.; Biesold, G. M.; He, Y.; Hao, S.-M.; Choi, W.; Liu, Y.; Peng, J.; Lin, Z., Bottlebrush polymers: From controlled synthesis, self-assembly, properties to applications. *Prog. Polym. Sci.* **2021,** *116*, 101387.

130. Verduzco, R.; Li, X.; Pesek, S. L.; Stein, G. E., Structure, function, self-assembly, and applications of bottlebrush copolymers. *Chem. Soc. Rev.* **2015,** *44*, 2405-2420.

131. Xie, G.; Martinez, M. R.; Olszewski, M.; Sheiko, S. S.; Matyjaszewski, K., Molecular Bottlebrushes as Novel Materials. *Biomacromol.* **2019,** *20*, 27-54.

132. Varlas, S.; Hua, Z.; Jones, J. R.; Thomas, M.; Foster, J. C.; O'Reilly, R. K., Complementary Nucleobase Interactions Drive the Hierarchical Self-Assembly of Core–Shell Bottlebrush Block Copolymers toward Cylindrical Supramolecules. *Macromol.* **2020,** *53*, 9747-9757.

133. Charleux, B.; Delaittre, G.; Rieger, J.; D'Agosto, F., Polymerization-Induced Self-Assembly: From Soluble Macromolecules to Block Copolymer Nano-Objects in One Step. *Macromol.* **2012,** *45*, 6753-6765.

134. Lotz, B.; Kovacs, A.; Bassett, G.; Keller, A. In Morphology of single-crystal copolymers of polyethylene oxide and polystyrene, *J. Appl. Phys.*, Amer inst Physics Circulation fulfillment div: 1965; pp 2618-&.

135. Schmelz, J.; Schedl, A. E.; Steinlein, C.; Manners, I.; Schmalz, H., Length Control and Block-Type Architectures in Worm-like Micelles with Polyethylene Cores. *J. Am. Chem. Soc.* **2012,** *134*, 14217-14225.

136. Gilroy, J. B.; Gädt, T.; Whittell, G. R.; Chabanne, L.; Mitchels, J. M.; Richardson, R. M.; Winnik, M. A.; Manners, I., Monodisperse cylindrical micelles by crystallization-driven living self-assembly. *Nat. Chem.* **2010,** *2*, 566-570.

137. He, W.-N.; Zhou, B.; Xu, J.-T.; Du, B.-Y.; Fan, Z.-Q., Two Growth Modes of Semicrystalline Cylindrical Poly (ε-caprolactone)-b-poly (ethylene oxide) Micelles. *Macromol.* **2012,** *45*, 9768-9778.

138. Sun, L.; Pitto-Barry, A.; Thomas, A. W.; Inam, M.; Doncom, K.; Dove, A. P.; O'Reilly, R. K., Core functionalization of semi-crystalline polymeric cylindrical nanoparticles using photo-initiated thiol–ene radical reactions. *Polym. Chem.* **2016,** *7*, 2337-2341.

139. Schmelz, J.; Schacher, F. H.; Schmalz, H., Cylindrical crystalline-core micelles: pushing the limits of solution self-assembly. *Soft Matter* **2013,** *9*, 2101-2107.

140. Inam, M.; Cambridge, G.; Pitto-Barry, A.; Laker, Z. P. L.; Wilson, N. R.; Mathers, R. T.; Dove, A. P.; O'Reilly, R. K., 1D vs. 2D shape selectivity in the crystallization-driven self-assembly of polylactide block copolymers. *Chem. Sci.* **2017,** *8*, 4223-4230.

141. Qiu, H.; Gao, Y.; Boott, C. E.; Gould, O. E. C.; Harniman, R. L.; Miles, M. J.; Webb, S. E. D.; Winnik, M. A.; Manners, I., Uniform patchy and hollow rectangular platelet micelles from crystallizable polymer blends. *Sci.* **2016,** *352*, 697-701.

142. Hua, Z.; Jones, J. R.; Thomas, M.; Arno, M. C.; Souslov, A.; Wilks, T. R.; O'Reilly, R. K., Anisotropic polymer nanoparticles with controlled dimensions from the morphological transformation of isotropic seeds. *Nat. Commun.* **2019,** *10*, 5406.

143. Patterson, J. P.; Robin, M. P.; Chassenieux, C.; Colombani, O.; O'Reilly, R. K., The analysis of solution self-assembled polymeric nanomaterials. *Chem. Soc. Rev.* **2014,** *43*, 2412-2425.

144. Patterson, J. P.; Xu, Y.; Moradi, M.-A.; Sommerdijk, N. A. J. M.; Friedrich, H., CryoTEM as an Advanced Analytical Tool for Materials Chemists. *Acc. Chem. Res.* **2017,** *50*, 1495-1501.

145. Thompson, R. F.; Walker, M.; Siebert, C. A.; Muench, S. P.; Ranson, N. A., An introduction to sample preparation and imaging by cryo-electron microscopy for structural biology. *Methods* **2016,** *100*, 3-15.

146. Wilson, N. R.; Pandey, P. A.; Beanland, R.; Young, R. J.; Kinloch, I. A.; Gong, L.; Liu, Z.; Suenaga, K.; Rourke, J. P.; York, S. J.; Sloan, J., Graphene Oxide: Structural Analysis and Application as a Highly Transparent Support for Electron Microscopy. *ACS Nano* **2009,** *3*, 2547-2556.

147. Patterson, J. P.; Sanchez, A. M.; Petzetakis, N.; Smart, T. P.; Epps, I. I. I. T. H.; Portman, I.; Wilson, N. R.; O'Reilly, R. K., A simple approach to characterizing block copolymer assemblies: graphene oxide supports for high contrast multi-technique imaging. *Soft Matter* **2012,** *8*, 3322-3328.

2 : Nucleobase-containing nanoparticles with pathway dependent morphologies through interactions between complementary nucleobase-containing synthetic polymers in aqueous solutions

2.1 Introduction

The self-assembly of amphiphilic block copolymers has been an attractive field due to the wide range of morphologies that can be formed, and the possibility to incorporate specific functional molecules. The wide range of morphologies include spherical micelles,[1] cylindrical micelles,[2-4] bicontinuous structures,[5] lamellae,[6] and vesicles,[1, 7-8] among others. By tuning the hydrophobic/hydrophilic weight fraction, which influences the packing parameter of the block copolymers, morphologies can be predicted for a given system.[9-10] Nanostructure size and morphologies are critical parameters in applications such as imaging, medical or energy-based, and tuning these parameters to optimise performance is of great interest. For instance, cylindrical micelles, which thanks to their elongated shape, can persist in the blood circulation up to ten times longer than their spherical analogues.[11] Several techniques can be used to access these different morphologies, such as standard post-polymerization self-assembly methods (*e.g.*, solvent switch or direct dissolution),[12-13] crystallization-driven self-assembly (CDSA),[14-15] or polymerization-induced self-assembly (PISA).[16-17]

Inspired by the way DNA assembles in nature, research into nucleobase-containing synthetic polymers have been widely exploited as cheap and more readily available alternatives to DNA and DNA containing-materials, to template polymerization,[18-19] and to control polymer composition or sequence.[20-21] Nucleobase interactions have also been studied and utilized for driving self-assembly process,[22-26] and to achieve biomimetic segregation/templating approach to polymer synthesis.[27]

O'Reilly and co-workers reported that distinct self-assembled morphologies could be formed with nucleobase copolymers with different composition, and morphological evolutions were observed during RAFT dispersion polymerization of nucleobase-

containing monomers.[21, 28-29] However, due the poor solubility and slow hydrolysis of nucleobase-containing monomers in water, their applications are limited in aqueous solutions and relatively little research into self-assembly of nucleobase-containing polymers in aqueous solutions.[25, 30-32]

Van Hest and coworkers reported in 2006 the self-assembly behavior of nucleobase-containing amphiphilic copolymers in aqueous solutions and, due to complementary (adenine:thymine) nucleobase interactions, an increase of overall hydrophilicity of the diblock was observed by an improved shielding of the hydrophobic blocks.[25] Hence, there is significant interest in the exploration of complementary nucleobase interactions embedded within synthetic polymers to allow for access to new classes of responsive and tuneable materials and nanostructures.

In 2016, Hua *et al.* reported well-defined spherical micelles were obtained in aqueous solution from nucleobase-containing diblock copolymers, and demonstrated that nanoparticle morphology could be tuned through the complementary nucleobase interactions using a relatively long hydrophobic block for the micelle.[33] However, no control over the length or width was possible, which was thought due to polymer exchange and reorganization. Previous studies have demonstrated that polymer chain exchange in aqueous solution was dependent on the hydrophobic block length,[34-35] as longer hydrophobic blocks have a larger interface with the solvent. It was therefore proposed that increasing the length of the hydrophobic block would "freeze" the aggregates, preventing chain exchange and enabling control over the morphing process to be retained. Following on the 2016's report, the same group reported a new mechanism with control over the dimensions of anisotropic nanoparticles, which was termed morphological transformation (MORPH).[36] In this mechanism, the growth of well-

defined anisotropic nanoparticles from isotropic seeds, is based on the hydrogen bonding interaction between complementary nucleobases. To an aqueous solution of nanoparticles consisting of a long hydrophobic synthetic nucleic acid core and a hydrophilic corona poly(4-acryloylmorpholine)-*b*-poly(3-(thymin-1-yl)propylacrylamide) ($PNAM_{40}$-*b*-$PTAm_{300}$), another diblock copolymer with the complementary nucleobase poly(4-acryloylmorpholine)-*b*-poly(3-(adenine-9-yl)propyl acrylamide) ($PNAM_{40}$-*b*-$PAAm_{20}$) was added. The base pairing interaction between adenine (A) and thymine (T) drove insertion of the complementary nucleobase copolymer anywhere into the core of the nanoparticles. Addition of further polymer triggered a global transformation of the nanoparticles from spheres to dumbbells, and then ultimately worms in a highly controlled and reproductible manner.

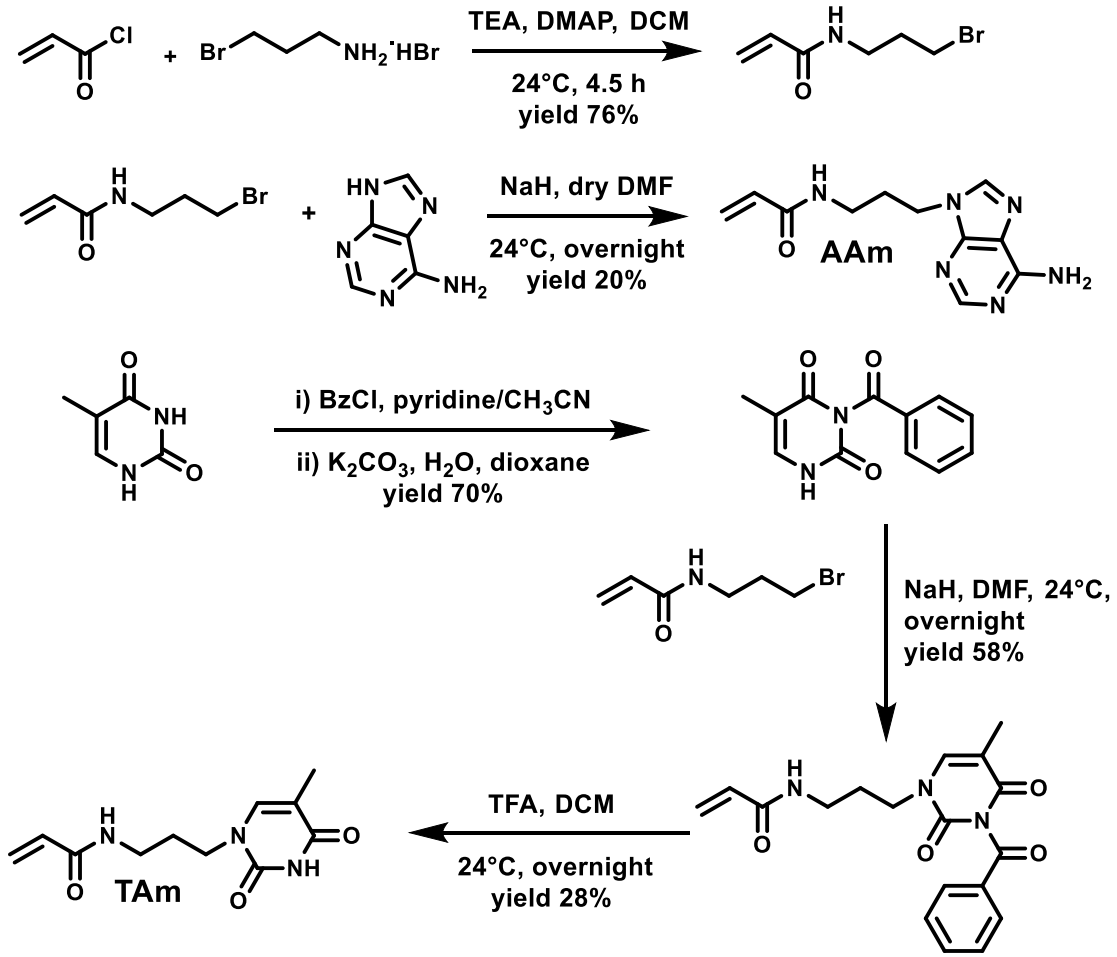
Following on from this study, herein the synthesis and assembly of nucleobase-containing block copolymers and their corresponding micelles with tuneable morphologies through the introduction of complementary nucleobase interactions within the core of the micelles was reported. The initial micellar constructs in water consist of the same synthetic nucleic acid cores and hydrophilic coronas (PNAM-*b*-PTAm), with corona block length varying from similar to longer block and a core block varying from similar length to shorter block).[36] Another diblock copolymer with the complementary nucleobase (PNAM-*b*-PAAm) was utilized to induce a morphological change in these micelles. Different micellar solutions were prepared from thymine-containing block copolymers of different length and self-assembled *via* solvent-switch method. In the present study, the effect of hydrophobic and hydrophilic block lengths of thymine-containing micelles on the morphological transformations induced by the complementary polymer were investigated. Tuneable morphologies for the different thymine-containing micelles were

observed with the introduction of the complementary diblock copolymer , PNAM-*b*-PAAm. A morphological change from spheres to cylinders was also observed with an increasing amounts on the complementary diblock copolymer.

2.2 Results and discussion

2.2.1 Synthesis of nucleobase-containing acrylamide monomers TAm and AAm

The synthesis of nucleobase-containing acrylamide monomers has been reported previously in our group[33]. Acrylamide-type monomers compared to the intensively investigated methacrylate[37] and methacrylamide[21] analogues are more reactive and water-soluble. First, *N*-(3-bromopropyl)acrylamide an alkylating agent was synthesized by nucleophilic addition with a yield of 76%. This alkylating agent was very unstable and needed to be used immediately after the synthesis since a substitution between the amide and bromide could not be completely prevented. The synthesis of the nucleobase-containing acrylamide monomers 3-(adenine-9-yl) propyl acrylamide (**AAm**) and 3-(thymin-1-yl)propyl acrylamide (**TAm**) was achieved *via* an alkylation using *N*-(3-bromopropyl)acrylamide (Scheme 2.1).



Scheme 2.1. Syntheses of adenine and thymine acrylamide monomers (AAm and TAm).

The adenine monomer (**AAm**) was synthesized by direct substitution (Scheme 2.1 and Figures 2.1 and 2.2) with an acceptable yield of 20%.

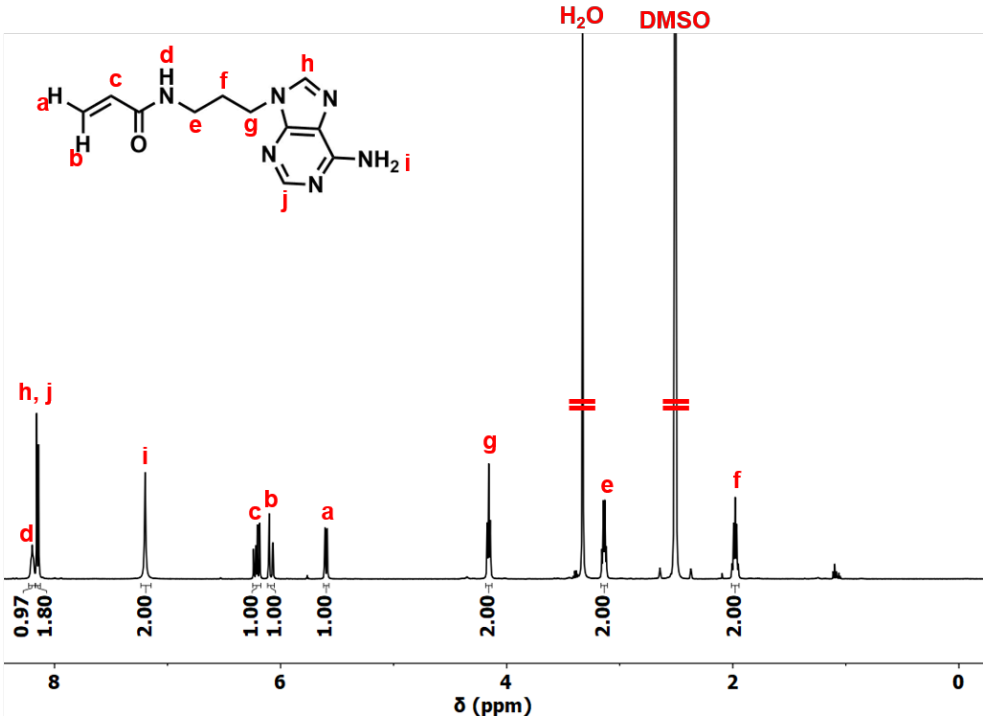


Figure 2.1. [1]H NMR spectrum of 3-(adenine-9-yl) propyl acrylamide (**AAm**) in DMSO-d_6 (500 MHz).

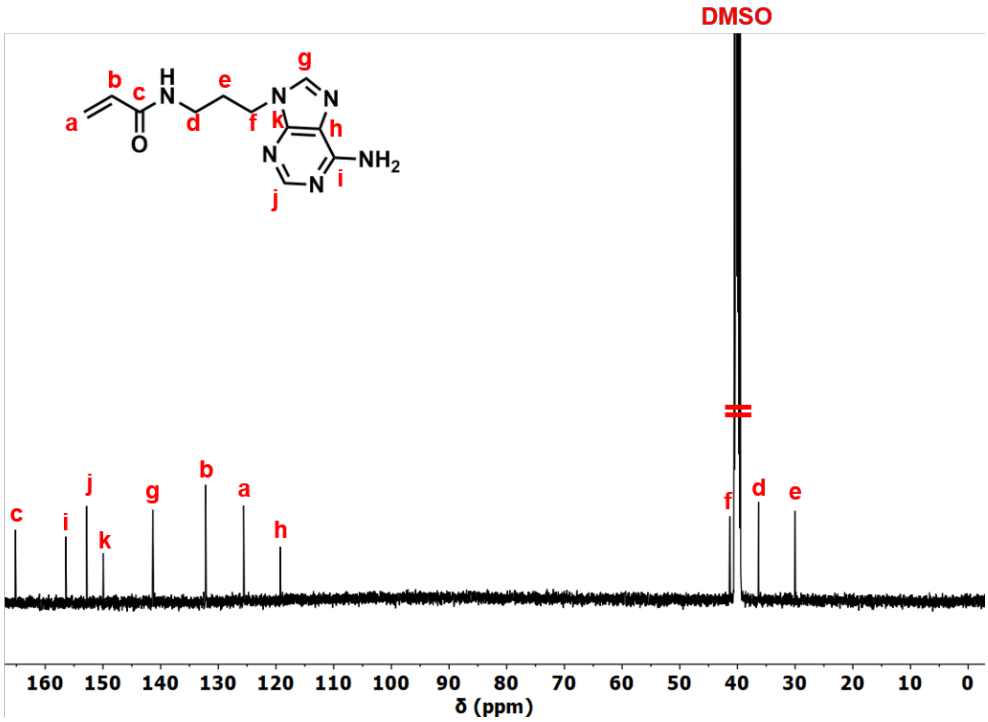


Figure 2.2. [13]C NMR spectrum of 3-(adenine-9-yl) propyl acrylamide (AAm) in DMSO-d_6 (500 MHz).

In contrast with **AAm**, the thymine monomer (**TAm**) was obtained with a three steps synthesis containing a selective protection of the thymine first and then a deprotection step (Scheme 2.1). A direct alkylation of the thymine could not be done since it led to a mixture of different species including a *N*1 substitution and *N*1-*N*3 double substitution of the thymine with *N*-(3-bromopropyl) acrylamide. The three steps synthesis of **TAm** led to a pure product with a moderate overall yield of 11% (Figures 2.3 and 2.4).

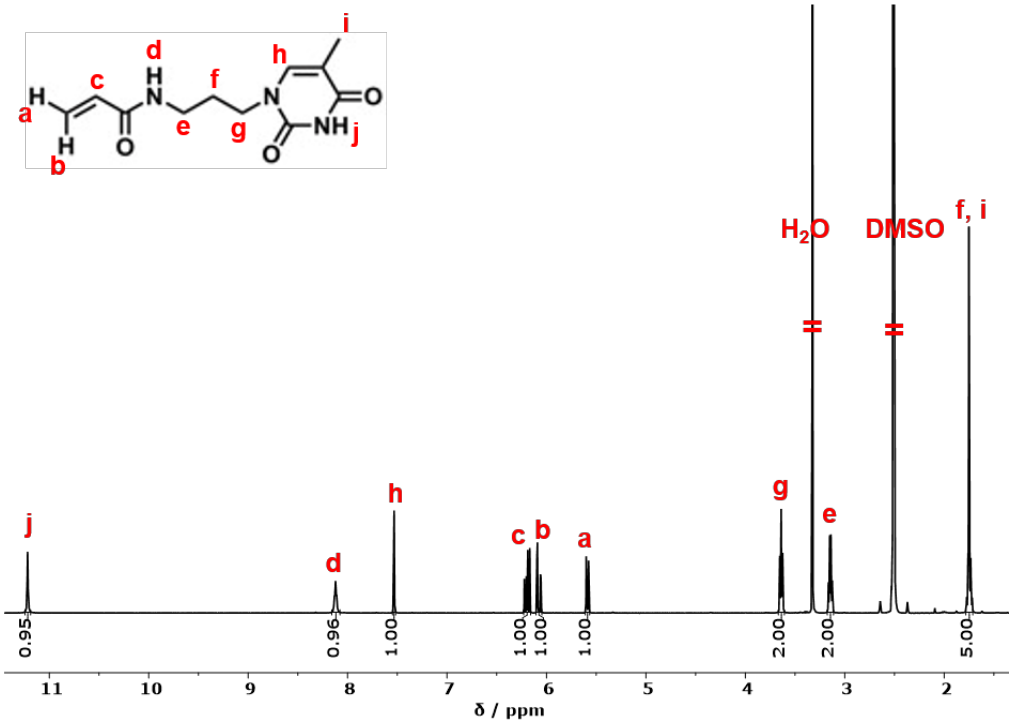


Figure 2.3. ^{1}H NMR spectrum of 3-(thymine-1-yl)propyl acrylamide (**TAm**) in DMSO-d_6 (500 MHz).

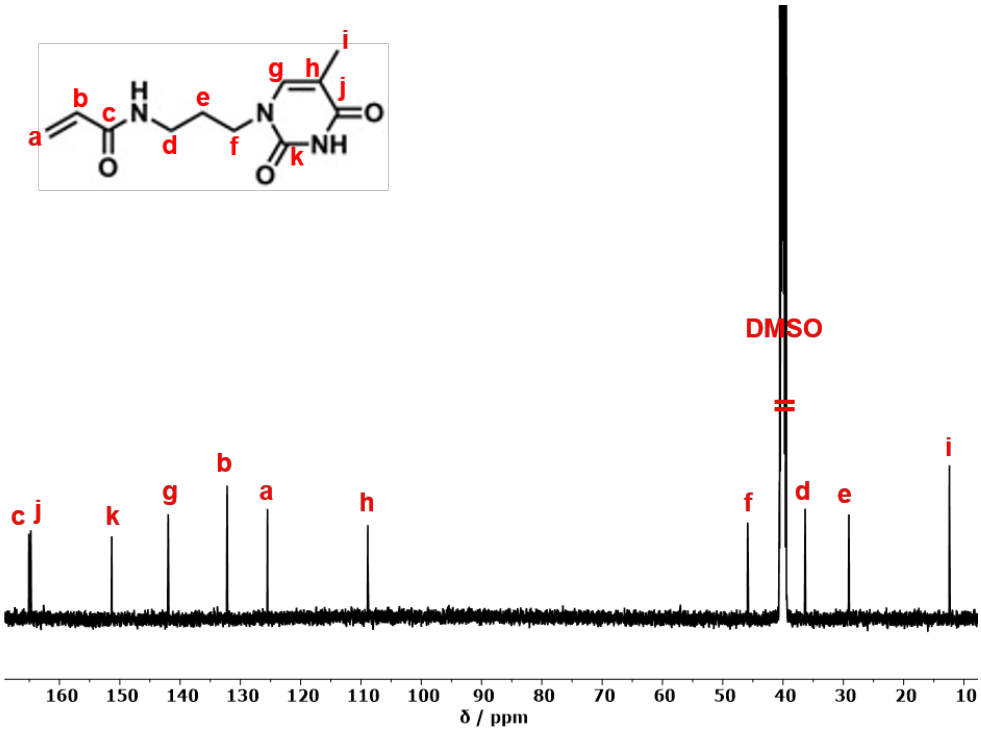


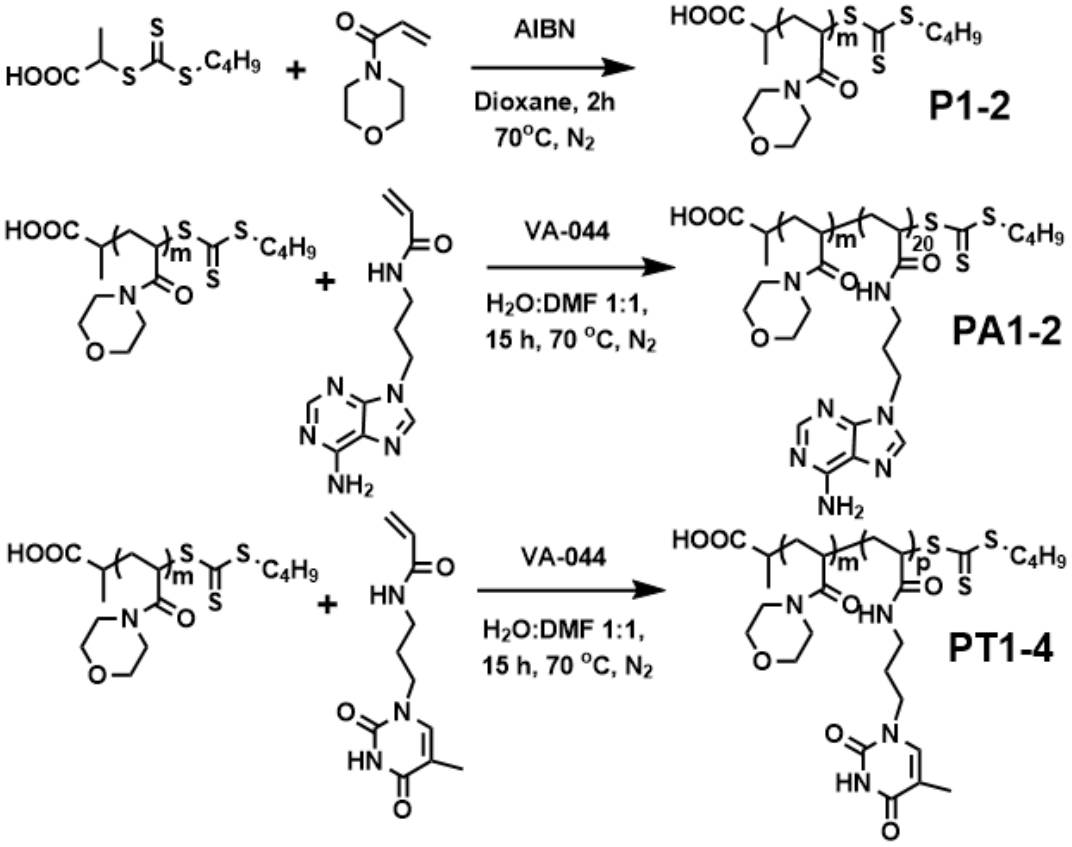
Figure 2.4. ^{13}C NMR spectrum of 3-(thymine-1-yl)propyl acrylamide (**TAm**) in DMSO-d_6 (500 MHz).

2.2.2 Synthesis and characterization of nucleobase-containing synthetic diblock copolymers

As well as the polymers synthesized to reproduce the original MORPH mechanism (**PT4** and **PA1**), a library of copolymers bearing the same nucleobase functionalities but with different corona and core lengths were synthesized to study the MORPH mechanism, since we were interested to explore whether the hydrophobic/hydrophilic ratio determines the morphological transitions.

First, a series of PNAM macro-CTAs with different length were synthesized (**P1** and **P2**) in 1,4-dioxane using 2,2'-Azobis(2-methylpropionitrile) (AIBN) as the initiator for 2h at 70°C under nitrogen atmosphere (Scheme 2.2). ^{1}H NMR spectroscopy was used to calculate the degree of polymerization (DP) by comparing the integrated signals corresponding to the backbone protons (δ= 1.62 ppm) with those of the methyl group

from the CTA (δ= 0.87 ppm) (Schemes 2.3 and 2.4, Figures 2.15, 2.16, 2.17 and 2.18 in Experimental section).



Scheme 2.2. Synthetic routes for the preparation of $PNAM_{40}$ and $PNAM_{100}$, **P1** and **P2** respectively and the nucleobase-containing block copolymers, **PA1** ($PNAM_{40}$-*b*-$PAAm_{20}$)**, PA2** ($PNAM_{100}$-*b*-$PAAm_{20}$), **PT1** ($PNAM_{40}$-*b*-$PAAm_{100}$), **PT2** ($PNAM_{40}$-*b*-$PAAm_{200}$), **PT3** ($PNAM_{40}$-*b*-$PAAm_{300}$) and **PT4** ($PNAM_{100}$-*b*-$PAAm_{300}$).

The $PNAM_m$ macro-CTAs were then chained-extended with **AAm** or **TAm** in a mixture of water and DMF *via* RAFT polymerization. Figure 2.5 shows the NMR spectra of **P1**, **PA1** and **PT3** respectively and Figure 2.6 the SEC traces of the chain extended macro-CTA with either **AAm** or **TAm** at different DPs.

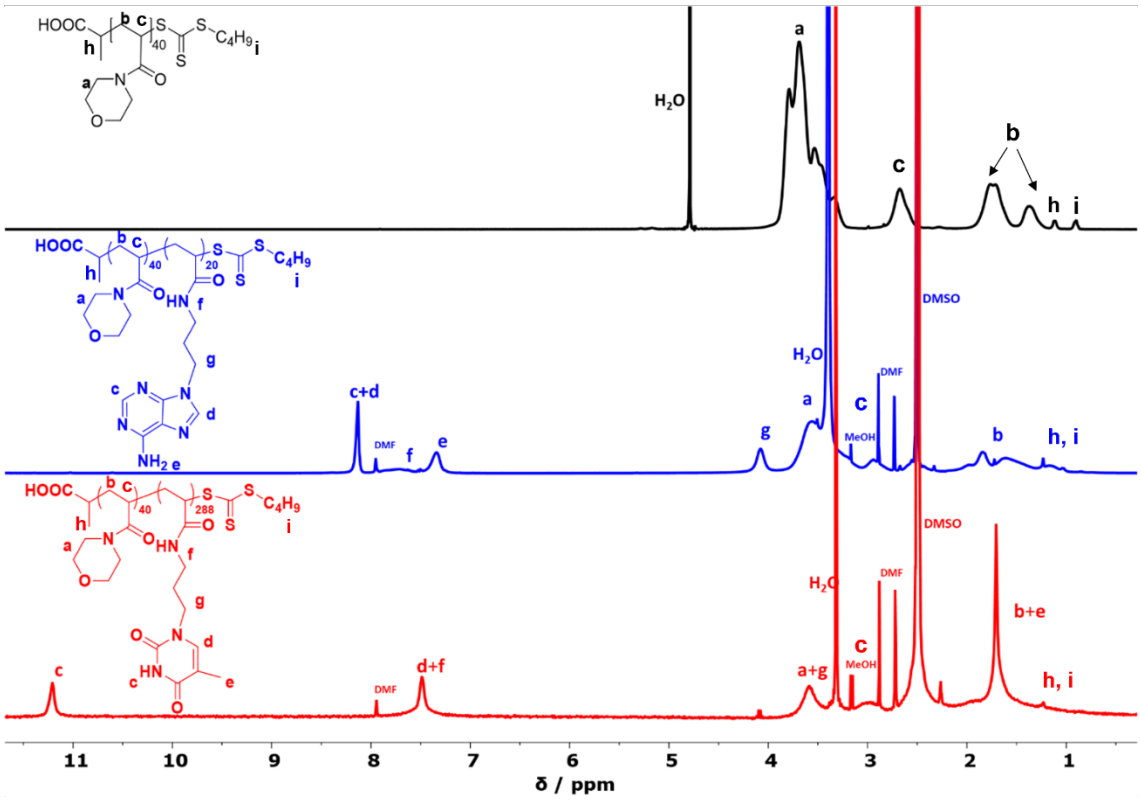


Figure 2.5. ^{1}H NMR spectra of $PNAM_{40}$ in D_2O, **PA1** ($PNAM_{40}$-*b*-$PAAm_{20}$) and **PT3** ($PNAM_{40}$-*b*-$PTAm_{288}$) in DMSO-d_6 (400 MHz).

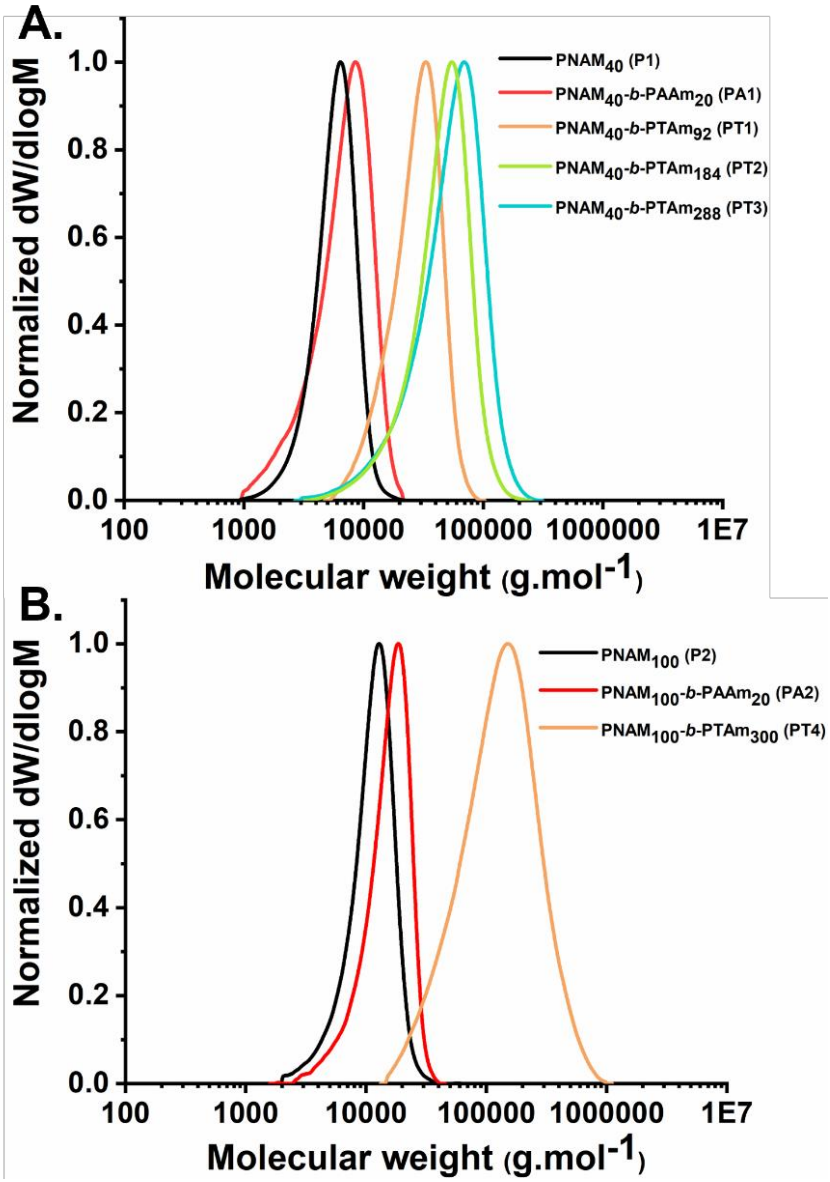


Figure 2.6. SEC traces of macro-CTAs chain extended with different PNAM macroCTA, (A) $PNAM_{40}$ (**P1**), **PA1**, **PT1**, **PT2** and **PT3**. (B) $PNAM_{100}$ (**P2**), **PA2** and **PT4** (DMF + 5 mM NH_4BF_4 as eluent, PMMA standard.

SEC traces indicated unimodal molecular weight distributions for the different macro-CTA with a molecular weight of 5.2 kDa for **P1** and 10 kDa for **P2**. The dispersities ($Đ_M$) for **P1**, **P2** were quite low with a $Đ_M$ of 1.18 and 1.21 respectively. For **PT1**, **PT2**, **PT3** and **PT4**, the SEC traces indicated unimodal molecular weight distributions as well with a molecular weight of 24.1 kDa, 36.4 kDa, 40.5 kDa and 95.8 respectively, and dispersities values of

1.25, 1.39, 1.33 and 1.68 respectively. A general trend toward higher dispersities is observed when the hydrophobic or hydrophilic block length increases. As for **PA1** and **PA2**, the SEC traces also showed unimodal molecular weight distributions, with molecular weights of 9.8 kDa and 15.9 kDa respectively. The dispersities were also quite low, with a $Đ_M$ of 1.18 and 1.20 for **PA1** and **PA2** respectively. These results showed the synthesis of nucleobase-containing diblock copolymers with relatively high blocking efficiencies through RAFT polymerization, where long thymine-containing core block were obtained with up to 300 units and a series of short adenine-containing core block with relatively low dispersity were obtained as well. Table 2.1 shows the ^{1}H NMR and SEC characterization data of the different polymers synthesized.

Table 2.1. Characterization data of macro-CTA and nucleobase-containing diblock copolymers.

Polymers	Structures	Conversion %	$M_{n,NMR}$[a] kDa	$M_{n,SEC}$[b] kDa	$Đ_M$[b]
P1	$PNAM_{40}$	> 99	5.6	5.2	1.18
P2	$PNAM_{100}$	> 99	14.1	10	1.21
PT1	$PNAM_{40}$-*b*-$PTAm_{92}$	> 92	27.1	24.1	1.25
PT2	$PNAM_{40}$-*b*-$PTAm_{184}$	> 92	48.7	36.4	1.39
PT3	$PNAM_{40}$-*b*-$PTAm_{288}$	> 96	73.1	40.5	1.33
PT4	$PNAM_{100}$-*b*-$PTAm_{297}$	> 99	83.6	95.8	1.68
PA1	$PNAM_{40}$-*b*-$PAAm_{20}$	> 99	10.7	9.8	1.18
PA2	$PNAM_{100}$-*b*-$PAAm_{20}$	> 99	19.1	15.9	1.20

[a]Determined by ^{1}H NMR spectroscopy (400 MHz) in deuterated DMSO. [b]Determined by DMF SEC with poly(methyl methacrylate) (PMMA) standards.

The synthesized polymer library was then used to obtain self-assemblies in order to study the effect of the block copolymer lengths on the morphological transformation upon addition of a short polymer (**PA1** and **PA2**).

2.2.3 Self-assembly of nucleobase-containing diblock copolymers

2.2.3.1 Self-assembly of PT diblock copolymers

The block copolymers **PT1**, **PT2**, **PT3** and **PT4** were self-assembled into well-defined thymine-containing micelles through a solvent switch from DMF to water.[36] The block copolymers were dissolved in DMF at a concentration of 8 mg mL^{-1} and then water was added at a rate of 1 mL h^{-1} to obtain a final solution of concentration 1 mg mL^{-1}. DMF was then removed by dialysis against water, incorporating at least 6 water changes. For the rest of the discussion the self-assemblies of polymers into micelles will be referred as **MT1-4**.

DLS analysis of the different micellar solutions showed the formation of nanoparticles from the copolymers **MT1**, **MT2**, **MT3** and **MT4** with an average diameter of 57, 104, 156 and 131 nm respectively (Figure 2.7). The obtained samples were then imaged by TEM using graphene oxide (GO) grids without staining.[38] TEM analysis also confirmed spherical nanoparticles were formed from polymers **MT1**, **MT2**, **MT3** and **MT4**, with an average diameter of 43, 64, 82 and 113 nm (Figure 2.8 and 2.9). The diameters measured from TEM analysis was found to be slightly smaller than the one from DLS analysis as a consequence of the drying effect of the particles when preparing the samples for TEM analysis. The error bars found in Figure 2.9E after TEM analysis also suggest that **MT3** and **MT4** have similar sizes, due in part to **MT4** having a population of particles of different sizes compared to **MT3**. In general, the different diblock copolymers **PT1-4** could efficiently self-assembled to form micelles **M1-4** with an increase in the size with longer core or corona block length (Figure 2.9E and Table 2.2).

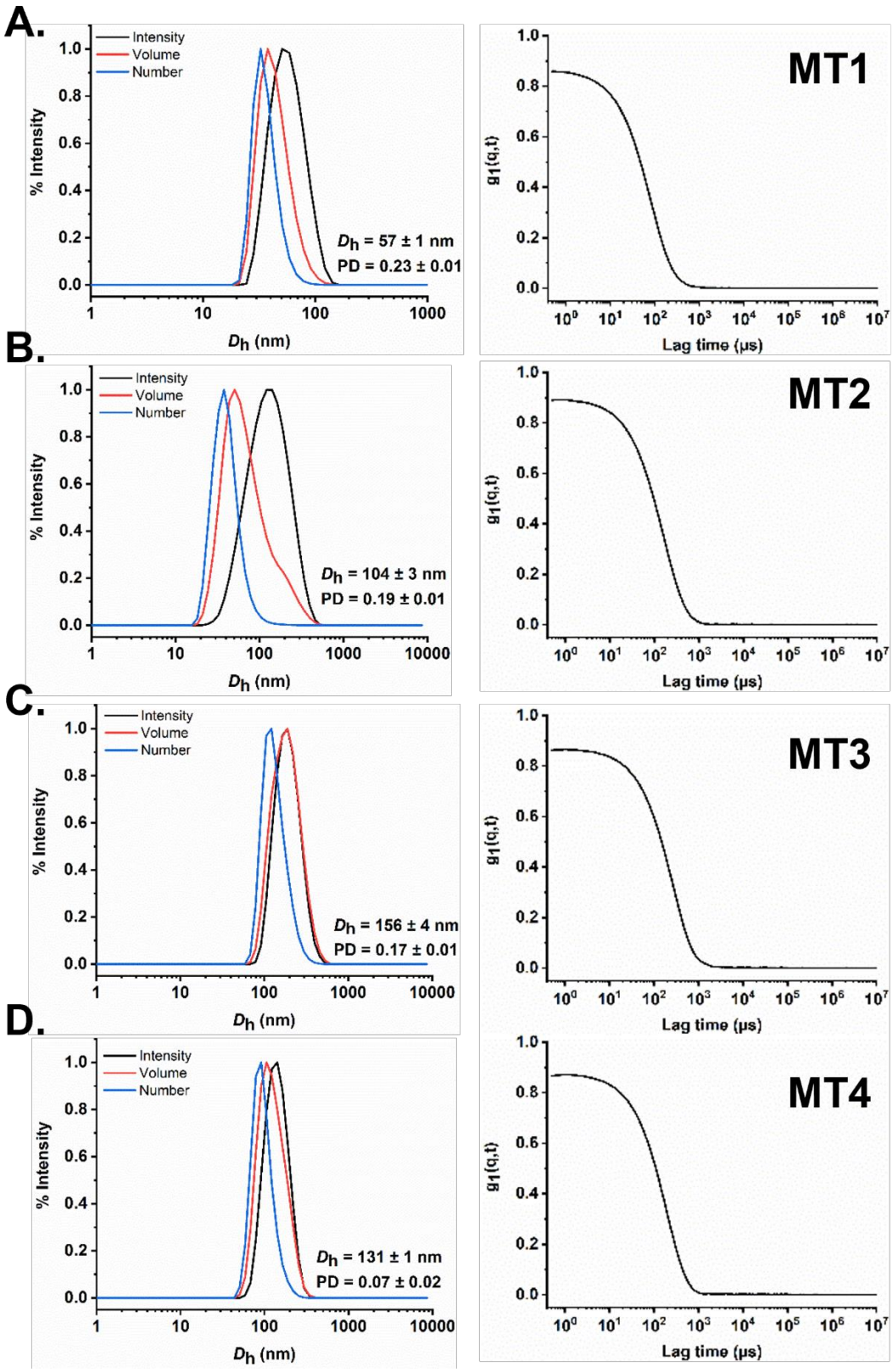


Figure 2.7. (A), (B), (C), and (D) DLS analysis of self-assembled micelles **MT1**, **MT2**, **MT3** and **MT4** respectively at 0.5 mg mL^{-1}.

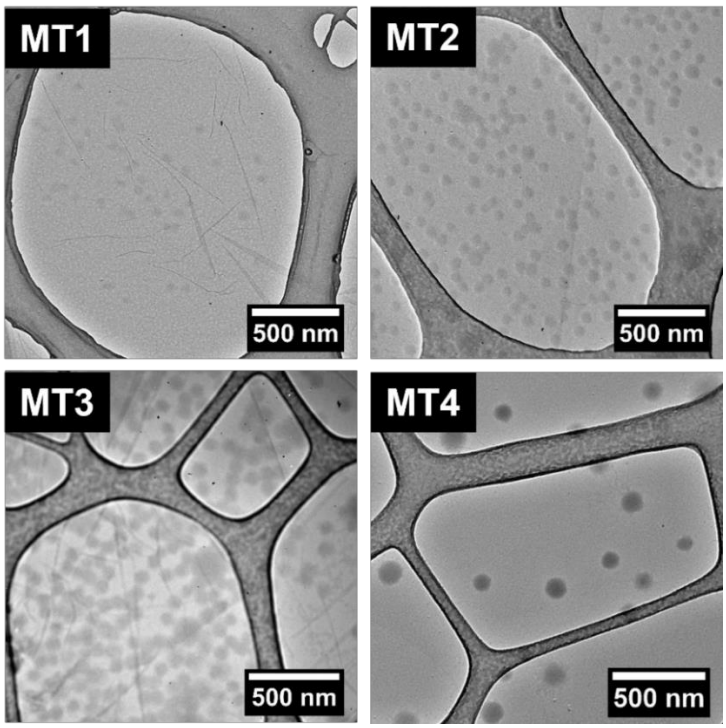


Figure 2.8. TEM images of self-assembled micelles **MT1**, **MT2**, **MT3** and **MT4** respectively. obtained samples were then imaged by TEM using graphene oxide (GO) grids without staining.[38]

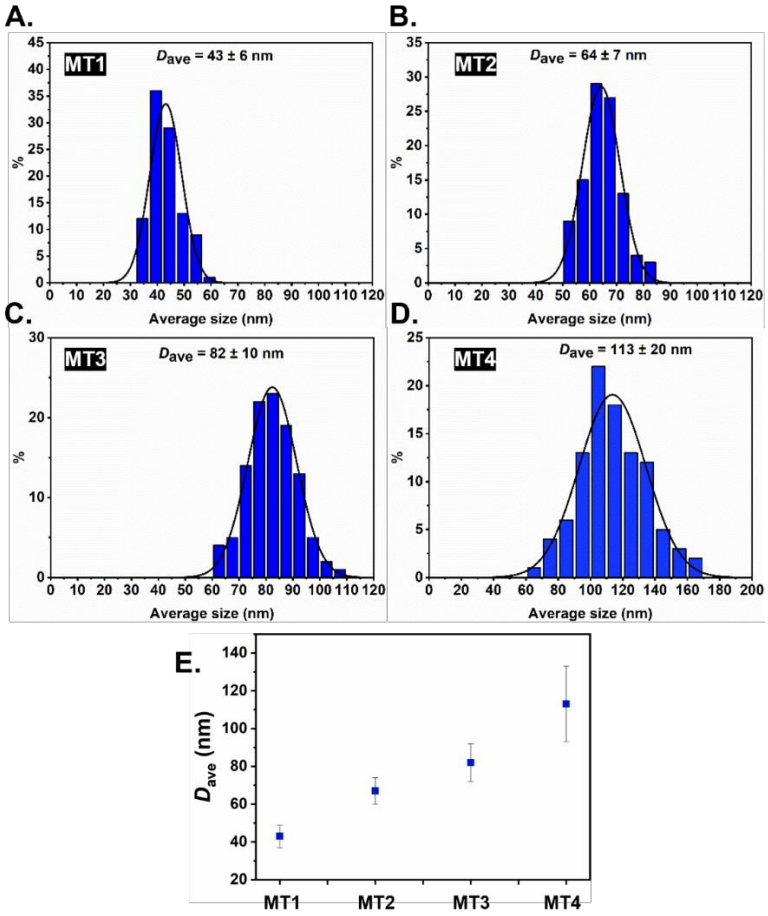


Figure 2.9. Histograms of the diameters of PNAM-*b*-PTAm spherical micelles (A) **MT1**, (B) **MT2**, (C) **MT3** and (D) **MT4** as determined by TEM analysis. The TEM image was analysed using the ImageJ software, and over 100 particles were counted to obtain number-average diameter D_n. (E) represents the Dave evolution when increasing either the corona or core block length of the **MT** micelles.

Table 2.2. Summary of DLS and TEM characterization data of micelles **MT1-4**.

Polymers	**Particles**	D_h **(nm)**[a]	**PD**[a]	D_{ave} **(nm)**[b]
$PNAM_{40}$-*b*-$PTAm_{92}$	**MT1**	57 ± 1	0.23 ± 0.01	43 ± 6
$PNAM_{40}$-*b*-$PTAm_{184}$	**MT2**	104 ± 3	0.19 ± 0.01	64 ± 7
$PNAM_{40}$-*b*-$PTAm_{288}$	**MT3**	156 ± 4	0.17 ± 0.01	82 ± 10
$PNAM_{100}$-*b*-$PTAm_{300}$	**MT4**	131 ± 1	0.07 ± 0.02	113 ± 20

[a]D_h and PD values measured from DLS analysis (the error shows the standard deviation from 3 repeat measurements). [b]D_{ave} values obtained from TEM analysis (size measured over at 100 particles using image J).

2.2.3.2 Direct dissolution and self-assembly of PA diblock copolymers

The adenine-containing diblock copolymers **PA1** and **PA2** were dissolved in water at a concentration of 5 mg mL^{-1} and stirred for 2 h in two sperate vials to obtain **MA1** and **MA2** respectively. DLS analysis showed nanoparticles **MA1** and **MA2** with diameters of 13 and 23 nm were obtained (Figure 2.10). TEM imaging confirmed the spherical nature of the micelles with an average size of 17 and 15 nm respectively (Figure 2.11 and Table 2.3).

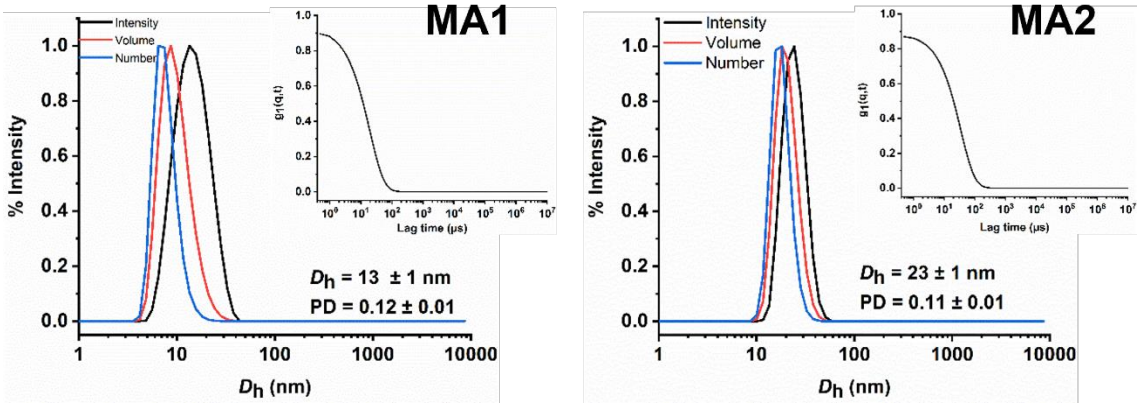


Figure 2.10. DLS analysis and corresponding correlogram of self-assemblies **MA1** and **MA2** in water of $PNAM_{40}$-*b*-$PAAm_{20}$, and $PNAM_{100}$-*b*-$PAAm_{20}$.

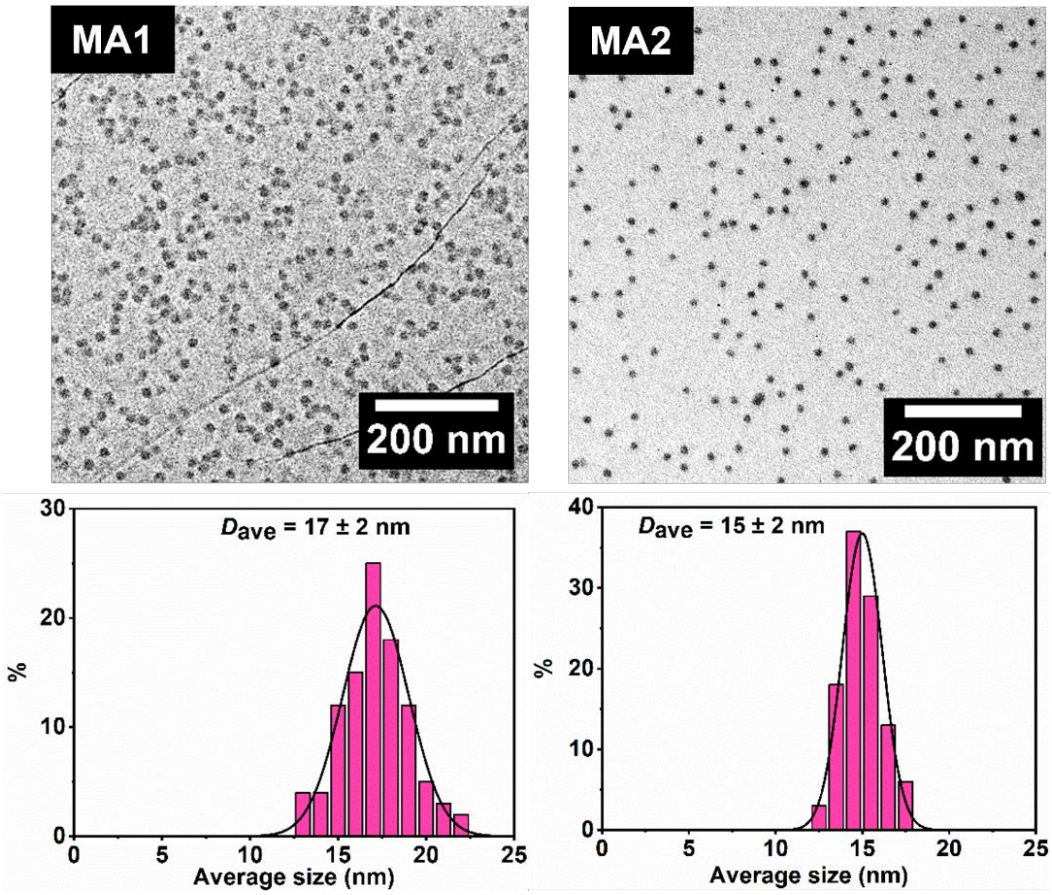


Figure 2.11. Histograms of the diameters of PNAM-*b*-PAAm spherical micelles **MA1** and **MA2** as determined by TEM analysis using graphene oxide (GO) grids without staining.[38] 100 particles were measured and analyzed using imageJ software.

Table 2.3. Summary of DLS and TEM characterization data of micelles **MA1** and **MA2**.

Polymers	**Particles**	D_h **(nm)**[a]	**PD**[a]	D_{ave} **(nm)**[b]
$PNAM_{40}$-*b*-$PAAm_{20}$	**MA1**	13 ± 1	0.12 ± 0.01	17 ± 2
$PNAM_{100}$-*b*-$PAAm_{20}$	**MA2**	24 ± 1	0.11 ± 0.01	15 ± 2

[a]D_h and PD values measured from DLS analysis (the error shows the standard deviation from 3 repeat measurements).[b]D_{ave} values obtained from TEM analysis (size measured over at 100 particles using image J). [c]Morphologies observed from dry-state TEM imaging, without staining.

2.2.4 Tuning spherical thymine-containing micelles through complementary nucleobase interactions

2.2.4.1 Tuning the hydrophobic length of the thymine-containing diblock copolymers

Polymer chain exchange is limited by the kinetic requirements of the length of the hydrophobic block.[34-35] Has it be shown previously, a long hydrophobic block with a higher interfacial tension with the solvent, was sufficient enough to freeze the aggregates and therefore preventing chain exchange.[36] To explore this, similar experiments were performed, as described in the previous study. [36] However, thymine-containing polymers with different hydrophobic block lengths were synthesized and self-assembled (**MT1-3**) instead.

Following the formation of micelles **MT1-3**, the complementary nucleobase polymer (**MA1**) was introduced into the initials **MT** solutions. Different molar ratios of **MA1** were added to micelles **MT1-3** and stirred for 2 h at room temperature. The different samples were then analyzed by DLS and imaged by TEM (Figure 2.12). A similar trend from the original study was observed, but the morphological transition happened at higher A:T molar ratios. Spherical micelles were observed when adding **MA1** up to molar ratio 0.33, with nanoparticles with a size of 43 ± 10 nm and 49 ± 17 nm for **MT1** and **MT2** respectively. Uniform dumbbell-like nanoparticles were formed at A:T molar ratio of 1 instead of lower molar ratio with lengths of 68 ± 14 nm and 75 ± 6 nm using micelles **MT1** and **MT2** respectively. When adding **MA1** with A:T molar ratio of 1.33, where we expected to observe a disassembly of the nanoparticles,[36] elongation of the dumbbell-like nanoparticles to long worms was observed instead. Worm-like nanoparticles with average

lengths of 145 and 200 nm were observed when mixing **MA1** with **MT1** and **MT2** micelles respectively (compared to 1000 nm with **MT3** in the previous study, Figures 2.19 and 2.20 in Experimental section). The morphological transformation of micelles **MT1** and **MT2** from spheres to dumbbells and worms with the addition of the complementary diblock copolymers **PA1** at different molar ratios of A:T happened at later stages of the process compared to the original study.

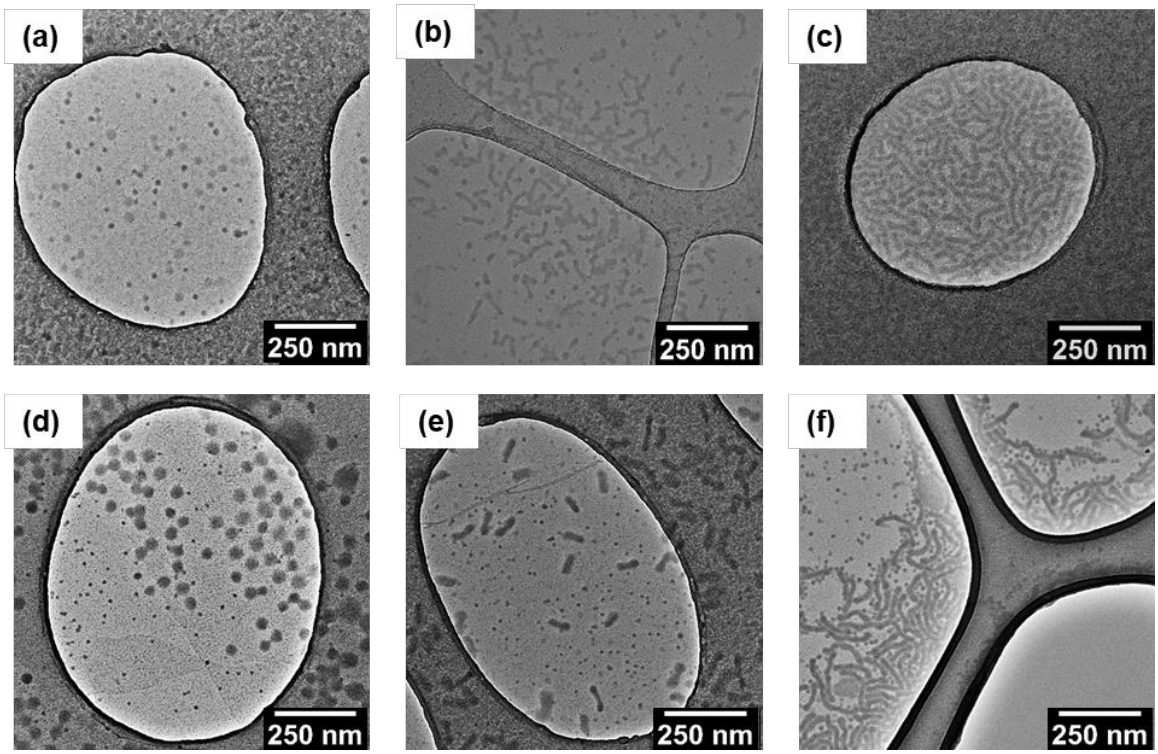


Figure 2.12. Dry-state TEM images on GO grids of micelles (a-c) **MT1** after addition of the complementary copolymer **MA1** at (a) A:T = 0.33, (b) A:T = 1 and (c) A:T = 1.33. (b-e) **MT2** after addition of the complementary copolymer **MA1** at (a) A:T = 0.33, (b) A:T = 1 and (c) A:T = 1.33.

Table 2.4. Summary of DLS and TEM characterization data of morphological transformation of **MT1** with the addition of **MA1** at different A:T molar ratios.

Ratios	D_h (nm)[a]	PD[a]	L_{ave} (nm)[b]
0	57 ± 1	0.23 ± 0.01	43 ± 6
0.33	68 ± 5	0.46 ± 0.2	43 ± 10
1	74 ± 1	0.37 ± 0.01	68 ± 14
1.33	62 ± 1	0.10 ± 0.02	145 ± 38

[a]D_h and PD values measured from DLS analysis (the error shows the standard deviation from 3 repeat measurements).[b]L_{ave} values obtained from dry-state TEM analysis (size measured over at 100 particles using the imageJ software).

Table 2.5. Summary of DLS and TEM characterization data of morphological transformation of **MT2** with the addition of **MA1** at different A:T molar ratios.

Ratios	D_h (nm)[a]	PD[a]	L_{ave} (nm)[b]
0	104 ± 3	0.19 ± 0.01	64 ± 7
0.33	106 ± 3	0.20 ± 0.1	49 ± 17
1	148 ± 1	0.26 ± 0.05	75 ± 5
1.33	122 ± 3	0.23 ± 0.01	200 ± 72

[a]D_h and PD values measured from DLS analysis (the error shows the standard deviation from 3 repeat measurements).[b]L_{ave} values obtained from dry-state TEM analysis (size measured over at 100 particles using the imageJ software).

2.2.4.2 Tuning the hydrophilic length of the thymine-containing diblock copolymers

A longer hydrophilic block could form larger and more stable micelles and therefore may limit their ability to induce complementary interactions and morphological transformation upon mixing. Therefore, in this section we explored the effect of

complementary diblock copolymers with longer hydrophilic block on the morphological transformation mechanism.

Similar experiments were performed in this section utilizing a longer block hydrophilic (DP = 100 instead of 40) for the thymine-containing and the complementary diblock copolymers instead (**PT4** and **PA2** respectively). The self-assembled micelles **MT4** were then mixed with the complementary polymer at different A:T molar ratios (Figure 2.13). When adding **MA2** into **MT4** at molar ration A:T = 0.33, worms with an average length of 420 nm were observed. Much longer worms with length *ca.* 775 and 1000 nm were formed when **MT4** was mixed with **MA2** at A:T = 1 and 1.33 respectively. A mixture of worms and spheres were observed when adding more complementary copolymers in the micellar solution (Figure 2.13c).

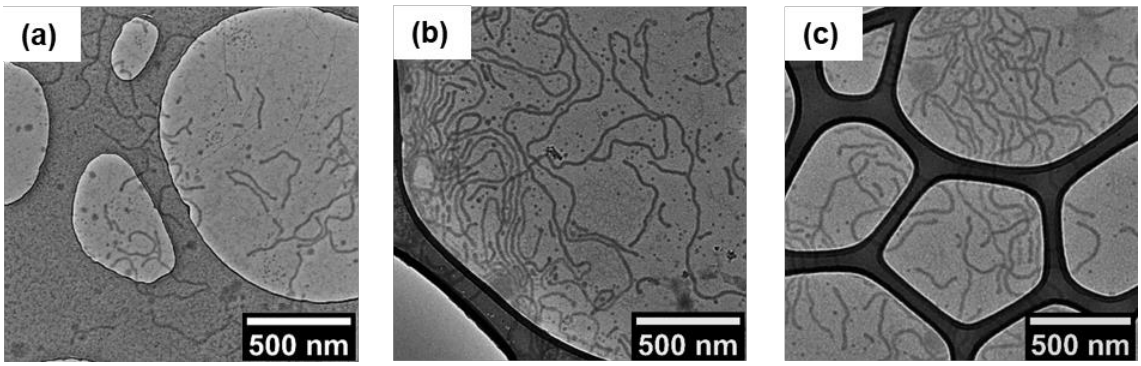


Figure 2.13. Dry-state TEM images on GO grids of micelles **MT4** after addition of the complementary copolymer **MA1** at (a) A:T = 0.33, (b) A:T = 1 and (c) A:T = 1.33.

Table 2.6. Summary of DLS and TEM characterization data of morphological transformation of **MT4** with the addition of **MA2** at different A:T molar ratios.

Ratios	D_h (nm)[a]	PD[a]	L_{ave} (nm)[b]
0.33	68 ± 5	0.46 ± 0.2	421 ± 197
1	74 ± 1	0.37 ± 0.01	775 ± 350
1.33	62 ± 1	0.10 ± 0.02	1000 ± 450

[a]D_h and PD values measured from DLS analysis (the error shows the standard deviation from 3 repeat measurements).[b]L_{ave} values obtained from dry-state TEM analysis (size measured over at 100 particles using the imageJ software).

2.2.4.3 Effect of chain length on the mechanism of the morphological transformation

TEM images were used to give an approximative width for the nanoparticles following the morphological transformations at different A:T molar ratios. Thymine-containing micelles **MT1-4** evolved from spheres (with average size of 43, 64, 82 and 113 nm respectively), to dumbbells (with average width of 20 and 29 nm) after the addition of **MA1** at molar ratio A:T = 1 into **MT1** and **MT2** respectively (Figure 2.14A and C). Worm-like micelles with an average width of 18 nm were formed when **MT1** and **MT2** were mixed with **MA1** at molar ratio A:T = 1.33. As for **MT4** mixed with **MA2**, worms width evolved from 20 nm at molar ratio A:T = 1.33 to 17 nm for A:T = 1 and 1.33 respectively (Figure 2.14B and D).

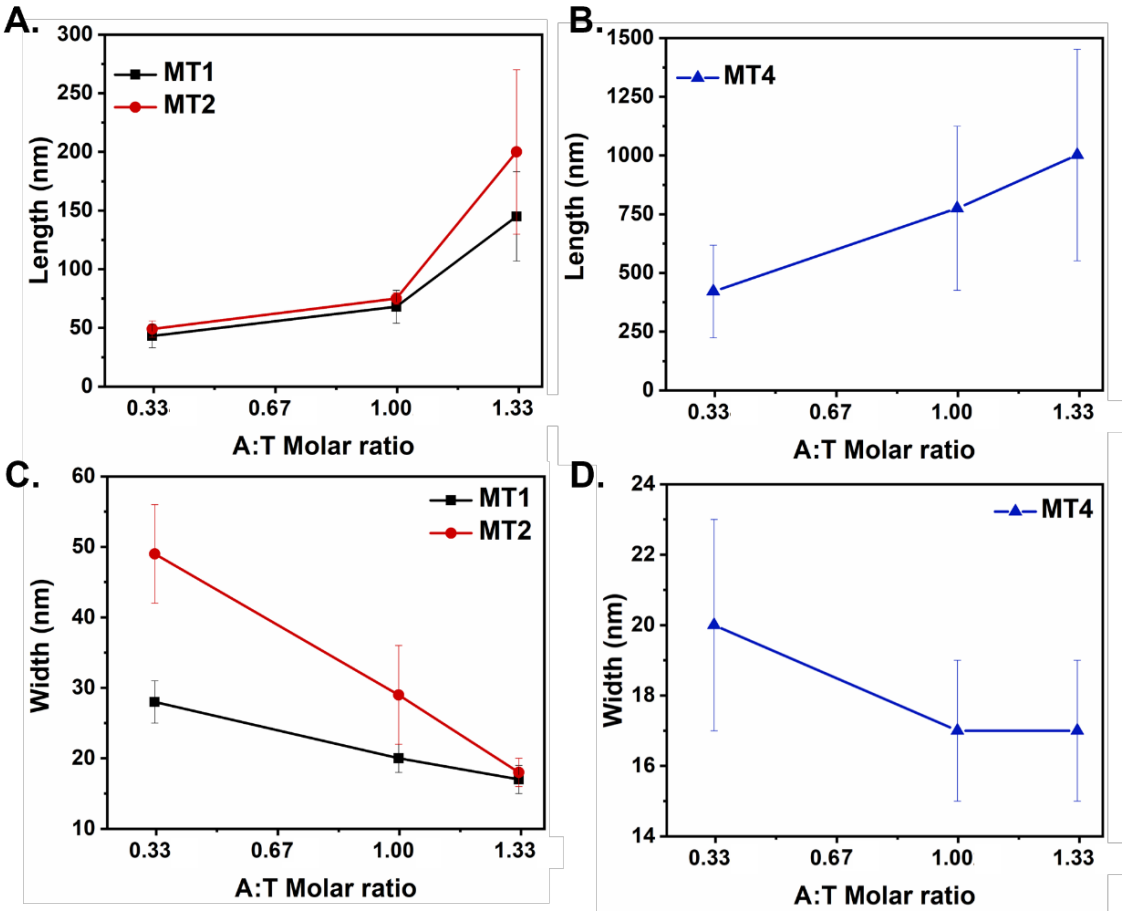


Figure 2.14. Analysis of lengths (A) and widths (C) of the nanoparticles **MT1**and **MT2** after addition of **MA1**. Analysis of lengths (B) and widths (D) of the nanoparticles **MT4** after addition of **MA2**.

Since the main factors influencing the morphological transformation in this system are the corona chain repulsion and core-chain stretching from the insertion of complementary copolymers, by tuning the length of the worms, the reorganization of the polymer chains upon insertion will be modified.

Decreasing the hydrophobic block length of the **MT** micelles (**MT1** and **MT2**) and then therefore increased the hydrophilic ratio, resulted to the formation of worms at later stages of morphological transformation process than the original study. Micelles with shorter hydrophobic blocks were capable of incorporating more **MA1** before a morphological transformation occurred since the core-chain stretching was reduced. Since each **MT**

nanoparticles core can act as a reservoir of material capable of driving the transformation of the micelles and elongation of the worms with the addition of the complementary polymer,[36] shorter thymine core chains could lead to shorter worms due to smaller thymine reservoir (Table 2.7).

The increased hydrophilic chain lengths enhanced the chain mobility and increased core or corona repulsions when complementary chains were combined upon mixing, resulted in a faster progression of the morphological transformation pathway with the formation of worms at lower molar ratio (A:T = 0.33) as shown by TEM (Figures 2.13 and 2.14)

The lengths of worm-like micelles can still be effectively tuned with the addition of complementary copolymers using micelles of different core or corona block lengths.

Table 2.7. Morphologies and nanoparticles dimensions comparison between the different polymers **PT1-4** with the addition of the complementary polymer **PA1** or **PA2**.

Polymers / **Ratios**	**PT1** (nm)	**PT2** (nm)	**PT3*** (nm)	**PT4** (nm)
0.07	N/A	N/A	S 78	N/A
0.2	N/A	N/A	D 81	N/A
0.33	S 43	S 49	W 300	W 420
1	D 68	D 75	W 1000	W 775
1.33	W 145	W 200	W disassembly	W 1000

Morphologies observed from dry-state TEM imaging, using graphene oxide without staining (Key: S – spheres, W – worm-like micelles, D –dumbbells). L_{ave} values obtained from dry-state TEM analysis (size measured over at 100 particles using the imageJ software). * Corresponds to the previous study.

2.3 Conclusion

To summarize, nucleobase-containing acrylamide monomers were successfully synthesized, and nucleobase-containing synthetic block copolymers were then made *via* RAFT polymerization. The block copolymers were characterized by ^{1}H NMR spectroscopy, DMF SEC, DLS and TEM. Monodisperse spherical nanoparticles were formed for **MT1-4** and **MA1-2** as evidenced by DLS and TEM. Sphere, dumbbell, and worm-like nanoparticles of different sizes could be easily accessed through morphological transformations from initial spherical micelles **MT1-4**. Furthermore, the influence of the core and/or the corona block length on this morphological transformation mechanism was studied, showing shorter thymine-containing core block led to transformation into worms at higher A:T molar ratios than the original study. Whereas the same core block length but longer corona block led to transformations into worm-like micelles at lower A:T ratios. These results highlighted that by making straightforward adjustments to the polymers involved, the process of morphological transformation and thus nanoparticle dimensions can be tuned in a control manner.

2.4 General experimental section

2.4.1 Materials

2, 2'-Azo-bis(isobutyronitrile) (AIBN) was obtained from Molekula and recrystallized from methanol. 2,2'-Azobis[2-(2-imidazolin-2-yl)propane]di-hydrochloride (VA-044, Wako) was used without further purification. Adenine was received from Sigma and Thymine was bought from Acros. Sodium hydride (60% dispersion in mineral oil) was purchased from Aldrich. 4- Acryloylmorpholine (NAM) was bought from Aldrich and was purified by vacuum distillation. Triethylamine was received from Fisher Chemical and used without any purification. Acryloyl chloride and pyridine were used as received from Sigma-Aldrich. Dialysis membranes (MWCO = 3.5 kDa) were purchased from Spectra/Por. DMF, DMSO and other chemicals were obtained from Fisher Chemicals and used without further purification. Dry solvents were obtained by passing over a column of activated alumina using an Innovative Technologies solvent purification system.

2.4.2 Instrumentations and analysis

NMR Spectroscopy

NMR spectra were recorded on a Bruker DPX-300, DPX-400 or HD500 spectrometer with D_2O, DMSO-d_6 or $CDCl_3$ as the solvent. Shifts are quoted in δ in parts per million.

High-Resolution Mass Spectrometry.

HRMS spectra were recorded by the MS Analytical Facility Service at the University of Birmingham on a Waters Xevo G2-XS QTof Quadrupole Time-of-Flight mass spectrometer.

Size Exclusion Chromatography (SEC)

Size exclusion chromatography (SEC) in DMSO was performed on an Agilent 1260 Infinity II LC system equipped with a Wyatt Optilab T-rEX differential refractive index detector (RI), an Agilent guard column (PLGel 5 μM, 50 × 7.5 mm) and two Agilent Mixed-C columns (PLGel 5 μM, 300 × 7.5 mm). The mobile phase was DMSO (HPLC grade) containing 0.1% w/w LiBr at 50 °C at flow rate of 1.0 mL min^{-1}. Detection was conducted using an ultraviolet (UV) detector set to either λ_{mCTA} = 360 nm, $\lambda_{BODIPY\text{-}FL}$ = 509 nm or $\lambda_{BODIPY\text{-}TR}$ = 630 nm, respectively. Number average molecular weights (M_n), weight average molecular weights (M_w) and dispersities ($Đ_M = M_w/M_n$) were determined using the Agilent GPC/SEC software (vA.02.01) against a 12-point calibration curve (Mp = 550–2,210,000 g mol-1) based on poly(methyl methacrylate) standards (Easivial PM, Agilent).

Differential Scanning Calorimetry

Determination of the glass transition temperature (Tg) for $PNAM_{40}$-*b*-$PAAm_{200}$ (**PA1**) and $PNAM_{40}$-*b*-$PTAm_{20}$ (**PT_{20}**) block copolymer was performed using a Mettler Toledo DSC 3 differential scanning calorimeter by heating the sample from 25 °C to 190 °C at a rate of 10 °C/min for two heating/cooling cycles. The Tg was determined from the inflection point in the second heating cycle of DSC. Collected data were processed using STARe software.

Dynamic Light Scattering (DLS) Analysis

Hydrodynamic diameters (D_h, app) and size distributions of the self-assemblies were determined by dynamic light scattering (DLS). The DLS instrumentation consisted of a Malvern Zetasizer NanoZS instrument operating at 25 °C with a 4 mW He-Ne 633 nm

laser module. Measurements were made at a detection angle of 173° (back scattering), 4runs for each samples and Malvern DTS 6.20 software was used to analyse the data.

Zeta Potential Analysis

Zeta potential was measured by the technique of microelectrophoresis, using a Malvern Zetasizer Nano ZS instrument, at room temperature at 633 nm. All reported zeta potential values were the average of at least three runs with at least 40 measurements recorded for 3 runs. Zeta potential was calculated from the corresponding electrophoretic mobilities (μE) by using the Henry's correction of the Smoluchowski equation ($\mu E = 4\pi\ \varepsilon 0\ \varepsilon r\ \zeta\ (1+\kappa r)/6\pi\ \mu$).

Transmission Electron Microscopy (TEM)

Dry-state TEM imaging was performed on a JEOL JEM 1400 electron microscope at an acceleration voltage of 80 kV. All TEM samples were prepared on formvar-coated copper grids (EM Resolutions). Generally, a drop of sample (8 μL) was pipetted on a grid and left for roughly min, excess sample was blotted from the grid and then the grid was stained with an aqueous 1% w/w uranyl acetate (UA) solution for 1 min as well prior to blotting, drying and analysis. TEM images were analysed using the ImageJ software, and over 100 particles were counted for each sample to obtain number-average diameter D_n.

Cryogenic Transmission Electron Microscopy (Cryo-TEM)

Cryo-TEM imaging was performed on a JEOL JEM-2100 plus microscope operating at an acceleration voltage of 200 kV. Samples for cryo-TEM were prepared on lacey carbon grids (EM Resolutions). After 200-fold dilution with deionized water, 8 μL of sample were deposited onto the grid followed by blotting for approximately 5 s and plunging into a pool of liquid ethane, cooled using liquid nitrogen in order to vitrify the samples. Then, transfer into a pre-cooled cryo-TEM holder using liquid nitrogen, was performed prior to

the microscopic analysis. Cryo-TEM images were analysed using the ImageJ software, and over 100 particles were counted for each sample to obtain either number-average diameter *D*n or the membrane thickness.

Confocal Laser Scanning Microscopy

Samples were prepared at 100-fold dilution and deposited on a glass slide. Images were acquired using an Olympus FV3000 confocal laser Scanning Microscope and ImageJ image processing software after evaporation of the solvent. Assemblies tagged with BODIPY-FL amine dye (green) were excited using a 488 nm laser, while assemblies tagged with BODIPY 630/650 amine dye (red) were excited using a 633 nm laser. Both channels were used at the same time to detect the presence of green or red assemblies and overlays were produced.

2.4.3 Synthetic methods

Synthesis of N-(3-bromopropyl)acrylamide

N-(3-Bromopropyl) acrylamide was synthesized using procedures similar to the previous literature.[33] To a solution of 3-bromopropylamine (10.1 g, 45 mmol), triethylamine (TEA) (14 mL, 100 mmol) and 4-(dimethylamino)pyridine (DMAP) (288 mg, 2.3 mmol) in CH_2Cl_2 (150 mL), acryloyl chloride (4.2 mL, 50 mmol) was added dropwise in an ice bath and then left at room temperature for another 4.5 h. The reaction solution was washed with saturated $NaHCO_3$ aqueous solution (100 mL) and water (2 × 100 mL). The organic layer was collected and dried with anhydrous $MgSO_4$ and filtered. Then 2,6-bis(1,1-dimethylethyl)-4-methylphenol (6.3 mg, 1.5 mmol) was added to the filtrate followed by concentration under vacuum to give a brown oil. The brown oil (7 g, 81% yield) was used for following reaction immediately without further purification. ^{1}H NMR (400 MHz, $CDCl_3$) δ = 6.27 (d, *J* = 16.8 Hz, 1H, C*H*=CH-CO), 6.11 (d, *J* = 10.0 Hz, 1H, C*H*=CH-

CO), 6.06 (s, 1H, N*H*CO), 5.63 (dd, *J* = 16.8 Hz, 10.0 Hz, 1H, CH2=C*H*-CO), 3.42-3.50 (m, 4H, C*H*2-CH2-C*H*2-Br), 2.08-2.15 (m, 2H, CH2-C*H*2-CH2-Br) ppm; ^{13}C NMR (400 MHz, $CDCl_3$) δ = 166.0, 130.8, 126.7, 38.2, 32.2, 31.0 ppm.

Synthesis of 3-(adenine-9-yl) propyl acrylamide (AAm)

The **AAm** monomer was synthesized according to our previous work[33]. To a suspension of adenine (3.0 g, 24.2 mmol) in dry DMF (100 mL), 60% NaH dispersed in mineral oil (1.0 g, 25.4 mmol NaH) was slowly added in small portions under a nitrogen atmosphere. The mixture was stirred for 1 h until no gas was produced. The viscous mixture was immersed into an ice bath and *N*-(3-bromopropyl) acrylamide freshly synthesized (5.4 g, 28.2 mmol) was added dropwise. The ice bath was left in place and the yellow viscous mixture was stirred overnight. The resulting suspension was concentrated under high vacuum at 50 °C to give a highly viscous oil, to which CH_2Cl_2 was added and the contents mixed by gentle swirling. The CH_2Cl_2 was then poured off and the process repeated several times, followed by concentration under vacuum. The crude residue was further purified by column chromatography using a mixture of CH_2Cl_2 and CH_3OH as eluent and a gradient from 1:0 to 9:1 to give a white solid, **AAm** (1.25 g, 20%). ^{1}H NMR (400 MHz, DMSO-d_6) δ = 8.19 (t, *J*=5.2 Hz, CON*H*), 8.15 (s, 1H, purine H-2), 8.14 (s, 1H, purine H-8), 7.20 (s, 2H, N*H*2), 6.21 (dd, *J* = 16.8 Hz, 10.0 Hz, 1H, C=C*H*-CO), 6.08 (dd, *J* = 16.8 Hz, 2.0 Hz, 1H, C*H*=C-CO), 5.59 (dd, *J* = 10.0 Hz, 2.0 Hz, 1H, C*H*=C-CO), 4.15 (t, 2H, *J* =6.8 Hz, CH2-purine) 3.13 (m, 2H, OC-N-C*H*2), 1.97 (m, 2H, OC-N-C-C*H*2-C-purine); ^{13}C NMR (400 MHz, DMSO-d_6) δ = 165.6, 153.3, 150.4, 141.8, 132.6, 126.1, 119.7, 41.8, 36.8, 30.4 ppm; HR-MS (m/z) found 269.1119, calc 269.1127 $[M+Na]^+$.

Synthesis of 3-(3-benzoylthymin-1-yl)propyl acrylamide (TAm)

To a solution of 3-benzoylthymine (2.3 g, 10.0 mmol) in dry DMF (50 mL), 60% NaH (0.42 g, 10.5 mmol NaH) was slowly added. The mixture was stirred for 1 h until no gas was produced. The viscous mixture was immersed in an ice bath and *N*-(3-bromopropyl) acrylamide freshly synthesized (2.3 g, 12.0 mmol) was added dropwise. The ice bath was left in place and the yellow, viscous mixture was stirred overnight. The resulting solution was concentrated under high vacuum at 50 °C. The residue was partitioned between EtOAc and water. The aqueous layer was extracted three times with EtOAc, and the combined organic layers were dried over anhydrous $MgSO_4$. The solvent was removed under vacuum. The mixture was further purified by column chromatography using EtOAc as eluent to give a viscous liquid (2 g, 58%). ^{1}H NMR (400 MHz, DMSO-d_6) δ= 8.17 (t, J = 5.2 Hz, CONH), 7.96 (d, J = 6.0 Hz, 2H, benzene-H1,H5), 7.79 (s, 1H, pyrimidine-H6), 7.77 (t, J = 6.0 Hz, 1H, benzene-H3), 7.59 (d, J = 6.0 Hz, 2H, benzene-H2,H4), 6.20 (dd, J = 17.0 Hz, 10.0 Hz, 1H, C=CHa-CO), 6.10 (dd, J = 17.0 Hz, 2.0 Hz, 1H, CHb=C-CO), 5.58 (dd, J = 10.0 Hz, 2.0 Hz, 1H, CHc=C-CO), 3.73 (t, 2H, J = 7.0 Hz, CH2-pyrimidine), 3.20 (m, 2H, OC-N-CH2), 1.84 (t, 2H, J = 6.8 Hz, CH3-pyrimidine), 1.82 (m, 2H, OC-N-C-CH2-C-pyrimidine); 13C NMR (400 MHz, DMSO-d_6) δ = 170.3, 165.2, 163.4, 149.9, 143.0, 135.9, 132.1, 131.7, 130.8, 130.0, 125.6, 109.0, 46.6, 36.3, 28.9, 12.3 ppm.

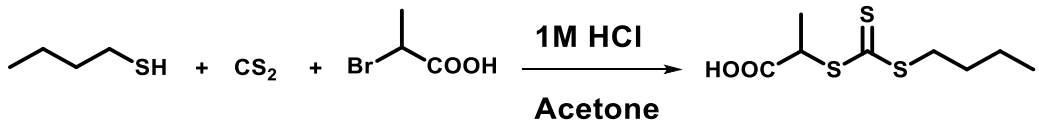
Synthesis of 3-(thymin-1-yl)propyl acrylamide (TAm)

The **TAm** was synthesized as reported previously.[33] (3-Benzoylthymin-1-yl)propyl acrylamide (2.0 g, 5.9 mmol) was dissolved in a mixture of TFA/CH_2Cl_2 (3:1) (20 mL). The reaction solution was stirred at room temperature overnight. After completion of the reaction, solvent was removed under vacuum. The residue was purified by column chromatography with a gradient of $CHCl_3$/CH_3OH from 1:0 to 93:7to give a viscous liquid. Ethanol (20 mL)

was then added, and the solution cooled to −20 °C to precipitate a white solid, **TAm** (0.4 g, 28%). ^{1}H NMR (500 MHz, DMSO-d_6) δ = 11.2 (s, 1H, pyrimidine-H3), 8.12 (t, *J* = 5.2 Hz, CON*H*),7.51 (s, 1H, pyrimidine-H6), 6.18 (dd, *J* = 16.8 Hz, 10.0 Hz, 1H, C=C*H*-CO), 6.07 (dd, *J* = 16.8 Hz, 2.0 Hz, 1H, C*H*=C-CO), 5.58 (dd, *J* = 10.0 Hz, 2.0 Hz, 1H, C*H*=C-CO), 3.63 (t, 2H, *J* = 6.8 Hz, CH2-pyrimidine), 3.14 (m, 2H, OC-N-C*H*2), 1.74 (d, 2H, *J* = 1.0 Hz, CH3-pyrimidine), 1.74 (m, 2H, OC-N-C-C*H*2-C-pyrimidine); ^{13}C NMR (500 MHz, DMSO-d_6) δ = 165.1, 164.8, 151.3, 142.0, 132.2, 125.6, 108.9, 45.9, 36.4, 29.1, 12,4 ppm; HR-MS (m/z) found 260.1013, calc 260.1011 [M+Na]+.

Synthesis of 2-(((butylthio)carbonothiolyl)thio)propanoic acid (CTA)

The procedure was adapted from a previous work.[39] K_3PO_4 (20.9 g, 99 mmol) and butanethiol (10.7 mL, 99 mmol) were dissolved in 100 mL of acetone. An excess of carbon dislufide (CS_2) (8.93 mL, 148.5 mmol) was added and stirred for half an hour. 2-Bromopropanoic acid (8.91 mL, 99 mmol) was added, and a precipitate is observed. The reaction mixture was stirred for 2 h. The solution was then filtrate and concentrated under reduced pressure. 1M HCl (50 mL) was added, and the solution was washed with EtOAc (2 x 100 mL) and brine (2 x 100 mL). The organic layer was dried over $MgSO_4$. The solvent was removed under vacuum. The product was recrystallized from hot hexane to afford a yellow powder (5.6 g, 23%). ^{1}H NMR (400 MHz, $CDCl_3$) δ = 9.82 (br, 1H, COO*H*), 4.87 (q, *J* = 10.0 Hz, 1H, *H*C-CO), 3.38 (t, *J* = 10.0 Hz, 2H, SC(=S)-CH2), 1.64 (m, 2H, SC(=S)-C-C*H*2), 1.62 (d, *J* = 10.0 Hz, 3H, OC-C-CH3), 1.43 (m, 2H, SC(=S)-C-C-CH2), 0.91 (t, *J* = 10.0 Hz, 3H, CH2CH3); ^{13}C NMR (400 MHz, $CDCl_3$) δ = 177.4, 165.2, 47.7, 37.3, 30.1, 22.3, 16.8, 13.8 ppm; HR-MS (m/z) found 261.0055, calc 261.0054 $[M+Na]^+$.



Scheme 2.3. Synthesis of 2-(((butylthio)carbonothiolyl)thio)propanoic acid (CTA).

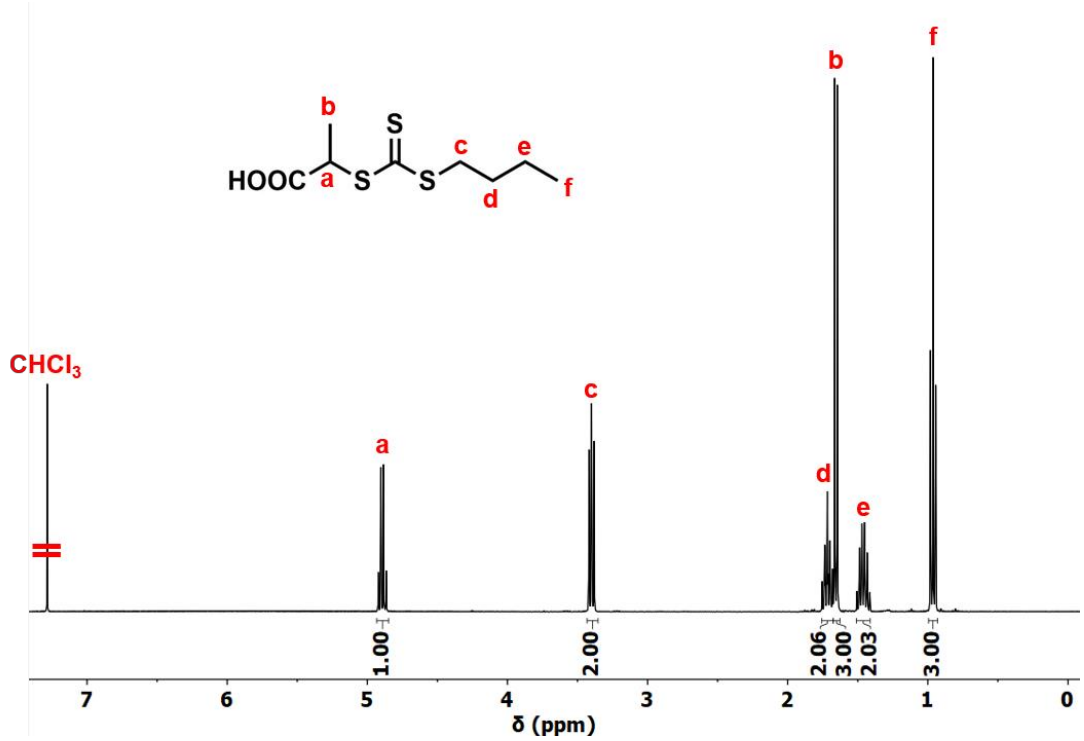


Figure 2.15. ^{1}H NMR spectrum of 2-(((butylthio)carbonothiolyl)thio)propanoic acid (CTA) in $CDCl_3$ (400 MHz).

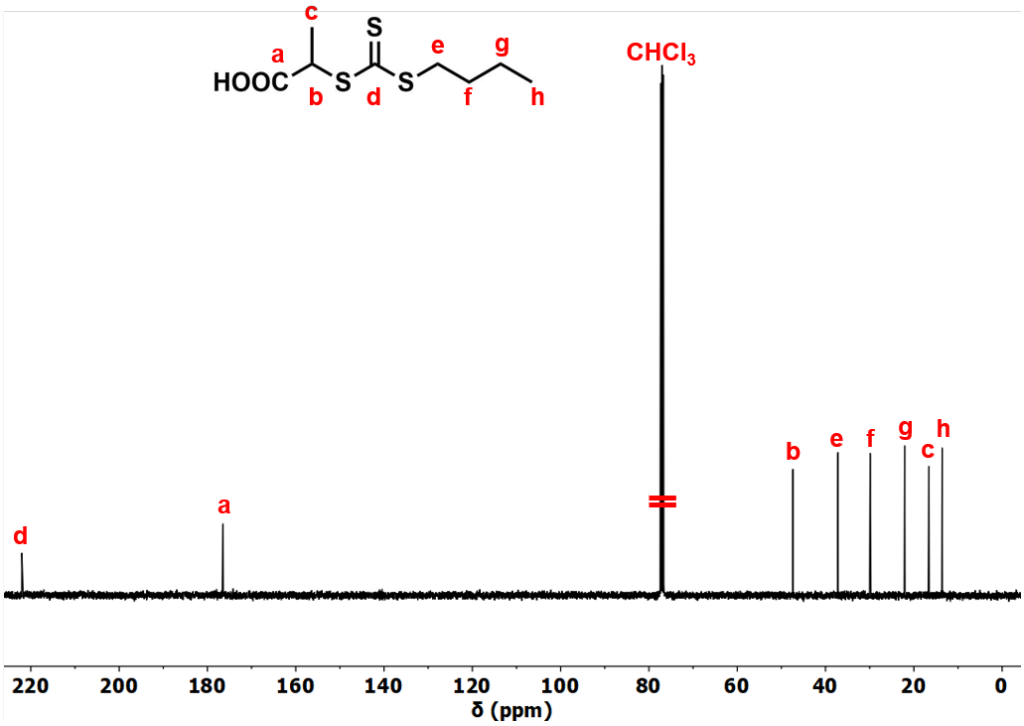
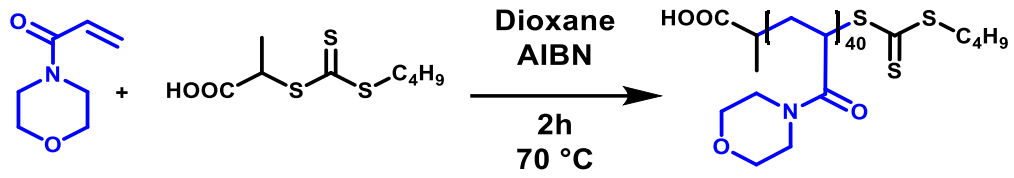


Figure 2.16. ^{13}C NMR spectrum of 2-(((butylthio)carbonothiolyl)thio)propanoic acid (CTA) in $CDCl_3$ (400 MHz).

Synthesis of $PNAM_{40}$ macro-CTA *via* RAFT polymerization

The procedure was adapted from our previous work.[33] For $PNAM_{40}$, a 10 mL ampoule was charged with NAM (126 µL, 1.0 mmol), 2-(((butylthio)carbonothiolyl)thio)propanoic acid (2.4 mg, 0.01mmol), AIBN (1.025 mg, 0.01 mmol) and 0.5 mL of 1.4 dioxane. The mixture was thoroughly degassed *via* 4 freeze-pump-thaw cycles, filled with nitrogen and then immersed in an oil bath at 70 °C for 2 h. The polymerization solution was then diluted in water (2 mL) and dialysed against water, incorporating at least 6 water changes. Water was removed by freeze-drying to afford a light-yellow polymer. The polymer was analyzed by ^{1}H NMR spectroscopy and DMF SEC. The degree of polymerization (DP) of this PNAM macro-CTA was calculated to be 40 using ^{1}H NMR spectroscopy by comparing the integrated signals corresponding to the backbone signals (δ= 1.62 ppm)

with those of the methyl group from the CTA (δ= 0.87 ppm). $M_{n,\ SEC\ RI}$ = 8100 g mol^{-1}, $D_{M,\ SEC\ RI}$ = 1.13.



Scheme 2.4. Synthesis of poly(4-acryolylmorpholine)$_{40}$ (PNAM$_{40}$) macro-CTA.

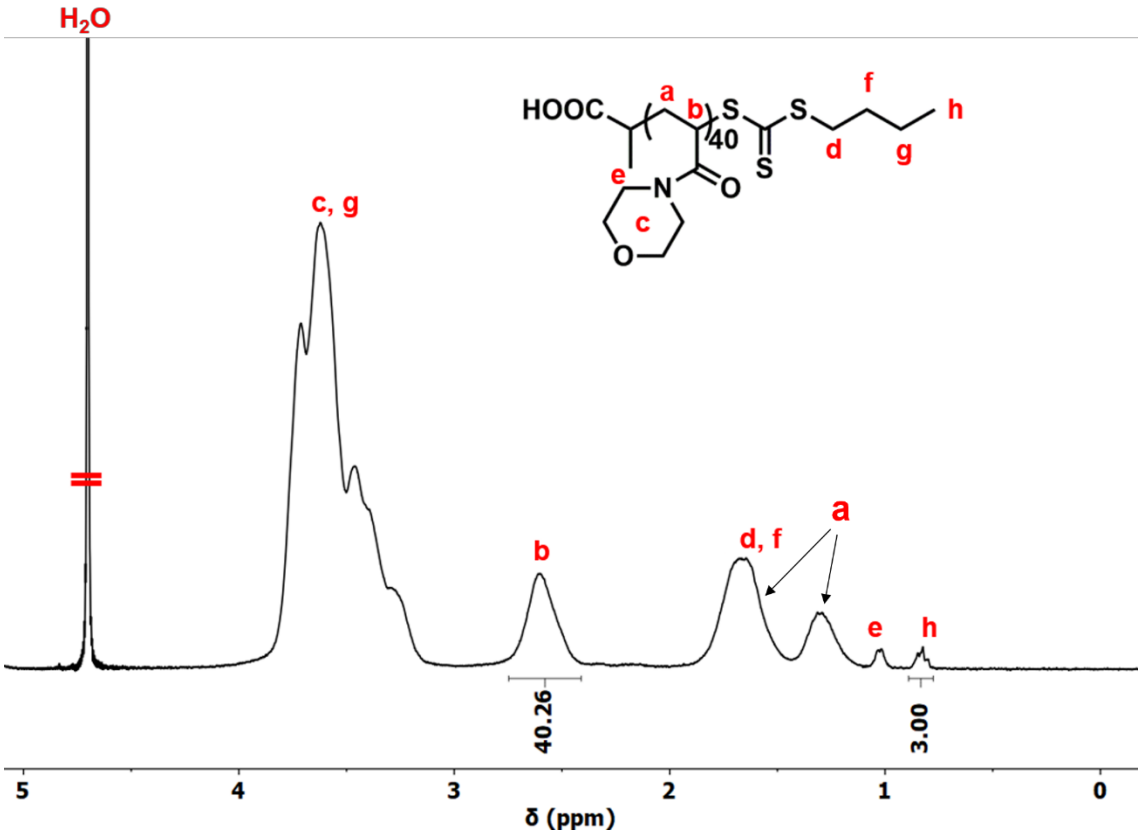


Figure 2.17. ^{1}H NMR of the PNAM$_{40}$ macro-CTA in D_2O (300 MHz).

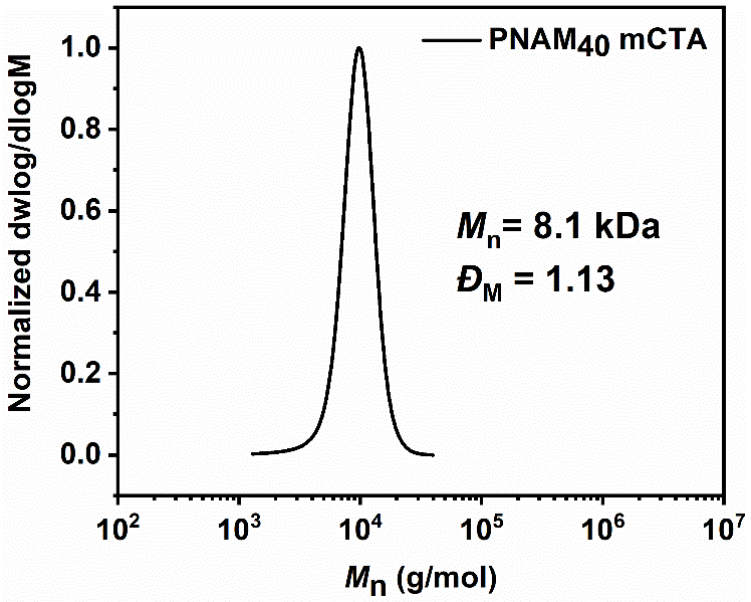


Figure 2.18. Normalized molecular weight distribution trace of $PNAM_{40}$macro-CTA (DMSO + 0.1% w/w LiBr as eluent, PMMA standards).

Self-Assembly of PT into MT nanoparticles by solvent-switch method

The nanoparticles of PT were reassembled as follows. First, the polymers were freeze-dried in order to obtain a solid polymer as shown in the previous study.[36] The copolymer was dissolved in DMSO (at 8 mg mL^{-1}) and stirred for 2 h at 70 °C. Then an excess of 18.2 MΩ·cm water was added *via* a syringe pump at a rate of 1 mL h^{-1}. The final volume ratio between water and organic solvent was about 8:1. The solution was then dialyzed against 18.2 MΩ·cm water, incorporating at least 6 water changes, to afford self-assemblies nanoparticles of **MT** at a concentration of ca. 1 mg mL^{-1}.

Supplementary data on the morphological transformation pathway of MT3 with the addition of MA1

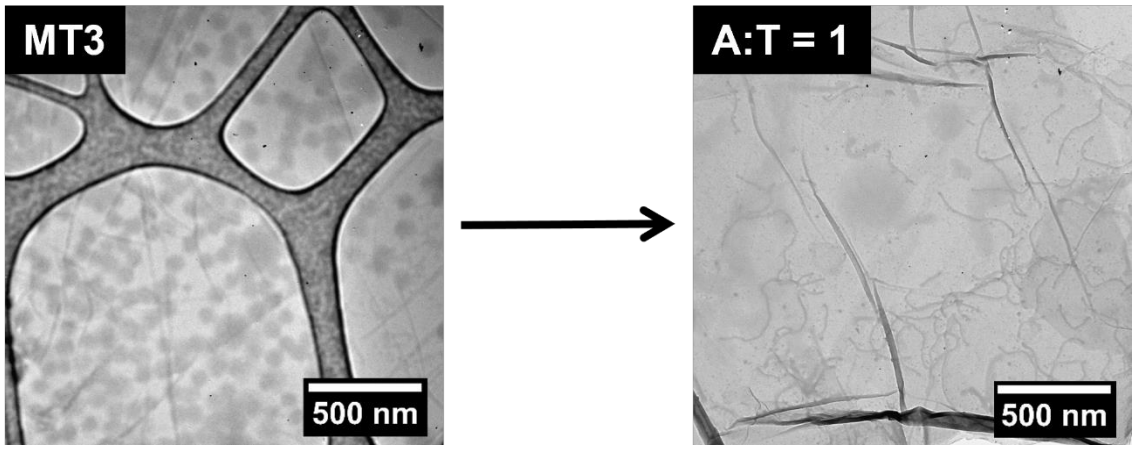


Figure 2.19. TEM images of micelle **MT3** (Left) and **MT3** after addition of **MA1** at molar ratio A:T = 1 (right). Dry-state on graphene oxide without stain.

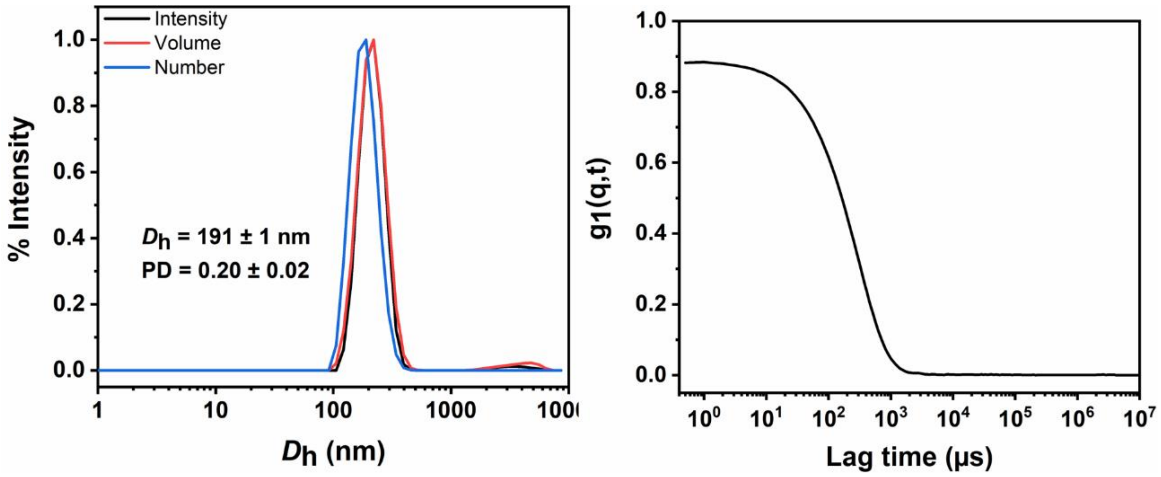


Figure 2.20. DLS analysis of micelle **MT3** after addition of **MA1** at molar ratio A:T = 1.

2.5 References

1. Zhang, L.; Eisenberg, A., Multiple Morphologies of "Crew-Cut" Aggregates of Polystyrene-b-poly(acrylic acid) Block Copolymers. *Sci.* **1995,** *268*, 1728-1731.

2. Won, Y.-Y.; Davis, H. T.; Bates, F. S., Giant Wormlike Rubber Micelles. *Sci.* **1999,** *283*, 960-963.

3. Cui, H.; Chen, Z.; Zhong, S.; Wooley, K. L.; Pochan, D. J., Block Copolymer Assembly via Kinetic Control. *Sci.* **2007,** *317*, 647-650.

4. Wang, X.; Guerin, G.; Wang, H.; Wang, Y.; Manners, I.; Winnik, M. A., Cylindrical Block Copolymer Micelles and Co-Micelles of Controlled Length and Architecture. *Sci.* **2007,** *317*, 644-647.

5. Jain, S.; Bates, F. S., On the origins of morphological complexity in block copolymer surfactants. *Sci.* **2003,** *300*, 460-464.

6. Yang, P.; Ratcliffe, L. P. D.; Armes, S. P., Efficient Synthesis of Poly(methacrylic acid)-block-Poly(styrene-alt-N-phenylmaleimide) Diblock Copolymer Lamellae Using RAFT Dispersion Polymerization. *Macromol.* **2013,** *46*, 8545-8556.

7. Discher, D. E.; Eisenberg, A., Polymer Vesicles. *Sci.* **2002,** *297*, 967-973.

8. Howse, J. R.; Jones, R. A. L.; Battaglia, G.; Ducker, R. E.; Leggett, G. J.; Ryan, A. J., Templated formation of giant polymer vesicles with controlled size distributions. *Nat. Mat.* **2009,** *8*, 507-511.

9. Israelachvili, J. N.; Mitchell, D. J.; Ninham, B. W., Theory of self-assembly of hydrocarbon amphiphiles into micelles and bilayers. *J. Chem. Soc., Faraday Trans. 2* **1976,** *72*, 1525-1568.

10. Antonietti, M.; Förster, S., Vesicles and Liposomes: A Self-Assembly Principle Beyond Lipids. *Adv. Mater.* **2003,** *15*, 1323-1333.

11. Geng, Y.; Dalhaimer, P.; Cai, S.; Tsai, R.; Tewari, M.; Minko, T.; Discher, D. E., Shape effects of filaments versus spherical particles in flow and drug delivery. *Nat. Nanotechnol.* **2007,** *2*, 249-255.

12. O'Reilly, R. K.; Hawker, C. J.; Wooley, K. L., Cross-linked block copolymer micelles: functional nanostructures of great potential and versatility. *Chem. Soc. Rev.* **2006,** *35*, 1068-1083.

13. Choucair, A.; Eisenberg, A., Control of amphiphilic block copolymer morphologies using solution conditions. *Eur. Phys. J. E.* **2003,** *10*, 37-44.

14. Nazemi, A.; Boott, C. E.; Lunn, D. J.; Gwyther, J.; Hayward, D. W.; Richardson, R. M.; Winnik, M. A.; Manners, I., Monodisperse Cylindrical Micelles and Block Comicelles of Controlled Length in Aqueous Media. *J. Am. Chem. Soc.* **2016,** *138*, 4484-4493.

15. Gilroy, J. B.; Gädt, T.; Whittell, G. R.; Chabanne, L.; Mitchels, J. M.; Richardson, R. M.; Winnik, M. A.; Manners, I., Monodisperse cylindrical micelles by crystallization-driven living self-assembly. *Nat. Chem.* **2010,** *2*, 566-570.

16. Blanazs, A.; Madsen, J.; Battaglia, G.; Ryan, A. J.; Armes, S. P., Mechanistic Insights for Block Copolymer Morphologies: How Do Worms Form Vesicles? *J. Am. Chem. Soc.* **2011,** *133*, 16581-16587.

17. Warren, N. J.; Armes, S. P., Polymerization-Induced Self-Assembly of Block Copolymer Nano-objects via RAFT Aqueous Dispersion Polymerization. *J. Am. Chem. Soc.* **2014,** *136*, 10174-10185.

18. South, C. R.; Weck, M., Template-Enhanced Ring-Opening Metathesis Polymerization. *Macromol.* **2007,** *40*, 1386-1394.

19. Lo, P. K.; Sleiman, H. F., Nucleobase-Templated Polymerization: Copying the Chain Length and Polydispersity of Living Polymers into Conjugated Polymers. *J. Am. Chem. Soc.* **2009,** *131*, 4182-4183.

20. Akashi, M.; Takada, H.; Inaki, Y.; Takemoto, K., Functional monomers and polymers. XXXXI. Template polymerization of methacryloyl-type monomers containing nucleic acid bases. *J. Polym. Sci.* **1979,** *17*, 747-757.

21. Kang, Y.; Lu, A.; Ellington, A.; Jewett, M. C.; O'Reilly, R. K., Effect of Complementary Nucleobase Interactions on the Copolymer Composition of RAFT Copolymerizations. *ACS Macro Lett.* **2013,** *2*, 581-586.

22. McHale, R.; O'Reilly, R. K., Nucleobase Containing Synthetic Polymers: Advancing Biomimicry via Controlled Synthesis and Self-Assembly. *Macromol.* **2012,** *45*, 7665-7675.

23. Ilhan, F.; Galow, T. H.; Gray, M.; Clavier, G.; Rotello, V. M., Giant Vesicle Formation through Self-Assembly of Complementary Random Copolymers. *J. Am. Chem. Soc.* **2000,** *122*, 5895-5896.

24. Bazzi, H. S.; Sleiman, H. F., Adenine-Containing Block Copolymers via Ring-Opening Metathesis Polymerization: Synthesis and Self-Assembly into Rod Morphologies. *Macromol.* **2002,** *35*, 9617-9620.

25. Spijker, H. J.; Dirks, A. J.; van Hest, J. C. M., Synthesis and assembly behavior of nucleobase-functionalized block copolymers. *Polym. Chem.* **2006,** *44*, 4242-4250.

26. Sijbesma, R. P.; Beijer, F. H.; Brunsveld, L.; Folmer, B. J. B.; Hirschberg, J. H. K. K.; Lange, R. F. M.; Lowe, J. K. L.; Meijer, E. W., Reversible Polymers Formed from Self-Complementary Monomers Using Quadruple Hydrogen Bonding. *Sci.* **1997,** *278*, 1601-1604.

27. McHale, R.; Patterson, J. P.; Zetterlund, P. B.; O'Reilly, R. K., Biomimetic radical polymerization via cooperative assembly of segregating templates. *Nat. Chem.* **2012,** *4*, 491.

28. Kang, Y.; Pitto-Barry, A.; Maitland, A.; O'Reilly, R. K., RAFT dispersion polymerization: a method to tune the morphology of thymine-containing self-assemblies. *Polym. Chem.* **2015,** *6*, 4984-4992.

29. Kang, Y.; Pitto-Barry, A.; Willcock, H.; Quan, W.-D.; Kirby, N.; Sanchez, A. M.; O'Reilly, R. K., Exploiting nucleobase-containing materials – from monomers to complex morphologies using RAFT dispersion polymerization. *Polym. Chem.* **2015,** *6*, 106-117.

30. Tao, Y.; Yang, Y.; Shi, D.; Chen, M.; Yang, C.; Liu, X., Micelles formation of polystyrene-co-poly (N-acryloylthymine) and its aggregation behavior induced by triple hydrogen bonding. *Polym.* **2012,** *53*, 1551-1557.

31. Lee, R.-S.; Peng, K.-Y.; Wang, S.-W.; Li, Y.-Z., Synthesis and characterization of amphiphilic poly(pseudo-amino acid) polymers containing a nucleobase. *Polym. J.* **2014,** *46*, 710-721.

32. Kuang, H.; Wu, S.; Xie, Z.; Meng, F.; Jing, X.; Huang, Y., Biodegradable amphiphilic copolymer containing nucleobase: synthesis, self-assembly in aqueous solutions, and potential use in controlled drug delivery. *Biomacromol.* **2012,** *13*, 3004-3012.

33. Hua, Z.; Pitto-Barry, A.; Kang, Y.; Kirby, N.; Wilks, T. R.; O'Reilly, R. K., Micellar nanoparticles with tuneable morphologies through interactions between nucleobase-containing synthetic polymers in aqueous solution. *Polym. Chem.* **2016,** *7*, 4254-4262.

34. Nicolai, T.; Colombani, O.; Chassenieux, C., Dynamic polymeric micelles versus frozen nanoparticles formed by block copolymers. *Soft Matt.* **2010,** *6*, 3111-3118.

35. Wright, D. B.; Patterson, J. P.; Gianneschi, N. C.; Chassenieux, C.; Colombani, O.; O'Reilly, R. K., Blending block copolymer micelles in solution; obstacles of blending. *Polym. Chem.* **2016,** *7*, 1577-1583.

36. Hua, Z.; Jones, J. R.; Thomas, M.; Arno, M. C.; Souslov, A.; Wilks, T. R.; O'Reilly, R. K., Anisotropic polymer nanoparticles with controlled dimensions from the morphological transformation of isotropic seeds. *Nat. Commun.* **2019,** *10*, 5406.

37. Inaki, Y., Synthetic nucleic acid analogs. *Prog. Polym. Sci.* **1992,** *17*, 515-570.

38. Patterson, J. P.; Sanchez, A. M.; Petzetakis, N.; Smart, T. P.; Epps, I. I. I. T. H.; Portman, I.; Wilson, N. R.; O'Reilly, R. K., A simple approach to characterizing block copolymer assemblies: graphene oxide supports for high contrast multi-technique imaging. *Soft Matter* **2012,** *8* (12), 3322-3328.

39. Ferguson, C. J.; Hughes, R. J.; Nguyen, D.; Pham, B. T. T.; Gilbert, R. G.; Serelis, A. K.; Such, C. H.; Hawkett, B. S., Ab Initio Emulsion Polymerization by RAFT-Controlled Self-Assembly. *Macromol.* **2005,** *38*, 2191-2204.

3 : Synthesis and characterization of adenine-containing block copolymers prepared *via* aqueous RAFT-mediated PISA

3.1 Introduction

Since 1953, and the elucidation of the structure of DNA by Watson and Crick,[1] scientists have been inspired to mimic this powerful molecular recognition system to direct the assembly of advanced/functional materials.[2-4] Because DNA-based materials are expensive, incorporating nucleobases into synthetic polymers has received particular attention because of their potential to copy the advanced functions of DNA, while remaining cheap and scalable, allowing access to new classes of responsive and tuneable materials.

Research into synthetic nucleobase polymers began in 1967 with the attachment of nucleobases to preformed natural polymers, such as cellulose.[5] Roberts and coworkers studied the interactions of polynucleotides with a guanine derivative of cellulose, and the possibility of separating polynucleotides of different compositions. This was followed by the preparation of synthetic nucleic acid analogues prepared through conventional free radical polymerization of *N*-vinyl derivatives bearing nucleobase functionalities by T'so[6] and Takemoto.[7]

However, free radical polymerization is uncontrolled, resulting in a broad molecular weight distribution and subsequent poor control over the macroscopic properties of the resulting polymers. Therefore, the further development of nucleobase polymerization had to wait until controlled polymerization techniques compatible with the nucleobase functionality had been developed. In 2006, Van Hest and coworkers reported the synthesis of block copolymers composed of a poly(ethylene glycol) (PEG) chain and a thymine- or adenine-functional polymethacrylate block *via* atom transfer radical polymerization (ATRP).[8] Sleiman and coworkers reported a nucleobase-templated polymerization inspired by biological processes, which demonstrated good control of the

molecular weight and a low dispersity for the resulting polymers.[9] The template was synthesized by ring opening metathesis polymerization (ROMP) to give a thymine-containing polymer with a narrow molecular weight distribution. A daughter (the produced polymer) adenine-functionalized polymer was obtained by a templated Sonogashira polymerization with a similar narrow distribution and degree of polymerization to the template.[10] This report demonstrated how nucleobase-templated polymerization could be used to address the poor control of step-growth polymerizations. It has also been demonstrated that using reversible addition-fragmentation chain transfer (RAFT) polymerization conditions allows for the synthesis of nucleobase-containing polymers with high degrees of polymerization (DPs) and moderate dispersities. In 2013, methacryloyl monomers containing adenine and thymine where synthesized by Kang *et al.*[11] using RAFT polymerization with good control over their molecular weight. This was followed using acrylamide-based monomers reported by Hua[12-13] – acrylamide monomers polymerize more rapidly compared to their methacryloyl analogues, allowing better control and the synthesis of longer polymer chains. RAFT has also proved an efficient method to prepare multi-block polymers with nucleobase functionalities.[14-16]

In 2016, Hua *et al.* used amphiphilic nucleobase-containing diblock copolymers synthesized by RAFT polymerization to form self-assemblies.[17-18] Well-defined spherical micelles were obtained in aqueous solution and tunable nanoparticle morphologies were obtained through the introduction of a complementary nucleobase-containing block copolymer. However, no control over the length or width was possible, which was thought to be due to polymer chain exchange and reorganization.

Recently, Hua *et al.* reported a new mechanism with control over the dimensions of anisotropic nanoparticles, which was termed morphological transformation (MORPH).[19]

This mechanism involves the growth of well-defined anisotropic nanoparticles from isotopic seeds, based on the hydrogen bonding interaction between complementary nucleobases. Where a thymine-containing block copolymer prepared *via* RAFT polymerization was then self-assembled in water to obtained micelles. A complementary adenine-containing block copolymer was synthesized the same way and added into the aqueous thymine solution. The base pairing interaction between adenine (A) and thymine (T) drove insertion of the complementary nucleobase copolymer into the core of the nanoparticles, leading to the formation of worm-like micelles by varying the amount of adenine-containing polymer introduced into the nanoparticle solution (and thereby altering the A:T molar ratio), control over morphology was achieved from spheres to cylinders of different lengths.

The exploration of MORPH could lead to new fundamental understanding of the self-assembly processes. To further understand this mechanism, investigations have been conducted to prove that this process could be general and used with different monomers and interacting groups. As an example, towards this would be to investigate whether MORPH also takes place when A and T are switched, *i.e.*, polymers of T inserting into particles of A

In this work, efforts towards the synthesis of adenine-containing polymer nanoparticles are described. It is demonstrated that aqueous polymerization-induced self-assembly (PISA) can be used to synthesize adenine-containing polymers with higher degrees of polymerization (DPs) than those accessible *via* conventional RAFT polymerization. By varying key reaction parameters such as target DP and solids concentration, a range of nanoparticle morphologies were obtained. Allowing exploration of MORPH with different types of seed nanoparticles. Different behaviors were observed for the obtained

nano-objects when varying parameters during the PISA process, showing that polymer chain length, and monomer concentrations affect the morphologies and nano-objects properties. In this chapter, the fabrication of adenine-containing nano-objects is investigated *via* aqueous RAFT-mediated PISA.

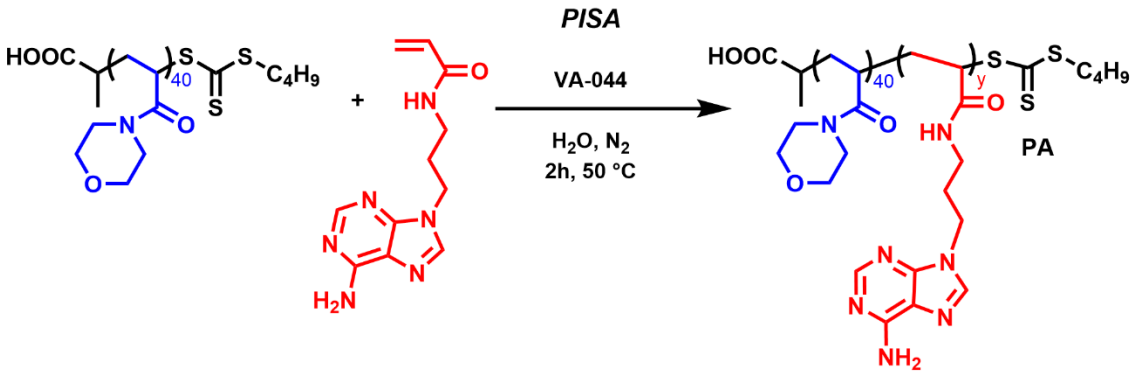
3.2 Results and discussion

3.2.1 RAFT-mediated PISA

3.2.1.1 Synthesis of $PNAM_{40}$-*b*-$PAAm_y$ diblock copolymer nano-objects

In the original report of MORPH, a poly(4-acryloylmorpholine)-*b*-poly(3-(thymin-1-yl)propylacrylamide) (PNAM-*b*-PTAm) (**PT**) with a degree of polymerization (DP) of 300 was used to make seed nanoparticles. To explore a so called "reverse" MORPH mechanism, the creation of seed particles of poly(4-acryloylmorpholine)-*b*-poly(3-(adenine-9-yl)propyl acrylamide) (PNAM-*b*-PAAm) (**PA**), of high DPs for the adenine monomer were required. Chain-extension of the adenine monomer by conventional RAFT polymerization was limited due to solubility issues of the adenine and low conversion.[20] Therefore, long chains up to 300 units of **PA**, analogous to what has been reported PT, could not be obtained.[19] This study involves the use of adenine-containing acrylamide monomer as core-forming block during aqueous RAFT dispersion-mediated PISA using a $PNAM_{40}$ water soluble macro chain transfer agent (macro-CTA) as the steric stabilizer block. This trithiocarbonate CTA was used as it is most suitable for the polymerization of acrylamides.[21] The macro-CTA was first synthesized *via* RAFT polymerization (see scheme 3.2 in Experimental section). The reaction was performed under thermal initiation at 70°C using 2, 2'-Azobis(isobutyronitrile) (AIBN) as initiator under nitrogen atmosphere for 2 h. Size exclusion chromatography (SEC) of the macro-CTA indicated unimodal molecular weight distribution, with a molecular weight (M_n) of 8.1 kDa (Figure 3.21 in Experimental section) and a dispersity ($Đ_M$) of 1.13. The macro-CTA was then used as the soluble block for further chain extension for PISA in water. The AAm monomer was used as the core-forming block since it is relatively easy to synthesize and was soluble in water upon heating[22] (up to 10 %w/w). The reactions were

performed under thermal initiation conditions at 50 °C under nitrogen using 2,2'-Azobis[2-(2-imidazolin-2-yl)propane]di-hydrochloride (VA-044) as initiator for 2 h, a range of different degrees of polymerization (DP) were targeted (DP = 20, 28, 50, 100 and 200) and different solids concentrations (2.5, 5 and 10% w/w) were employed (Scheme 3.1 and Figure 3.1).



Scheme 3.1. Synthesis of $PNAM_{40}$-*b*-$PAAm_y$ diblock copolymer nano-objects by aqueous RAFT-mediated polymerization-induced self-assembly (PISA).

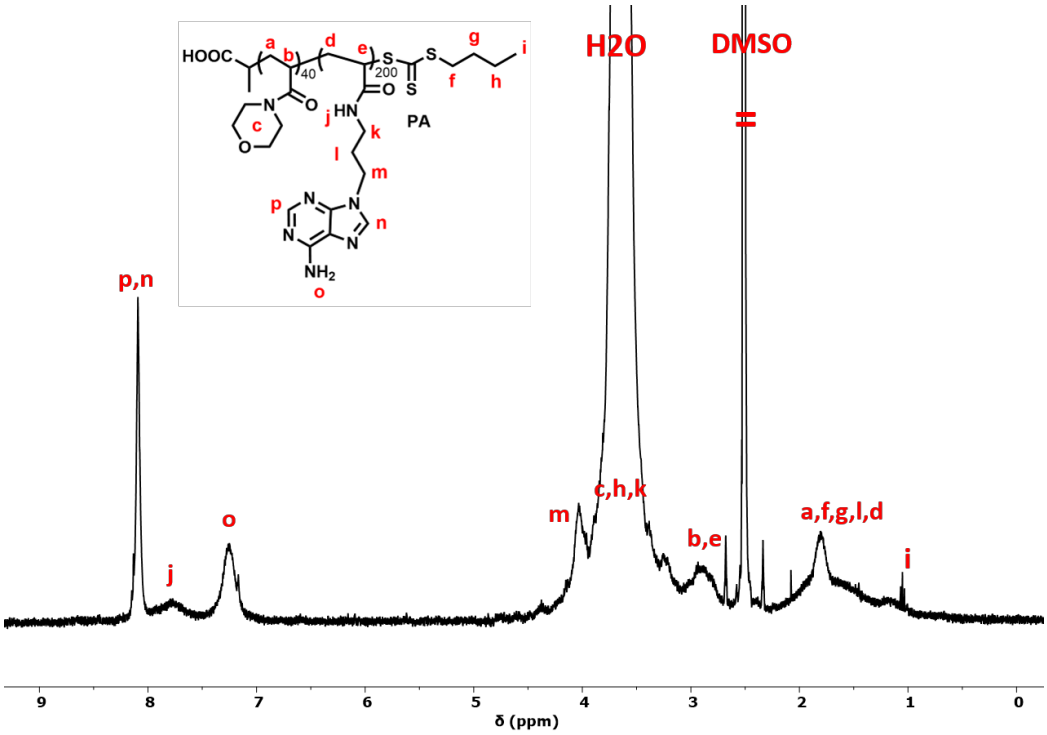


Figure 3.1. ^{1}H NMR spectrum of crude of $PNAM_{40}$-b-$PAAm_{200}$ obtained by aqueous RAFT-mediated PISA in DMSO-d_6 (400 MHz).

Using PISA[23] longer hydrophobic blocks compared to traditional RAFT and monomer conversions of at least 70% were obtained.

At 2.5% w/w, polymerizations were performed with targeted DPs of 20, 28, 50, 100, 200 and 300, and conversion of >99% up to DP 50 and 84% for the targeted DP = 100 (for the rest of the discussion, polymers will be referred as % w/w – DP, *e.g.*, 2.5-DP84), were obtained giving DPs of 20, 28, 50 and 84 respectively. The average final monomer conversion was determined by ^{1}H NMR spectroscopic analysis in DMSO-d_6 of the crude copolymer samples (Table 3.1). No polymers were obtained with a DP higher than 84, even after multiple attempts to obtain the desired polymers. SEC showed monomodal traces for the different polymers obtained, molecular weight (M_n) of 11, 18.4, 26.9 and 38.8 kDa were obtained with dispersities of 1.28, 1.36, 1.43 and 1.66 respectively (Figure 3.2).

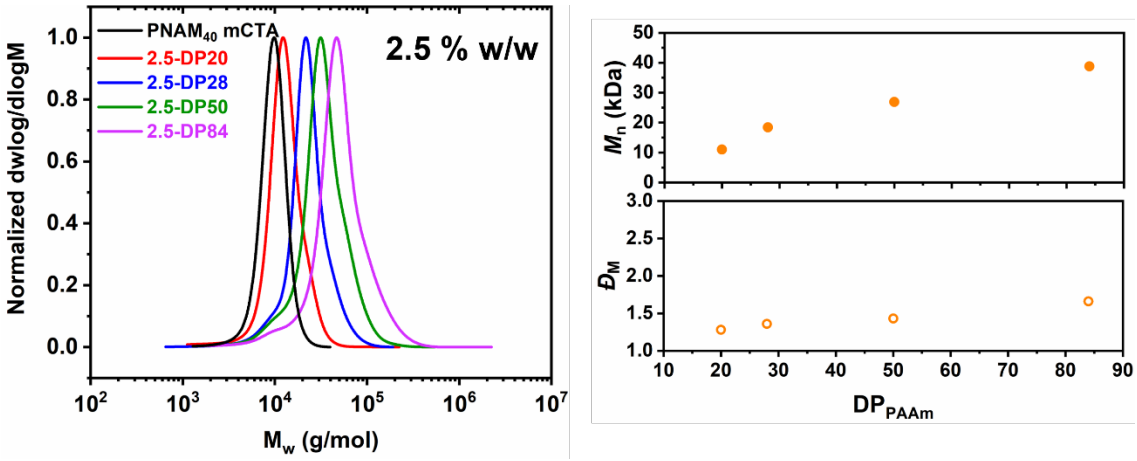


Figure 3.2. SEC traces of different polymerizations of $PNAM_{40}$-b-$PAAm_y$ at 2.5% w/w (DMSO + 0.1% w/w LiBr as eluent, PMMA standards).

At 5% w/w, polymerizations were performed with targeted DPs of 20, 28, 50, 100, 200 and 300, and conversion of >99% up to DP 200 and 70% for Dp = 300 were obtained giving DPs of 20, 28, 50, 100, 200 and 210 respectively. SEC showed monomodal traces for the different polymers obtained up to DP 200 and a slightly broader trace with a high

molecular weight shoulder for DP 300, molecular weight (M_n) of 12.2, 19.6, 28.4, 43.3, 80.7 and 72.8 kDa were obtained with dispersities of 1.30, 1.26, 1.36, 1.83, 2.41 and 2.47 respectively (Figure 3.3).

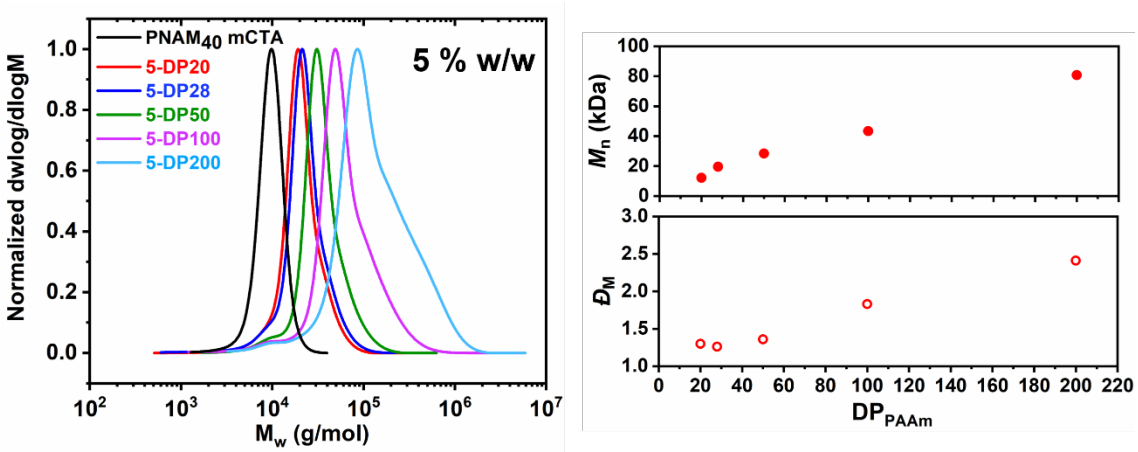


Figure 3.3. SEC traces of different polymerizations of $PNAM_{40}$-b-$PAAm_y$ at 5% w/w (DMSO + 0.1% w/w LiBr as eluent, PMMA standards).

At 10% w/w, polymerizations were performed with targeted DPs of 20, 28, 50, 100, 200 and 300, and conversion of >99% up to DP 200 and 97% for DP = 300 were obtained giving DPs of 20, 28, 50, 100, 200 and 291 respectively. SEC showed monomodal traces for the different polymers obtained, up to DP 200 and a broader trace with a high molecular weight shoulder for DP 300 molecular weight (M_n) of 12.2, 19.6, 27.8, 50.4, 77.9 and 123.9 kDa were obtained with dispersities of 1.20, 1.26, 1.27, 1.66, 1.59 and 2.13 respectively (Figure 3.4).

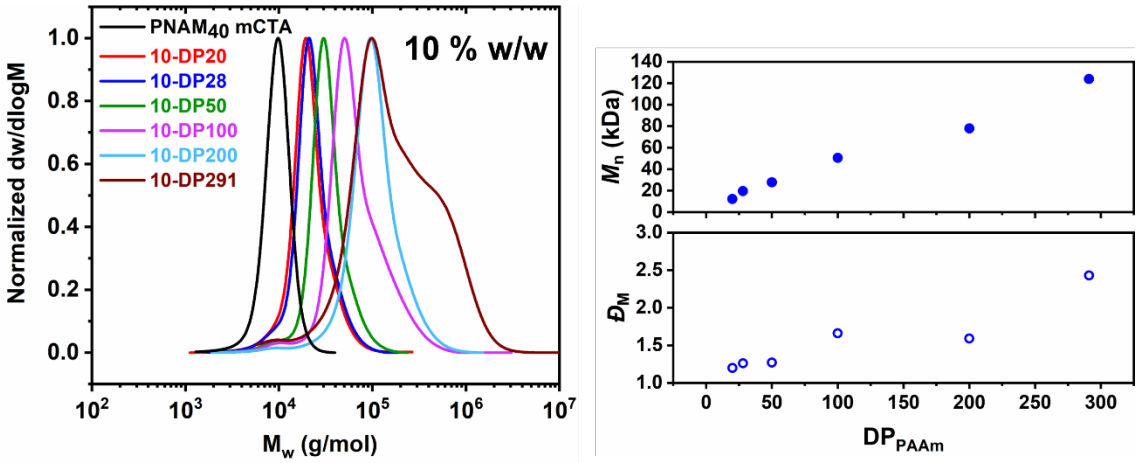


Figure 3.4. SEC traces of different polymerizations of $PNAM_{40}$-b-$PAAm_y$ at 10% w/w (DMSO + 0.1% w/w LiBr as eluent, PMMA standards).

Polymer with core-forming blocks DPs up to 300 units were obtained due to the high local monomer concentration within the nanoparticles, due to the so-called PISA effect. In the PISA formulation, the soluble macro-CTA is chain-extended using a monomer whose becomes insoluble during the polymerization in the chosen solvent, here water. Thus, the growing second block (core-forming one) eventually becomes insoluble at some critical DP, which will drive an *in situ* self-assembly to form the diblock copolymer nano-object. The unreacted monomer acts essentially as a processing aid (or cosolvent) for the insoluble block.[24] PISA can be performed at relatively high solids contents (here up to 10% w/w) [25-26], this enables high monomer conversions to be reached within shorter reaction times compared to conventional solution polymerization,[27-28] since once micellar nucleation is initiated, the unreacted monomer is preferentially located within the growing nanoparticles. Especially in this study, the adenine-adenine interaction will also increase this local monomer concentration in the micelles.[29-30] This high local concentration will then lead to significant rate acceleration in the polymerization process.[31-32]

Overall, polymers with similar M_n and dispersity were obtained at the different % w/w up to DP100, and differences started to appear above than DP. As the DP increases the conversion decreases for DPs higher than 200 and low dispersity values ($Đ_M$) were calculated when targeting shorter PAAm blocks. However, increasing either the core-forming block or the DP or the total solids content led to higher $Đ_M$.

SEC data showed symmetrical monomodal molecular weight distributions were observed for relatively short DPs (up to 100), and broader distribution for polymers 5-DP210 and 10-DP291 were observed and this could be due to a potential loss of end-group fidelity, which is typical for the PISA process.[33]

The SEC data for low DPs, also showed that the solids concentration used for the polymerization had little effect on the molecular weight distribution obtained. One another note, the increasing dispersity seems to trend more with DP than solids content. This behaviour is typical for dispersion PISA systems.[34-35] In the RAFT process, the higher the targeted DP and solids content are, the lower the CTA concentration. This lowers the absolute number of living chains and limits termination events. Therefore, using high monomer concentration in the media, will lead to the formation of polymers with high molecular weight with higher disperties.[35-36] This could also explain why lower conversion could be seen as lower solids concentration, the monomer concentration will prevent the polymer-monomer interactions since so little in solution and therefore the monomer-monomer interactions will be favoured causing lower conversion at low % w/w.

Table 3.1. Characterization data of $PNAM_{40}$-b-$PAAm_y$ adenine-containing diblock copolymers obtained *via* aqueous RAFT-mediated PISA.

Sample	Targeted DP	% Conv.[a]	$M_{n,NMR}$[b] /kDa	$M_{n,SEC}$[c] /kDa	$Đ_{M,SEC}$[c]
2.5-DP20	20	> 99	10.6	11.0	1.28
2.5-DP28	28	> 99	14.4	18.4	1.36
2.5-DP50	50	> 99	18.2	26.9	1.43
2.5-DP84	100	> 84	24.6	38.8	1.66
2.5-DP200	200	-	-	-	-
2.5-DP300	300	-	-	-	-
5-DP20	20	> 99	10.6	12.2	1.30
5-DP28	28	> 99	14.4	19.6	1.26
5-DP50	50	> 99	18.2	28.4	1.36
5-DP100	100	> 99	30.8	43.3	1.83
5-DP200	200	> 99	56.1	80.7	2.41
5-DP210	300	> 70	58.5	72.8	2.47
10-DP20	20	> 99	10.6	12.2	1.20
10-DP28	28	> 99	14.4	19.6	1.26
10-DP50	50	> 99	18.2	27.8	1.27
10-DP100	100	> 99	30.8	50.4	1.66
10-DP200	200	> 99	56.1	77.9	1.59
10-DP291	300	> 97	78.7	123.9	2.43

[a]Monomer conversion calculated from ^{1}H-NMR spectroscopy in DMSO-d_6 (400 MHz). [b]Calculated from conversion. [c]M_n and $Đ_M$ values calculated from DMSO + 0.1% w/w LiBr as the eluent with PMMA standards.

3.2.1.2 Phase diagram of the nano-objects

The resulting diblock copolymers were characterized by dynamic light scattering (DLS), dry-state-stained transmission electron microscopy (TEM) imaging and zeta potential, which enabled the construction of a detailed phase diagram of the $PNAM_{40}$-*b*-$PAAm_y$ diblock copolymer nano-objects (shown in Figure 3.5).

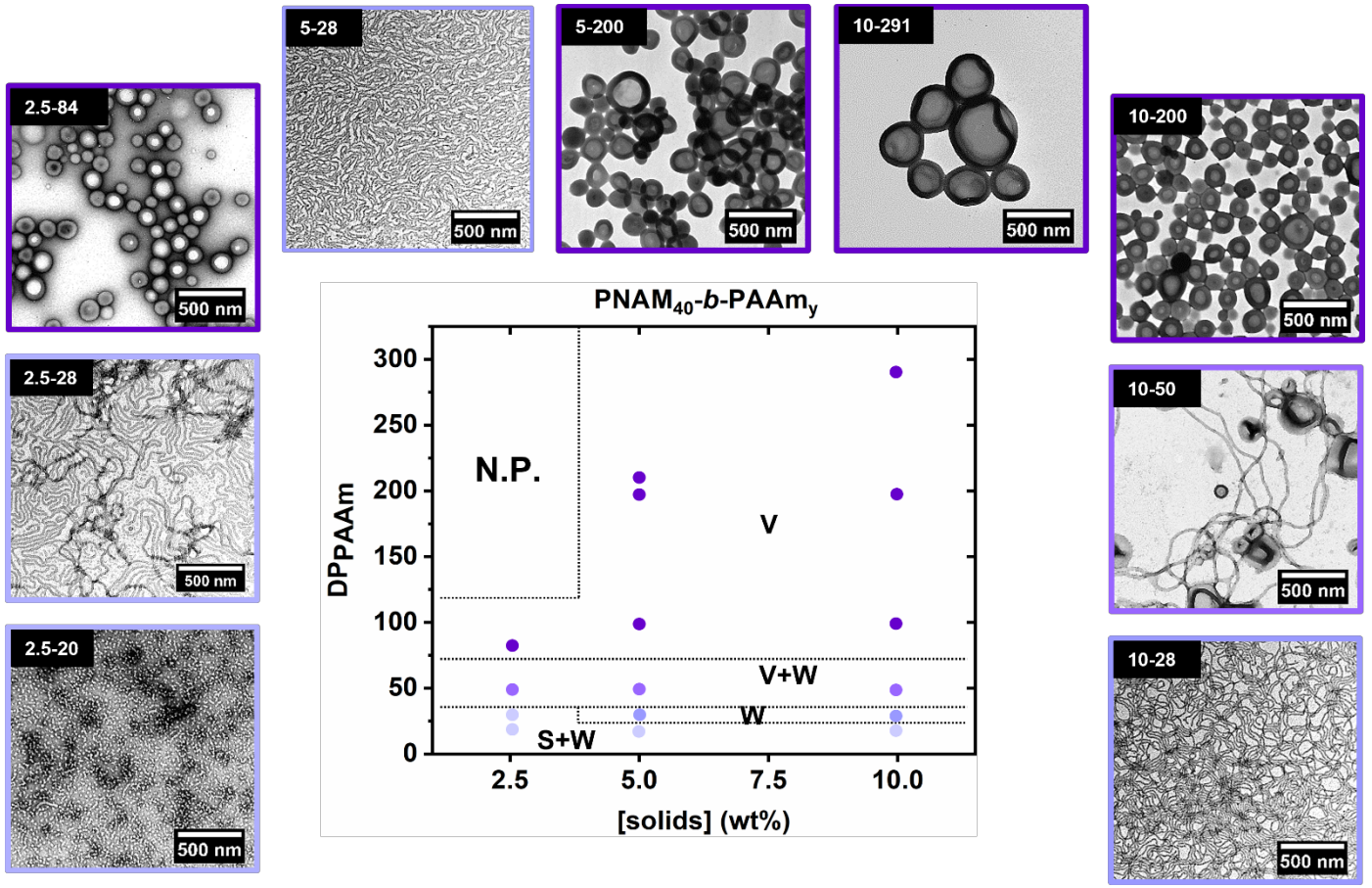


Figure 3.5. Pseudo phase diagram for $PNAM_{40}$-b-$PAAm_y$ diblock copolymer nanoparticles prepared by aqueous RAFT-mediated PISA using VA-044 initiator at 50 °C. The diblock copolymer morphologies were assigned by dry-state TEM stained with 1% w/w uranyl acetate (UA) solution. (Key: S – spheres, W – worm-like micelles, V – vesicles. N.P.: No polymer obtained.

As shown on the phase diagram, as higher DPs are targeted, morphologies evolve from mixed spherical micelles/ worm-like micelles (S+W, spheres-worms) to purely worm-like micelles (W, worms) to mixed worm-like micelle / vesicular nanostructures until finally a pure vesicular nanostructure phase (V, vesicles) is observed . In the evolution of the copolymer morphology during the PISA process, the initial event is the fusion of two spheres to form a spherical dimer that will lead to the formation of worms and then to vesicles.[37] Monomer concentration or solid content is also an important parameter, which determines morphology in the PISA process. A higher monomer concentration will promote the formation of higher-order morphologies through plasticizing of the core chains and increase the number of particles per unit volume in the reaction medium.[38] This high concentration also increases the inelastic collisions that result in inter-micelle fusion. A pure sphere phase could not be obtained at each % w/w for DP = 20 as shown in Figure 3.6 with presence of spheres and worms.

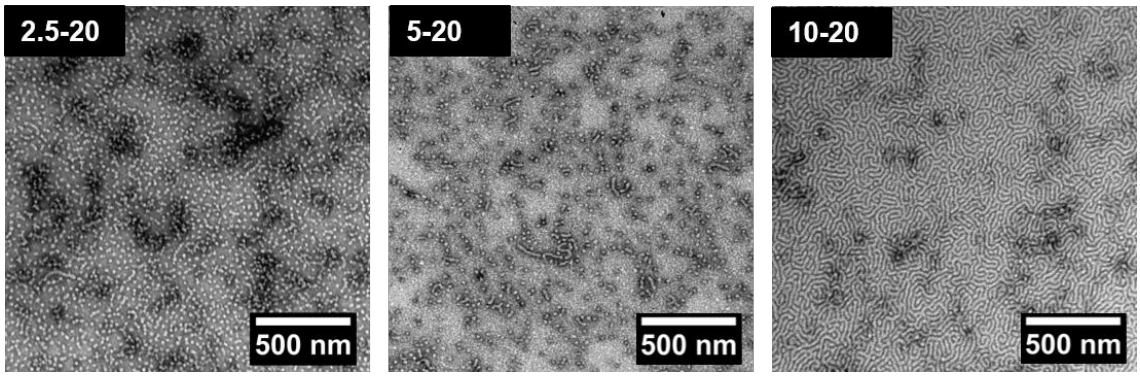


Figure 3.6. TEM images of $PNAM_{40}$-b-$PAAm_{20}$ diblock copolymer nanoparticles prepared by aqueous RAFT-mediated PISA using VA-044 initiator at 50 °C at 2.5, 5 and 10% w/w. The samples were stained with 1% w/w uranyl acetate (UA) solution.

For DP 20, hydrodynamic diameter (D_h) of 16 ± 1, 19 ± 1 and 16 ± 1 nm and dispersity (PD) of 0.28 ± 0.1, 0.24 ± 0.1 and 0.28 ± 0.1 values were measured for polymerizations at 2.5, 5 and 10% w/w, respectively, accompanied by multimodal particle size

distributions due to the existence of mixed morphologies of small and larger nano-objects (Figure 3.7). Here, the obtained mixed morphology of short worms and spheres instead of a pure sphere phase could be due to the low weight percentage affecting the inelastic sphere-sphere fusion,[24] since particle fusion and chain reorganization are more favourable at higher solids content.[39]

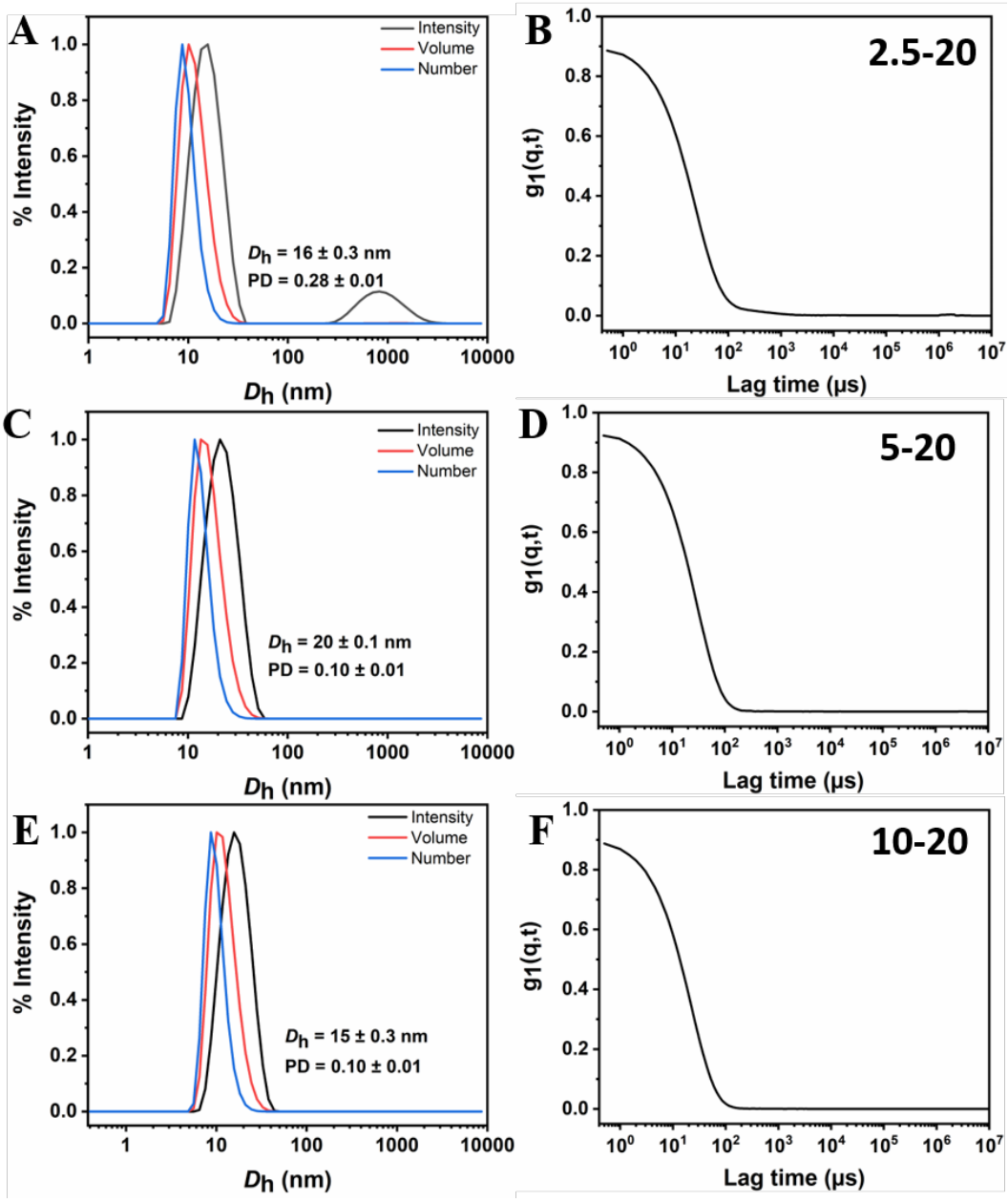


Figure 3.7. DLS (A,C and E) and corresponding correlogram (B, D and F) graph results of $PNAM_{40}$-*b*-$PAAm_{20}$ nano-objects obtained *via* aqueous RAFT-mediated PISA at 2.5, 5 and 10% w/w.

At DP = 28, a mixture of short worms and spheres was obtained at 2.5% w/w, whereas a pure phase of worms could be accessed for the same block copolymer composition at 5 and 10% w/w. This was evident macroscopically by the formation of a clear freestanding gel in the reaction vial after RAFT-mediated PISA and by TEM (Figure 3.8).

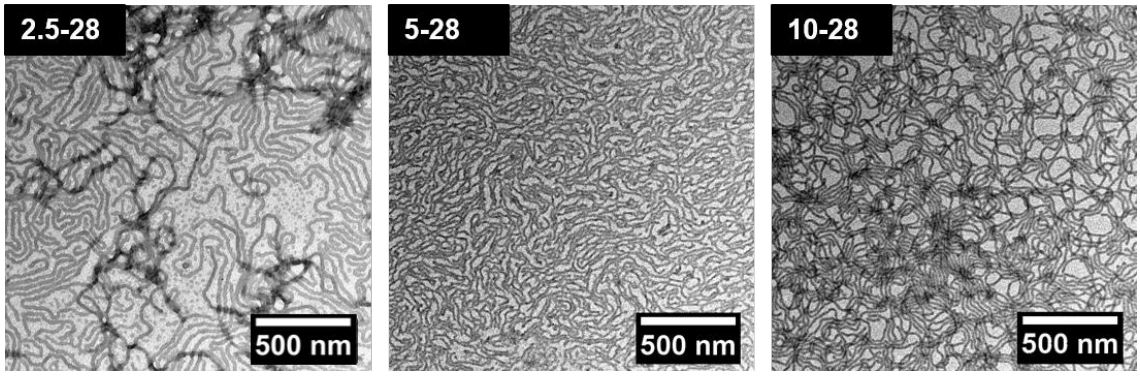


Figure 3.8. TEM images of $PNAM_{40}$-b-$PAAm_{28}$ diblock copolymer nanoparticles prepared by aqueous RAFT-mediated PISA using VA-044 initiator at 50 °C at 2.5, 5 and 10% w/w. The samples were stained with 1% w/w uranyl acetate (UA) solution.

For DP 28, D_h of 129 ± 1, 122 ± 1 and 128 ± 3 nm and PD of 0.23 ± 0.01, 0.24 ± 0.01 and 0.24 ± 0.01 values were measured for polymerizations at 2.5, 5 and 10% w/w, respectively. Again, this higher dispersity is due to presence of mixed morphologies as shown by DLS (Figure 3.9) and TEM analysis.

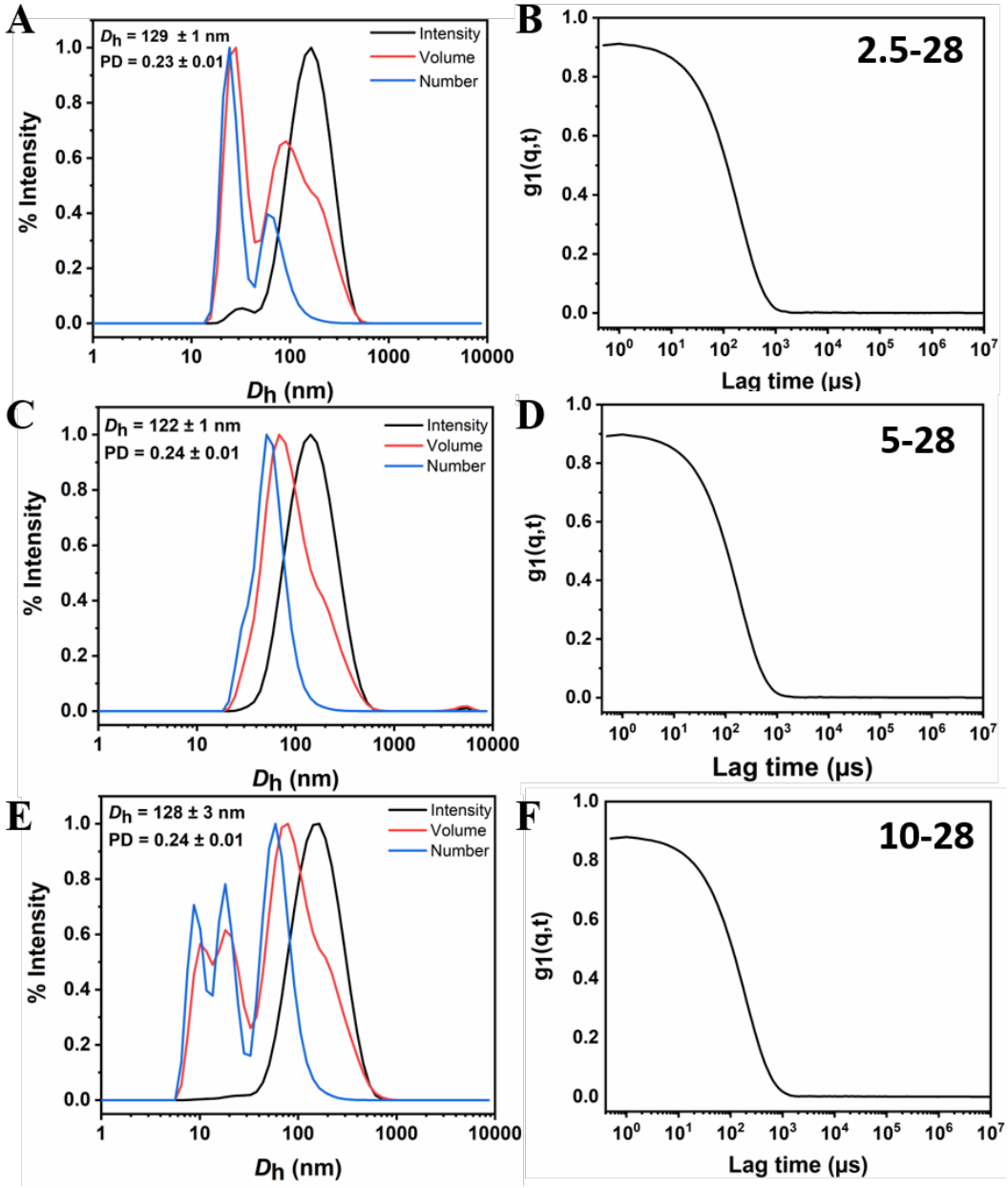


Figure 3.9. DLS (A,C and E) and corresponding correlogram (B, D and F) graph results of PNAM40-b-PAAm28 nano-objects obtained *via* aqueous RAFT-mediated PISA at 2.5, 5 and 10% w/w.

The formation of worms is expected as the DP increases, it could also be favoured due to the high hydrophobicity of the adenine monomer.[40]

Aqueous RAFT-mediated PISA targeting $DP_{PAAm} = 50$ at each % w/w led to the formation of a mixed phase of worms-like micelles and vesicles morphologies (W + V) (Figure 3.10).

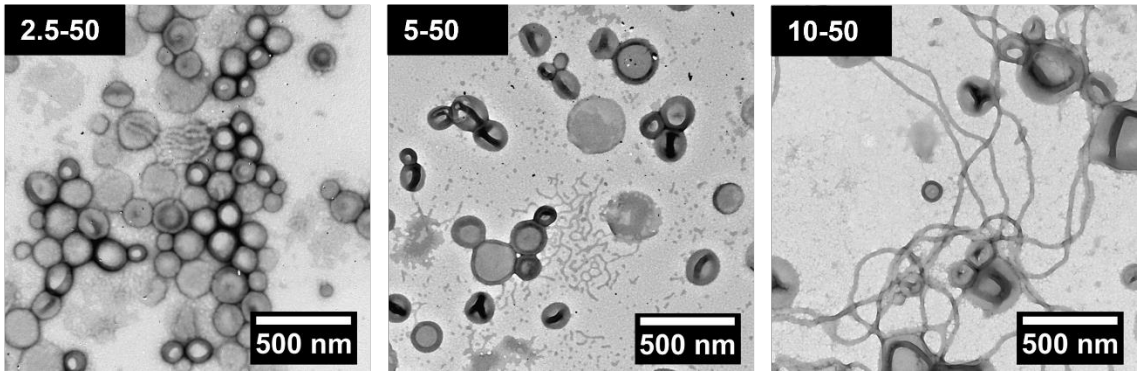


Figure 3.10. TEM images of $PNAM_{40}$-b-$PAAm_{50}$ diblock copolymer nanoparticles prepared by aqueous RAFT-mediated PISA using VA-044 initiator at 50 °C at 2.5, 5 and 10% w/w. The samples were stained with 1% w/w uranyl acetate (UA) solution.

D_h of 145 ± 2, 185 ± 4 and 257 ± 9 nm and PD of 0.04 ± 0.01, 0.02 ± 0.01 and 0.21 ± 0.01 values were measured for polymerizations at 2.5, 5 and 10% w/w, respectively. Again, higher dispersity is due to presence of mixed morphologies as shown by DLS (Figure 3.11) and TEM analysis.

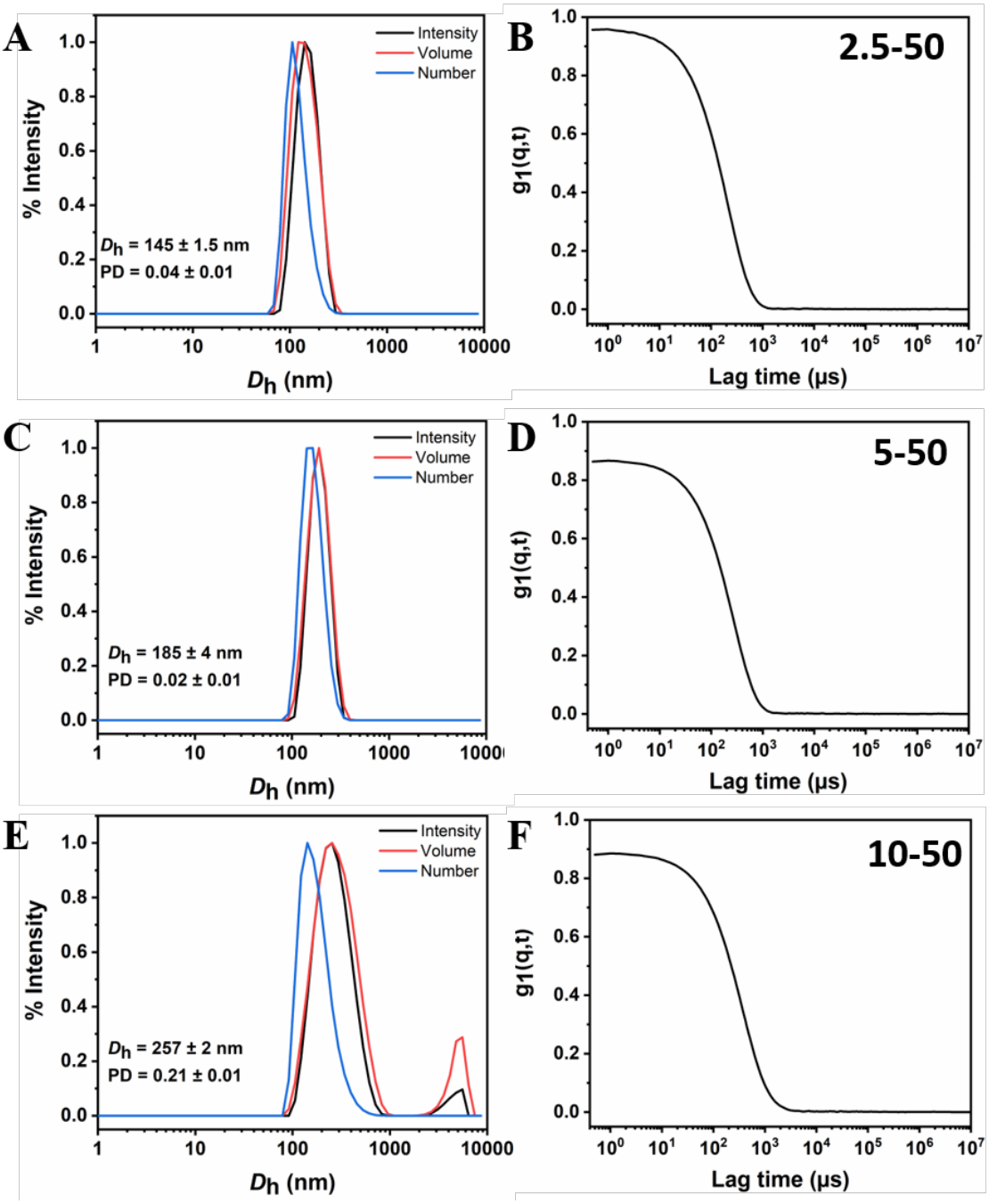


Figure 3.11. DLS (A,C and E) and corresponding correlogram (B, D and F) graph results of $PNAM_{40}$-*b*-$PAAm_{50}$ nano-objects obtained *via* aqueous RAFT-mediated PISA at 2.5, 5 and 10% w/w.

At $PNAM_{40}$-*b*-PAAm DP ≥100 a pure vesicle phase was obtained as shown in Figure 3.12. Vesicles occupy a broad space of the phase diagram, including also low DP areas (DP_{PAAm} = 50).

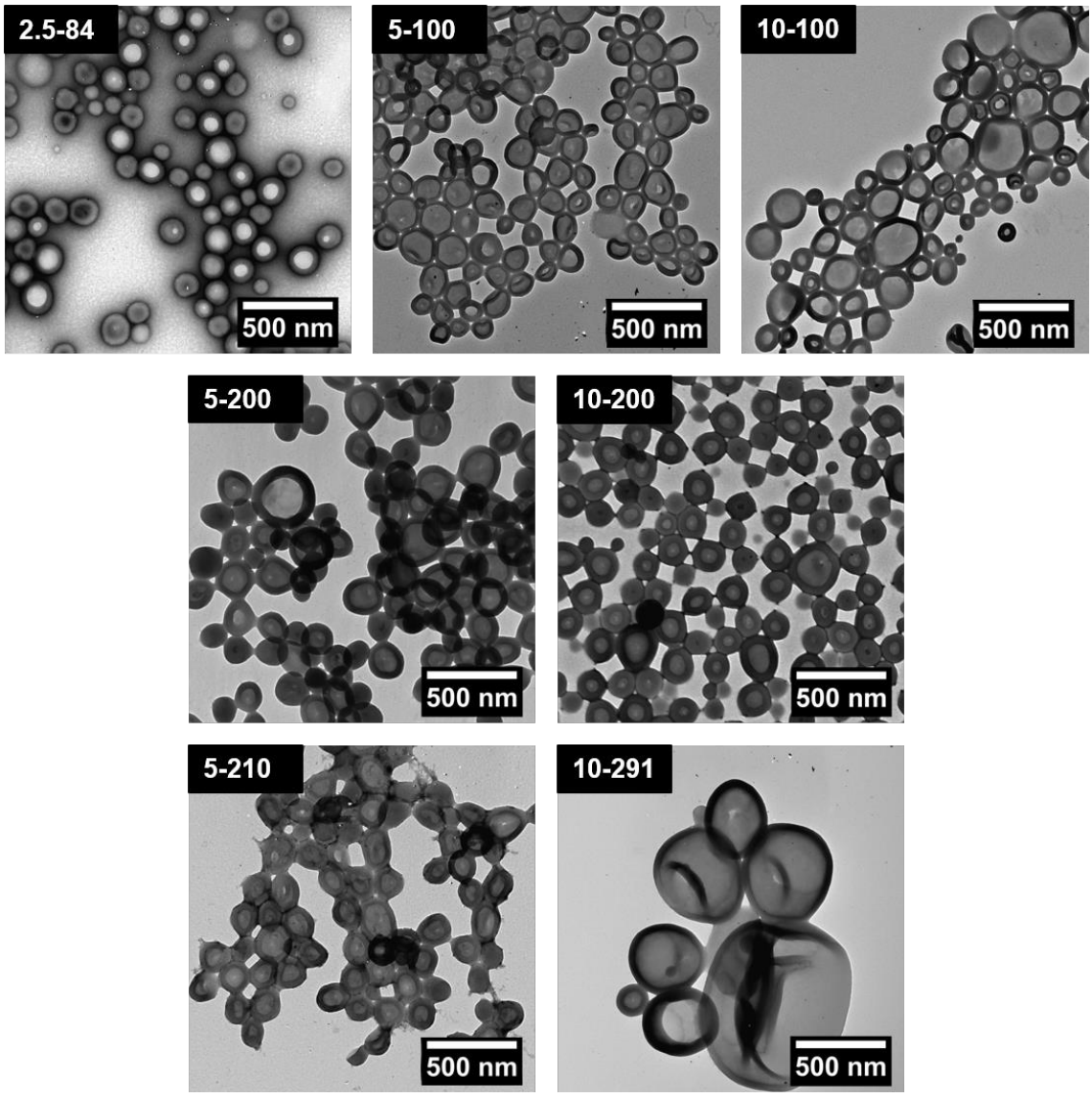


Figure 3.12. TEM images of $PNAM_{40}$-b-$PAAm_n$ diblock copolymer nanoparticles prepared by aqueous RAFT-mediated PISA using VA-044 initiator at 50 °C at 2.5, 5 and 10 % w/w at DP ≥ 100. The samples were stained with 1% w/w uranyl acetate (UA) solution.

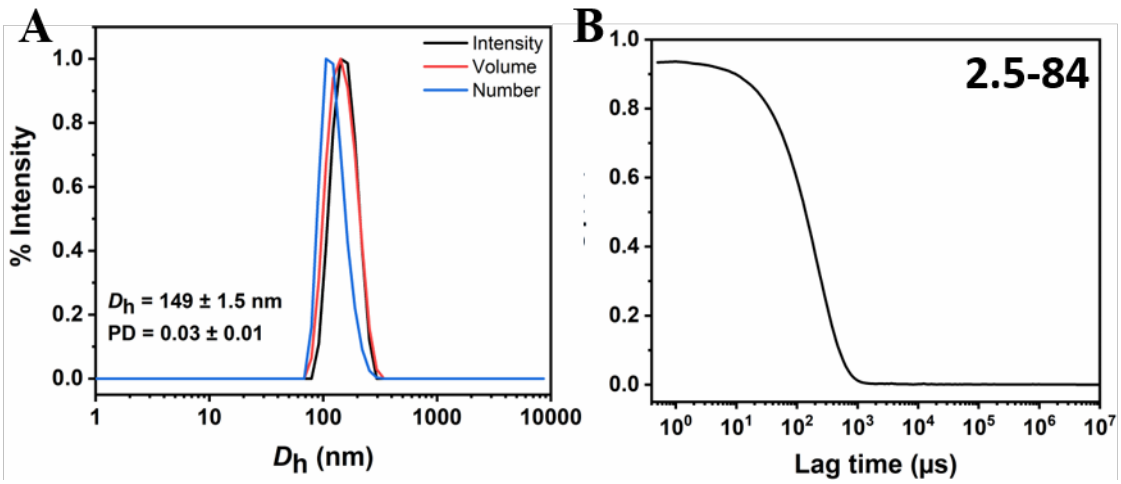
For targeted DP 100 , D_h of 149 ± 2, 180 ± 5 and 426 ± 16 nm and PD of 0.03 ± 0.01, 0.03 ± 0.01 and 0.18 ± 0.01 values were measured for polymerizations at 2.5, 5 and 10% w/w, respectively. For targeted DP 200, D_h of 239 ± 8, and 193 ± 4 nm and PD of 0.18 ± 0.01 and 0.03 ± 0.01 values were measured for polymerizations at 5 and 10% w/w, respectively. For targeted DP 300, D_h of 160 ± 7 and 669 ± 9 nm and PD of 0.03 ± 0.01

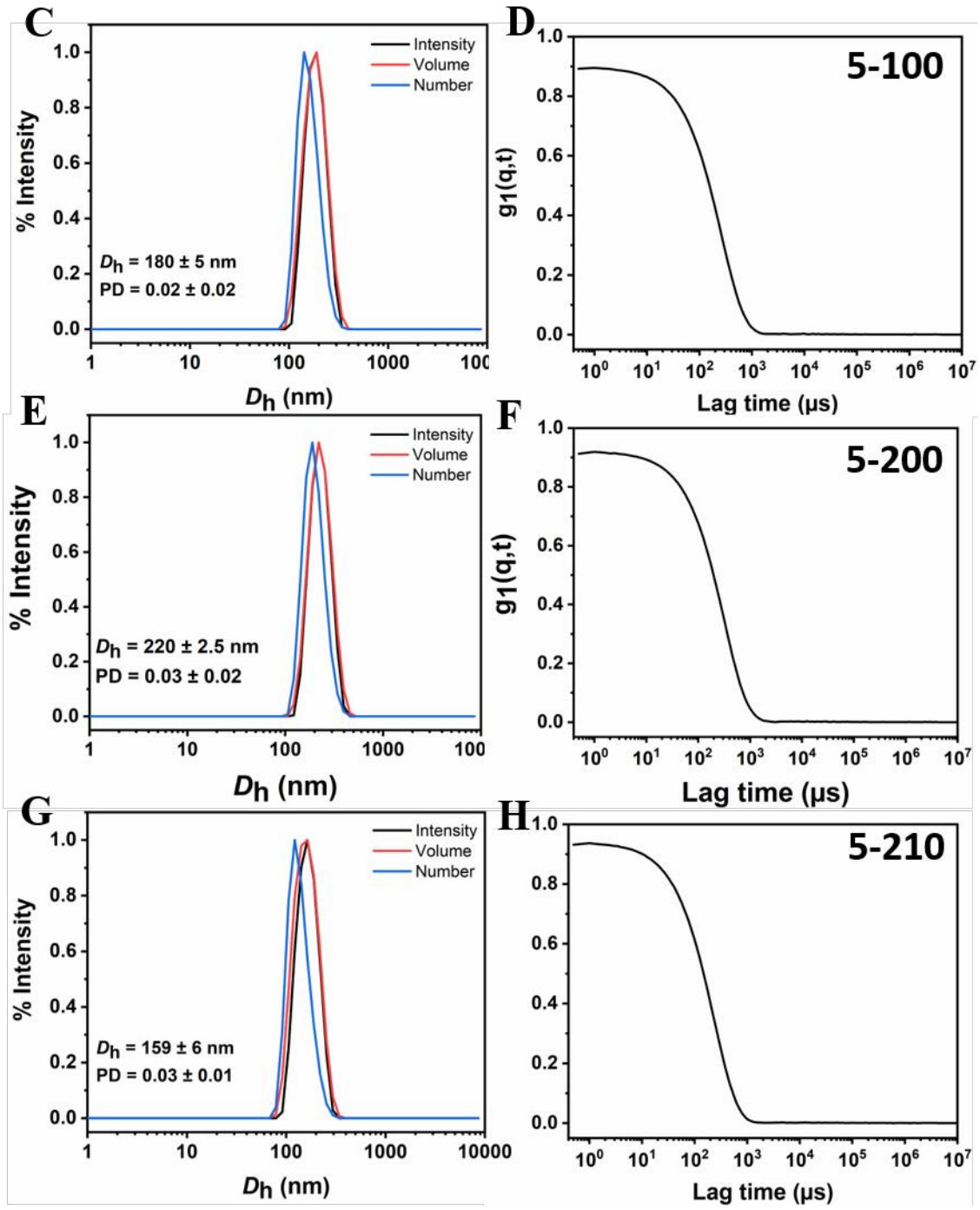
and 0.19 ± 0.01 values were measured for polymerizations at 5 and 10% w/w, respectively.

The presence of vesicles at such low DPs could be explain by low interfacial curvature caused by H-bonding self-complementarity of the adenine units within the micellar core,[10, 41] creating a non-covalent crosslinking of the micellar core and thus providing a certain rigidity and resistance toward the high interfacial curvature required to form spheres.

Another explanation could be due to the presence of π-π stacking. It is well known that adenine-adenine interaction is a strong interaction, due to the hydrogen bonding and also π–π stacking (which refers to attractive and noncovalent interactions between aromatic rings).[30] The π-conjugated property of the polymer chains could also provide an additional attraction between the core blocks.[42] Therefore, could influence the self-assembled structures and morphologies causing a decrease in the surface curvature and explain the presence of vesicles at such low DP.

Vesicles could not be obtained at DP higher than 84 for the polymerization at 2.5% w/w even after multiple attempts to obtain the block copolymers as previously explained.




C
D
E
F
G
H
Intensity
Volume
Number
% Intensity
D_h (nm)
D_h = 180 ± 5 nm
PD = 0.02 ± 0.02
D_h = 220 ± 2.5 nm
PD = 0.03 ± 0.02
D_h = 159 ± 6 nm
PD = 0.03 ± 0.01
g1(q,t)
Lag time (μs)
5-100
5-200
5-210

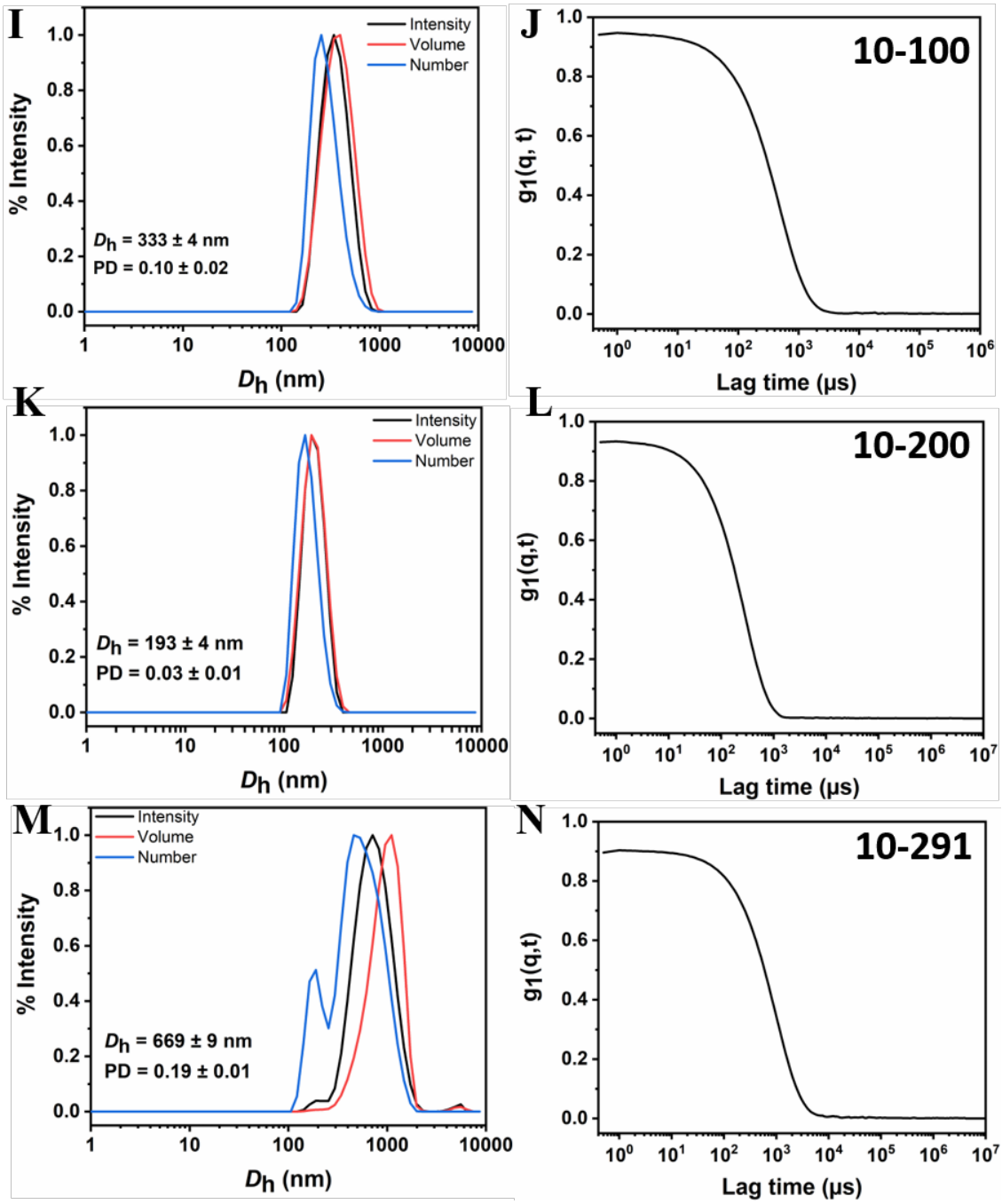


Figure 3.13. DLS (A,C,E,G,I,K and M) and corresponding correlogram (B, D, F, H, J, L and FN) graph results of $PNAM_{40}$-*b*-$PAAm_n$ nano-objects obtained *via* aqueous RAFT-mediated PISA at 2.5, 5 and 10% w/w for DPs ≥ 100.

In all these cases, the increase in the D_h is explained by the increase of the DP and the narrow dispersity by the pure vesicle phase obtained. Cryo-TEM (see section 3.3.2.1)

technique was used in order to confirm the average diameter (D_{ave}) for the different vesicles particles obtained as well as determine the average membrane thickness (M_{ave}) of each formulation. The D_{ave} was obtained after 100 particles were measured for each sample. Similar D_{ave} was obtained after cryo-TEM analysis. Table 3.2 summarizes all the data concerning the diblock copolymer nano-objects obtained for the construction of a detailed phase diagram. The nanoparticles exhibited negative zeta potential values of approximately – 25 mV (zeta-potential = -38.4 to -20.3 mV) measured from microelectrophoretic analysis at neutral pH revealing the presence of charges on the outer surface of particles. This is attributed to the presence of the carboxylic acid end group of the macro-CTA on the surface of the nanoparticles and the free oxygen group present on the PNAM block.

Table 3.2. Summary of DLS and TEM characterization data of the different $PNAM_{40}$-b-$PAAm_y$ block copolymer nano-objects obtained by aqueous RAFT-mediated PISA

Sample	D_h (nm)[a]	PD[a]	D_{ave}[b] (nm)	Morphology[c]	Zeta-potential (mV) at pH 7
2.5-DP20	16 ± 1	0.28 ± 0.01	-	W+S	-28.1 ± 8.6
2.5-DP28	129 ± 1	0.23 ± 0.01	-	W+S	-20.3 ± 4.8
2.5-DP50	145 ± 2	0.04 ± 0.01	-	W+V	-31.9 ± 8.1
2.5-DP84	149 ± 2	0.03 ± 0.01	126 ± 20	V	-38.4 ± 9.1
5-DP20	19 ± 1	0.24 ± 0.01	-	W+S	-32.4 ± 4.4
5-DP28	122 ± 1	0.24 ± 0.01	-	W	-28.4 ± 2.3
5-DP50	185 ± 4	0.02 ± 0.01	-	W+V+S	-39.2 ± 5.6
5-DP100	180 ± 5	0.03 ± 0.01	164 ± 32	V	-38.1 ± 6.1
5-DP200	239 ± 8	0.18 ± 0.01	174 ± 19	V	-36.8 ± 6.6
5-DP210	160 ± 7	0.03 ± 0.01	179 ± 28	V	-33.5 ± 6.6
10-DP20	16 ± 1	0.28 ± 0.01	-	W+S	-29.5 ± 3.9
10-DP28	128 ± 3	0.24 ± 0.01	-	W	-24.2 ± 1.1
10-DP50	257 ± 9	0.21 ± 0.01	-	W+V	-30.2 ± 5.4
10-DP100	426 ± 16	0.18 ± 0.01	310 ± 141	V	-39.3 ± 4.7
10-DP200	193 ± 4	0.03 ± 0.01	191 ± 39	V	-36.1 ± 7.3
10-DP291	669 ± 9	0.19 ± 0.01	459 ± 234	V	-38.4 ± 4.2

[a] D_h and PD values measured from DLS analysis (the error shows the standard deviation from 4 repeat measurements). [b] D_{ave} values obtained from Cryo-TEM analysis (size measured over at 100 particles using image J) and were calculated only for pure vesicle phase. [c] Morphologies observed from dry-state TEM imaging, using 1% w/w uranyl acetate (UA) solution for staining (Key: S – spheres, W – worm-like micelles, V – vesicles).

3.2.2 Study of the vesicle phase

3.2.2.1 Characterization of the vesicles

Cryo-TEM was used for the analysis of the vesicle membrane, since contrary to the dry-state technique it does not have a drying effect causing the vesicles to collapse and therefore leading to inaccurate measurements of membrane thickness values. As mentioned in the above section (Table 3.2), the D_{ave} obtained using cryo-TEM technique were similar to the ones obtained by DLS analysis. Interestingly, cryo-TEM images also showed that the membrane thickness increased with the DP and the weight percentage. Figures 3.14 and 3.15 show the membrane thickness data obtained.

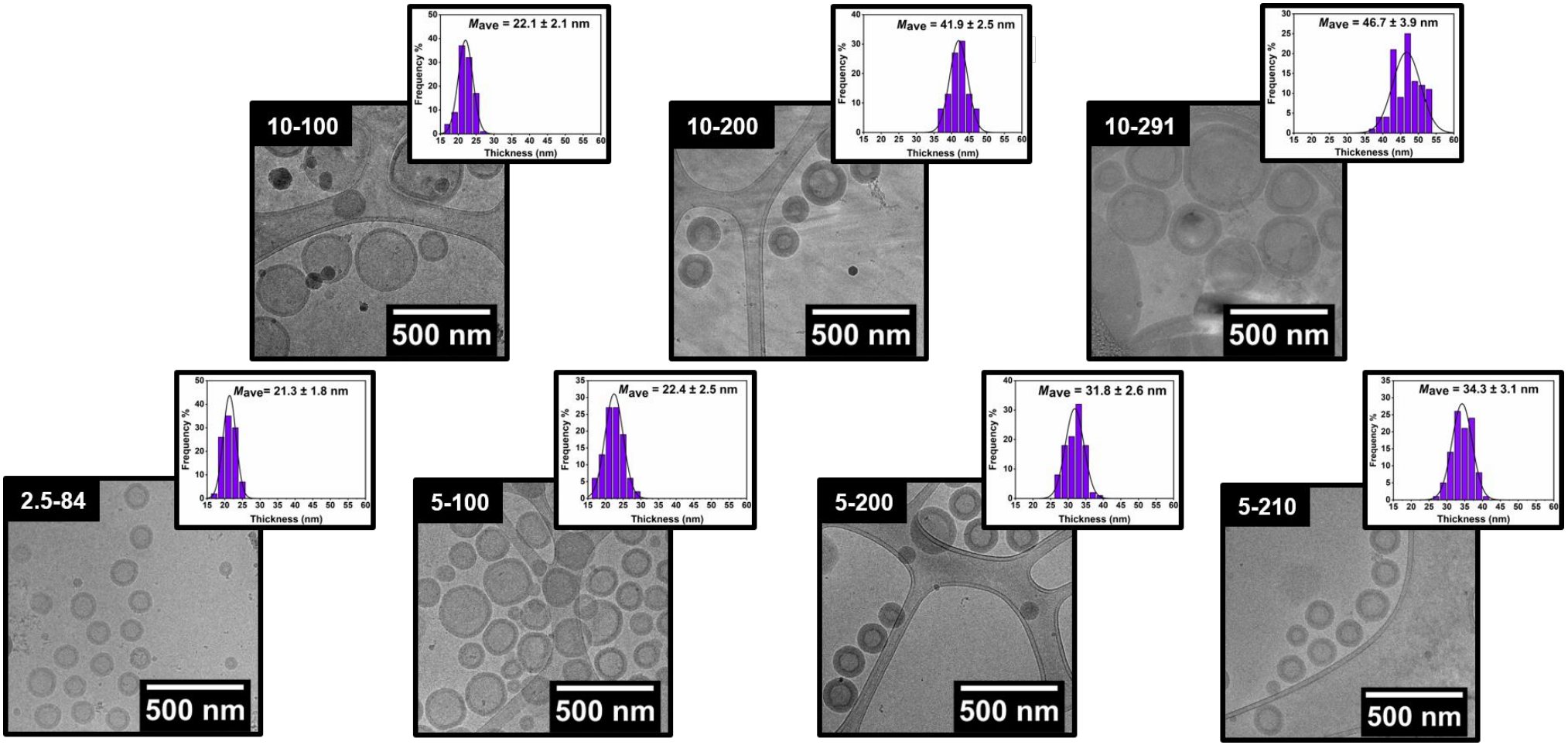
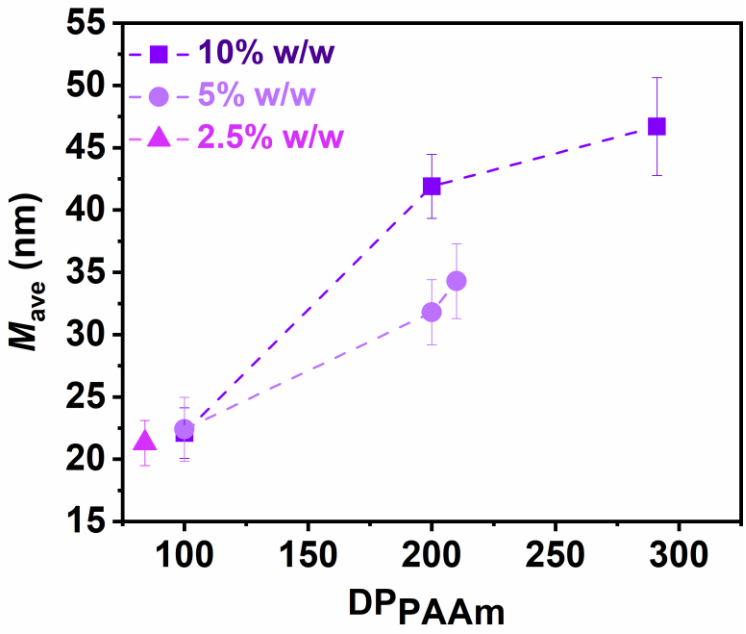


Figure 3.14. Representative cryo-TEM images of PNAM-b-PAAm$_y$ diblock copolymers vesicle nano-objects at different DP and [solids] along with their corresponding membrane thicknesses measured over at least 100 particles using image J.

.



[Solids] (% w/w)	Target DP	Actual DP	M_{ave} (nm)
2.5	100	84	21.3 ± 1.8
5	100	100	22.4 ± 2.5
	200	200	31.8 ± 2.6
	300	210	34.3 ± 3.1
10	100	100	22.1 ± 2.1
	200	200	41.9 ± 2.5
	300	291	46.7 ± 3.9

Figure 3.15. Top image, the degree of polymerization of PAAm at different solids concentration versus the vesicle membrane thickness, (the error bars represent the standard deviation from 100 measurements). With the corresponding table (bottom).

The vesicles thicknesses varied from 21 ± 2 nm (lowest solid concentration and DP) to 46 ± 4 nm for the highest DP and solids concentrations. Two trends can be seen here, the first one as the DP increases, the membrane thickness increases as well. These results could be explained by the increase of the hydrophobic core block as the DP increased. The volume fraction of PAAm in the membrane increases (the polymer molecules from the solution are replacing the solvent molecules inside the membrane), causing an

increased steric repulsion between the PAAm and the PNAM blocks in the membrane and consequently causing the blocks to stretch, leading to an increase in membrane thickness (Figure 3.16).[43] As for the increase of the membrane thickness with the solids concentration, the monomer concentration is different for the same DP and the number of polymer chains in the media is greater in higher % w/w, which could cause the polymer chains to pack in a way to welcome more chains and causes the increase in the membrane thickness.

Another explanation for the increase in the membrane thickness could come from the hydrogen-bonds and π-π stacking between adenine moieties. As mentioned the section 3.4.1.2, the π-conjugated property of the polymer chains could provide an additional attraction between the core blocks, and therefore could influence the self-assembled structures and morphologies causing the increase in the membrane thickness.[44] The introduction of π–π stacking could enhance the degree of polymer chains alignment (due to the increase of the rigidity between the polymer chains) in the membrane and increasing the order parameter with increasing π–π strength. π–π stacking could modify the membrane structure from a thinner and disordered arrangement to a thicker and ordered one similar to a bilayer arrangement. The obtained data also indicated that the kinetics (defined by experimental conditions, for example polymer concentration) with which the thermodynamic regimes are traversed could affect both the details of the formation mechanism and the final morphology.[45]

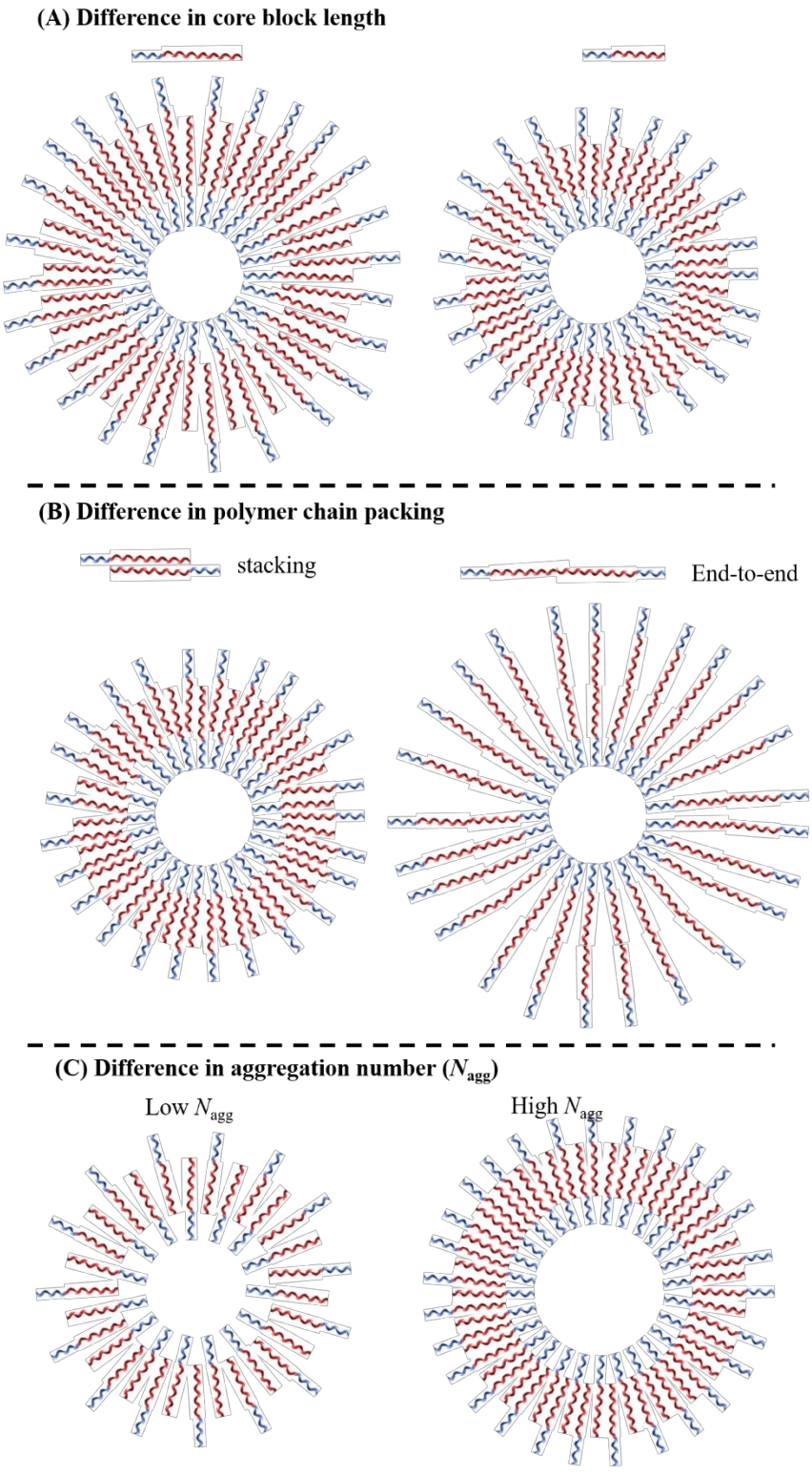


Figure 3.16. Representation of the difference in the polymer core block chain length (A),packing (B) and aggregation number (N_{agg}) (C) on the size of the vesicles which could explain the difference in the membrane thickness.

Studies about the dynamics of block copolymer chain exchange among micelles and bulk solution showed that when the dispersing solvent is a very poor solvent for the hydrophobic blocks (in here water only was used), it will affect the mobility of the core in a way that it will kinetically 'freeze' the morphology of the particles. Therefore, even though the morphologies of nanoparticles are mainly controlled by thermodynamics, kinetic effects can as well determine the formation of a large variety of metastable aggregates in the case of polymeric amphiphiles.[46] Block copolymers morphologies depend on their self-assembly methods.[47] Therefore, it can be hypothesized that polymer self-assemblies prepared by dilution of the copolymer from a good solvent (a solvent good for both blocks) into a selective solvent (a solvent-switch method) would tend to produce aggregate morphologies that are closer to equilibrium than those prepared by aqueous RAFT-mediated PISA. Thermodynamically favoured structures can be yielded since solvent switch method induces more flexibility to the single chains during the self-assembly process as they start from being freely dissolved unimers rather than a bulk material.[17] Therefore, in the next section this specific experiment will be discuss in order to try to confirm the first hypothesis

Warren *et al.* showed that during PISA, the formation on vesicle could happened with four possible particle growth mechanisms.[48] Where in the first case both the inner and outer diameters increase during vesicle growth. In another case, the inner vesicle diameter remains constant, while the outer diameter increases. Or the outer diameter increases, and the inner diameter is simultaneously reduced and finally in the last case, the outer vesicle diameter is fixed, and the inner vesicle diameter is reduced as the membrane thickens. A systematic increase in membrane thickness M_{ave} was observed when targeting longer membrane-forming blocks, e.g., from 22.4 nm for 5-DP100 to 34.3 nm for 5-DP210 (see

Figure 3.15). It has been reported previously that M_{ave} should increase according to the scaling relationship, $M_{ave} = k_{FH}x^a$, where x is the degree of polymerization of the membrane-forming block, k_{FH} is a constant related to the Flory−Huggins interaction parameter at the block junction (here we are using $k_{FH} = 0.495$ for polyacrylamide in water), and a is a scaling exponent that is determined by the conformation of the membrane-forming chains. Where a = 0.50 for completely collapsed coils and a = 1.00 for fully stretched chains (e.g., for the alkyl chains in phospholipid-based liposomes). From the data shown in Figure 3.15, an intermediate scaling exponent of an average of 0.76 for the different particles obtained at 5% w/w using the cryoTEM data, which suggest that the vesicle membranes comprise partially stretched chains. In order to construct a graph to show this trend and to further understand this phenomenon, more points would be needed for the different % w/w with more DP (e.g., DP = 120, 150, 180, 220 and 250).

3.2.2.2 Characterization of reassembled particles prepared by solvent-switch

As mentioned in the section above, we hypothesized that the difference in the membrane thicknesses with the solids concentration could be due to particles being trapped kinetically. In order to understand why one can, observe these changes in the membrane thickness, one specific experiment has been conducted. Vesicle nano-objects with DP = 100 and 200 at 5 and 10% w/w were used in this study for comparison due to similar conversion for each of these samples. Those four different vesicles made by RAFT-mediated PISA were reassembled *via* a solvent-switch method. The polymers were first freeze-dried then dissolved in DMSO (a good solvent for both PNAM and PAAm blocks)

to give a concentration of 8 mg.mL^{-1}. Then a specific water volume was adding using a syringe pump with a flow rate of 0.5 mL.h^{-1} to achieve a final concentration of 1 mg.mL^{-1}. The polymers solutions where then dialysed against water for 2-3 days in order to remove any DMSO traces using dialysis membrane bags of 3.5 kDa. The reassembled particles where then characterised by DLS, TEM and cryo-TEM. Table 3.3 and Figure 3.15 show the DLS results for the reassembled particles at different DP and % w/w. The results at 5% w/w, show that the reassembled particles have similar size from their PISA homologues, the size varies from 180 to 155 nm for DP 100 (dispersity varies from 0.02 to 0.20) and 238 to 230 nm for DP 200 (with a dispersity that varies from 0.18 to 0.14). On the other hand, the results obtained for 10% w/w show that the reassembled particles sizes were very different from the original one, the size changes from 425 to 162 nm for DP 100 (with a dispersity that varies from 0.18 to 0.07) and 193 to 247 nm for DP 200 (dispersity varies from 0.03 to 0.20). No significant changes were observed for the polymers at 5% w/w, the difference in size for 10% w/w could be due kinetically trapped nature of the PISA particles. Further characterization by TEM and cryo-TEM was conducted in order to better understand the difference in the reassembled particles.

Table 3.3. Comparison of the DLS results for PISA and reassembled particles.

	PISA particles				Reassembled particles			
Particles	**D_h (nm)[a]**	**PD[a]**	**D_{ave} (nm)[b]**	**Morphology[c]**	**D_h (nm)**	**PD**	**D_{ave} (nm)[b]**	**Morphology[c]**
5-DP100	180 ± 5	0.02 ± 0.02	164 ± 32	V	155 ± 11	0.20 ± 0.01	156 ± 44	V
10-DP100	425 ± 16	0.18 ± 0.01	310 ± 141	V	162 ± 9	0.14 ± 0.03	183 ± 58	MV
5-DP200	238 ± 8	0.18 ± 0.01	174 ± 19	V	230 ± 7	0.07 ± 0.03	230 ± 75	V
10-DP200	193 ± 4	0.03 ± 0.01	191 ± 39	V	247 ± 33	0.2 ± 0.08	181 ± 34	MV

[a]D_h and PD values measured from DLS analysis (the error shows the standard deviation from 4 repeat measurements).[b]D_{ave} values obtained from Cryo-TEM analysis (size measured over at 100 particles using image J). [c]Morphologies observed from dry-state TEM imaging, using 1% w/w uranyl acetate (UA). solution for staining (Key: V – vesicles, MV – multi compartment vesicles).

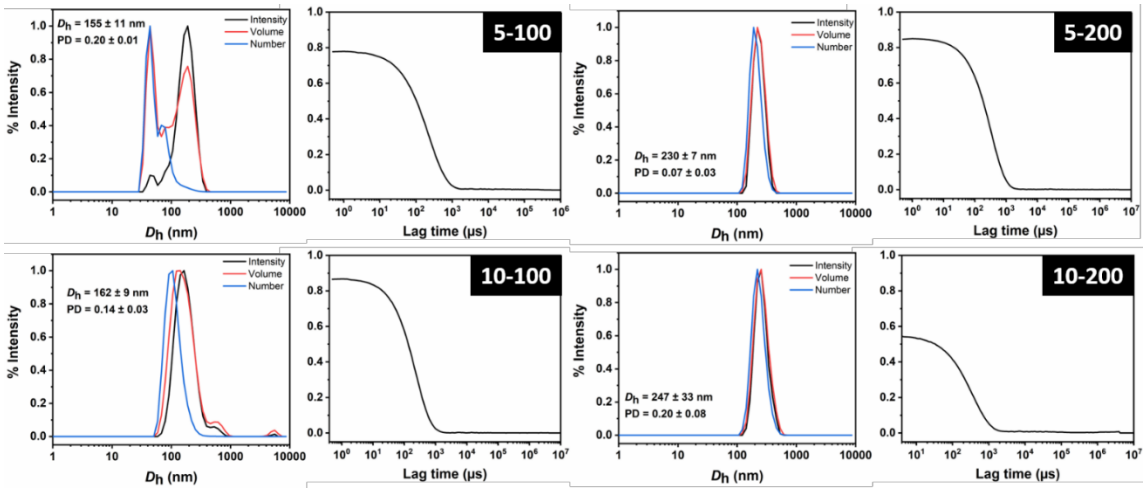


Figure 3.17. DLS analysis of the reassembled particles obtained by solvent-switch method at different DP and % w/w and their corresponding correlograms.

Figure 3.18 shows the TEM comparison between the PISA vesicles and the reassembled particles. Particles obtained at 5% w/w DP 100 and 200 were vesicles and similar to the PISA particles. As for the reassembled particles obtained at 10% w/w, dry-state TEM could not discern the real internal structure of the particles. Therefore, cryo-TEM imaging was used in order to give us a more precise particle structure. Those results, showed a similar structure for DP 100 and different one for DP 200, indicate that these structures are the thermodynamically most stable ones.[49]

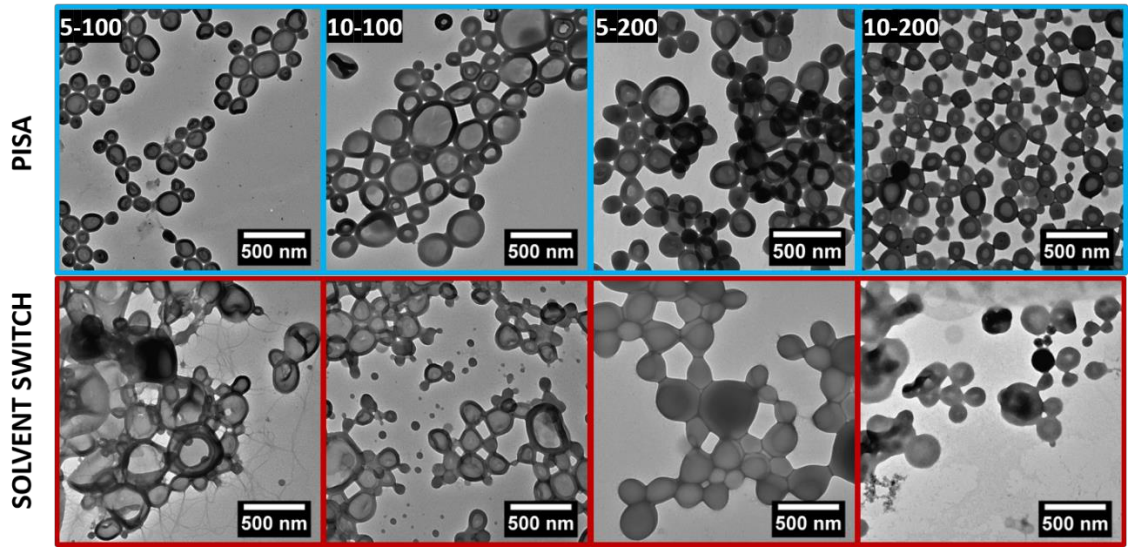


Figure 3.18. Comparison of PISA and reassembled particles by dry-state TEM. The top images show the TEM images of the PISA particles at different DP and % w/w. The bottom ones show the results for the reassembled particles. Using 1% w/w uranyl acetate (UA) solution for staining.

Figure 3.19 shows the cryo-TEM comparison between PISA vesicles and the corresponding obtained reassembled particles. The cryo-TEM images confirmed the morphology obtained for the particles at 5% w/w. For 10% w/w, the cryo-TEM images show that vesicles with intermembrane neck connection or multi compartment vesicles were obtained. These results confirmed that the PISA process created some kind of kinetically trapped structures at high DPs and upon reassembly it allows the block copolymers to assembly into a more thermodynamically favourable morphology. Hu *et al.*, showed that computer simulations suggested that a variety of high-order vesicles may be formed from block copolymers in the thermodynamically metastable state.[50] This also indicated that the origin of the formation of various vesicular morphologies comes from the competition of two kinetic processes: the macrophase separation of amphiphiles blocks from the solvent and the microphase separation between amphiphilic molecular blocks.[51]

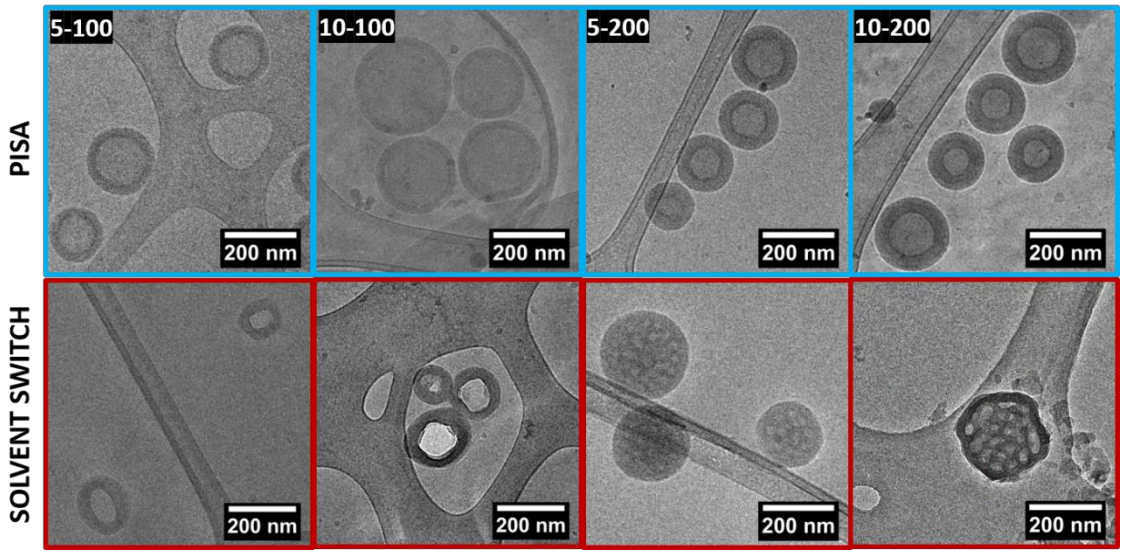


Figure 3.19. Comparison of PISA and reassembled particles by cryo-TEM. The top images show the cryo-TEM images of the PISA particles at different DP and % w/w. The bottom ones show the results for the reassembled particles.

Hu *et al.*, also showed that a range of higher-order membrane structures have been created and their evolutionary process has been presented based on a series of block copolymers with different lengths, where different type of high-ordered vesicles was obtained by varying the core block length, concentration, solubility parameter (by using different organic solvents) in the formulation process. They also showed that block copolymers with relatively short core block (DP up to 100) were mainly producing single-compartment vesicles, which corresponds to what it can be seen in this study as well. Block copolymers with longer hydrophobic blocks (DP > 200) were producing vesicles with more complex membrane structures. One parameter that has been using in this paper but not in the current study was the water contented ratio, since they've been using co-solvents for the self-assemblies. Although, it's important to say that multi-compartment vesicles were obtained at the highest water ratios. Those results are in concordance with what can be seen in Figure 3.19. This kind of high-ordered vesicles could be explained by the collision and fusion of the membrane. In addition, simple vesicles (or single-

compartment vesicles) appear at a lower molecular weight of PAAm hydrophobic block (DP = 100), while complex vesicles become dominant at a higher molecular weight PAAm block (DP = 200) (Figure 3.20). This may be because the longer PAAm chains tend to reach a metastable state during phase separation, leading to the appearance of multi-compartment vesicles. This evolution from single-membrane vesicle to higher-order membrane vesicle could provide not only a general protocol and principle for the synthesis of hollow particles with patterned internal nanostructures, as well as some hints to understand the evolution of biomembranes.

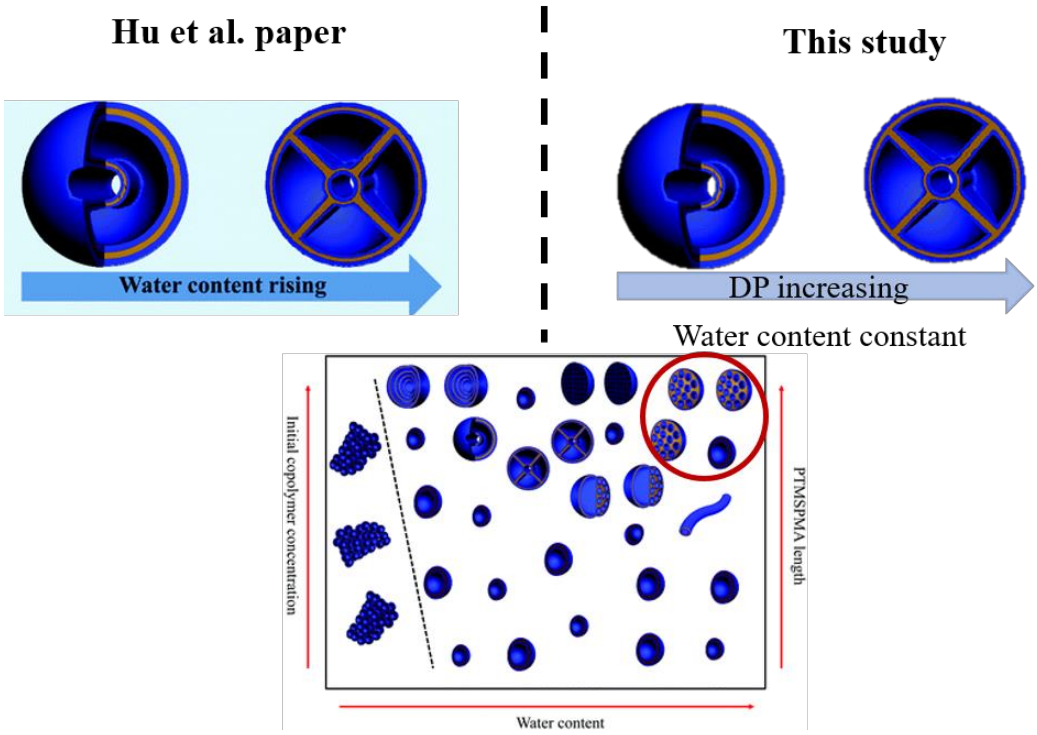


Figure 3.20. Comparison between Hu *et al.* paper and this study on the formation of multicompartment vesicles. The circled area correspond to the similar parameters used in both studies, adapted from ref.[49]

In order to test the hypothesis that adenine-adenine interactions are responsible for the observed effects on membrane thicknesses and the prevalence of vesicles some experiments could be done to validate the hypothesis. By using a methylated adenine-containing monomer and perform RAFT/PISA experiments and see if blocking the H-

bonds donors could affect morphology in the expected way.[19] As well as, performing the PISA reactions in the presence of free thymine or succinimide and see if it blocks the H-bonding units as well. Performing the PISAs reaction in the presence of an additive such as DMSO to see if this has the expected effects of inhibiting the H-bonding interactions. And finally, trying to find another monomer capable of performing PISA with similar properties to the monomer used in this study (*e.g.*, π-π stacking, H-bonding) and see if similar results can be obtained or not.

3.3 Conclusions

To conclude, we demonstrate an efficient methodology for the fabrication of nucleobase-containing block copolymer nano-objects with different morphologies and different concentrations using aqueous RAFT-mediated PISA. This new methodology allows for the chain-extension of nucleobase-containing acrylamide monomers to high DPs, which was not possible with conventional RAFT polymerization. As evidenced by the construction of a phase diagram, a range of nano-object morphologies including higher-order structures was obtained.

The observed vesicular nano-objects occupied a broad phase space with membrane thicknesses values that varied with DP and solid concentrations, indicating that incorporating adenine-containing monomer into an aqueous RAFT-mediated PISA reaction has a great impact to the phase diagram. Kinetically trapped structures were obtained *via* aqueous RAFT-mediated PISA, forming single membrane vesicles with an increase in the membrane thickness with an increase in the DP_{AAm} and % w/w. The adenine moieties had a big impact on the membrane thickness due to its self-complementary and π-π stacking interactions. This was confirmed when different morphologies were obtained upon thermodynamic reassembly of the particles; particles at higher DP went from single-membrane vesicle to multicompartment ones. This evolution in the membrane could provide not only a general protocol and principle for the synthesis of hollow particles with patterned internal nanostructures, as well as some hints to understand the evolution of biomembranes.

In the next chapter, we will be discussing on how those adenine-containing particles with different morphologies can be used to explore the MORPH process by accessing new morphologies upon the addition of the complementary thymine-containing polymer.

3.4 Experimental section

3.4.1 Materials

2, 2'-Azobis(isobutyronitrile) (AIBN) was obtained from Molekula and recrystallized from methanol. 2,2'-Azobis[2-(2-imidazolin-2-yl)propane]di-hydrochloride (VA-044) was purchased from Wako and was used without further purification. Adenine, sodium hydride (60% dispersion in mineral oil), acryloyl chloride, pyridine and 4-Acryloylmorpholine (NAM) was purchased from Sigma-Aldrich and was purified by vacuum distillation. Triethylamine was received from Fisher Scientific and used without any purification. Dialysis membrane (MWCO = 3.5 kDa) were purchased from Spectra/Por. DMF, DMSO and other chemicals were obtained from Fisher Scientific and used without further purification. Dry solvents (DMF and dioxane) were obtained by passing over a column of activated alumina using an Innovative Technologies solvent purification system.

3.4.2 Instrumentations and analysis

See general experimental section 2.5.3

3.4.3 Synthetic methods

Synthesis of N-(3-bromopropyl)acrylamide

N-(3-Bromopropyl) acrylamide was synthesized using procedures similar to the previous literature.[17] Description of the protocol can be found in the experimental section of Chapter 2.

Synthesis of 3-(adenine-9-yl) propyl acrylamide (AAm)

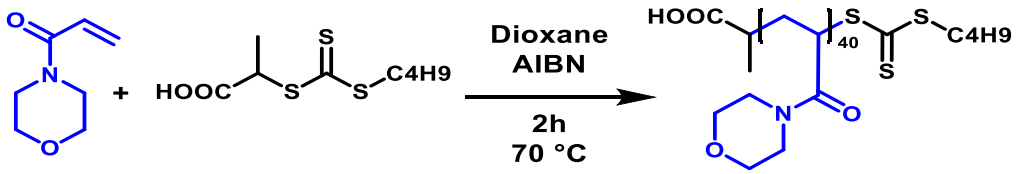
The **AAm** monomer was synthesized according to our previous work.[17] Description of the protocol can be found in the experimental section of Chapter 2.

Synthesis of 2-(((butylthio)carbonothiolyl)thio)propanoic acid (CTA)

The procedure was adapted from a previous work.[21] Description of the protocol can be found in the experimental section of Chapter 2.

Synthesis of $PNAM_{40}$ macro-CTA *via* RAFT polymerization

The procedure was adapted from our previous work.[17] Description of the protocol can be found in the experimental section of Chapter 2.



Scheme 3.2. Synthesis of poly(4-acryolylmorpholine)$_{40}$ ($PNAM_{40}$) macro-CTA.

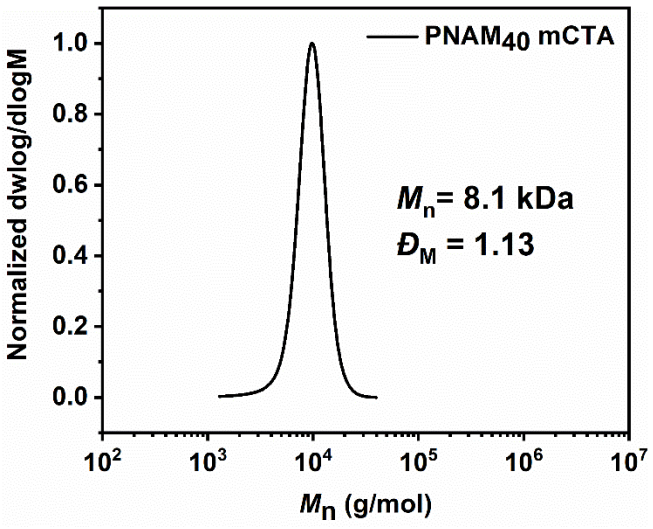


Figure 3.21. Normalized molecular weight distribution trace of $PNAM_{40}$macro-CTA (DMSO + 0.1% w/w LiBr as eluent, PMMA standards).

Synthesis of $PNAM_{40}$-*b*-$PAAm_y$ diblock copolymer nano-objects by aqueous RAFT-mediated polymerization-induced self-assembly (PISA)

A typical synthetic procedure to achieve $PNAM_{40}$-*b*-$PAAm_{200}$ diblock copolymer vesicles at [solids] = 10% w/w *via* aqueous RAFT-mediated PISA is described. $PNAM_{40}$ macro-CTA (9 mg, 1.59×10^{-6} mol, 1 eq.), AAm (80 mg, 3.17×10^{-4} mol, 200 eq.) and VA-044 (0.10 mg, 3.17×10^{-7} mol, 0.2 eq.) (a stock solution of 2 mg of VA-044 in 1 mL of water was made prior, a volume of 51.5 μL was taken and added to the reaction mixture) were dispersed in deionized (DI) water (0.89 mL) and sealed in a 7 mL vial bearing a magnetic stirrer bar. The resulting monomer-in-water solution was degassed by sparging with N_2(g) for 15 min. The sealed vial was heated at 50 °C with magnetic stirring for 2 hours to ensure full monomer conversion. After this period, the reaction mixture was exposed to air and allowed to cool to room temperature. ^{1}H-NMR in DMSO-d_6 and SEC analyses in DMSO + 0.1% w/w LiBr of the pure diblock copolymers were performed after reaction. DLS analysis and dry-state and cryo-TEM imaging were performed on samples after dilution to an appropriate analysis concentration. ^{1}H-NMR (400 MHz, DMSO-d_6): δ (ppm) 8.09 (br s, N-C***H*****$_2$***=N of PAAm side chain*), 7.77 (br s, N***H*** of PAAm side chain), 7.25 (br s, *CH=N****H****-C* of PAAm side chain), 4.03 (br s, *CH_2-C****H*****$_2$-N* of PAAm side chain), 3.64-3.25 (br m, *CH_2-C****H*****$_2$-N x 2* of PNAM and NH-C***H*****$_2$**-CH_2 of PAAm side chain), 2.95-2.68 (br m, *CH_2-C****H*****$_2$-CH_2* of PAAm and PNAM backbone), 2.20-1.27 (br m, C***H*****$_2$-*CH* of PNAM and PAAm backbone and *CH_2-C****H*****$_2$-CH_2 of PAAm side chain*).

Self-Assembly of nanoparticles by solvent-switch method

The nanoparticles of PA were reassembled as follows. First, the polymers were freeze-dried in order to obtain a solid polymer as shown in the previous study.[19] The copolymer was dissolved in DMSO (at 8 mg mL^{-1}) and stirred for 2 h at 70 °C. Then an excess of

18.2 MΩ·cm water was added *via* a syringe pump at a rate of 1 mL h^{-1}. The final volume ratio between water and organic solvent was about 8:1. The solution was then dialyzed against 18.2 MΩ·cm water, incorporating at least 6 water changes, to afford self-assemblies nanoparticles of **PA** at a concentration of ca. 1 mg mL^{-1} .

3.5 References

1. Watson, J. D.; Crick, F. H., Molecular structure of nucleic acids; a structure for deoxyribose nucleic acid. *Nat.* **1953,** *171*, 737-8.

2. Williams, D. S.; Pijpers, I. A. B.; Ridolfo, R.; van Hest, J. C. M., Controlling the morphology of copolymeric vectors for next generation nanomedicine. *J. Controlled Release* **2017,** *259*, 29-39.

3. Seeman, N. C.; Sleiman, H. F., DNA nanotechnology. *Nat. Rev. Mater.* **2017,** *3*, 17068.

4. Sivakova, S.; Rowan, S. J., Nucleobases as supramolecular motifs. *Chem. Soc. Rev.* **2005,** *34*, 9-21.

5. Jones, A. S.; Parsons, D. G.; Roberts, D. G., The interaction of polynucleotides with a guanine derivative of cellulose. *Eur. Polym. J.* **1967,** *3*, 187-198.

6. Pitha, J.; Ts'o, P. O. P., N-Vinyl derivatives of substituted pyrimidines and purines. *J. Org. Chem.* **1968,** *33*, 1341-1344.

7. Ueda, N.; Konda, K.; Kono, M.; Takemoto, K.; Imoto, M., Vinyl polymerization. 217. Vinyl compounds of nucleic acid basis. I. Synthesis of N-vinylthymine, and N-vinyladenine. *Makromol. Chem.* **1968,** *120*, 13-20.

8. Spijker, H. J.; Dirks, A. J.; van Hest, J. C. M., Synthesis and assembly behavior of nucleobase-functionalized block copolymers. *Polym. Chem.* **2006,** *44*, 4242-4250.

9. Lo, P. K.; Sleiman, H. F., Nucleobase-Templated Polymerization: Copying the Chain Length and Polydispersity of Living Polymers into Conjugated Polymers. *J. Am. Chem. Soc.* **2009,** *131*, 4182-4183.

10. Bazzi, H. S.; Sleiman, H. F., Adenine-Containing Block Copolymers via Ring-Opening Metathesis Polymerization: Synthesis and Self-Assembly into Rod Morphologies. *Macromol.* **2002,** *35*, 9617-9620.

11. Kang, Y.; Lu, A.; Ellington, A.; Jewett, M. C.; O'Reilly, R. K., Effect of Complementary Nucleobase Interactions on the Copolymer Composition of RAFT Copolymerizations. *ACS Macro Lett.* **2013,** *2*, 581-586.

12. Kang, Y.; Pitto-Barry, A.; S. Rolph, M.; Hua, Z.; Hands-Portman, I.; Kirby, N.; O'Reilly, R. K., Use of complementary nucleobase-containing synthetic polymers to prepare complex self-assembled morphologies in water. *Polym. Chem.* **2016,** *7*, 2836-2846.

13. Fong, D.; Hua, Z.; Wilks, T. R.; O'Reilly, R. K.; Adronov, A., Dispersion of single-walled carbon nanotubes using nucleobase-containing poly(acrylamide) polymers. *Polym. Chem.* **2017,** *55*, 2611-2617.

14. Gody, G.; Maschmeyer, T.; Zetterlund, P. B.; Perrier, S., Exploitation of the Degenerative Transfer Mechanism in RAFT Polymerization for Synthesis of Polymer of High Livingness at Full Monomer Conversion. *Macromol.* **2014,** *47*, 639-649.

15. Gody, G.; Maschmeyer, T.; Zetterlund, P. B.; Perrier, S., Rapid and quantitative one-pot synthesis of sequence-controlled polymers by radical polymerization. *Nat. Commun.* **2013,** *4*, 2505.

16. Mather, B. D.; Baker, M. B.; Beyer, F. L.; Berg, M. A. G.; Green, M. D.; Long, T. E., Supramolecular Triblock Copolymers Containing Complementary Nucleobase Molecular Recognition. *Macromol.* **2007,** *40*, 6834-6845.

17. Hua, Z.; Pitto-Barry, A.; Kang, Y.; Kirby, N.; Wilks, T. R.; O'Reilly, R. K., Micellar nanoparticles with tuneable morphologies through interactions between nucleobase-containing synthetic polymers in aqueous solution. *Polym. Chem.* **2016,** *7*, 4254-4262.

18. Kang, Y.; Pitto-Barry, A.; Maitland, A.; O'Reilly, R. K., RAFT dispersion polymerization: a method to tune the morphology of thymine-containing self-assemblies. *Polym. Chem.* **2015,** *6*, 4984-4992.

19. Hua, Z.; Jones, J. R.; Thomas, M.; Arno, M. C.; Souslov, A.; Wilks, T. R.; O'Reilly, R. K., Anisotropic polymer nanoparticles with controlled dimensions from the morphological transformation of isotropic seeds. *Nat. Commun.* **2019,** *10*, 5406.

20. Hua, Z. Synthetic nucleobase-containing acrylamide polymers and their applications in aqueous solutions. University of Warwick, 2018.

21. Ferguson, C. J.; Hughes, R. J.; Nguyen, D.; Pham, B. T. T.; Gilbert, R. G.; Serelis, A. K.; Such, C. H.; Hawkett, B. S., Ab Initio Emulsion Polymerization by RAFT-Controlled Self-Assembly. *Macromol.* **2005,** *38*, 2191-2204.

22. Ts'o, P. O. P.; Melvin, I. S.; Olson, A. C., Interaction and Association of Bases and Nucleosides in Aqueous Solutions. *J. Am. Chem. Soc.* **1963,** *85*, 1289-1296.

23. Fielding, L. A.; Derry, M. J.; Ladmiral, V.; Rosselgong, J.; Rodrigues, A. M.; Ratcliffe, L. P. D.; Sugihara, S.; Armes, S. P., RAFT dispersion polymerization in non-polar solvents: facile production of block copolymer spheres, worms and vesicles in n-alkanes. *Chem. Sci.* **2013,** *4*, 2081-2087.

24. Blanazs, A.; Ryan, A. J.; Armes, S. P., Predictive Phase Diagrams for RAFT Aqueous Dispersion Polymerization: Effect of Block Copolymer Composition, Molecular Weight, and Copolymer Concentration. *Macromol.* **2012,** *45*, 5099-5107.

25. Cunningham, V. J.; Alswieleh, A. M.; Thompson, K. L.; Williams, M.; Leggett, G. J.; Armes, S. P.; Musa, O. M., Poly(glycerol monomethacrylate)–Poly(benzyl methacrylate) Diblock Copolymer Nanoparticles via RAFT Emulsion Polymerization: Synthesis, Characterization, and Interfacial Activity. *Macromol.* **2014,** *47*, 5613-5623.

26. Derry, M. J.; Fielding, L. A.; Armes, S. P., Industrially-relevant polymerization-induced self-assembly formulations in non-polar solvents: RAFT dispersion polymerization of benzyl methacrylate. *Polym. Chem.* **2015,** *6*, 3054-3062.

27. Chaduc, I.; Girod, M.; Antoine, R.; Charleux, B.; D'Agosto, F.; Lansalot, M., Batch Emulsion Polymerization Mediated by Poly(methacrylic acid) MacroRAFT Agents: One-Pot Synthesis of Self-Stabilized Particles. *Macromol.* **2012,** *45*, 5881-5893.

28. Blanazs, A.; Madsen, J.; Battaglia, G.; Ryan, A. J.; Armes, S. P., Mechanistic Insights for Block Copolymer Morphologies: How Do Worms Form Vesicles? *J. Am. Chem. Soc.* **2011,** *133*, 16581-16587.

29. Hemp, S. T.; Hunley, M. T.; Cheng, S.; DeMella, K. C.; Long, T. E., Synthesis and solution rheology of adenine-containing polyelectrolytes for electrospinning. *Polym.* **2012,** *53*, 1437-1443.

30. Sabury, S.; Collier, G. S.; Ericson, M. N.; Kilbey, S. M., Synthesis of a soluble adenine-functionalized polythiophene through direct arylation polymerization and its fluorescence responsive behavior. *Polym. Chem.* **2020,** *11*, 820-829.

31. Penfold, N. J. W.; Yeow, J.; Boyer, C.; Armes, S. P., Emerging Trends in Polymerization-Induced Self-Assembly. *ACS Macro Lett.* **2019,** *8*, 1029-1054.

32. Jones, E. R.; Semsarilar, M.; Wyman, P.; Boerakker, M.; Armes, S. P., Addition of water to an alcoholic RAFT PISA formulation leads to faster kinetics but limits the evolution of copolymer morphology. *Polym. Chem.* **2016,** *7*, 851-859.

33. Cunningham, V. J.; Derry, M. J.; Fielding, L. A.; Musa, O. M.; Armes, S. P., RAFT Aqueous Dispersion Polymerization of N-(2-(Methacryloyloxy)ethyl)pyrrolidone: A Convenient Low Viscosity Route to High Molecular Weight Water-Soluble Copolymers. *Macromol.* **2016,** *49*, 4520-4533.

34. Karagoz, B.; Esser, L.; Duong, H. T.; Basuki, J. S.; Boyer, C.; Davis, T. P., Polymerization-Induced Self-Assembly (PISA) – control over the morphology of nanoparticles for drug delivery applications. *Polym. Chem.* **2014,** *5*, 350-355.

35. Jones, E. R.; Mykhaylyk, O. O.; Semsarilar, M.; Boerakker, M.; Wyman, P.; Armes, S. P., How Do Spherical Diblock Copolymer Nanoparticles Grow during RAFT Alcoholic Dispersion Polymerization? *Macromol.* **2016,** *49*, 172-181.

36. Perrier, S., 50th Anniversary Perspective: RAFT Polymerization—A User Guide. *Macromol.* **2017,** *50*, 7433-7447.

37. Warren, N. J.; Armes, S. P., Polymerization-Induced Self-Assembly of Block Copolymer Nano-objects via RAFT Aqueous Dispersion Polymerization. *J. Am. Chem. Soc.* **2014,** *136*, 10174-10185.

38. D'Agosto, F.; Rieger, J.; Lansalot, M., RAFT-Mediated Polymerization-Induced Self-Assembly. *Angew. Chem. Int. Ed.* **2020,** *59*, 8368-8392.

39. Semsarilar, M.; Jones, E. R.; Blanazs, A.; Armes, S. P., Efficient Synthesis of Sterically-Stabilized Nano-Objects via RAFT Dispersion Polymerization of Benzyl Methacrylate in Alcoholic Media. *Adv. Mater.* **2012,** *24*, 3378-3382.

40. Varlas, S.; Foster, J. C.; Arkinstall, L. A.; Jones, J. R.; Keogh, R.; Mathers, R. T.; O'Reilly, R. K., Predicting Monomers for Use in Aqueous Ring-Opening Metathesis Polymerization-Induced Self-Assembly. *ACS Macro Lett.* **2019,** *8*, 466-472.

41. Bintang Ilhami, F.; Huang, S.-Y.; Chen, J.-K.; Kao, C.-Y.; Cheng, C.-C., Multifunctional adenine-functionalized supramolecular micelles for highly selective and effective cancer chemotherapy. *Polym. Chem.* **2020,** *11*, 849-856.

42. Umadevi, D.; Sastry, G. N., Quantum Mechanical Study of Physisorption of Nucleobases on Carbon Materials: Graphene versus Carbon Nanotubes. *J. Phys. Chem. Lett.* **2011,** *2*, 1572-1576.

43. Ianiro, A.; Wu, H.; van Rijt, M. M. J.; Vena, M. P.; Keizer, A. D. A.; Esteves, A. C. C.; Tuinier, R.; Friedrich, H.; Sommerdijk, N. A. J. M.; Patterson, J. P., Liquid–liquid phase separation during amphiphilic self-assembly. *Nat. Chem.* **2019,** *11*, 320-328.

44. Lin, Y.-L.; Chang, H.-Y.; Sheng, Y.-J.; Tsao, H.-K., Structural and mechanical properties of polymersomes formed by rod–coil diblock copolymers. *Soft Matter* **2013,** *9*, 4802-4814.

45. Kita-Tokarczyk, K.; Grumelard, J.; Haefele, T.; Meier, W., Block copolymer vesicles—using concepts from polymer chemistry to mimic biomembranes. *Polym.* **2005,** *46*, 3540-3563.

46. Cerritelli, S.; Fontana, A.; Velluto, D.; Adrian, M.; Dubochet, J.; De Maria, P.; Hubbell, J. A., Thermodynamic and Kinetic Effects in the Aggregation Behavior of a Poly(ethylene glycol-b-propylene sulfide-b-ethylene glycol) ABA Triblock Copolymer. *Macromol.* **2005,** *38*, 7845-7851.

47. Mai, Y.; Eisenberg, A., Self-assembly of block copolymers. *Chem. Soc. Rev.* **2012,** *41*, 5969-5985.

48. Warren, N. J.; Mykhaylyk, O. O.; Ryan, A. J.; Williams, M.; Doussineau, T.; Dugourd, P.; Antoine, R.; Portale, G.; Armes, S. P., Testing the Vesicular Morphology to Destruction: Birth and Death of Diblock Copolymer Vesicles Prepared via Polymerization-Induced Self-Assembly. *J. Am. Chem. Soc.* **2015**, 137, 1929−1937.

49. Nicolai, T.; Colombani, O.; Chassenieux, C., Dynamic polymeric micelles versus frozen nanoparticles formed by block copolymers. *Soft Matter* **2010,** *6*, 3111-3118.

50. Hu, Y.; Chen, Y.; Du, J., Evolution of diverse higher-order membrane structures of block copolymer vesicles. *Polym. Chem.* **2019,** *10*, 3020-3029.

51. Sevink, G. J. A.; Zvelindovsky, A. V., Self-Assembly of Complex Vesicles. *Macromol.* **2005,** *38*, 7502-7513.

4 : Nucleation, growth, and detachment of worm-like nanoparticles from an isotropic polymersome seed/template

4.1 Introduction

Scientists have long been interested in mimicking biological organization to create synthetic materials with similar outstanding properties. A key outstanding problem is the creation of nanostructures with anisotropic dimensions. As materials are usually created under thermodynamic control, surface area is minimized – *i.e.*, spherical particles result. Anisotropy and complex shapes can be widely found in the biological world, such as tobacco mosaic virus or red blood cell. They are structures with high surface area, internal volume, and rigidity.[1-2] The development of synthetic chemistry over the last century has given chemists a diverse toolbox to control molecular assembly, *e.g.*, total synthesis. The ability to control assembly at higher length scales, *e.g.*, the nanoscale is much less developed. Biology can perform complex tasks because it has exquisite organization at every length scale. Chemists must do the same, a broad range of applications have demonstrated the advantages of using anisotropic nanoparticles (*i.e.,* plates, rods, worms *etc*.) compared to isotropic particles (*i.e.,* spheres) such as drug delivery,[3-6] in vivo imaging[7], photonics[1, 8-9] and photovoltaics. [10-11]

A variety of synthetic building blocks have been used over the past decades to create well-defined (high shape fidelity, low dispersity) anisotropic nanostructures *via* bottom-up self-assembly processes.[12] For example, inorganic nanoparticles , which are commercially available can produce high aspect ratio structures, such as gold (Au) or silver (Ag), but with limited control over functionality, which can be overcome through surface modification with organic coatings such as polymers or small molecules).[13] DNA nanotechnology [14-16] also allows to obtain well-defined anisotropic nanostructures, *i.e.*, high degree of programmability, replicate exact sequences, but is degradable, can only be handled in certain solvents and pH and also remains an expensive material despite recent

advances.[17] Synthetic polymers are highly promising building blocks, with advantages compare to other types such as inorganic nanoparticles. Their chemical composition can also be tuned in virtually an unlimited number of ways (i.e., not restricted to 4 nucleobases). The creation of well-defined anisotropic polymer nanoparticles with control over their dimensions remains a key challenge in materials science.[18]

Several groups have reported the formation of anisotropic polymer nanostructures,[3-4, 19-21] including those which can be switched between different shapes.[22-23] For instance, using polymerization-induced self-assembly[20] pure worm-like nanoparticles phases can be generated but with a poor control over the length and width. Manners and coworkers reported crystallization-driven self-assembly (CDSA), a 1D epitaxial growth driven by polymer chain crystallization as one solution to this problem.[24-25] Although CDSA is nowadays a widely studied process, finding crystallizable polymers is difficult. Our group has recently reported a new mechanism with control over the dimensions of anisotropic nanoparticles based on the hydrogen bonding interaction between complementary nucleobases, which was termed morphological transformation (MORPH)[26] and has been discussed in Chapter 2.

This mechanism involves the growth of well-defined anisotropic nanoparticles from isotopic seeds. The particles are grown by a mechanism that intrinsically causes anisotropy, in contrast to CDSA where anisotropy has to be there at the start.

To further understand this mechanism, investigations have been conducted to determine whether MORPH was a general mechanism that was not limited to just one nanoparticle system, A first step towards this was whether MORPH also takes place when A and T are switched, *i.e.,* polymers of T inserting into particles of A. Compared to thymine-thymine interactions which are quite weak, adenine-adenine ones are much more stronger due to

the self-complementarity of adenine moieties.[27] Starting with seed particles with stronger self-interaction could affect the MORPH mechanism and potentially no global transformation could be observed due to change of reorganization inside the seeds.

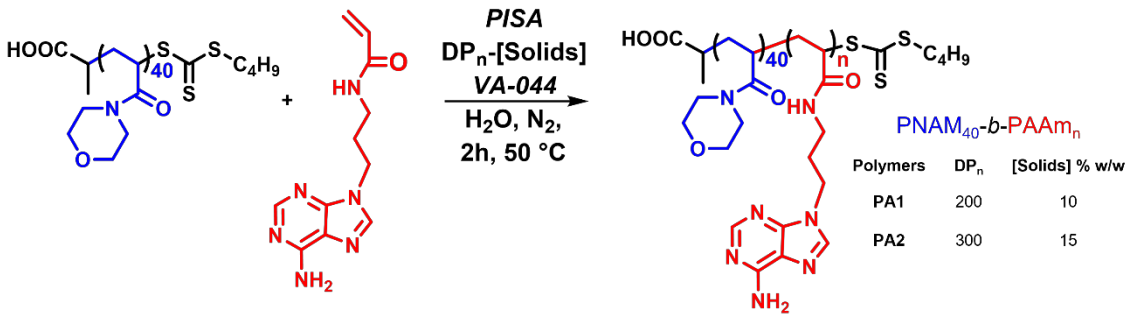
In this chapter, we explored whether MORPH could be applied to seed particles with different curvatures and surface areas, and how it could affect this general mechanism. Therefore, vesicular adenine-containing shapes were designed, and it was found that MORPH can be used to graft nodes from a vesicle.

4.2 Results and discussion

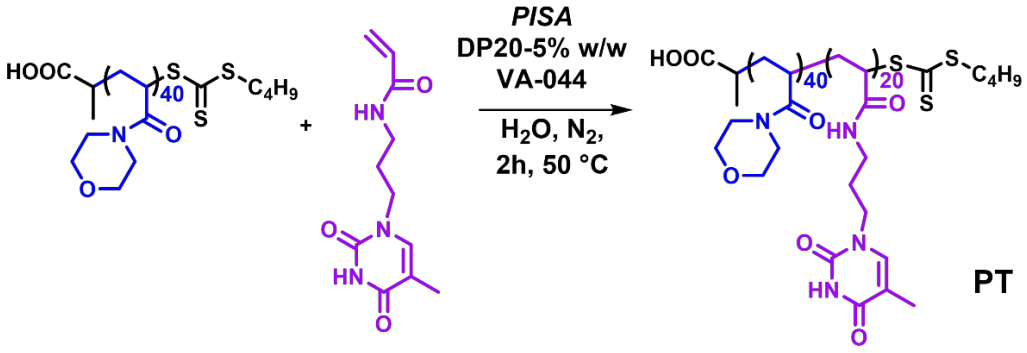
4.2.1 Synthesis and characterization of adenine and thymine-containing block copolymers *via* RAFT-mediated PISA

4.2.1.1 Synthesis and self-assembly of $PNAM_{40}$-*b*-$PAAm_y$ and $PNAM_{40}$-*b*-$PTAm_{20}$ diblock copolymers *via* aqueous RAFT-mediated PISA

This study involved the synthesis of adenine and thymine-containing acrylamide diblock copolymers obtained *via* aqueous RAFT-mediated PISA using a poly(acryloylmorpholine) **PNAM**$_{40}$ water soluble macro chain transfer agent (CTA) as the hydrophilic block. The **PNAM** macro-CTA was synthesized by RAFT polymerization in a mixture of water and 1,4-dioxane (see Scheme 4.5 and Figure 4.21 in Experimental section).[28] The macro-CTA was chain extended using either an adenine (**AAm**) or thymine (**TAm**) containing acrylamide monomer . The reactions were performed in water under thermal initiation conditions at 50 °C under nitrogen using 2,2'-Azobis[2-(2-imidazolin-2-yl)propane]di-hydrochloride (VA-044) as initiator for 2 h in order to obtain complementary block copolymers (Schemes 4.1 and 4.2 and Figure 4.1).



Scheme 4.1. Schematic representation of the synthetic route followed for the development of **$PNAM_{40}$-*b*-$PAAm_n$** diblock copolymer nano-objects *via* aqueous RAFT-mediated PISA, sing a water-soluble $PNAM_{40}$ macroinitiator.



Scheme 4.2. Synthesis of $PNAM_{40}$-*b*-$PTAm_{20}$ (**PT_{20}**) diblock copolymer nano-objects by aqueous RAFT-mediated polymerization-induced self-assembly.

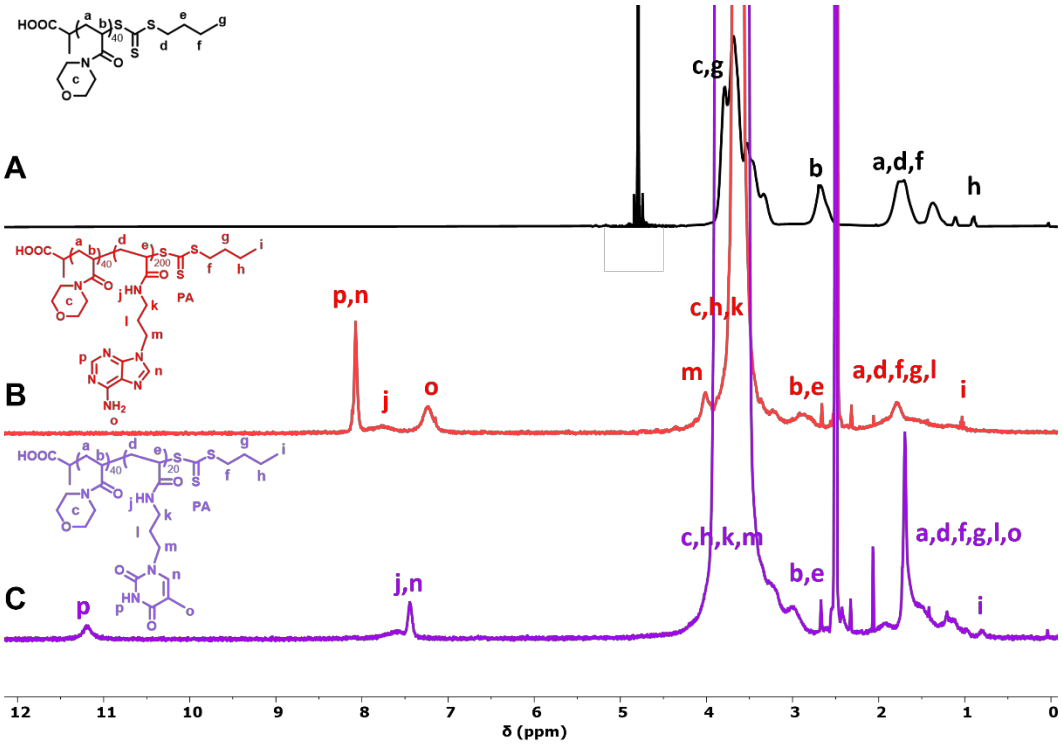


Figure 4.1. ^{1}H NMR spectra of (A) $PNAM_{40}$ macroCTA in D_2O, (B) crude $PNAM_{40}$-b-$PTAm_{20}$ (**PT_{20}**) and (C) crude $PNAM_{40}$-b-$PAAm_{200}$ (**PA1**) obtained by aqueous RAFT-mediated PISA recorded in DMSO-d_6 (400 MHz).

Two sets of long hydrophobic blocks have been synthesised using **AAm** *via* the aqueous RAFT-mediated PISA process using different solid contents (% w/w) and degree of polymerization (DP). A conversion of > 99% was achieved for the $PNAM_{40}$-b-$PAAm_{200}$ (**PA1**) at 10% w/w and a conversion of 72% (DP = 216) for polymer (**PA2**) $PNAM_{40}$-b-

$PAAm_{222}$ (target DP 300 at 15% w/w). Two different polymers were targeted for comparison for the rest of this study. The lower degree of polymerization for **PA2** was due to the higher solid contents, reducing conversion. This was preventing further conversion due to a higher adenine monomer concentration in the media causing more adenine-adenine interactions and therefore less polymerization (See Chapter 2 for complementary information on the adenine monomer **AAm** on the PISA process). As for the thymine-containing monomer, **TAm**, a short polymer was obtained with a DP of 20 at 5% w/w after full conversion (**PT_{20}**), 5% w/w was used for this polymer since full conversion was observed. Figure 4.2 shows SEC data obtained for the diblock copolymers **PA1**, **PA2** and **PT_{20}** (DMSO + 0.1% w/w LiBr eluent). SEC traces revealed monomodal molecular weight distributions ($Đ_M$ < 1.60) for **PT_{20}** and **PA1** and a high molecular shoulder for **PA2** ($Đ$M = 3.05). This result is typical for a PISA process as explained in the previous chapter.[29-30] These results indicated diblock nucleobase copolymers were obtained with an overall relatively high blocking efficiencies through RAFT polymerization. The characterization data for the polymers are summarized in Table 4.1.

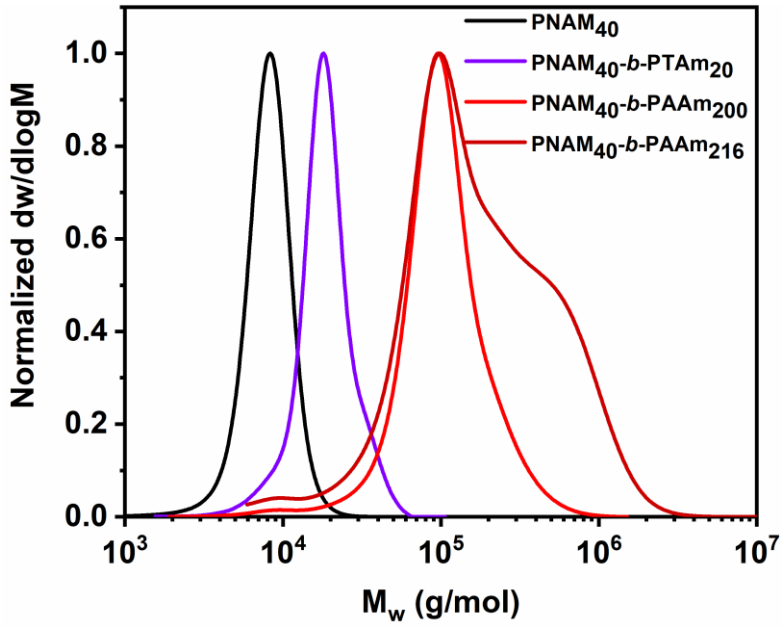


Figure 4.2. Combined SEC traces of $PNAM_{40}$ macroCTA, **PT_{20}**, **PA1** and **PA2** (recorded in DMSO + 0.1% w/w LiBr as eluent, PMMA standards).

Table 4.1. Characterization data of $PNAM_{40}$-b-$PAAm_y$ adenine-containing diblock copolymers obtained *via* aqueous RAFT-mediated PISA.

Polymers	**Structures**	**% Conv.**[a]	$M_{n,NMR}$[b] **/kDa**	$M_{n,SEC}$[c] **/kDa**	$Đ_{M,SEC}$[c]
mCTA	$PNAM_{40}$	> 99	5.6	8.1	1.13
PT_{20}	$PNAM_{40}$-b-$PTAm_{20}$	> 99	10.3	16.6	1.18
PA1	$PNAM_{40}$-b-$PAAm_{200}$	> 99	56.1	77.9	1.59
PA2	$PNAM_{40}$-b-$PAAm_{216}$	>72	60.1	92.0	3.05

[a]Monomer conversion calculated from ^{1}H-NMR spectroscopy in DMSO-d_6 by comparing the integrated signals corresponding to the backbone protons (δ= 1.62 ppm) with those of the methyl group from the monomers (between δ = 8-6 ppm) (400 MHz). [b]Calculated from conversion. [c]M_n and $Đ_M$ values calculated from DMSO + 0.1% w/w LiBr as the eluent with PMMA standards.

4.2.1.2 Characterization of the nano-objects

4.2.1.2.1 Characterization of adenine-containing nano-objects (PA1n and PA2n)

The polymer nano-objects obtained *via* RAFT-mediated PISA where then characterised by transmission electron microscopy (TEM) and dynamic light scattering (DLS). Figures 4.3 and 4.4 show that a uniform population of spherical vesicles were obtained for the nanoparticles **PA1n** and **PA2n**. CryoTEM was also used to confirm the size and the vesicular character of the obtained particles. **PA1n** vesicles have an average size of 193 ± 40 nm and a membrane thickness (M_{ave}) of 42 ± 2.5 nm and for **PA2n** an average size of 698 ± 338 nm with an M_{ave} = 44 ± 4 nm. The difference in size and membrane thickness could be explained by the relative increase of the hydrophobic core block length between **PA1n** and **PA2n**. Longer core-forming chains (and hence a more voluminous tail) are increasingly hydrophobic and more dehydrated, reducing the chain mobility and inhibiting the morphological evolution.[31] The volume fraction of PAAm in the membrane increases (the polymer molecules from the solution are replacing the solvent molecules inside the membrane), causing an increased steric repulsion between the PAAm and the PNAM blocks in the membrane and consequently causing the blocks to stretch, leading to an increase in size and membrane thickness.[32] The difference could also come from the increase of the initial PAAm concentration for **PA2** (15% w/w instead of 10% w/w for **PA1**). The number of polymer chains present in solution increases in higher % w/w, possibly causing the polymer chains to pack in a way to accommodate more chains and leading to an increase of the membrane thickness.[33]

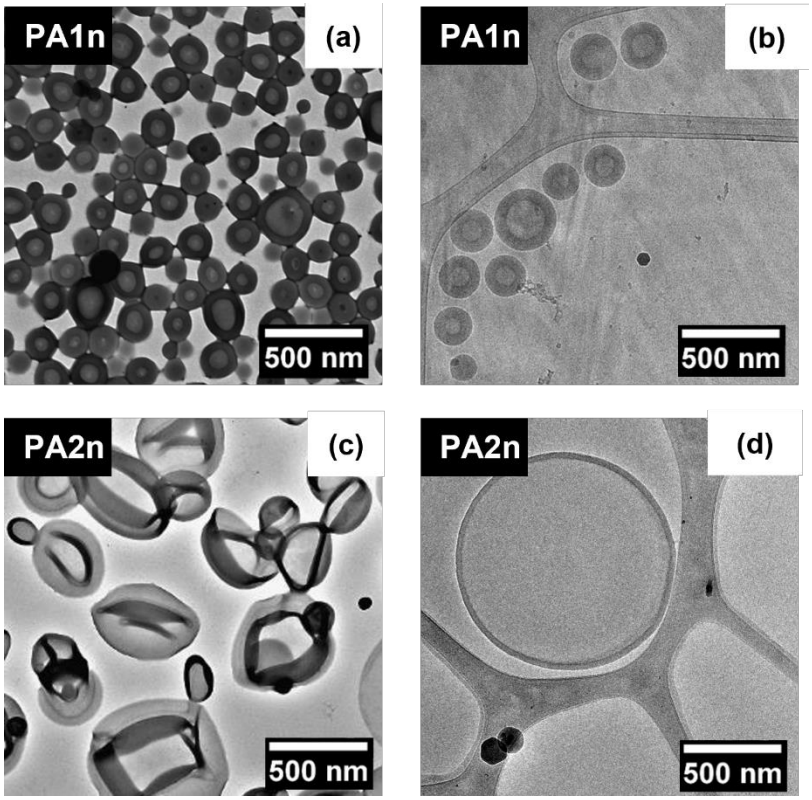


Figure 4.3. (a, c) TEM images of **PA1n** and **PA2n** and (b, d) CryoTEM images of **PA1n** and **PA2n**, respectively. (a, c) The samples were stained with 1% w/w uranyl acetate (UA) solution.

Particles solutions were measured by DLS to give relative size of the particles in solution. **PA1n** size was measured to be 193 ± 4 nm with a dispersity of 0.03 ± 0.01 and for **PA2n** 867 ± 16 nm and a dispersity of 0.22 ± 0.01 (Figure 4.4). A unimodal distribution was obtained for **PA1n**, and a trace with a small hump for **PA2n** causing a higher dispersity. The corresponding correlation functions confirmed the unimodal spherical character of the particles as well.

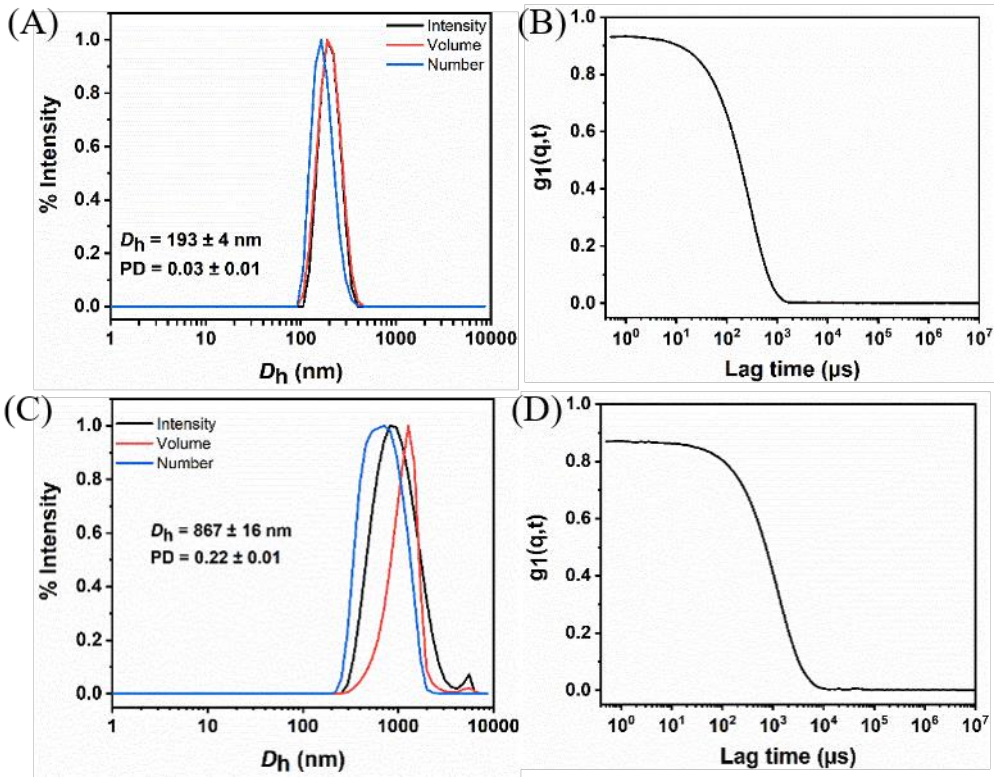


Figure 4.4. DLS (A, C) and corresponding correlogram (B, D) graph results of **PA1** and **PA2** respectively.

4.2.1.2.2 Characterization of the thymine-containing nano-object ($PT_{20}n$)

Characterization of thymine-containing complementary short block copolymer **$PT_{20}n$** shows revealed a mixture of spheres and worm morphologies (Figure 4.5).

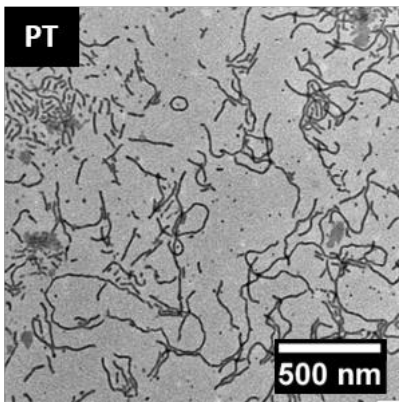


Figure 4.5. TEM image of **$PT_{20}n$** ($PNAM_{40}$-b-$PTAm_{20}$) diblock copolymer nanoparticles. The sample was stained with 1% w/w uranyl acetate (UA) solution.

DLS analysis of **PT$_{20}$n** also suggested the mixed morphology with an average size of 14 nm and a high dispersity (0.24 ± 0.01),as expected for a mixture of morphologies (Figure 4.6).[33] The ability of **PT$_{20}$n** to form worms at low DP could be explained by the hydrogen-bonding self-complementarity of the thymine units within the micellar core, a non-covalent crosslinking of the micellar core that provides rigidity that is not best accommodated within spheres with high interfacial curvature.[34-35]

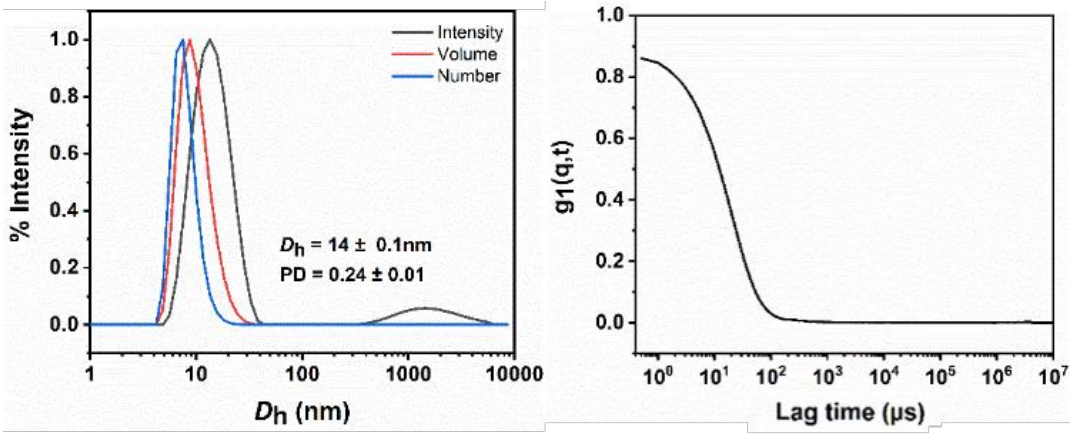


Figure 4.6. DLS and corresponding correlogram graph results of short thymine-containing block copolymer **PT$_{20}$n**.

The characterization data for the polymers **PA1n**, **PA2n** and **PT$_{20}$n** are summarized in Table 4.2.

Table 4.2. Summary of DLS and TEM characterization data of **PT$_{20}$n**, **PA1n** and **PA2n** block copolymer nano-objects obtained by aqueous RAFT-mediated PISA.

Particles	D_h (nm)[a]	PD[a]	D_{ave} (nm)[b]	M_{ave} (nm)[b]	Morphology[c]
PT$_{20}$n	18 ± 1.0	0.24 ± 0.01	-	-	S+W
PA1n	193 ± 4	0.03 ± 0.01	191 ± 39	41.9 ± 2.5	V
PA2n	867 ± 16	0.22 ± 0.01	698 ± 338	44.4 ± 4.2	V

[a]D_h and PD values measured from DLS analysis (the error shows the standard deviation from 3 repeat measurements).[b]D_{ave} values obtained from Cryo-TEM analysis (size measured over at 100 particles using the imageJ software) and were calculated only for pure vesicle phase. [c]Morphologies observed from dry-state TEM imaging, using 1% w/w uranyl acetate (UA) solution for staining (Key: S – spheres, W – worm-like micelles, V – vesicles).

4.2.2 Co-assembly of nano-objects

The obtained nano-objects were then subjected to the MORPH process. The same mixing conditions were used as those in the original report of MORPH.[26] Initial seed particles solutions of **PA1n** and **PA2n** were prepared at a concentration of 0.5 mg mL^{-1}, whilst **PT$_{20}$n** was diluted to 5 mg mL^{-1}. **PT$_{20}$n** was added to **PA1n**/**PA2n** in different ratios of adenine-thymine (A:T ratios) and stirred for 2 h.

4.2.2.1 Co-assembly of nano-objects using small vesicle particles PA1n

Preformed PNAM$_{40}$-*b*-PAAM$_{200}$ vesicles (**PA1n**) were mixed with PNAM$_{40}$-*b*-PTAm$_{20}$ (**PT$_{20}$n**) at different adenine-thymine ratios (or molar equivalents of **PT$_{20}$n**, see equations S4.1 and S4.2 for calculations) from 0.2 to 2.5. The obtained samples were then imaged by TEM (Figure 4.7). Instead of the long worms observed in the original report and in Chapter 1, here vesicles with nodes attached to the surface of the particles were obtained, suggesting that polymers **PAn1** and **PT$_{20}$n** rapidly associate, preventing the self-assembly of **PT$_{20}$**. For molar ratio T:A = 0.2, 0.33 and 0.67 respectively, an increase of number of

nodes on the particles was observed by TEM (Figure 4.7). T:A = 1 to be the threshold in after which it that all the particles have nodes on their surface. At molar ratio 1.33, the number of nodes stays constant (Figure 4.9) and start to elongate away from the outer surface of the vesicles, which progresses as the molar ratio further increases (T:A = 1.5 and 2). the number and length of the nodes are increasing as well. After a molar ratio of 2.5, nodes start to detach from the seed particles and are seen as worms.

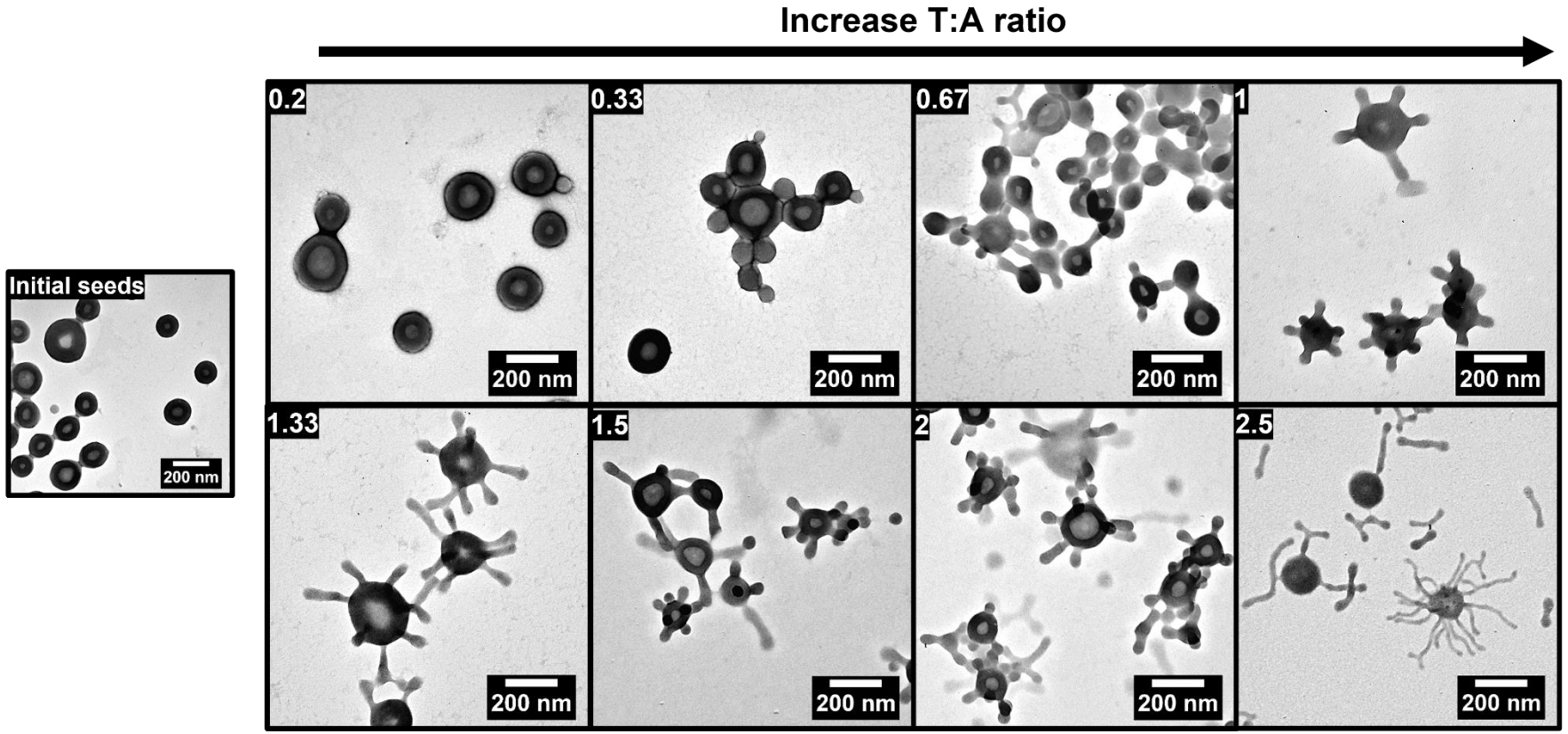


Figure 4.7. Particles with different morphologies were prepared through mixing complementary **$PT_{20}n$** solution into the initial spherical micelle **PA1n** under stirring at room temperature. Dry-state TEM images **PA1n** after adding **$PT_{20}n$** with variable molar ratios of T:A: 0.2, 0.33, 0.67, 1.00, 1.33, 1.5, 2 and 2.5.

CryoTEM was used to confirm that the nodes were attached to the surface of the particles (Figure 4.8). At molar ratio T:A =1, the nodes are connecting to the membrane with an area that appears narrower that the node itself, similar to a neck. This neck region corresponds to the insertion point of the complementary polymer **$PT_{20}n$**. At ratio T:A = 1.33, this neck region is observed as well, with an elongation of the nodes. As the T:A increases to 2 and 2.5, cryoTEM analysis show that the nodes became longer and thinner (Figure 4.8 and Table 4.10 in Annex).

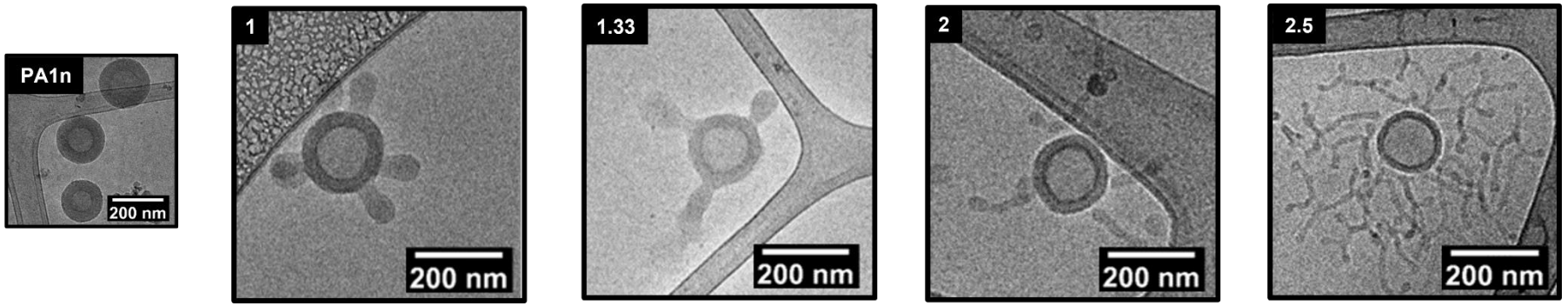


Figure 4.8. CryoTEM images of nanoparticles **PA1n** before and after adding **PT$_{20}$n** with variable molar ratios of **T:A** 1.00, 1.33, 2 and 2.5.

Here the particles are too big to go under a universal transformation and undergo instead is a local deformation instead with the addition of the complementary polymer into **PA1n** solution.[36-37] These observations point to a two-step mechanism. First, the nucleation of nodes on the surface of **PA1n** caused by the complementary H-bonding as this is more energetically favorable until nucleation sites are depleted. Next the nodes grow in length due to less favorable thymine-thymine interactions. The apparent size of the **PA1n** vesicles did not change with the addition of **PT$_{20}$n** according to DLS analysis suggesting that **PT$_{20}$n** only grew on the surface (See Figures 4.10C, table 4.3 and Figure 4.28 in annex).

Table 4.3. DLS results of the mixing experiments of PA1n with **PT$_{20}$n** at different ratios of T:A.

Ratios	D_h (nm)	PD
0.2	191 ± 4	0.02 ± 0.01
0.33	186 ± 2	0.07 ± 0.03
0.67	192 ± 5	0.02 ± 0.02
1	233 ± 4	0.04 ± 0.03
1.33	167 ± 1	0.16 ± 0.01
1.5	220 ± 4	0.06 ± 0.02
2	173 ± 4	0.12 ± 0.01
2.5	186 ± 3	0.16 ± 0.01

To further understand the morphological transformation observed by TEM, quantitative analysis measurements were performed. From ratio T:A = 0.2 to 0.67, the number of vesicles with nodes increases (Figure 4.9 and Table 4.28 in the annex). From ratios T:A = 1 to 2, the particles have an average of 5 nodes. At molar ratio T:A = 2.5, a loss of control over the number of nodes per particles was observed, with a broad dispersity and some vesicles with no nodes (Figure 4.9, T:A ratios = 2.5).

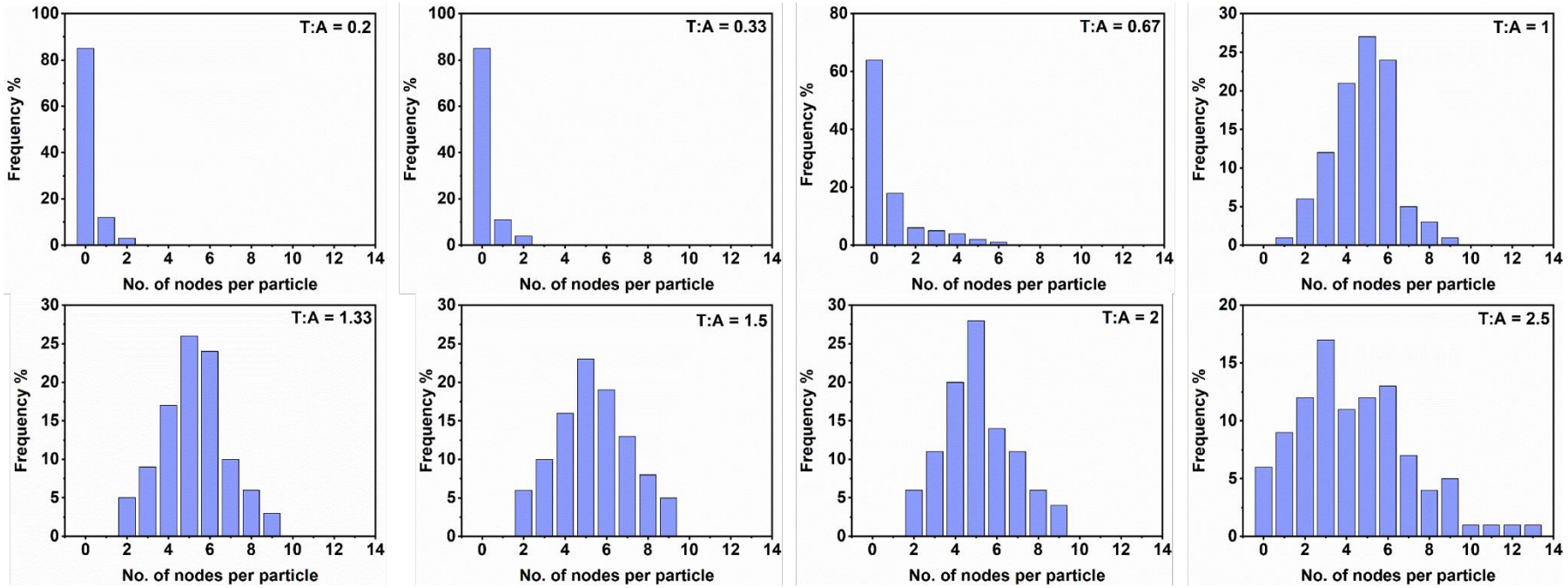


Figure 4.9. Number of nodes per **PA1n** particles at T:A ratios of 0.2, 0.33, 0.67, 1, 1.33, 1.5, 2 and 2.5. 100 particles were analysed for each T:A ratio.

Further quantitative analysis was undertaken (Figure 4.10). The size of the particles at different ratios was measured by DLS and TEM (Figure 4.10A). The size stayed the same for different ratios as showed by DLS and TEM, from 173 ± 4 nm to 233 ± 4 nm by DLS and 153 ± 32 nm to 214 ± 43 nm by TEM. This analysis also shows that the insertion of **$PT_{20}n$** at any molar ratios has no measurable effect on the membrane thickness of the **PA1n** vesicles (Figure 4.10B). Membrane thicknesses were measured to be the same within error, from 37 ± 3 nm to 40 ± 5 nm depending on the molar ratio, against 42 ± 2.5 nm for the **PA1n** vesicles. An increase of nodes per particle was observed with an increase in the molar ratio (Figure 10C). From T:A ratio 0.2 to 0.67 the average number of nodes is relatively low (from 0.18, 0.24 and 0.77 nodes/particle), then there is a rapid increase in the average number of nodes (4.86) at ratio T:A = 1. The maximum is reached at 1.33, with an average of 5.44 nodes per particle. The average number of nodes/particle starts to decrease from 5.41 to 5.1 and finally 4.31 for the molar ratios 1.5, 2 and 2.5 respectively. From a molar ratio 0.2 to 1 the length of the nodes is constant (Figure 4.10A), with a length variation from 72 ± 10 nm to 73 ± 14 nm. At molar ratio 1.33, the length increases slightly to 76 ± 34 nm. Then, the length of the nodes starts to increase rapidly from 99 ± 35 nm for molar ratio 1.5, 111 ± 40 nm at molar ratio 2 to 173 ± 54 nm at molar ratio 2.5. These quantitative results corroborate with the TEM results (Figure 4.7), showing that nucleation occurs until there are no more sites, then growth occurs, showing a two-step-controlled mechanism.

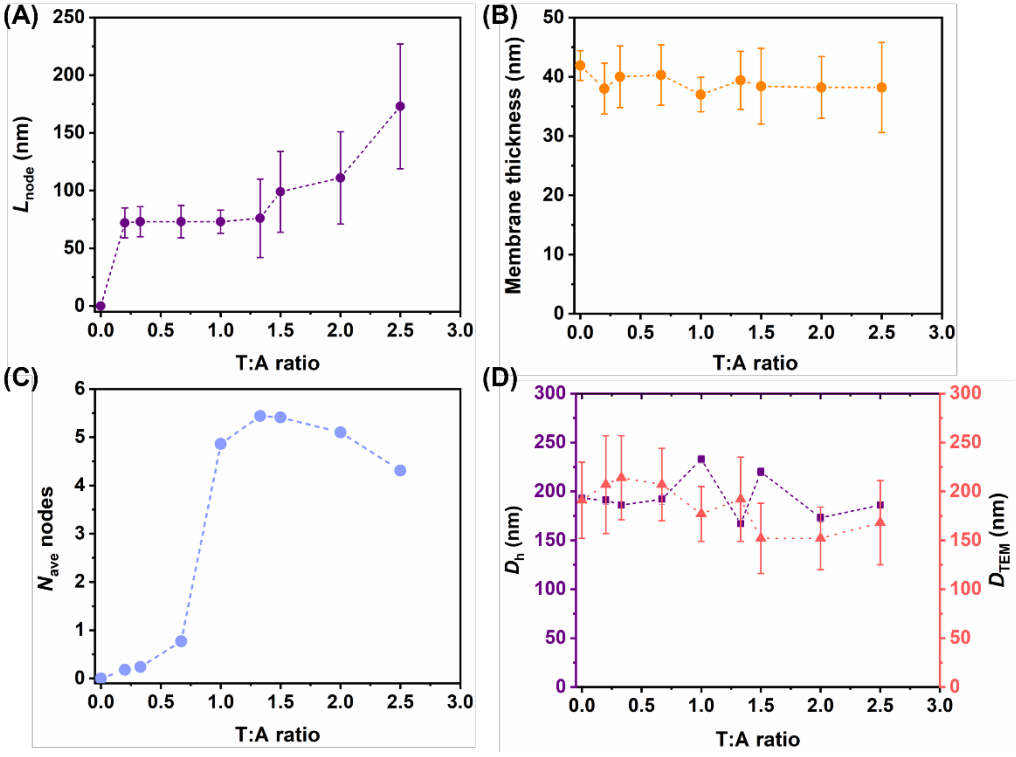


Figure 4.10. Quantitative analysis of the particles obtained at different T:A ratios. (A) Size obtained by DLS versus TEM, (B) Membrane thicknesses of **PA1n**, (C) number of nodes per particles and (D) length of the nodes per particles at different molar ratios, respectively. Particle counting and measurement were done over 100 particles for each parameter. The error bars represent the standard deviation.

4.3.2.2. Co-assembly of nano-objects using big vesicles PA2n

In this section, the co-assembly was studied analogously using particles **PA2n**. **PA2n** solution has been mixed with **PT$_{20}$n** at different T:A ratios to perform. TEM analysis (Figure 4.11) revealed that a similar mechanism of co-assembly was operating. Larger worm-vesicle grafts particles were observed with more nodes on the surface of the particles. A similar two-step mechanism is occurring as well with **PA2n** particles.

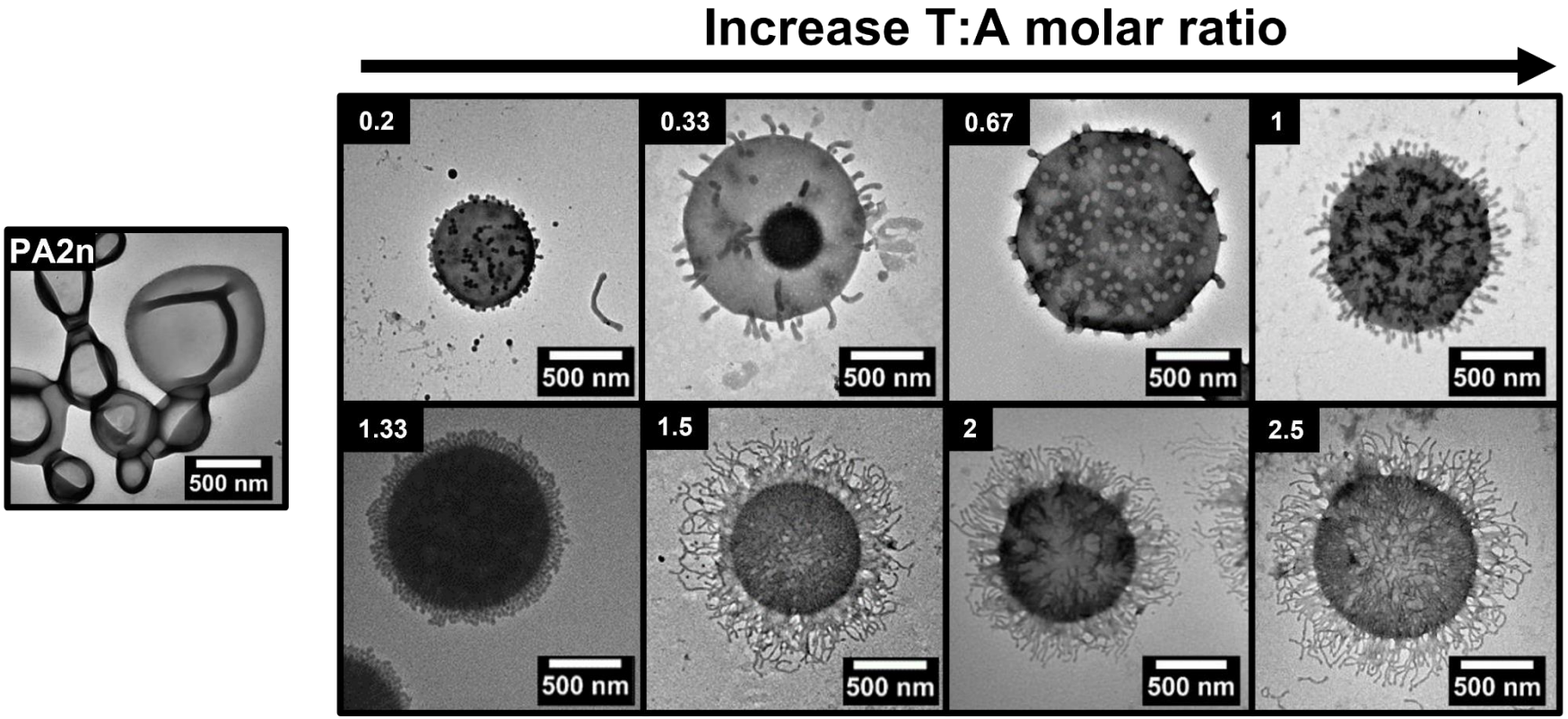


Figure 4.11. Dry-state TEM images **PA2n** after adding **$PT_{20}n$** with variable molar ratios of T:A 0.2, 0.33, 1.00, 1.33, 2 and 2.5.

CryoTEM was used again to confirm the new obtained morphologies (Figure 4.12). Ratio T:A = 1 shows particles with a dot pattern and as the molar ratios increases, it evolves to long worms. In contrast with **PA1n**, the cryoTEM imaging shows that the nodes remain attached to the particles even at high molar ratio.

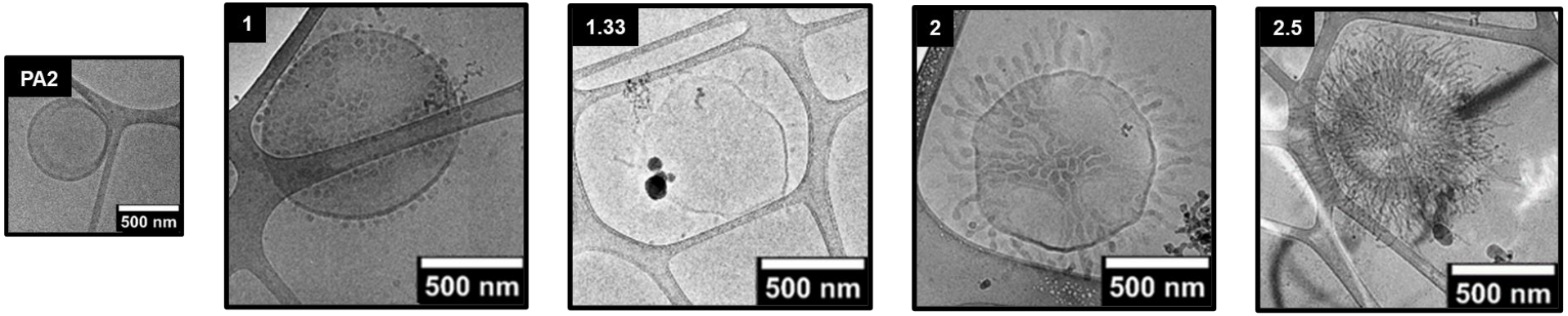


Figure 4.12. CryoTEM images of **PA2n** after adding **PT_{20}n** with variable molar ratios of T:A 1.00, 1.33 and 2.

The particles size at different molar ratios was measured either by DLS or TEM (Figure 3.14A and B). The sizes obtained by TEM vary from 833 ± 214 to 924 ± 254 nm depending on the molar ratio (red dots on Figure 4.13), against 816 ± nm 246 nm for the initial vesicles **PA2n**. While by DLS the size varies 441 ± 10 nm to 692 ± 22 nm (Purple dots on Figure 4.13) due to the presence of **PT$_{20}$n** in solution. The average sizes obtained by DLS were misleading and were not showing the average diameters of **PA2n**.They were then re-analyzed and the diameters of the "larger peaks" was added as an additional series of data as shown on Figure 4.13 (green dots). Quantitative analysis show the same trend as for the small particles, the length of the nodes increases with the molar ratio (Figure 4.13B, Fgure 4.29 and Table 4.11 in annex) . Starting from 39 ± 6 nm at ratio T:A = 0.2, 79 ± 11 nm for 0.33, then 102 ± 23 nm for molar ratio 1. And finally 174 ± 90 nm, 325 ± 103nm and 355 ± 81 nm for molar ratios 1.33, 2 and 2.5 respetively.

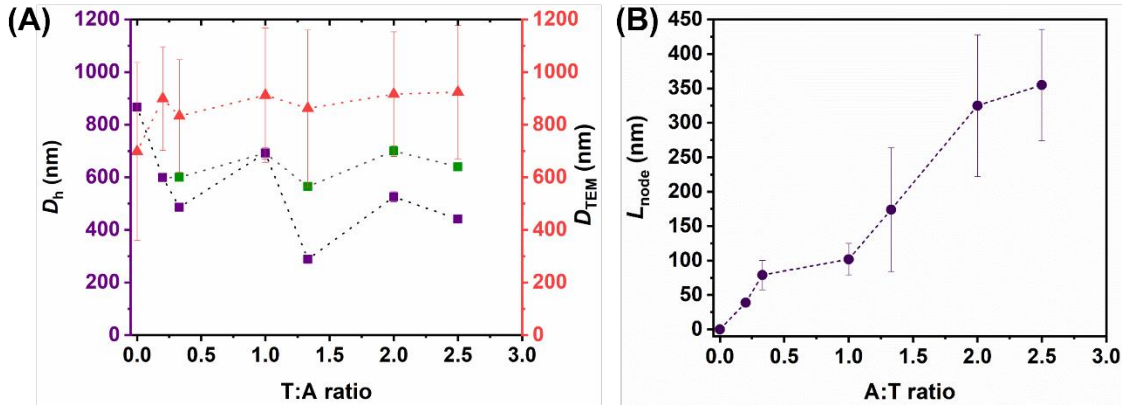


Figure 4.13. (A) Size obtained by DLS versus TEM per particle at different molar ratios (B) Length of the nodes per particle at different molar ratios. Particle counting and measurement were done over 100 particles for each parameter. The error bars represent the standard deviation.

4.2.3 Insertion mechanism

4.2.3.1 Control experiments

4.2.3.1.1 Addition of non-complementary block copolymers to a PA1n seed solution

DNA or RNA nucleobases interact in a complementary manner *via* non-covalent H-bonding. Based on this concept, we hypothesized that the driving force for the co-assembly of **PA1n** and **PA2n** with **PT$_{20}$n** is greater with complementary nucleobases and would assemble more weakly with block copolymer bearing the same nucleobase. In order to confirm that strong H-bonding between A and T was necessary to drive the morphological transformation process, a series of control experiments was performed using polymers in which H-bonding was either partially blocked or non-complementary but with a strong H-bonding self-complementarity. Firstly, two polymers were synthesized: a methylated thymine-containing short polymer (where H-bonding has been removed) PNAM$_{40}$-*b*-PTMAm$_{20}$ (**PT$^{Me}_{20}$**) (Experimental section, Figures 4.19 and 4.20) and a non-complementary short adenine-containing polymer,PNAM$_{40}$-*b*-PAAm$_{20}$ (**PA$_{20}$**). (Chapter 2 and Table 4.8 and Figure 4.22 and 4.23, Experimental section). **PT$^{Me}_{20}$n** and **PA$_{20}$n** solutions were then mixed with separate solutions of **PA1n** at a molar ratio A:A and T^{Me}:A of 1, and the resulting nanoparticles analysed by DLS and TEM (Figure 4.14). In no case was a morphological transformation observed. Instead, the initial vesicles kept the same shape after addition of the non-complementary copolymers confirming that the process was driven by the formation of strong complementary H-bonding interactions as opposed to weaker hydrophobic effects. DLS and TEM analysis (Figure 4.15 and Table 4.4) showed no significant changes in the hydrodynamic diameters of the nanoparticles,

and TEM analyses showed no noticeable changes in morphology. A mixture of vesicles **PA1n** and small aggregates formed by **PA$_{20}$n** in water were found when **PA1n** and **PA$_{20}$n** were mixed (Figure 4.14B). In contrast, **PT$^{Me}_{20}$n** could not be imaged under TEM, suggesting it stayed in solution instead of self-assembled. The absence of any polymer insertion into the polymersome membrane driven solely by the hydrophobic effect implies that H-bonding is the driving force for polymer insertion.

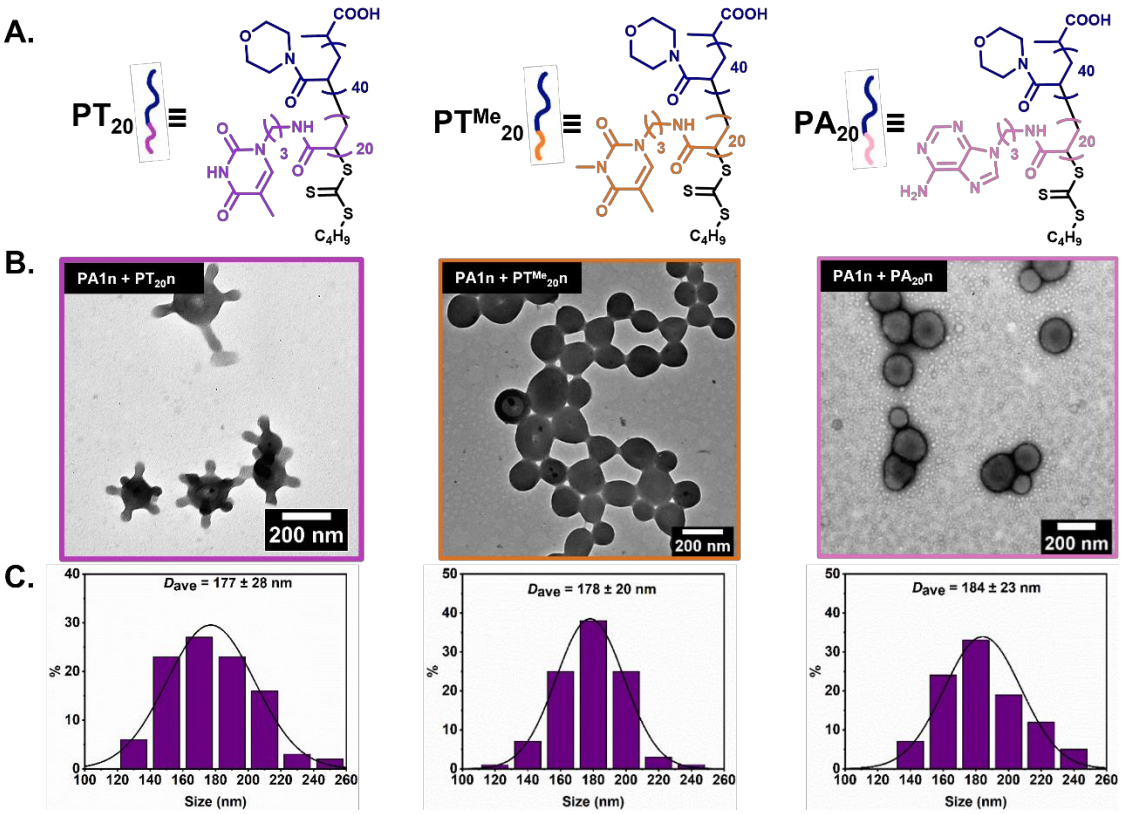


Figure 4.14. Control experiments. Dry state TEM images of the addition of short block copolymers with either partially blocked (**PT$^{Me}_{20}$n**) or non-complementary H-bonding (**PA$_{20}$n**) onto **PA1n** vesicles. Dry-state samples were stained using 1% w/w uranyl acetate (UA) solution.

The corresponding DLS results and TEM analysis on Figure 4.15, show a monomodal distribution for the mixing of **PA1n** with the non-complementary short adenine block copolymer (**PA$_{20}$n),** with D_h = 179 ± 1 nm and a dispersity of 0.02 ± 0.01, and a D_{ave} = 178 ± 20 nm, since the added polymers only formed small aggregates and scattering less

light compared to **PA1n** solution, leading to no obvious size change. Similar results were obtained as well for the mixing of **PA1n** using **PT$^{Me}_{20}$n** particles, with a D_h of 194 ± 3 nm and a dispersity of 0.02 ± 0.01, and a D_{ave} = 184 ± 23 nm.

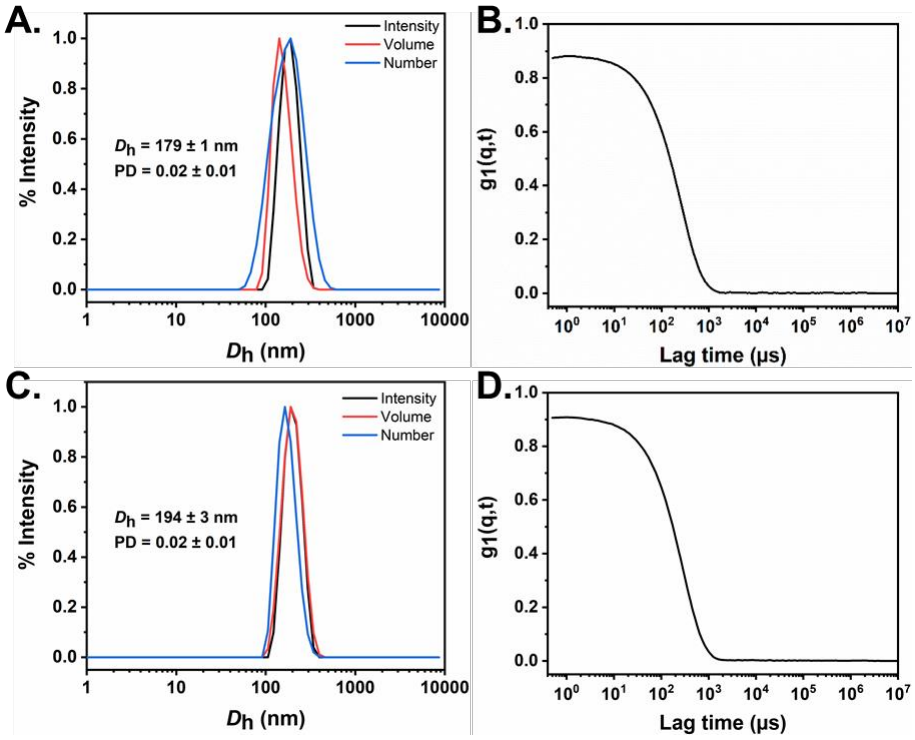


Figure 4.15. (A) and (C) combined DLS and corresponding correlogram graph (B) and (D) results of mixing experiments of **PA1n** with a short adenine-containing block copolymer **PA$_{20}$n** or a methylated short thymine-containing block **PT$^{Me}_{20}$n** respectively.

Table 4.4. Summary of DLS and TEM characterization data of control experiments.

Particles	D_h (nm)[a]	PD[a]	D_{ave} (nm)[b]	Morphology[c]	Comments
PA1n + PA$_{20}$n	179 ± 1	0.02 ± 0.01	178 ± 20	V	No change in morphology
PA1n + PT$^{Me}_{20}$n	194 ± 3	0.02 ± 0.01	184 ± 23	V	No change in morphology

[a]D_h and PD values measured from DLS analysis (the error shows the standard deviation from 3 repeat measurements).[b]D_{ave} values obtained from TEM analysis (size measured over at 100 particles using image J. [c]Morphologies observed from dry-state TEM imaging, using 1% w/w uranyl acetate (UA) solution for staining (Key: V – vesicles).

4.2.3.1.2 Sequential addition of $PT_{20}n$ and $PT^{Me}_{20}n$ into a PA1n seed solution

In order to understand the driving force for the elongation of the nodes on the surface of the particles, we performed another series of control experiments. A sequential addition of either complementary (**$PT_{20}n$)** or partially blocked H-bonding (**$PT^{Me}_{20}n$)** short block copolymers into **PA1n** was performed in order to assess if H-bonding was needed to observe the growth of the nodes. We started first by mixing **PA1n** with **$PT_{20}n$** at a molar ratio of 1 for 2h in two different vials and then added either **$PT_{20}n$** or **$PT^{Me}_{20}n$** to reach a molar ratio of 1.33. The resulting nanoparticles were then analysed by DLS and TEM (Figure 4.16 and Table 4.5). When we performed the sequential addition of **$PT_{20}n$** into **PA1n**, similar particles were obtained with elongated worms with a length of L_{node} = 104 ± 27 nm with the presence of small **$PT_{20}n$** particles. The second addition of (**$PT^{Me}_{20}n$**), didn't lead to elongated worms and small **$PT^{Me}_{20}n$** particles were not observed under TEM, suggesting they stayed in solution. Instead, the particles remained with the same morphology as for T:A molar ratio = 1, with a L_{node} = 72 ± 11 nm (Figure 4.16). The addition of **$PT^{Me}_{20}n$** didn't lead to the growth of the nodes on the particles, suggesting that H-bonding is required to drive the elongation of the nodes.

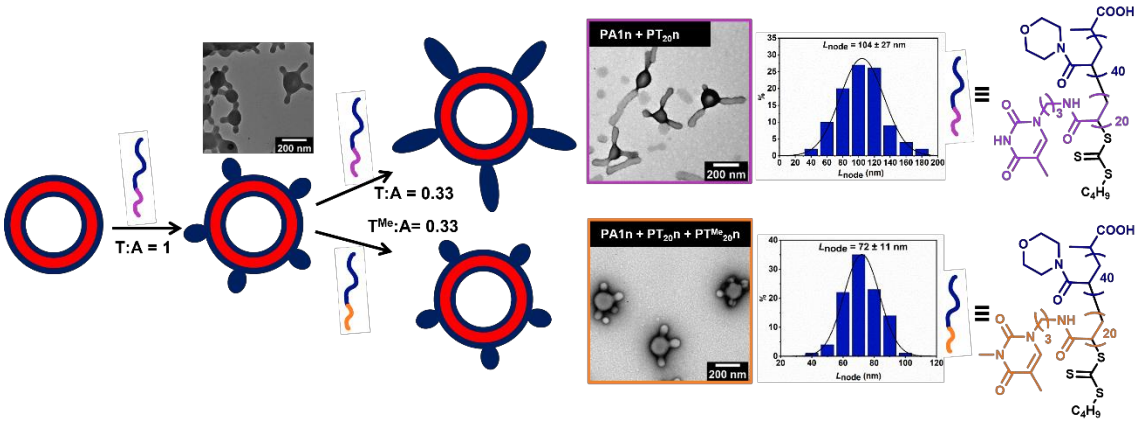


Figure 4.16. Control experiments. Dry state TEM images representing the sequential addition of **PT$_{20}$n** in **PA1n** solution (top) and 1 **PT$_{20}$n** + 0.33 **PT$^{Me}_{20}$n** in **PA1n** solutions (bottom). Dry-state samples were stained using 1% w/w uranyl acetate (UA) solution. Histogram representing the length of the nodes (length measured over at 100 particles using image J).

Table 4.5. Summary of DLS and TEM characterization data of control experiments.

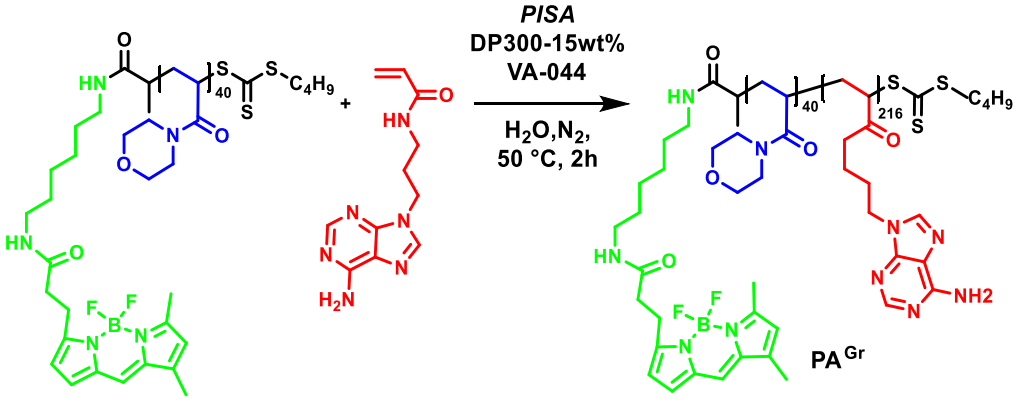
Particles	D_h (nm)[a]	PD[a]	D_{ave} (nm)[b]	L_{nodes} (nm)[b]	Morphology[c]
PA1n + 1PT$_{20}$n + 0.33PT$_{20}$n	174 ± 2	0.09 ± 0.1	181 ± 25	104 ± 27	Elongated nodes
PA1n + 1PT$_{20}$n + 0.33PT$^{Me}_{20}$n	219 ± 7	0.07 ± 0.01	185 ± 20	72 ± 11	No elongated nodes

[a]D_h and PD values measured from DLS analysis (the error shows the standard deviation from 3 repeat measurements).[b]D_{ave} values obtained from TEM analysis (size measured over at 100 particles using image J). [c]Morphologies observed from dry-state TEM imaging, using 1% w/w uranyl acetate (UA) solution for staining (Key: V – vesicles).

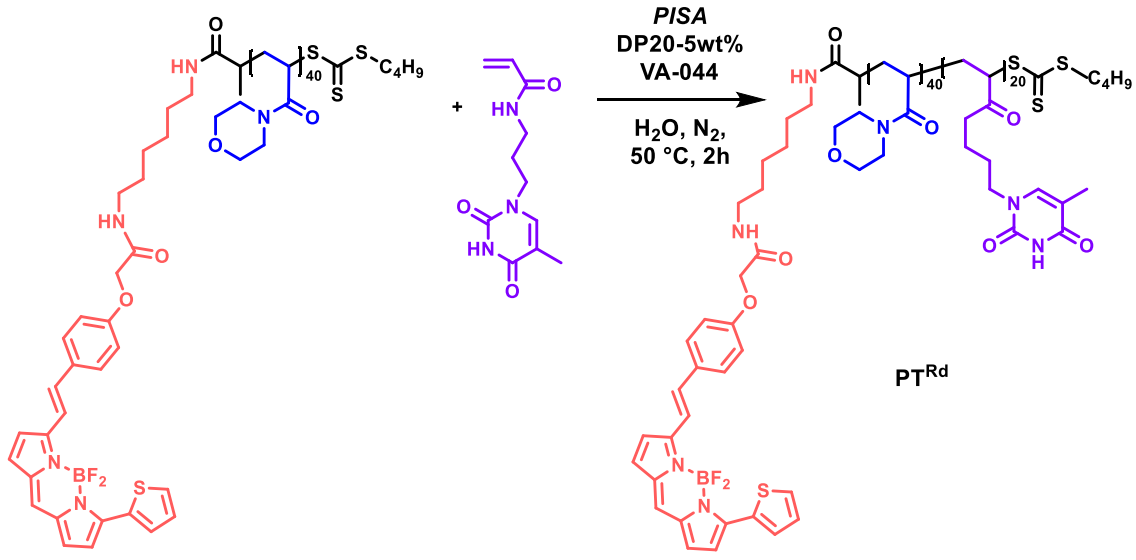
4.2.3.2 Following one insertion mechanism *via* confocal imaging

4,4-Difluoro-4-bora-3a,4a-diaza-s-indacene dyes (also known as boron dipyrromethenes, or BODIPYs) are versatile compounds with highly tuneable structures that allow the modulation of their solubility and spectroscopic properties,[38-39] making them suitable for various applications, including in fluorescence imaging.[40] To further demonstrate that requires complementary nucleobase interactions, **PA2** and **PT$_{20}$** were derivatised with two different dyes—BODIPY-FL (**PA1^{Gr}** and **PA2^{Gr}**) and -TR (**PTRd**) respectively.

PA2n was used in this study since the particles are large enough (D_h = 837 ± 16 nm) for good optical resolution in the confocal study. The two different macroCTA were prepared, see experimental section for synthesis and characterization (Experimental section, schemes 4.6 and 4.7, Figure 4.26 and table 4.29). RAFT-mediated PISA was then used to synthesis the corresponding modified, **PA2^{Gr}n** and **PTRdn** particles (Scheme 4.3 and 4.4).



Scheme 4.3. Synthesis of **PA^{Gr}** diblock copolymer nano-objects by aqueous RAFT-mediated polymerization-induced self-assembly (PISA).



Scheme 4.4. Synthesis of **PTRd** diblock copolymer nano-objects by aqueous RAFT-mediated polymerization-induced self-assembly (PISA).

SEC analysis shows similar results with the modified macroCTA (Figure 4.17 and table 4.6). A conversion > 99% was achieved for **PTRd** and a conversion of > 70% for **PA2^{Gr}**. A higher conversion for **PA2^{Gr}** couldn't be obtained, similar as for **PA2**. Similar *M*n values were obtained for the modified polymers with a M_n of 13.8 kDa for **PTRd** and 62.1 kDa for **PA2^{Gr}**.

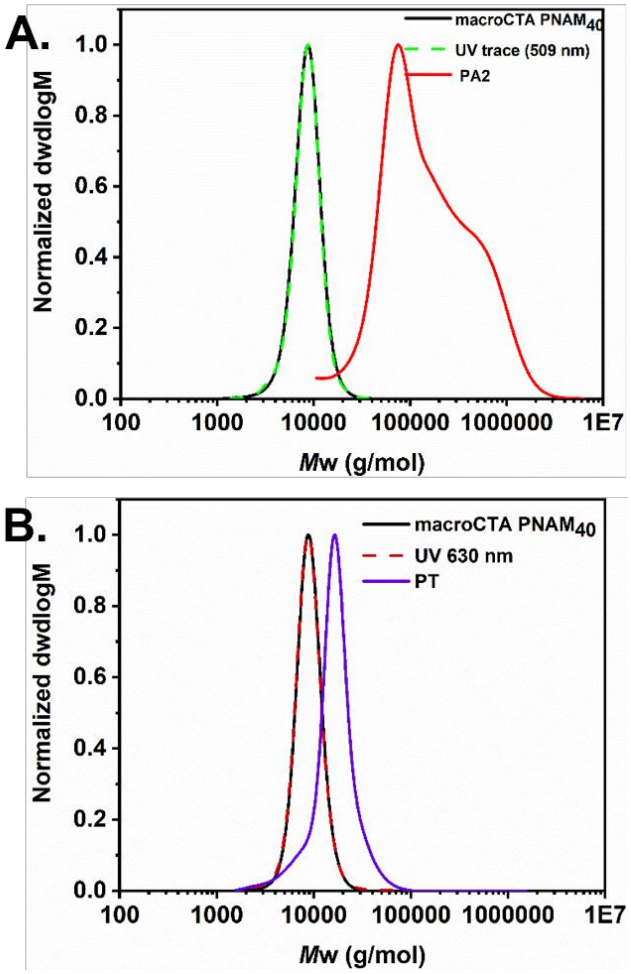


Figure 4.17. (A) Combined SEC traces of $PNAM_{40}$ macroCTA^{Gr} and **PA2^{Gr}** and (B) combined SEC traces of $PNAM_{40}$ macroCTARd and **PTRd** (DMSO + 0.1% w/w LiBr as eluent, PMMA standards).

Table 4.6. Characterization data of $PNAM_{40}$ macroCTA, **PA2** and $\mathbf{PT_{20}}$ modified block copolymers obtained *via* aqueous RAFT-mediated PISA.

Polymers	Structure	% Conv.[a]	$M_{n,NMR}$[b] /kDa	$M_{n,SEC}$[c] /kDa	$Đ_{M,SEC}$[c]
mCTA	$PNAM_{40}$	> 99	5.6	7.6	1.11
mCTARd	$PNAM_{40}^{Rd}$	> 99	5.6	8.4	1.10
mCTA^{Gr}	$PNAM_{40}^{Gr}$	> 99	5.6	7.9	1.13
PT$^{Rd}_{20}$	$PNAM_{40}$-*b*-$PTAm_{20}^{Rd}$	> 99	10.3	13.8	1.30
PA2^{Gr}	$PNAM_{40}$-*b*-$PAAm_{210}^{Gr}$	>70	60.1	62.1	3.68

[a]Monomer conversion calculated from ^{1}H-NMR spectroscopy in DMSO-d_6 (400 MHz). [b]Calculated from conversion. [c]M_n and $Đ_M$ values calculated from DMSO + 0.1% w/w LiBr as the eluent with PMMA standards.

The particles were then characterized by TEM and DLS (Figure 4.27 in Experimental section and Table 4.7). Results show that similar particles were obtained with the modified macroCTAs. Similar particles were obtained, suggested that the dye conjugation of the macroCTAs had little effect on the polymers and particles **PA2^{Gr}** and **PT$^{Rd}_{20}$**.

Table 4.7. Summary of DLS and TEM characterization data of **PT$^{Rd}_{20}$n** and **PA2^{Gr}n** block copolymer nano-objects obtained by aqueous RAFT-mediated PISA

Particles	D_h (nm)[a]	PD[a]	D_{ave} (nm)[b]	Morphology[C]
PT$^{Rd}_{20}$n	24 ± 0.2	0.6 ± 0.04	-	S+W
PA2^{Gr}n	781 ± 3	0.22 ± 0.01	616 ± 216	V

[a]D_h and PD values measured from DLS analysis (the error shows the standard deviation from 3 repeat measurements). [b]D_{ave} values obtained from TEM analysis (size measured over at 100 particles using image J) and were calculated only for pure vesicle phase. [c]Morphologies observed from dry-state TEM imaging, using 1% w/w uranyl acetate (UA) solution for staining (Key: S – spheres, W – worms and V – vesicles).

To a **PA2^{Gr}n** solution, **PT$^{Rd}_{20}$n** solution was added to aim a ratio A:T = 1 to perform MORPH. The resulting particles were characterized using confocal fluorescence microscopy and TEM (Figure 4.18). As expected, **PA2^{Gr}n** gave green, fluorescent spherical particles and **PT$_{20}$n** emitted a red signal. Confocal result shows a result a colocalization of the dyes where the green spherical particles with the red channel become completely red. Control over MORPHed vesicles was retained, as evidenced by TEM images.

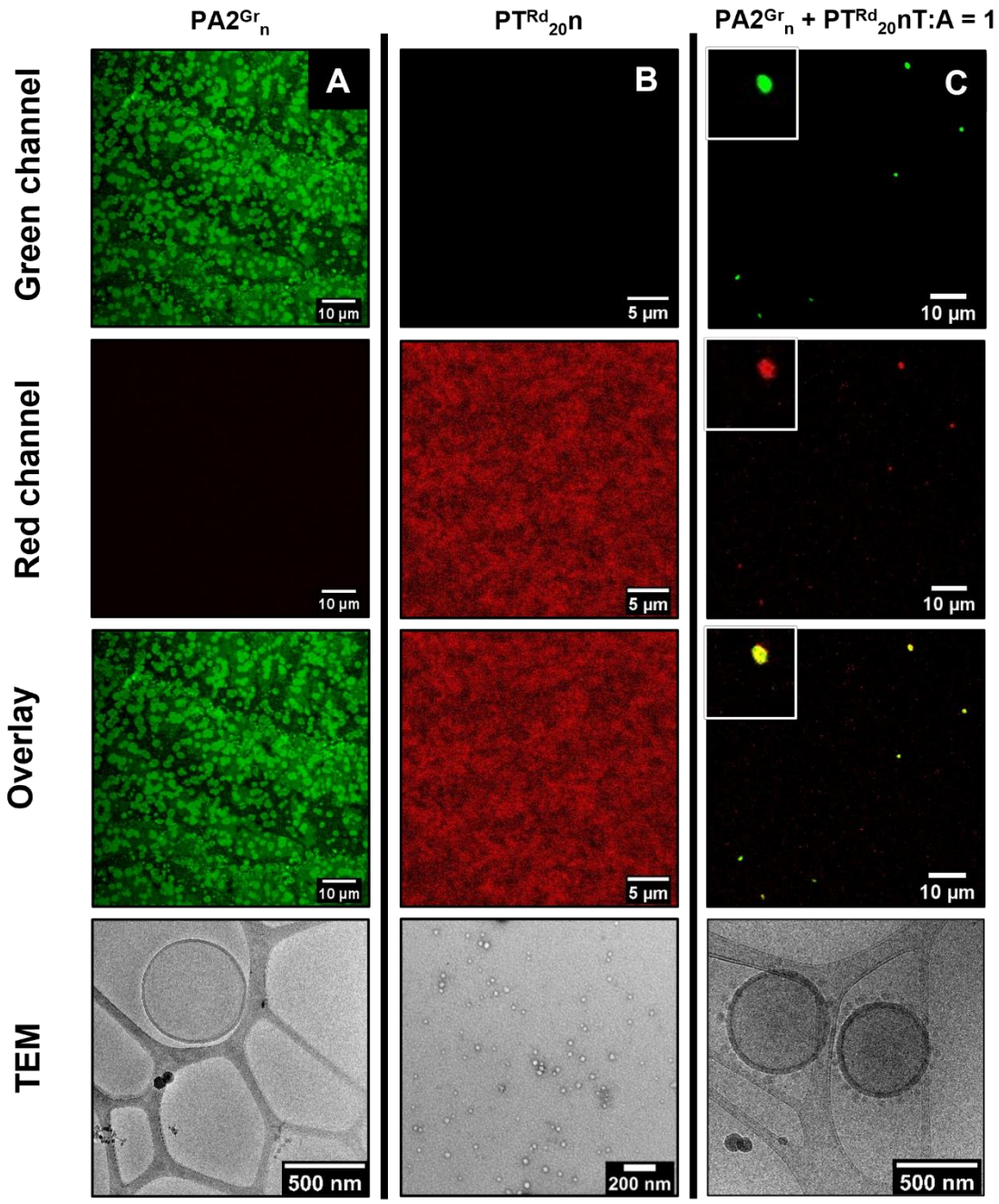


Figure 4.18. Representative confocal microscopy images for pure **PA2n** (green; A) and **PT$_{20}$n** (red; B) diblock copolymer nano-objects and resulting samples for investigation of mixing of **PA2n** and **PT$_{20}$n** at molar ratio T:A = 1. The scale bars are indicated in the images and the size of the insets is 10µm×10µm. Bottom row represents the cryo-TEM images (**PA2^{Gr}** and **PA2^{Gr}** + **PT$^{Rd}_{20}$**) and dry state (**PT$^{Rd}_{20}$**) of the corresponding experiments. Dry-state samples were stained using 1% w/w uranyl acetate (UA) solution.

Herein, MORPH operates differently from the previous study — as illustrated in Figures 4.7 and 4.11, with an apparition of nodes on the vesicles surface, whereas previously a global transformation and increase in worm length with a corresponding decrease in width was observed. The complementary copolymers **PT$_{20}$n** inserted homogeneously along the vesicles, as conformed by the TEM data showing even nodes distribution along the nanostructures. Contrary to a global morphological transformation, only local deformations were observed due to the higher surface area of the seed particles. Addition of further polymer led the elongation of the nodes. In this system, the process is shown as highly controlled giving worm-vesicle graft nanoparticles with well-defined dimensions determined simply by the amount of added complementary copolymer. The grafted particles retain their reactivity and remain capable of incorporating more of the complementary polymer as the nodes grow.

In this system, with higher surface area and lower curvature (from seeds particles with a size of 60 nm in the previous study, to 200 and 700 nm for **PA1n** and **PA2n** respectively), as well as stronger H-bonding interactions between adenine moieties, leads to another response of the nanoparticles to the insertion of a polymer at the core-corona interface (Figures 4.7 and 4.11). The physical model previously proposed suggested that the polymer diffused to the interface and inserted into the spherical nanoparticle core with an associated timescale τ_1, in a thin shell region due to the short core block length of the added polymer.[26] The insertion of the polymer created a steric crowding which was relieved by a rearrangement of the nanoparticles core chains, with timescale, τ_R. Since vesicles are morphologies with high surface area per unit volume and low curvature, an increase in the surface area of the nanoparticle's core-corona interface is highly disfavoured and instead, local budding will occur. The short thymine polymer will insert

into the membrane of the adenine-containing nanoparticles, the observed neck region (Figure 4.8, T:A ratio =1) showing the insertion of **$PT_{20}n$**. Once the budding is creating, insertion of additional short polymer will drive the elongation of the nodes creating worm-vesicle graft particles. The elongation process is driving by the formation of complementary H-bonding between **PAn** and **$PT_{20}n$** as shown in Figure 4.16. Addition of further polymer is not expected to drive disassembly but instead, the polymers will grow onto the nodes and a small part will stay in solution (Figures 4.7 and 4.11, for T:A ratios above 1.33).

4.3 Conclusions

The work presented here shows that the morphological transformation (MORPH) process operates when using vesicle-based seed and hence can be seen as generalised phenomena. A two-step mechanism, from the growth of nodes driven by complementary H-bonding interaction to the elongation driven by non-complementary H-bonding after saturation of the complementary ones. Adenine-containing vesicle seed particles were obtained by aqueous RAFT-mediated PISA. By mixing these nanoparticles (**PA1n** and **PA2n**) with the complementary thymine block copolymers (**$PT_{20}n$**), it was possible to use the MORPH process to obtain new morphologies. The effect of different molar ratios on the morphologies lead to worm-vesicles grafts particles and a control over the number and length of the nodes could be obtained as well. Using high DP polymers generated by PISA could help in testing the generality of MORPH by reversing the positions of A and T. The growing particles retain their reactivity and remain capable of incorporating more of the complementary polymer as they grow. As a result, node length scales approximately linearly with the amount of added copolymer, allowing specific particle dimensions to be targeted.

This new method shows a great potential for a better understanding of the MORPH mechanism itself and polymer self-assembly in general. These preliminary results also suggest that morphologies that are more complex could be obtained by exploiting nucleobase H-bonding.

4.4 Experimental section

4.4.1 Materials

2, 2'-Azobis(isobutyronitrile) (AIBN) was obtained from Molekula and recrystallized from methanol. 2,2'-Azobis[2-(2-imidazolin-2-yl)propane]di-hydrochloride (VA-044) was purchased from Wako and was used without further purification. Adenine, sodium hydride (60% dispersion in mineral oil), acryloyl chloride, pyridine and 4-Acryloylmorpholine (NAM) was purchased from Sigma-Aldrich and was purified by vacuum distillation. BDP FL amine and BDP 630/650 were purchased from Lumiprobe. Triethylamine was received from Fisher Scientific and used without any purification. Dialysis membrane (MWCO = 3.5 kDa) were purchased from Spectra/Por. DMF, DMSO and other chemicals were obtained from Fisher Scientific and used without further purification. Dry solvents (DMF and dioxane) were obtained by passing over a column of activated alumina using an Innovative Technologies solvent purification system.

4.4.2 Instrumentations and analysis

A list of instrumentations can be found in Chapter 2, section 2.5.

4.4.3 Synthetic methods

Synthesis of N-(3-bromopropyl)acrylamide

N-(3-Bromopropyl) acrylamide was synthesized using procedures similar to the previous literature.[41] Description of the protocol can be found in the experimental section of Chapter 2.

Synthesis of 3-(adenine-9-yl) propyl acrylamide (AAm)

The **AAm** monomer was synthesized according to our previous work[41]. Description of the protocol can be found in the experimental section of Chapter 2.

Synthesis of 3-(thymin-1-yl)propyl acrylamide (TAm)

The **TAm** monomer was synthesized as reported previously.[26] Description of the protocol can be found in the experimental section of Chapter 2.

Synthesis of 3-(3-methylthymin-1-yl)-propylacrylamide (T^{Me}Am)

The T^{Me}Am was synthesized as reported previously.[26] A mixture of 3-(thymin-1-yl)-propylacrylamide (TAm) (71 mg, 0.3 mmol), dry K2CO3 (66 mg, 0.48 mmol), and iodomethane (75 μL) in anhydrous DMF (0.4 mL) was stirred at room temperature for 24 h and then diluted with ethyl acetate (20 mL), washed with water (2 × 20 mL), and dried with anhydrous Na2SO4. The solvent was removed under vacuum. The mixture was further purified by column chromatography with a mixture of CH2Cl2/CH3OH (95:5) to give a white solid, TMeAm (73 mg, 0.29 mmol, 97%). ^{1}H NMR (500 MHz, DMSO-d_6) δ = 8.12 (t, J = 5.0 Hz, CONH), 7.59 (s, 1H, pyrimidine-H6), 6.18 (dd, J = 17.5, 10.5 Hz, 1H, CH2-CH−CO), 6.07 (dd, J = 17.5, 2.0 Hz, 1H, CH- CH−CO), 5.58 (dd, J = 10.5, 2.0 Hz, 1H, CH-CH−CO), 3.70 (t, 2H, J = 7.5 Hz, CH2-pyrimidine), 3.17 (s, 3H, OC−NCH3), 3.14 (m, 2H, OC−HN−CH2), 1.80 (s, 3H, CH3-pyrimidine), 1.76 (m, 2H, OC−NH−CH2−CH2−CH2-pyrimidine) ppm. ^{13}C NMR (125 MHz, DMSO-d_6) δ = 165.1, 163.8, 151.5, 140.4, 132.2, 125.5, 107.9, 47.1, 36.3, 29.0, 28.0, 13.1 ppm; HR-MS (m/z) found 274.1165, calcd 274.1162 [M + Na]+.

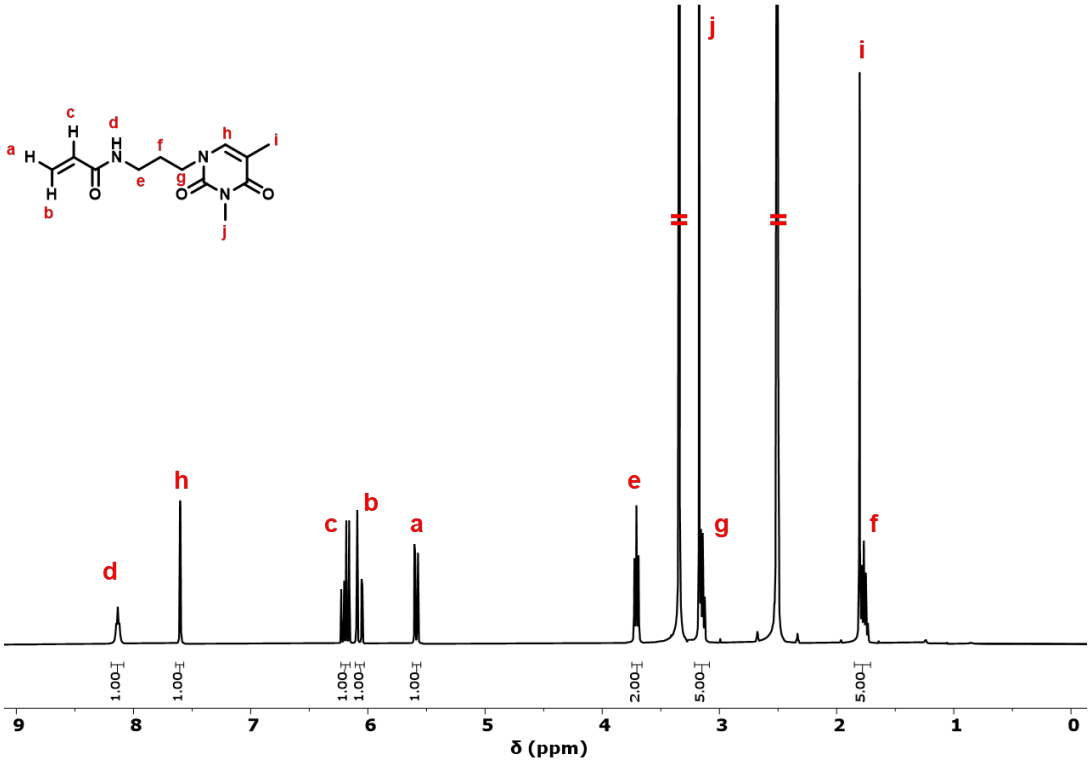


Figure 4.19. ^{1}H NMR spectrum of 3-(3-methylthymin-1-yl)-propylacrylamide ($T^{Me}Am$) in DMSO-d_6 (400 MHz).

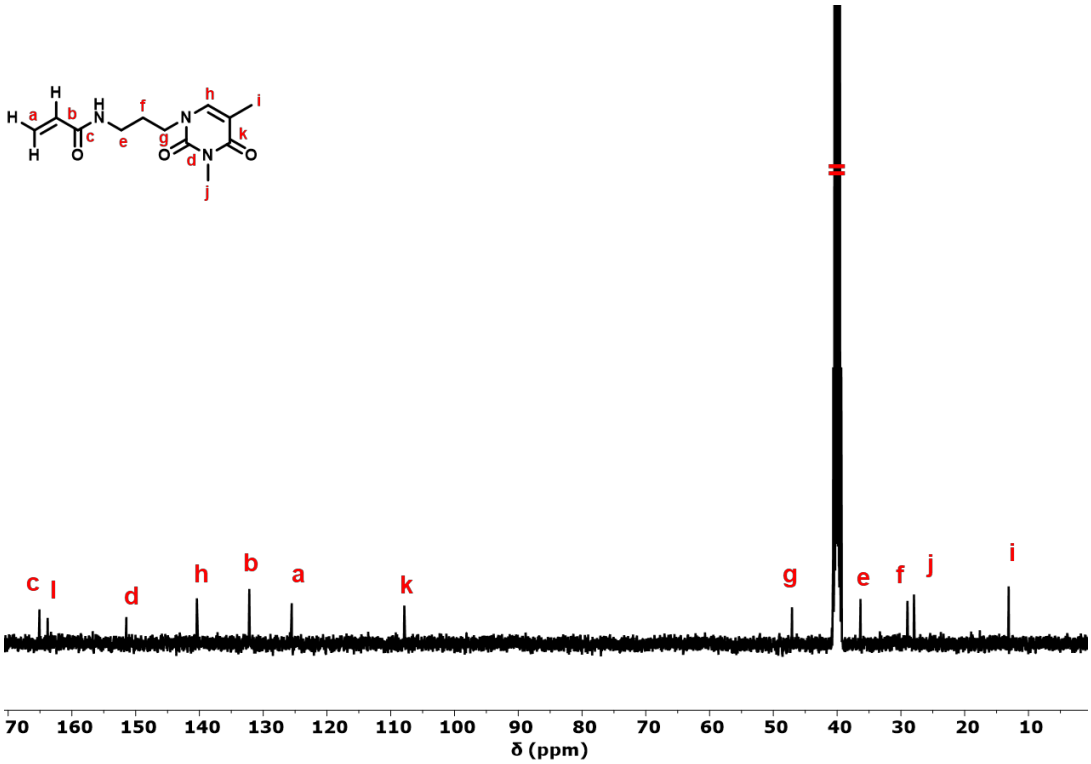
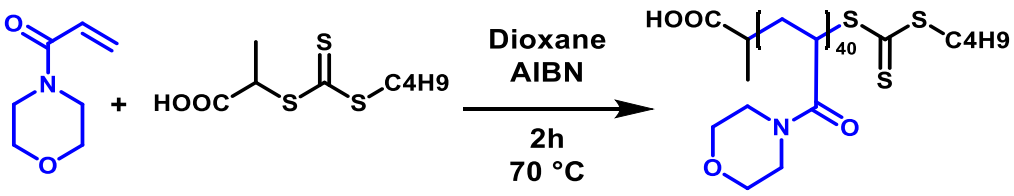


Figure 4.20. ^{13}C NMR spectrum of 3-(3-methylthymin-1-yl)-propylacrylamide (T^{Me}Am) in DMSO-d_6 (500 MHz).

Synthesis of 2-(((butylthio)carbonothiolyl)thio)propanoic acid (CTA)

The procedure was adapted from a previous work[42]. Full description of the protocol and characterization can be found in the experimental in Chapter 2.



Scheme 4.5. Synthesis of poly(4-acryolylmorpholine)$_{40}$ (PNAM$_{40}$) macro-CTA.

Synthesis of $PNAM_{40}$ macro-CTA *via* RAFT polymerization

The procedure was adapted from our previous work[41]. A full description of the protocol and characterization of the compound can be found in the experiment section in Chapter 2.

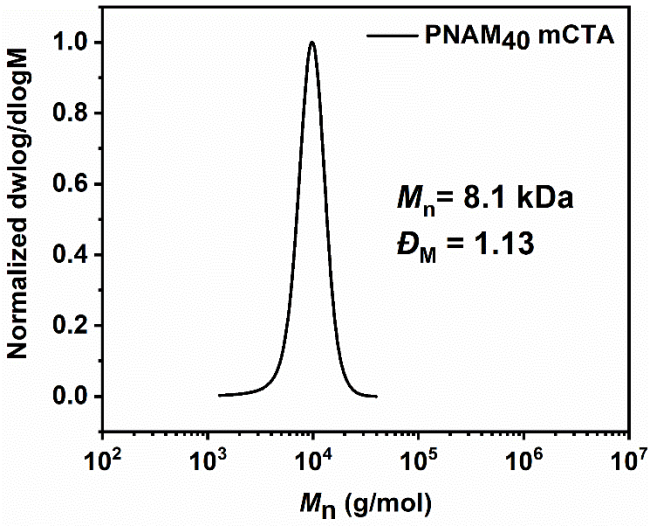


Figure 4.21. Normalized molecular weight distribution trace of $PNAM_{40}$ macro-CTA (DMSO + 0.1% w/w LiBr as eluent, PMMA standards).

Synthesis of $PNAM_{40}$-*b*-$PAAm_y$ diblock copolymer nano-objects by aqueous RAFT-mediated polymerization-induced self-assembly (PISA)

A typical synthetic procedure to achieve $PNAM_{40}$-*b*-$PAAm_{200}$ diblock copolymer vesicles at [solids] = 10% w/w *via* aqueous RAFT-mediated PISA is described. $PNAM_{40}$ macro-CTA (9 mg, 1.59×10^{-6} mol, 1 eq.), AAm (80 mg, 3.17×10^{-4} mol, 200 eq.) and VA-044 (0.10 mg, 3.17×10^{-7} mol, 0.2 eq.) (a stock solution of 2 mg of VA-044 in 1 mL of water was made prior, a volume of 51.5 μL was taken and added to the reaction mixture) were dispersed in deionized (DI) water (0.89 mL) and sealed in a 7mL vial bearing a magnetic stirrer bar. The resulting monomer-in-water solution was degassed by sparging with N_2(g) for 15 min. The sealed vial was heated at 50 °C with magnetic stirring

for 2 hours to ensure full monomer conversion. After this period, the reaction mixture was exposed to air and allowed to cool to room temperature. ^{1}H-NMR in DMSO-d_6 and SEC analyses in DMSO + 0.1% w/w LiBr of the pure diblock copolymers were performed after reaction. DLS analysis and dry-state and cryo-TEM imaging were performed on samples after dilution to an appropriate analysis concentration. ^{1}H-NMR (400 MHz, DMSO-d_6): δ (ppm) 8.09 (br s, N-C***H*****$_2$***=N of PAAm side chain*), 7.77 (br s, N***H*** of PAAm side chain), 7.25 (br s, *CH=N**H**-C* of PAAm side chain), 4.03 (br s, *CH$_2$-C**H$_2$**-N* of PAAm side chain), 3.64-3.25 (br m, *CH$_2$-C**H$_2$**-N x 2* of PNAM and NH-C***H*****$_2$**-CH$_2$ of PAAm side chain), 2.95-2.68 (br m, *CH$_2$-C**H$_2$**-CH$_2$* of PAAm and PNAM backbone), 2.20-1.27 (br m, C***H*****$_2$***-CH* of PNAM and PAAm backbone and *CH$_2$-C**H$_2$**-CH$_2$ of PAAm side chain*).

MORPH PISA: Calculations and mixing of the molar ratios of complementary nucleobase-containing block copolymers

The degree of polymerization (DP) of PNAM40-*b*-PAAm200 (**PA1**), PNAM40-*b*-PAAm216 (**PA2**) and PNAM40-*b*-PTAm20 (**PT$_{20}$**) were obtained from ^{1}H NMR spectroscopic analysis. The number-average molecular weight *M*n of the polymers can be calculated from the DP. The self-assemblies' solutions containing PNAM40-*b*-PAAm200 (**PA1**) and PNAM40-*b*-PTAm216 (**PA2**) were prepared by dilution to obtain a 0.5 mg mL^{-1} concentration. Since the mass concentration is known as *c*, thus the molar concentration can be calculated. Then, the mass *m* of PNAM96-*b*-PTAm20 (**PT$_{20}$**) with the relative molar ratios *n* were calculated according to PNAM40-*b*-PAAm200 (**PA1**) and PNAM40-*b*- PAAm216 (**PA2**) mass concentration and the volume *v* using Equation 4.1.

$$m = \frac{ncvM_{n,\mathbf{PT_{20}}}}{M_{n,\mathbf{PA1}}}$$

(Equation 4.1) Therefore, the molar ratios *R*A:T of complementary nucleobases A and T can also be calculated using the DPs of the AAm and TAm blocks as follows:

$$R_{\mathrm{A:T}} = n\frac{\mathrm{DP(T)_{PT_{20}}}}{\mathrm{DP(A)_{PA1}}}$$

(Equation 4.2) Where DP(T)**PT$_{20}$** is the degree of polymerization of the TAm block in polymer **PT$_{20}$**, and DP(A)**PA1** is the degree of polymerization of the AAm block in polymer **PA1**.

Supplementary Characterization for PNAM$_{40}$-*b*-PT^{Me}Am$_{20}$ (PT$^{Me}_{20}$) and PNAM$_{40}$-*b*-PAAm$_{20}$ (PA$_{20}$)

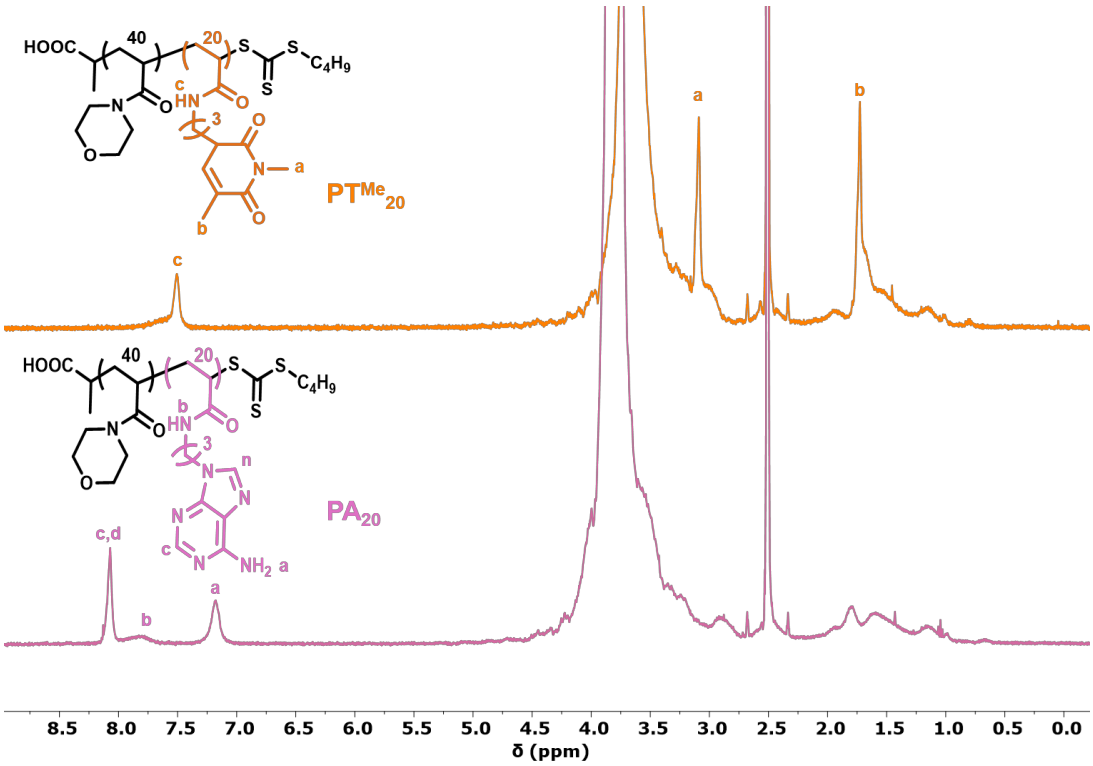


Figure 4.22. Representative ^{1}H-NMR spectra of crude (PNAM$_{40}$-*b*-PT^{Me}Am$_{20}$) **PT$^{Me}_{20}$** and PNAM$_{40}$-b-PAAm$_{20}$ (**PA$_{20}$**) obtained by aqueous RAFT-mediated PISA recorded in DMSO-d_6 (400 MHz).

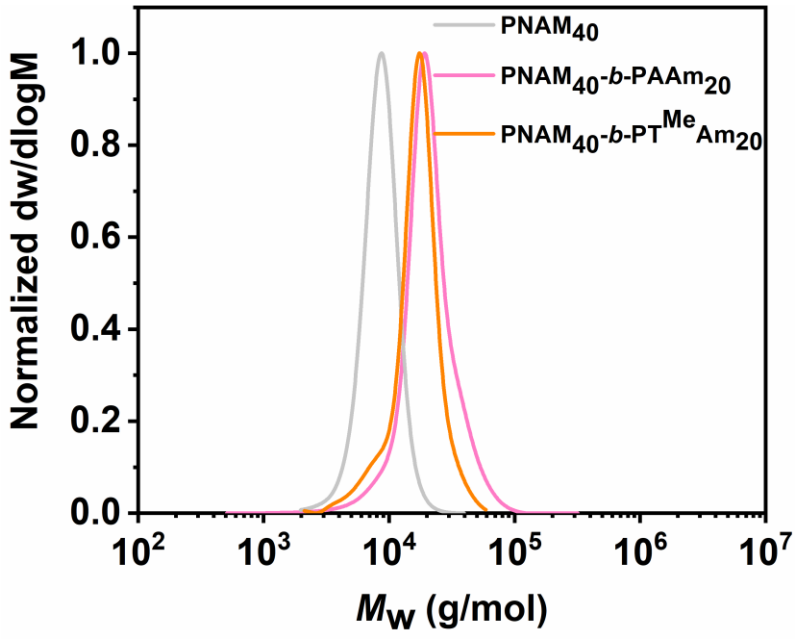


Figure 4.23. Normalized molecular weight distribution trace of $PNAM_{40}$ macro-CTA, $\mathbf{PT^{Me}_{20}}$ ($PNAM_{40}$-*b*-$PT^{Me}Am_{20}$) and $\mathbf{PA_{20}}$ ($PNAM_{40}$-*b*-$PAAm_{20}$) (DMSO + 0.1% w/w LiBr as eluent, PMMA standards).

Table 4.8. Characterization data of $PNAM_{40}$ mCTA, $\mathbf{PT^{Me}_{20}}$ ($PNAM_{40}$-*b*-$PT^{Me}Am_{20}$) and $\mathbf{PA_{20}}$ ($PNAM_{40}$-*b*-$PAAm_{20}$) obtained *via* aqueous RAFT-mediated PISA.

Polymers	% Conv.[a]	$M_{n,NMR}$[b] /kDa	$M_{n,SEC}$[c] /kD	$Đ_{M,SEC}$[c]
$PNAM_{40}$-*b*-$PAAm_{20}$	> 99	10.7	18.2	1.24
$PNAM_{40}$-*b*-$P^{Me}TAm_{20}$	> 99	11.1	14.2	1.25

[a]Monomer conversion calculated from ^{1}H-NMR spectroscopy in D_2O. [b]Calculated from conversion. [c]M_n and ĐM values calculated from PMMA standards using DMSO + 0.1% w/w LiBr as the eluent.

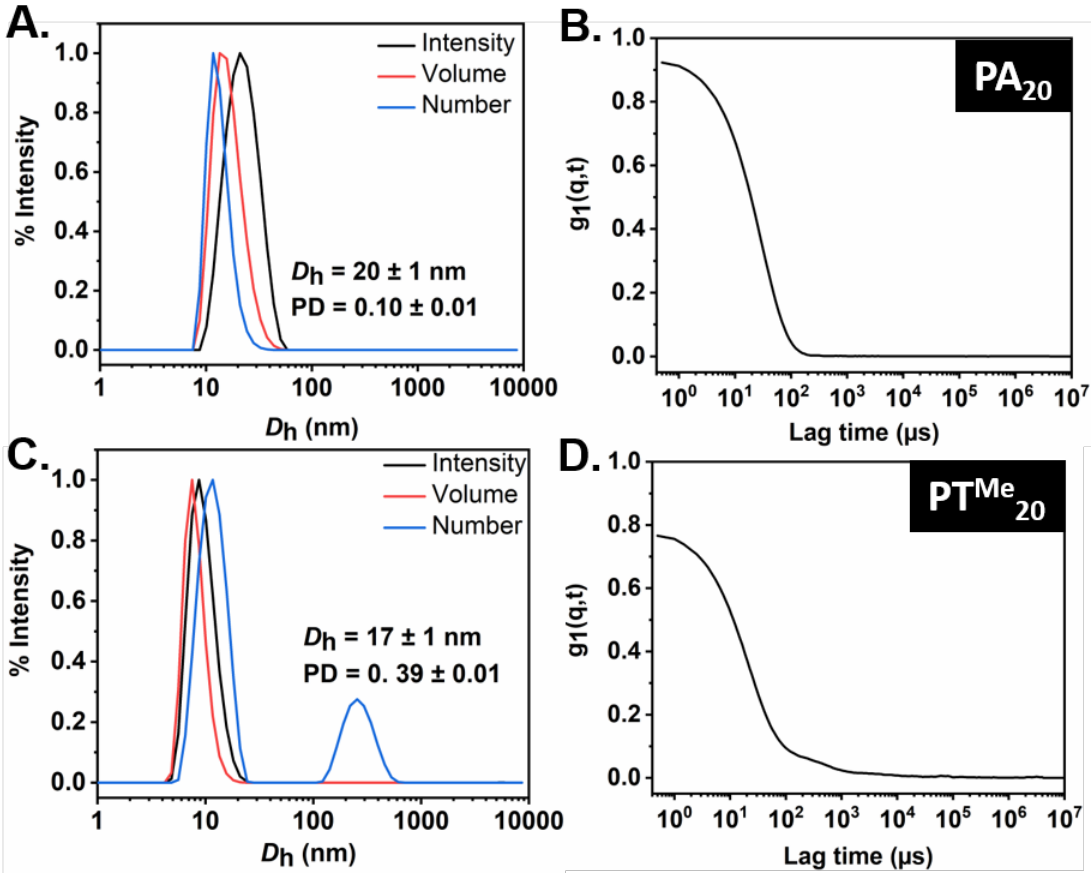
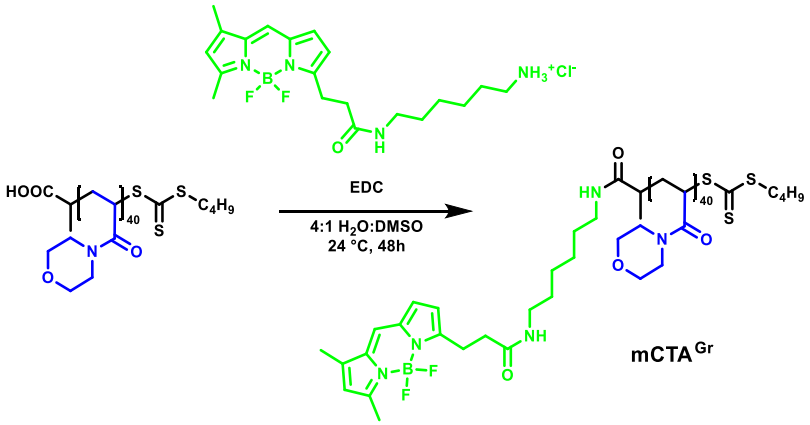


Figure 4.24. DLS (A) (C) and corresponding correlogram (B) (D) graph results of the short adeinine-containing block copolymer **PA$_{20}$** and methylated short thymine-containing block copolymer **PT$^{Me}_{20}$** respectively used in control experiments to demonstrate that complementary H-bonding interactions was needed to observe a shape transformation of the seed particles.

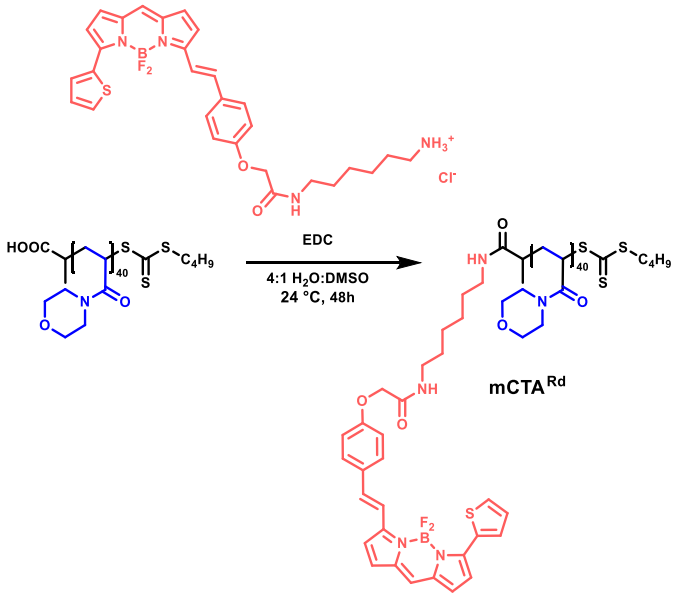
Fluorescent Tagging Using Morphological Transformation: Syntheses of Fluorescently Labelled PNAM40 macroCTA (mCTA^{Gr} and mCTARd)

PNAM$_{40}$ macroCTA were tagged with a green (**BODIPY FL**) or red (**BODIPY 630/650**) dye were synthesised as shown in Supplementary Schemes 4.5 and 4.6 by modifying the carboxylic acid end group of PNAM$_{40}$ macroCTA with amine-containing dye molecules. A typical procedure is as followed, 100 mg of PNAM$_{40}$ macroCTA was dissolved in 3 mL of water. 2.5 mg 1-Ethyl-3-(3-dimethylaminopropyl)carbodiimide (EDC) was added in the solution and stirred for at least 5 minutes. Stock solution of BODIPY FL and

BODIPY 630/650 were prepared in advance at 5 mg mL^{-1}. 140 µL was added for BODIY FL and 200 µL for BODIPY 630/650 solutions respectively. It was then stirred at room temperature for 48h. The solutions were then dialyzed against water for at least 3 days with 2 water changes per day. The samples were freeze dried and further characterized by ^{1}H NMR and SEC analysis.



Scheme 4.6. Synthesis of poly(4-acryolylmorpholine)$_{40}$ (PNAM$_{40}$) **mCTA^{Gr}** with BODIPY FL.



Scheme 4.7. Synthesis of poly(4-acryolylmorpholine)$_{40}$ (PNAM$_{40}$) **mCTARd** with BODPI 630/650.

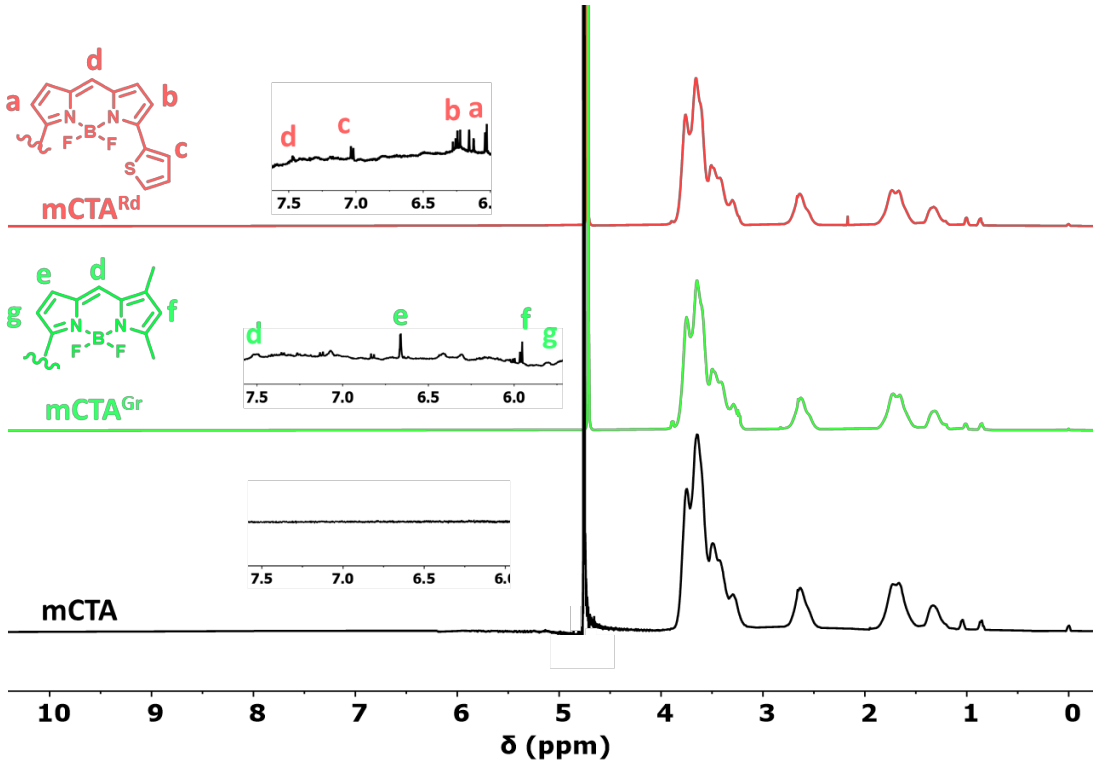


Figure 4.25. ^{1}H NMR spectra of $PNAM_{40}$ $mCTA^{Rd}$, $PNAM_{40}$ $mCTA^{Gr}$, and unmodified $PNAM_{40}$ recorded in DMSO-d_6 (500 MHz).

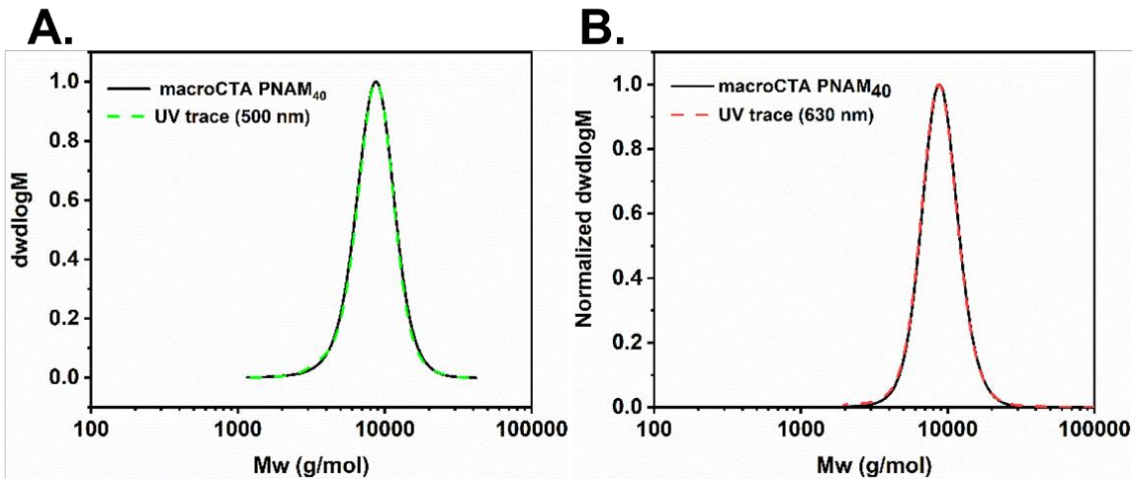


Figure 4.26. Normalized molecular weight distribution trace of poly(4-acryolylmorpholine)$_{40}$ ($PNAM_{40}$) **mCTA^{Gr}** with BODIPY FL (left) and poly(4-acryolylmorpholine)$_{40}$ ($PNAM_{40}$) **mCTARd** with BODIPY 630/650 (right). (DMSO + 0.1% w/w LiBr as eluent, PMMA standards).

Table 4.9. Characterization data of $PNAM_{40}$ mCTA, $mCTA^{Rd}$, $mCTA^{Gr}$, $PNAM_{40}$-*b*-$PTAm_{20}$ (**PT^{Rd}**)and $PNAM_{40}$-b-$PAAm_y$ (**$PA2^{Gr}$**)adenine-containing diblock copolymers obtained *via* aqueous RAFT-mediated PISA with modified macroCTA.

Polymers	Targeted DP	% Conv.[a]	$M_{n,NMR}$[b] /kDa	$M_{n,SEC}$[c] /kDa	$Đ_{M,SEC}$[c]
$PNAM_{40}$ mCTA	40	> 99	5.6	7.6	1.11
$PNAM_{40}$ $mCTA^{Rd}$	40	> 99	5.6	8.4	1.10
$PNAM_{40}$ $mCTA^{Gr}$	40	> 99	5.6	7.9	1.13
$PNAM_{40}$-*b*-$PTAm_{20}^{Rd}$	20	> 99	10.3	13.8	1.30
$PNAM_{40}$-*b*-$PAAm_{222}^{Gr}$	300	>74	60.1	91.2	3.1

[a]Monomer conversion calculated from ^{1}H-NMR spectroscopy in DMSO-d_6 (400 MHz). [b]Calculated from conversion. [c]M_n and $Đ_M$ values calculated from DMSO + 0.1% w/w LiBr as the eluent with PMMA standards.

Supplementary characterization of PA2^{Gr}n and PT$^{Rd}_{20}$n nano-objects with modified macroCTAs

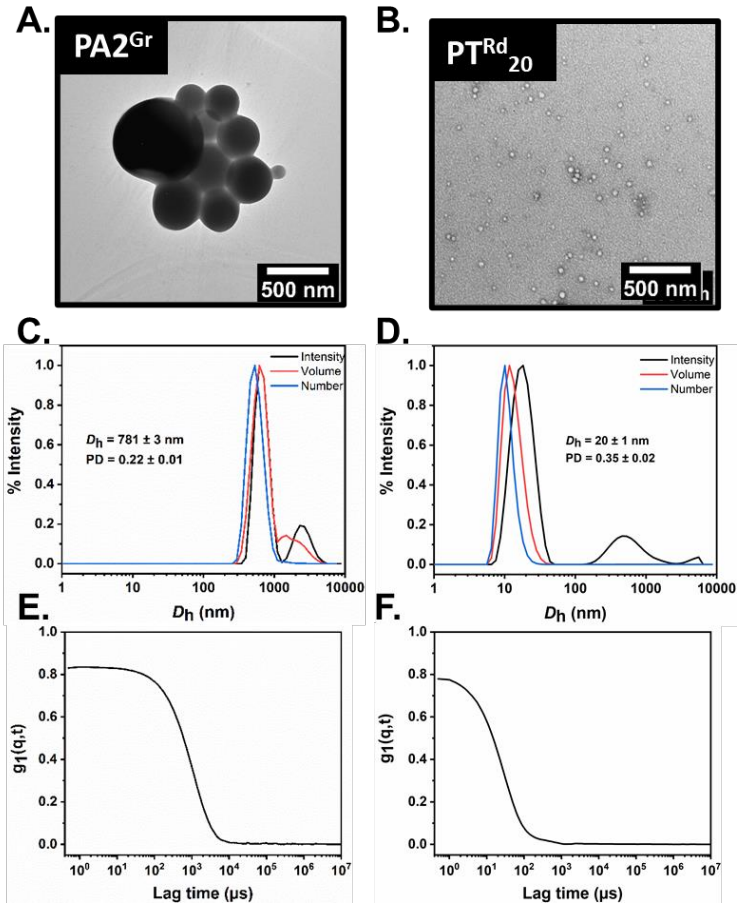


Figure 4.27. TEM images for **PA2^{Gr}** and **PT$^{Rd}_{20}$** (A) and (B) respectively. DLS results for, **PA2^{Gr}** and **PT$^{Rd}_{20}$** (C) and (D) respectively and their corresponding correlogram (E) and (F).

Vesicles were also obtained for **PA2^{Gr}n** with an average size of 781 ± 3 nm (compared to D_h = 867 ± 16 nm for **PA2n**) measured by DLS. TEM analysis confirmed those results with an average size of 616 ± 216 nm (compared to D_{ave} = 698 ± 338 nm for **PA2n**) . **PT$^{Rd}_{20}$n** particles were measured by DLS to have an average size of 24 ± 0.2 and a dispersity of 0.6 ± 0.04 suggesting a mixed morphology. This was confirmed also by TEM showing a mix of spheres and short worms.

4.5 References

1. Glotzer, S. C.; Solomon, M. J., Anisotropy of building blocks and their assembly into complex structures. *Nat. Mater.* **2007,** *6*, 557-562.

2. Sacanna, S.; Pine, D. J., Shape-anisotropic colloids: Building blocks for complex assemblies. *Curr. Opin. Colloid Interface Sci.* **2011,** *16*, 96-105.

3. Meyer, R. A.; Green, J. J., Shaping the future of nanomedicine: anisotropy in polymeric nanoparticle design. **2016,** *8*, 191-207.

4. Williams, D. S.; Pijpers, I. A. B.; Ridolfo, R.; van Hest, J. C. M., Controlling the morphology of copolymeric vectors for next generation nanomedicine. *J. Control Release* **2017,** *259*, 29-39.

5. Florez, L.; Herrmann, C.; Cramer, J. M.; Hauser, C. P.; Koynov, K.; Landfester, K.; Crespy, D.; Mailänder, V., How Shape Influences Uptake: Interactions of Anisotropic Polymer Nanoparticles and Human Mesenchymal Stem Cells. *Small,* **2012,** *8*, 2222-2230.

6. Kamaly, N.; Yameen, B.; Wu, J.; Farokhzad, O. C., Degradable Controlled-Release Polymers and Polymeric Nanoparticles: Mechanisms of Controlling Drug Release. *Chem. Rev.* **2016,** *116*, 2602-2663.

7. Reguera, J.; Jiménez de Aberasturi, D.; Henriksen-Lacey, M.; Langer, J.; Espinosa, A.; Szczupak, B.; Wilhelm, C.; Liz-Marzán, L. M., Janus plasmonic–magnetic gold–iron oxide nanoparticles as contrast agents for multimodal imaging. *Nanoscale* **2017,** *9*, 9467-9480.

8. Li, N.; Zhao, P.; Astruc, D., Anisotropic Gold Nanoparticles: Synthesis, Properties, Applications, and Toxicity. *Angew. Chem. Inter. Ed.* **2014,** *53*, 1756-1789.

9. Burrows, N. D.; Vartanian, A. M.; Abadeer, N. S.; Grzincic, E. M.; Jacob, L. M.; Lin, W.; Li, J.; Dennison, J. M.; Hinman, J. G.; Murphy, C. J., Anisotropic Nanoparticles and Anisotropic Surface Chemistry. *J. Phys. Chem. Lett.* **2016,** *7*, 632-641.

10. Thorkelsson, K.; Bai, P.; Xu, T., Self-assembly and applications of anisotropic nanomaterials: A review. *Nano Today* **2015,** *10*, 48-66.

11. Pearce, A. K.; Wilks, T. R.; Arno, M. C.; O'Reilly, R. K., Synthesis and applications of anisotropic nanoparticles with precisely defined dimensions. *Nat. Rev. Chem.* **2021,** *5*, 21-45.

12. Thiruvengadathan, R.; Korampally, V.; Ghosh, A.; Chanda, N.; Gangopadhyay, K.; Gangopadhyay, S., Nanomaterial processing using self-assembly-bottom-up chemical and biological approaches. *Rep. Prog. Phys.* **2013,** *76*, 066501.

13. Yi, C.; Zhang, S.; Webb, K. T.; Nie, Z., Anisotropic Self-Assembly of Hairy Inorganic Nanoparticles. *Acc. Chem. Res.* **2017,** *50*, 12-21.

14. Seeman, N. C.; Sleiman, H. F., DNA nanotechnology. *Nat. Rev. Mater.* **2017,** *3*, 17068.

15. Chen, Y.-J.; Groves, B.; Muscat, R. A.; Seelig, G., DNA nanotechnology from the test tube to the cell. *Nature Nanotechnol.* **2015,** *10*, 748-760.

16. Jester, S.-S.; Famulok, M., Mechanically Interlocked DNA nanostructures for Functional Devices. *Acc. Chem. Res.* **2014,** *47*, 1700-1709.

17. Praetorius, F.; Kick, B.; Behler, K. L.; Honemann, M. N.; Weuster-Botz, D.; Dietz, H., Biotechnological mass production of DNA origami. *Nat.* **2017,** *552*, 84-87.

18. Tritschler, U.; Pearce, S.; Gwyther, J.; Whittell, G. R.; Manners, I., 50th Anniversary Perspective: Functional Nanoparticles from the Solution Self-Assembly of Block Copolymers. *Macromol.* **2017,** *50*, 3439-3463.

19. Mai, Y.; Eisenberg, A., Self-assembly of block copolymers. *Chem. Soc. Rev.* **2012,** *41*, 5969-5985.

20. Warren, N. J.; Armes, S. P., Polymerization-Induced Self-Assembly of Block Copolymer Nano-objects via RAFT Aqueous Dispersion Polymerization. *J. Am. Chem. Soc.* **2014,** *136*, 10174-10185.

21. Hendricks, M. P.; Sato, K.; Palmer, L. C.; Stupp, S. I., Supramolecular Assembly of Peptide Amphiphiles. *Acc. Chem. Res.* **2017,** *50*, 2440-2448.

22. Grubbs, R. B.; Sun, Z., Shape-changing polymer assemblies. *Chem. Soc. Rev.* **2013,** *42*, 7436-7445.

23. Kelley, E. G.; Albert, J. N. L.; Sullivan, M. O.; Epps, I. I. I. T. H., Stimuli-responsive copolymer solution and surface assemblies for biomedical applications. *Chem. Soc. Rev.* **2013,** *42*, 7057-7071.

24. Wang, X.; Guerin, G.; Wang, H.; Wang, Y.; Manners, I.; Winnik, M. A., Cylindrical Block Copolymer Micelles and Co-Micelles of Controlled Length and Architecture. *Sci.* **2007,** *317*, 644-647.

25. Schmelz, J.; Schedl, A. E.; Steinlein, C.; Manners, I.; Schmalz, H., Length Control and Block-Type Architectures in Worm-like Micelles with Polyethylene Cores. *J. Am. Chem. Soc.* **2012,** *134*, 14217-14225.

26. Hua, Z.; Jones, J. R.; Thomas, M.; Arno, M. C.; Souslov, A.; Wilks, T. R.; O'Reilly, R. K., Anisotropic polymer nanoparticles with controlled dimensions from the morphological transformation of isotropic seeds. *Nat. Commun.* **2019,** *10*, 5406.

27. Sivakova, S.; Rowan, S. J., Nucleobases as supramolecular motifs. *Chem. Soc. Rev.* **2005,** *34*, 9-21.

28. Gody, G.; Maschmeyer, T.; Zetterlund, P. B.; Perrier, S., Rapid and quantitative one-pot synthesis of sequence-controlled polymers by radical polymerization. *Nat. Commun.* **2013,** *4*, 2505.

29. Perrier, S., 50th Anniversary Perspective: RAFT Polymerization—A User Guide. *Macromol.* **2017,** *50*, 7433-7447.

30. Jones, E. R.; Mykhaylyk, O. O.; Semsarilar, M.; Boerakker, M.; Wyman, P.; Armes, S. P., How Do Spherical Diblock Copolymer Nanoparticles Grow during RAFT Alcoholic Dispersion Polymerization? *Macromol.* **2016,** *49*, 172-181.

31. Blanazs, A.; Ryan, A. J.; Armes, S. P., Predictive Phase Diagrams for RAFT Aqueous Dispersion Polymerization: Effect of Block Copolymer Composition, Molecular Weight, and Copolymer Concentration. *Macromol.* **2012,** *45*, 5099-5107.

32. Ianiro, A.; Wu, H.; van Rijt, M. M. J.; Vena, M. P.; Keizer, A. D. A.; Esteves, A. C. C.; Tuinier, R.; Friedrich, H.; Sommerdijk, N. A. J. M.; Patterson, J. P., Liquid–liquid phase separation during amphiphilic self-assembly. *Nat. Chem.* **2019,** *11*, 320-328.

33. Doncom, K. E. B.; Blackman, L. D.; Wright, D. B.; Gibson, M. I.; O'Reilly, R. K., Dispersity effects in polymer self-assemblies: a matter of hierarchical control. *Chem. Soc. Rev.* **2017,** *46*, 4119-4134.

34. Spijker, H. J.; Dirks, A. J.; van Hest, J. C. M., Synthesis and assembly behavior of nucleobase-functionalized block copolymers. *Polym.Chem.* **2006,** *44*, 4242-4250.

35. Lutz, J.-F.; Thünemann, A. F.; Nehring, R., Preparation by controlled radical polymerization and self-assembly via base-recognition of synthetic polymers bearing complementary nucleobases. *J. Polym. Sci., Part A: Polym. Chem.* **2005,** *43*, 4805-4818.

36. Okano, T.; Inoue, K.; Koseki, K.; Suzuki, H., Deformation Modes of Giant Unilamellar Vesicles Encapsulating Biopolymers. *ACS Synthe. Biol.* **2018,** *7*, 739-747.

37. Tsuda, S.; Sakakura, T.; Fujii, S.; Suzuki, H.; Yomo, T., Shape Transformations of Lipid Vesicles by Insertion of Bulky-Head Lipids. *PLoS ONE* **2015,** *10*, e0132963.

38. Ge, Y.; O'Shea, D. F., Azadipyrromethenes: from traditional dye chemistry to leading edge applications. *Chem. Soc. Rev.* **2016,** *45*, 3846-3864.

39. Zhao, N.; Williams, T. M.; Zhou, Z.; Fronczek, F. R.; Sibrian-Vazquez, M.; Jois, S. D.; Vicente, M. G. H., Synthesis of BODIPY-Peptide Conjugates for Fluorescence Labeling of EGFR Overexpressing Cells. *Bioconjugate Chem.* **2017,** *28*, 1566-1579.

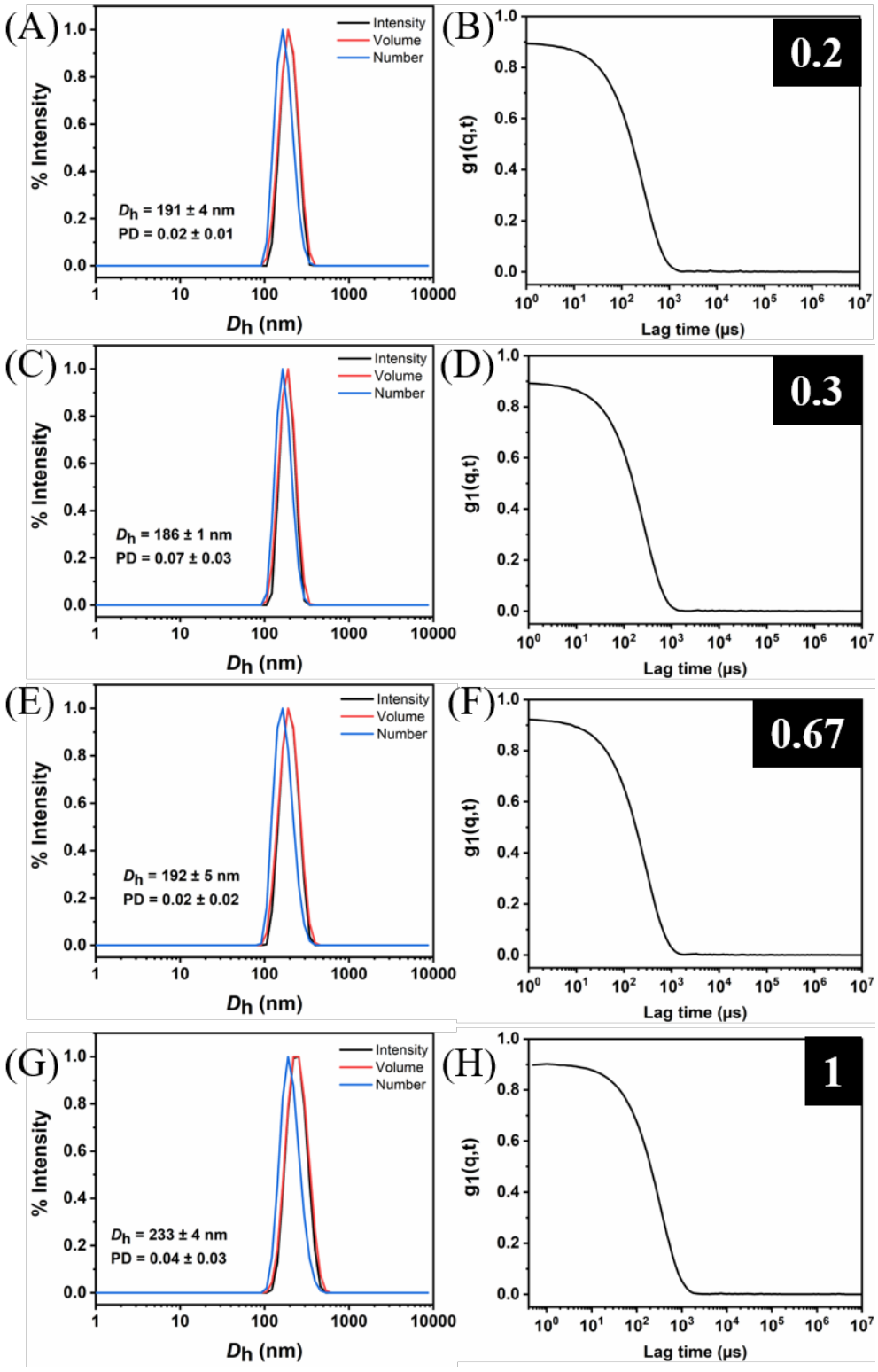
40. Niu, L. Y.; Guan, Y. S.; Chen, Y. Z.; Wu, L. Z.; Tung, C. H.; Yang, Q. Z., BODIPY-based ratiometric fluorescent sensor for highly selective detection of glutathione over cysteine and homocysteine. *J. Am. Chem. Soc.* **2012,** *134*, 18928-18931.

41. Hua, Z.; Pitto-Barry, A.; Kang, Y.; Kirby, N.; Wilks, T. R.; O'Reilly, R. K., Micellar nanoparticles with tuneable morphologies through interactions between nucleobase-containing synthetic polymers in aqueous solution. *Polym. Chem.* **2016,** *7*, 4254-4262.

42. Ferguson, C. J.; Hughes, R. J.; Nguyen, D.; Pham, B. T. T.; Gilbert, R. G.; Serelis, A. K.; Such, C. H.; Hawkett, B. S., Ab Initio Emulsion Polymerization by RAFT-Controlled Self-Assembly. *Macromol.* **2005,** *38*, 2191-2204.

4.6 Annex

Figures A4.1 and A4.2 show the DLS graph and corresponding correlogram of the MORPH PISA mixing experiments of **PA1n** and **PA2n** at different ratios of A:T from 0.2 to 2.5. Tables A1 and A2 summarize all the quantitative analysis data from the MORPH PISA experiments of **PA1n** and **PA2n** at different molar ratios.


(A)
Intensity
Volume
Number
% Intensity
D_h = 191 ± 4 nm
PD = 0.02 ± 0.01
D_h (nm)
(B)
0.2
g1(q,t)
Lag time (μs)
(C)
Intensity
Volume
Number
% Intensity
D_h = 186 ± 1 nm
PD = 0.07 ± 0.03
D_h (nm)
(D)
0.3
g1(q,t)
Lag time (μs)
(E)
Intensity
Volume
Number
% Intensity
D_h = 192 ± 5 nm
PD = 0.02 ± 0.02
D_h (nm)
(F)
0.67
g1(q,t)
Lag time (μs)
(G)
Intensity
Volume
Number
% Intensity
D_h = 233 ± 4 nm
PD = 0.04 ± 0.03
D_h (nm)
(H)
1
g1(q,t)
Lag time (μs)

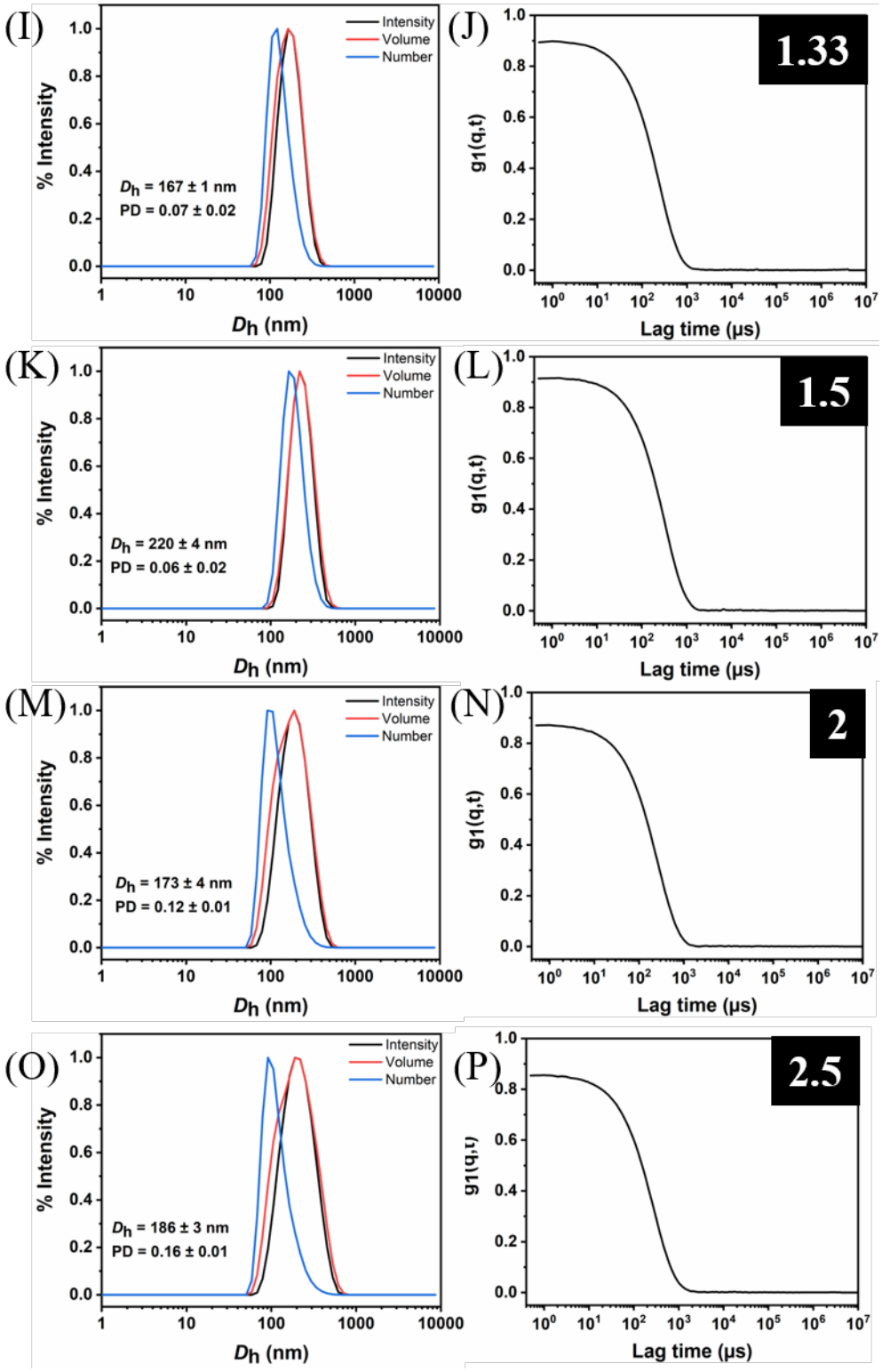
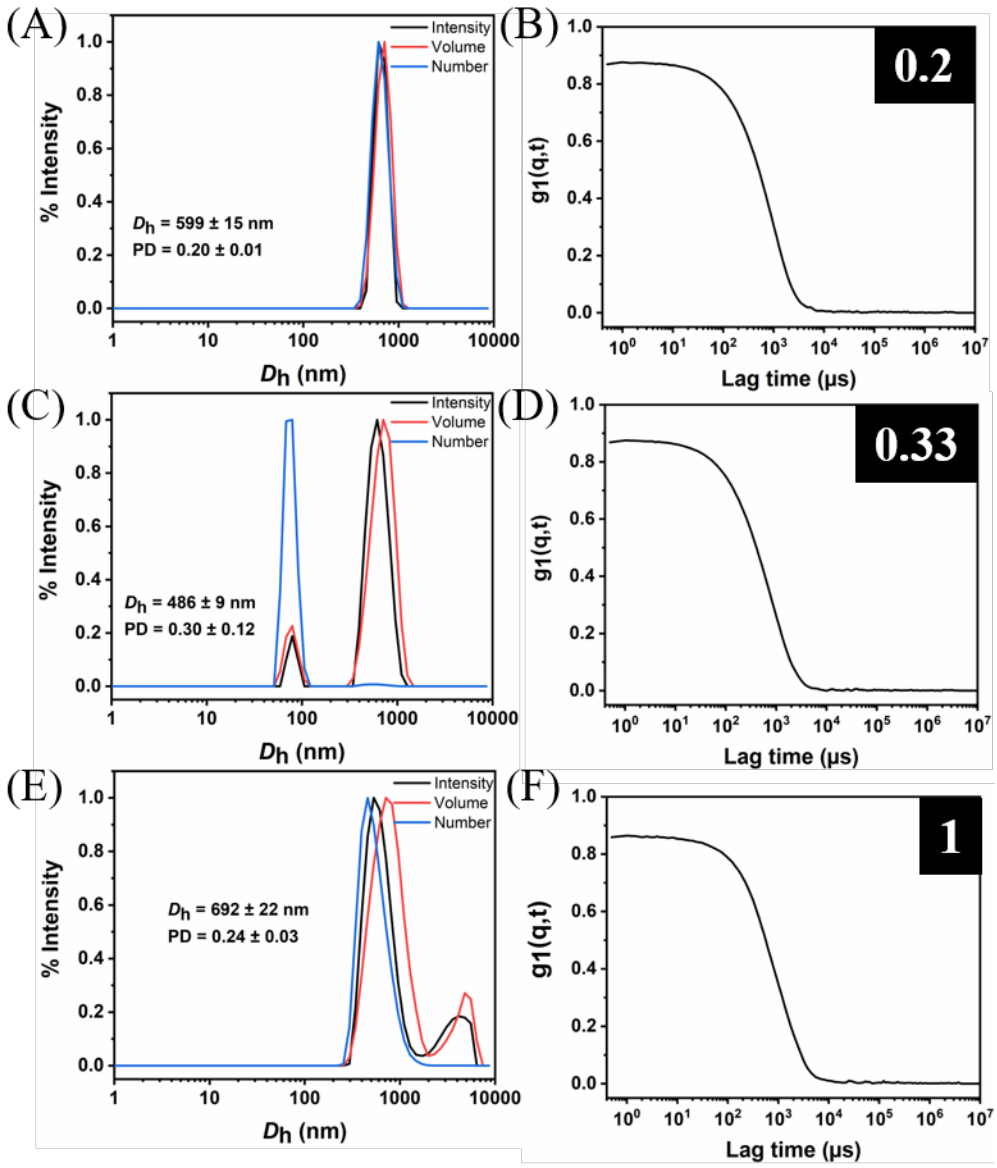


Figure 4.28. DLS results of the MORPH PISA mixing experiments of **PA1n** at different ratios of A:T.


(A)
Intensity
Volume
Number
% Intensity
D_h = 599 ± 15 nm
PD = 0.20 ± 0.01
D_h (nm)
(B)
0.2
g1(q,t)
Lag time (μs)
(C)
Intensity
Volume
Number
% Intensity
D_h = 486 ± 9 nm
PD = 0.30 ± 0.12
D_h (nm)
(D)
0.33
g1(q,t)
Lag time (μs)
(E)
Intensity
Volume
Number
% Intensity
D_h = 692 ± 22 nm
PD = 0.24 ± 0.03
D_h (nm)
(F)
1
g1(q,t)
Lag time (μs)

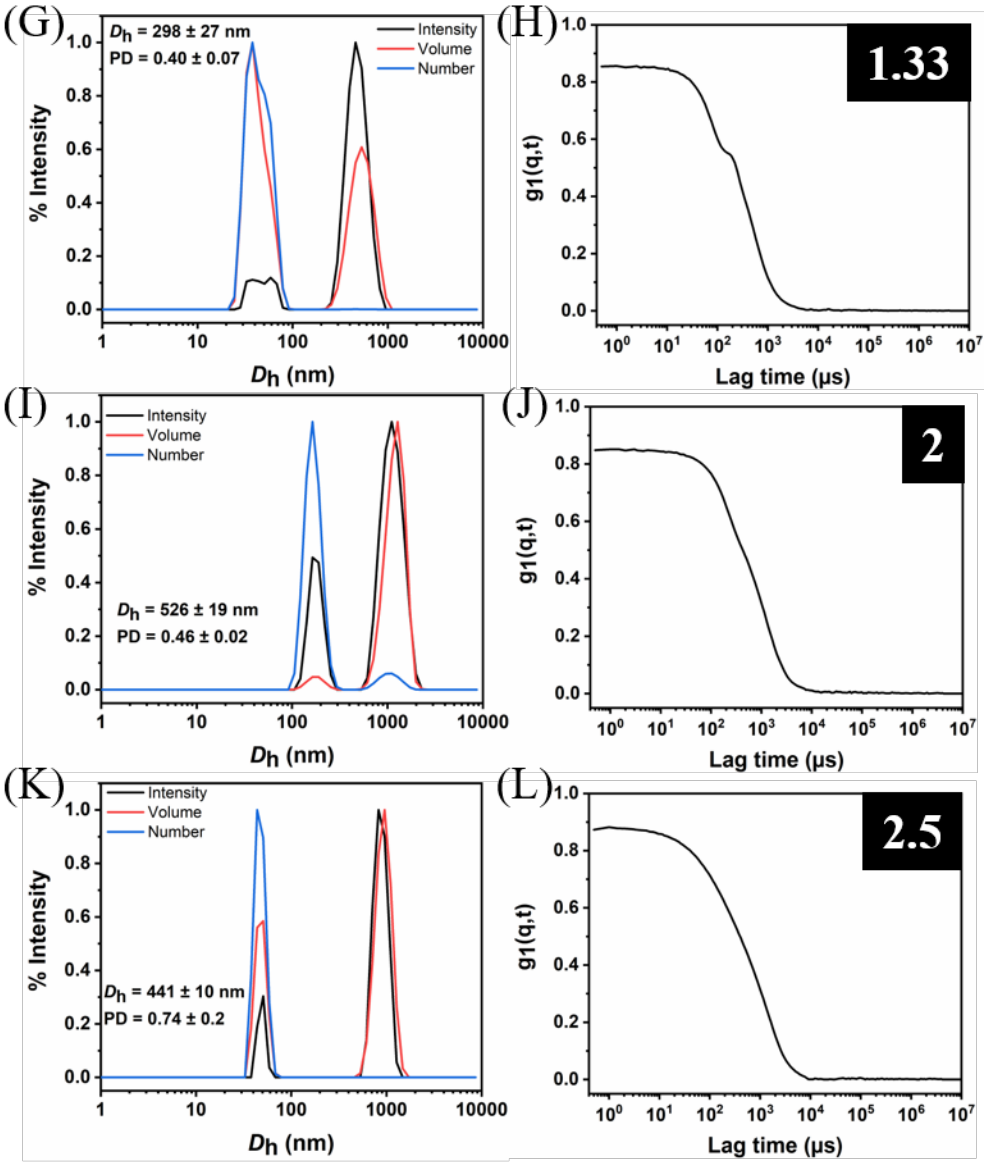


Figure 4.29. DLS results of the MORPH PISA mixing experiments of **PA2n** at different ratios of A:T.

.

Table 4.10. Summarize of data from the quantitative analysis of MORPH PISA using **PA1n** particles.

Ratios	**0.2**	**0.33**	**0.67**	**1**	**1.33**	**1.5**	**2**	**2.5**
Size DLS (nm)	191 ± 4	186 ± 2	192 ± 5	233 ± 4	167 ± 1	220 ± 4	173 ± 4	186 ± 3
Size TEM (nm)	207 ± 50	214 ± 43	207 ± 37	177 ± 28	192 ± 43	152 ± 36	152 ± 32	168 ± 43
Arms	72 ± 13	73 ± 13	73 ± 14	73 ± 10	76 ± 34	99 ± 35	111 ± 40	173 ± 54
thickness	38 ± 4.3	40 ± 5.2	40.3 ± 5.1	37 ± 2.9	39.4 ± 4.9	38.4 ± 6.4	38.2 ± 5.2	38.2 ± 7.6
No. nodes/particle	0.18	0.24	0.77	4.86	5.44	5.41	5.1	4.31
Nodes thickness (nm)	61 ± 6	56 ± 10	48 ± 4	47 ± 4	42 ± 10	28 ± 4	21 ± 2	20 ± 2

*100 particles were counting for each quantitative analysis

Table 4.11. Summarize of data from the quantitative analysis of MORPH PISA using **PA2n** particles.

Ratios	**0.2**	**0.33**	**1**	**1.33**	**2**	**2.5**
Size DLS (nm)	781 ± 3	486 ± 9	692 ± 22	288 ± 16	526 ± 19	408 ± 8
Size TEM (nm)	899 ± 197	833 ± 214	912 ± 256	862 ± 298	916 ± 237	924 ± 254
Arms	39 ± 6	79 ± 21	102 ± 23	174 ± 90	325 ± 103	355 ± 81
Thickness	- (*)	-	-	-	-	-
No. nods/particle	-	-	-	-	-	-

*100 particles were counting for each quantitative analysis. (*) data not obtained due to fact that the particles were too big.

5 : Conclusions and future work

Overall, this thesis has explored the synthesis and self-assembly of nucleobase-containing block copolymers in aqueous media.

Chapter 1 introduced polymers and an overview of the various polymerization mythologies that exist, with a focus on reversible addition-fragmentation chain transfer (RAFT) polymerization and polymerization-induced self-assembly (PISA). Then the effect of H-bonding interactions on self-assembly behaviours has been discussed. A brief overview of the synthesis, self-assembly and applications of synthetic nucleobase-containing polymers is presented. Finally, a discussion on the importance of achieving morphology and size control nanostructures.

In Chapter 2, the effect of complementary nucleobase interactions within micellar cores on the morphologies of self-assemblies in aqueous solutions was investigated. Nucleobase-containing (adenine and thymine) acrylamide monomers were successfully synthesized and polymerized *via* RAFT polymerization. A library of polymers with high DPs (up to 300) of thymine-containing core and low dispersity wad obtained. These nucleobase-containing amphiphilic block copolymers were then self-assembled into well-defined spherical nanostructures *via* solvent switch method using either slow or fast addition of water. This library of micelles was then characterized (TEM, DLS) and observed to selectively respond to complementary nucleobase-containing block copolymers. Interestingly, depending on the self-assembly method of the thymine-containing micelles, a morphological transformation could be observed or not, worm-like micelles with variable lengths (from 100 to 1000 nm) could be obtained through a stepwise addition of adenine-containing complementary block copolymers. These mechanism was named MORPH. Herein, by adjusting the nucleobase-containing synthetic polymers involved, complementary H-bonding interactions present in these

polymers could provide a new methodology to access and tune nanostructures dimensions.

In Chapter 3, an efficient methodology for the fabrication of nucleobase-containing block copolymer nano-objects with different morphologies and different concentrations using aqueous RAFT-mediated PISA was developed. This new methodology allows for the chain-extension of adenine-containing acrylamide monomers to high DPs, which was not possible with conventional RAFT polymerization. A wide range of nano-object morphologies was obtained, including vesicular structure, with a tuneable membrane thickness with DP and solid concentrations variation. This variation on the membrane thickness on these vesicles were related to the self-complementary and π-π stacking interactions from the adenine moieties inside the micelles. These structures were formed under kinetically process with single membrane vesicles. This was confirmed when different morphologies were obtained upon thermodynamic reassembly of the particles; particles at higher DP went from single-membrane vesicle to multicompartment ones.

This evolution in the membrane could provide not only a general protocol and principle for the synthesis of hollow particles with patterned internal nanostructures, as well assome hints to understand the evolution of biomembranes.

In Chapter 4, based on the knowledge gained from Chapters 2 and 3, we demonstrated that seed particles with strong self-complementarity hydrogen bonding interactions and lower surface curvature with higher surface area could undergo a morphological transformation upon addition of a complementary nucleobase-containing block copolymers. Adenine-containing vesicle seed particles were synthesized *via* aqueous RAFT-mediated PISA and mixed with the complementary thymine block copolymers to obtain unusual morphologies. The effect of different molar ratios on the morphologies

leads particles with nodes attached to the surface and a control over the number and length of the nodes could be achieved as well. These results suggested that more complex morphologies could be obtained by exploiting nano-objects structures and H-bonding interactions in complementary nucleobase-containing block copolymers.

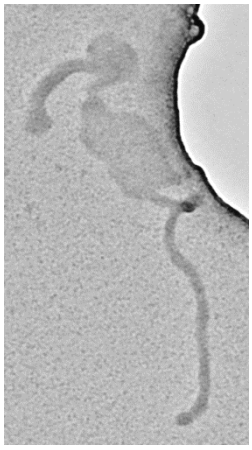
Compared to nucleic acids such DNAs, synthetic nucleobase-containing polymers require less effort to be synthesized, modified or scaled-up. They also show great potential to replace nucleic acids for numerous applications such as biological science or DNA nanotechnology among others. However, some limitations persist, and some aspects need to be resolved in order for synthetic nucleobase polymers applications to be more accessible. Although, nucleobase-containing monomers and polymers solubility reported before in water was limited, therefore more water-soluble compounds are highly desired. In addition, complementary H-bonding interactions are more favourable with acrylamide-type monomers in contrast to (meth)acrylates or styrene-type monomers for instance, due to a more flexible backbone and lower T_g.

Additional investigation could be carried to further study the influence of other complementary nucleobase-containing block polymers. With the synthesis and self-assembly of cytosine and guanine-containing block copolymers using either RAFT or RAFT-mediated PISA.

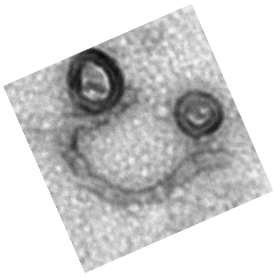
Annex

Finally, I would like to finish this thesis with some TEM images I've collected through my numerous session at the microscope over the years during my PhD.

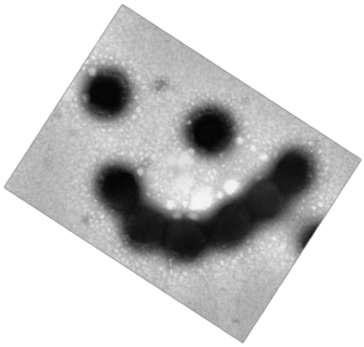
From animals,



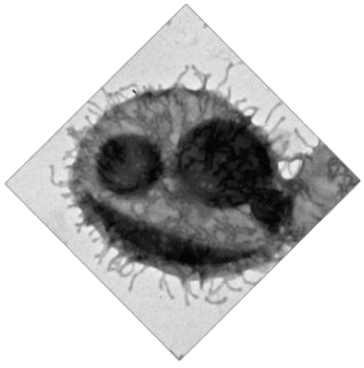
To friendly smiley faces,



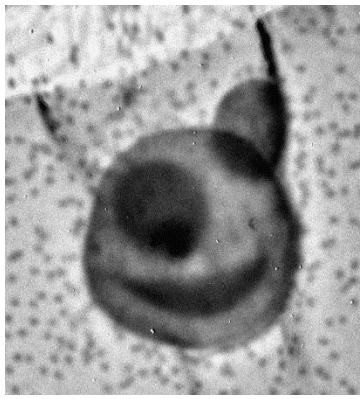




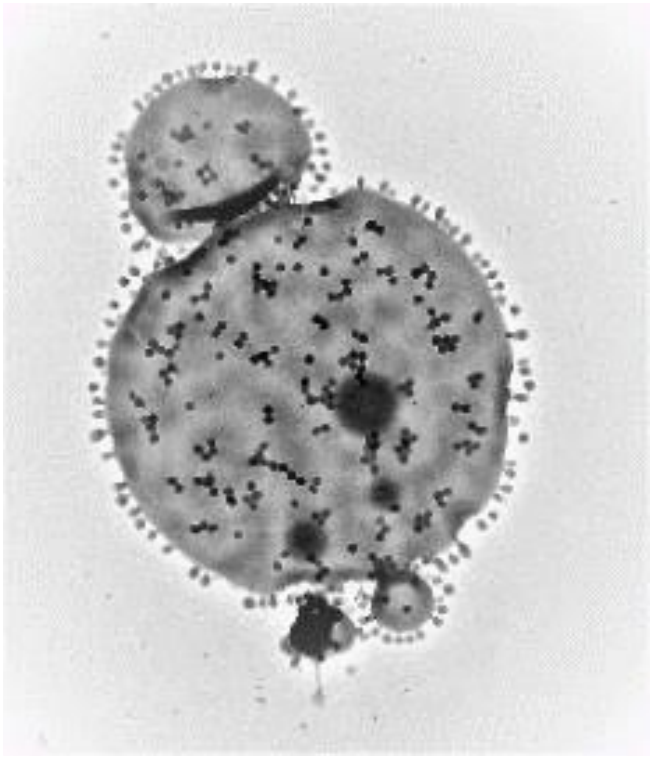


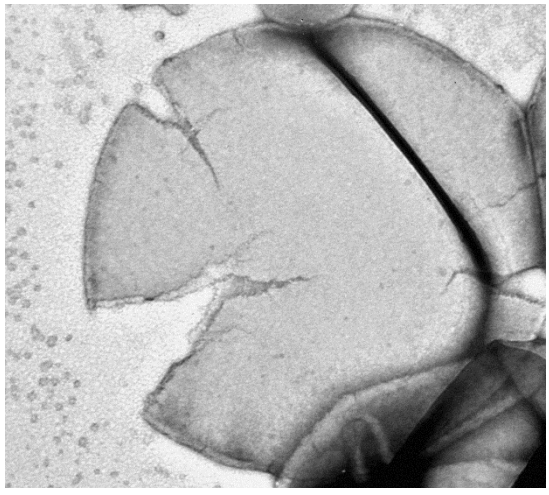


Or not…

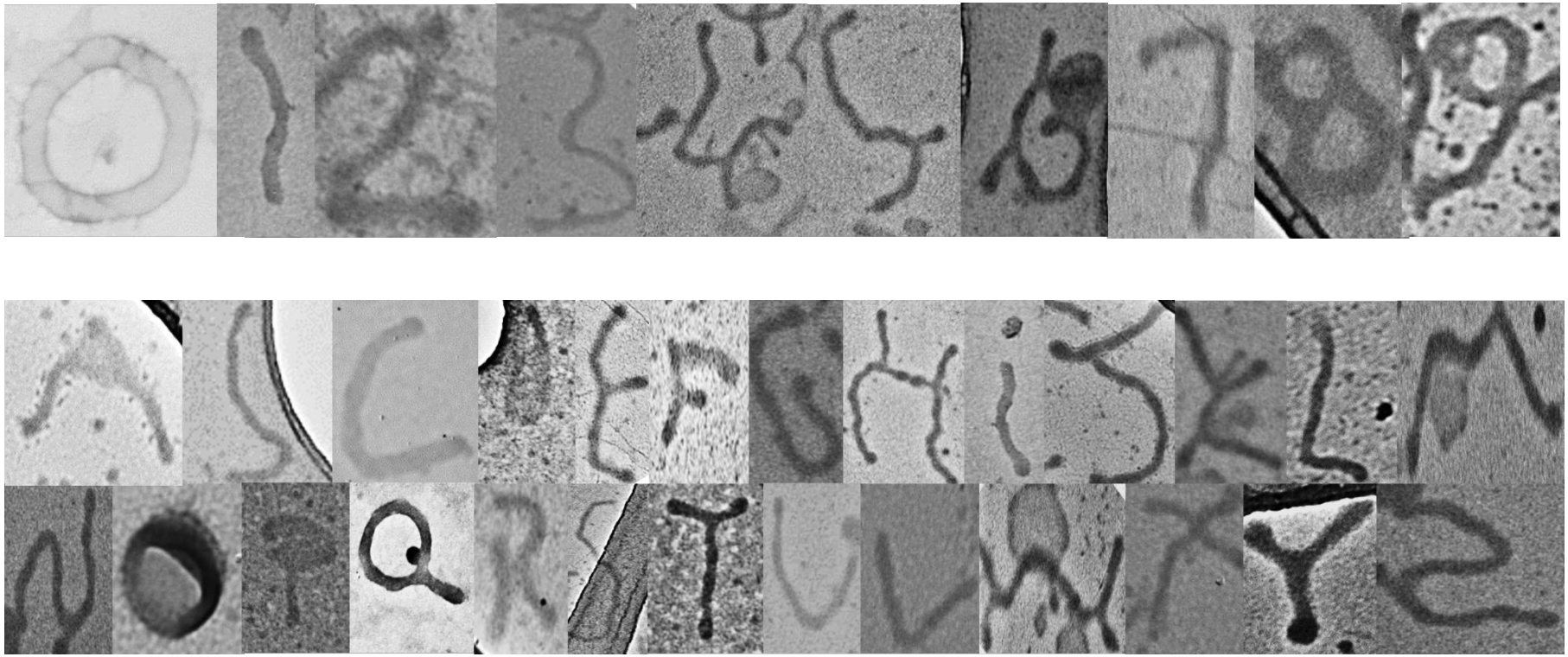


From Steve the snowman,

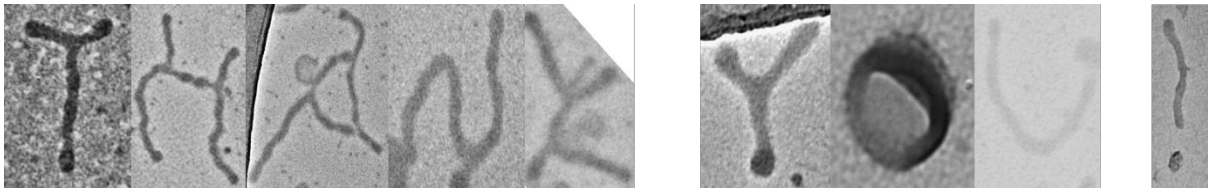




And for my numbers and polymer alphabet,



For you who have read this thesis,



This is

